Interactions between Flight Dynamics and Propulsion Systems of Air-Breathing Hypersonic Vehicles
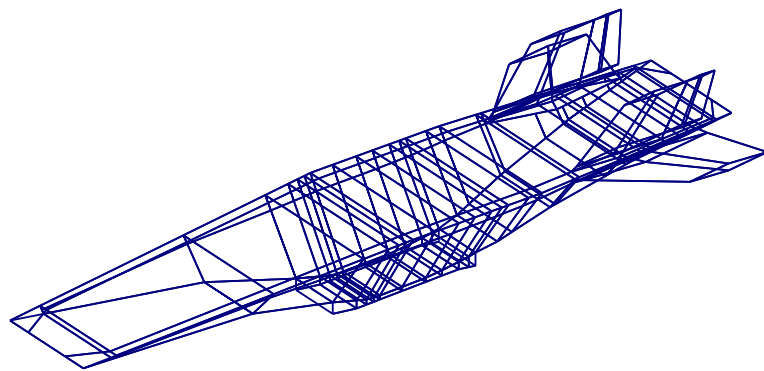
by

Derek J. Dalle

A dissertation submitted in partial fulfillment
of the requirements for the degree of
Doctor of Philosophy
(Aerospace Engineering)
in the University of Michigan
2013

Doctoral Committee:

Professor James F. Driscoll, Chair
Michael A. Bolender, Air Force Research Laboratory
Associate Professor Joaquim R. R. A. Martins
Assistant Professor David J. Singer

	Form Approved
Report Documentation Page	OMB No. 0704-0188

Public reporting burden for the collection of information is estimated to average 1 hour per response, including the time for reviewing instructions, searching existing data sources, gathering and maintaining the data needed, and completing and reviewing the collection of information. Send comments regarding this burden estimate or any other aspect of this collection of information, including suggestions for reducing this burden, to Washington Headquarters Services, Directorate for Information Operations and Reports, 1215 Jefferson Davis Highway, Suite 1204, Arlington VA 22202-4302. Respondents should be aware that notwithstanding any other provision of law, no person shall be subject to a penalty for failing to comply with a collection of information if it does not display a currently valid OMB control number.

1. REPORT DATE **2013**	2. REPORT TYPE	3. DATES COVERED **00-00-2013 to 00-00-2013**

4. TITLE AND SUBTITLE	5a. CONTRACT NUMBER
Interactions between Flight Dynamics and Propulsion Systems of Air-Breathing Hypersonic Vehicles	5b. GRANT NUMBER
	5c. PROGRAM ELEMENT NUMBER
6. AUTHOR(S)	5d. PROJECT NUMBER
	5e. TASK NUMBER
	5f. WORK UNIT NUMBER

7. PERFORMING ORGANIZATION NAME(S) AND ADDRESS(ES) **University of Michigan,Ann Arbor,MI,48109**	8. PERFORMING ORGANIZATION REPORT NUMBER

9. SPONSORING/MONITORING AGENCY NAME(S) AND ADDRESS(ES)	10. SPONSOR/MONITOR'S ACRONYM(S)
	11. SPONSOR/MONITOR'S REPORT NUMBER(S)

12. DISTRIBUTION/AVAILABILITY STATEMENT
Approved for public release; distribution unlimited

13. SUPPLEMENTARY NOTES

14. ABSTRACT

15. SUBJECT TERMS

16. SECURITY CLASSIFICATION OF:			17. LIMITATION OF ABSTRACT	18. NUMBER OF PAGES	19a. NAME OF RESPONSIBLE PERSON
a. REPORT **unclassified**	b. ABSTRACT **unclassified**	c. THIS PAGE **unclassified**	**Same as Report (SAR)**	**210**	

Standard Form 298 (Rev. 8-98)
Prescribed by ANSI Std Z39-18

2013

D E D I C A T I O N

This dissertation is dedicated to Sara Spangelo, who showed me that graduate school is more than fun, games, doing research, and writing papers. Among other things, it was also a lot of running, eating, running, and making pretty graphics. She also strongly recommended that I dedicate this dissertation to her.

Acknowledgments

I would like to thank Professor Driscoll for guiding me through the Ph.D. program and being a great advisor. My experience here was about as close to perfect as I could hope to expect, and Jim is more responsible for that than anyone else.

My colleague Dr. Sean M. Torrez, who was also a Ph.D. student of Professor Driscoll, was essential in the creation of the MASIV and MASTrim models. Also, we made a very good team.

I would also like to thank my committee for their support and work in reviewing my thesis.

TABLE OF CONTENTS

LIST OF FIGURES

LIST OF TABLES

LIST OF APPENDICES

LIST OF ABBREVIATIONS

CFD Computational Fluid Dynamics

ECEF Earth-Centered, Earth-Fixed

ECI Earth-Centered Inertial

GPS Global Positioning System

HSGTS Hypersonic Space and Global Transportation System

MASIV Michigan/AFRL Scramjet In Vehicle

MASTrim Michigan/AFRL Scramjet Trim

MAX-1 MAX-1 Vehicle Design

MDO multidisciplinary design optimization

NAI National Aerospace Initiative

NASP National Aerospace Plane

POST Program to Optimize Simulated Trajectories

RJPA Ramjet Performance Analysis Code

SAMURI Supersonic Aerodynamic Model Using Riemann Interactions

NOMENCLATURE

a	=	vehicle acceleration [m/s^2]
A	=	area, [m^2]
A	=	$\partial \mathbf{F}/\partial \mathbf{x}$, state linearization matrix
b_1, b_2	=	values used for Van Driest II boundary layer analysis
B_1, B_2	=	values used for Van Driest II boundary layer analysis
B	=	$\partial \mathbf{F}/\partial \mathbf{u}$, state linearization matrix
c_f	=	local friction coefficient
c_p	=	specific heat at constant pressure [J/kg·K]
C_D	=	drag coefficient
C_f	=	integrated friction coefficient
C_L	=	lift coefficient
C_{L_α}	=	$\partial C_L/\partial \alpha$, lift coefficient slope [1/rad]
C_T	=	thrust coefficient
C	=	$\partial \mathbf{G}/\partial \mathbf{x}$, output linearization matrix
C_a^b	=	rotation matrix from frame a to b
d_F	=	diameter of fuel injector [m]
D	=	diameter or hydraulic diameter [m]
D	=	$\partial \mathbf{G}/\partial \mathbf{u}$, output linearization matrix
E_x	=	momentum conservation error
ER	=	fuel-air equivalence ratio
$\mathbf{f}$	=	specific force [N/kg]
$\mathbf{F}$	=	nonlinear equations of motion function
g	=	9.80665 m/s^2, acceleration due to gravity
$\mathbf{g}$	=	specific gravitation vector [N/kg]
$\mathbf{G}$	=	function relating outputs ($\mathbf{y}$) to states ($\mathbf{x}$) and control variables ($\mathbf{u}$)
h	=	specific enthalpy [J/kg]
H	=	reference height [m]
I	=	moment or product of inertia divided by vehicle mass [m^2]
I_p	=	propulsive index [kg]
I_{sp}	=	specific impulse or trajectory specific impulse [s]

I	=	inertia tensor divided by vehicle mass [m^2]
L	=	physical length [m] or geodetic latitude [rad]
m	=	mass of vehicle [kg] or number of external inlet ramps
m_{fuel}	=	total mass of fuel assuming full tanks [kg]
m_{owe}	=	operational weight with no fuel or payload [kg]
$\dot{m}$	=	mass flow [kg/s]
$\dot{m}_f$	=	fuel mass flow rate [kg/s]
M	=	Mach number
M_∞	=	flight Mach number
M	=	specific moment [N·m/kg]
n	=	load factor or number of internal inlet ramps
n_{sp}	=	number of species in gas model
$\hat{\mathbf{n}}$	=	unit normal vector
p	=	pressure [Pa]
P	=	roll rate [rad/s]
Pr	=	Prandtl number
q	=	dynamic pressure [Pa]
Q	=	pitch rate [rad/s]
Q_R	=	fuel heating value [J/kg]
r_A	=	A_c/A, fraction of area that is outside separated boundary layer
r_f	=	fuel fraction, current fuel mass divided by m_{fuel}
r_p	=	inlet design compression ratio
r_{st}	=	stoichiometric fuel-air mass ratio
r	=	position vector [m]
R	=	radius of curvature [m], yaw rate [rad/s], or momentum ratio
Re$_x$	=	Reynolds number based on x
S	=	reference area [m^2]
T	=	temperature [K]
$\mathcal{T}$	=	thrust [N]
u	=	component of velocity in x-direction [m/s]
u	=	fluid velocity vector [m/s] or vector of control variables
U	=	‖**u**‖, magnitude of fluid velocity [m/s]
v	=	component of velocity in y-direction [m/s]
v	=	vehicle velocity vector [m/s]
V	=	‖**v**‖, magnitude of vehicle velocity [m/s]
w	=	width [m] or component of velocity in z-direction [m/s]

W	=	molecular weight [kg/kmol]
WR	=	weight ratio
x, y, z	=	spatial coordinates [m]
$\mathbf{x}$	=	vector of state variables
$\mathbf{y}$	=	vector of output variables
Y	=	gas species mass fraction
$\mathbf{Y}$	=	vector of mass fractions
α	=	angle of attack [rad]
β	=	shock angle (measured from flow) [rad], sideslip angle [rad], or unstart margin
γ	=	velocity flight path angle [rad] or ratio of specific heats
δ	=	deflection angle [rad]
δ_{CE}	=	$(\delta_{RE} + \delta_{LE})/2$, collective elevon angle, trailing edge down is positive [rad]
δ_{CR}	=	$(\delta_{RR} + \delta_{LR})/2$, collective elevon angle, trailing edge left is positive [rad]
δ_{DE}	=	$(\delta_{RE} - \delta_{LE})/2$, differential elevon angle [rad]
δ_{DR}	=	$(\delta_{RR} - \delta_{LR})/2$, differential rudder angle [rad]
θ	=	pitch angle [rad] or flow or wall angle, measured from x-axis [rad]
Θ	=	boundary layer momentum thickness [m]
λ	=	longitude [rad] or normalized inlet ramp length
μ	=	dynamic viscosity [kg/m·s]
$\boldsymbol{\xi}$	=	vector of input variables to trim process
ρ	=	density
σ	=	wave angle, measured from x-axis [rad]
$\boldsymbol{\upsilon}$	=	vector of variables to be solved during trim process
ϕ	=	roll angle [rad]
χ	=	velocity heading angle [rad]
ψ	=	yaw angle [rad]
ψ_E	=	elevon dihedral angle [rad]
$\dot{\omega}$	=	chemical reaction rate [kmol/m^2·s]
$\boldsymbol{\omega}_{ab}$	=	angular velocity vector between frames a and b [rad/s]
Ω_{ab}	=	angular velocity skew-symmetric matrix between frames a and b [rad/s]

Subscripts

0	=	stagnation value
$1, 2, \ldots$	=	station number or region number
∞	=	freestream or flight value
$A, B, \ldots$	=	region label

aw	=	value at wall assuming adiabatic wall
cg	=	center of gravity (mass)
C	=	fuel jet centerline
D	=	downward component
design	=	conditions used for inlet design
e	=	value at edge of boundary layer
E	=	eastward component
F	=	pertaining to fuel or injector
LE	=	left elevon
LR	=	left rudder
N	=	northward component
RE	=	right elevon
RR	=	right rudder
RS	=	conditions at ram-scram transition
ST	=	pertaining to isolator pre-combustion shock train
w	=	value at wall

Coordinate frames (subscript or superscript)

b	=	body frame, origin and axes fixed to rigid vehicle
e	=	Earth-fixed (ECEF) frame, origin at center of Earth
i	=	inertial frame, origin at center of Earth
n	=	navigation (north-east-down) frame, origin fixed to vehicle
v	=	velocity frame, origin fixed to vehicle, oriented along velocity vector

ABSTRACT

Interactions between Flight Dynamics and Propulsion Systems of Air-Breathing Hypersonic Vehicles

by

Derek J. Dalle

Chair: James F. Driscoll

The development and application of a first-principles-derived reduced-order model called MASIV (Michigan/AFRL Scramjet In Vehicle) for an air-breathing hypersonic vehicle is discussed. Several significant and previously unreported aspects of hypersonic flight are investigated. A fortunate coupling between increasing Mach number and decreasing angle of attack is shown to extend the range of operating conditions for a class of supersonic inlets. Detailed maps of isolator unstart and ram-to-scram transition are shown on the flight corridor map for the first time. In scram mode the airflow remains supersonic throughout the engine, while in ram mode there is a region of subsonic flow. Accurately predicting the transition between these two modes requires models for complex shock interactions, finite-rate chemistry, fuel-air mixing, pre-combustion shock trains, and thermal choking, which are incorporated into a unified framework here. Isolator unstart occurs when the pre-combustion shock train is longer than the isolator, which blocks airflow from entering the engine. Finally, cooptimization of the vehicle design and trajectory is discussed. An optimal control technique is introduced that greatly reduces the number of computations required to optimize the simulated trajectory.

CHAPTER 1

Introduction

Air-breathing hypersonic propulsion is a technology that has the potential to expand practical flight into a regime not currently realized by existing vehicles. Potential applications include access to space [1], high-speed transport [2, 3], and missiles [4]. At the same time, hypersonic flight introduces many challenges including high-temperature flows [5], aerothermoelasticity [6], decreased mass flow, lower lift-to-drag ratios [7], and increased coupling among the components of the vehicle [8].

Addressing the last of these issues is the focus of this work. Specifically, a better understanding is sought for the coupling between the flight dynamics and propulsion system. The tendency for hypersonic vehicles is toward engines that are large in relation to the vehicle and have performance that is sensitive to Mach number and angle of attack. These interactions pose challenges for hypersonic vehicles and any effort to model them or optimize their performance, and this justifies significant academic and industry research.

In this work, we introduce a new model derived from first principles for air-breathing hypersonic engines called Michigan/AFRL Scramjet In Vehicle (MASIV). This model incorporates complex phenomena such as inlet shock interactions, fuel-air mixing, finite-rate chemistry, exhaust plume expansion, and thermal choking. It expands on the work of Bolender and Doman [9] and attempts to model the physical phenomena that have the most impact on engine performance throughout the hypersonic regime. Despite the model complexity, it is possible to calculate the forces and moments for one operating condition in about 3 seconds on a single 2.6-GHz processor when the engine is operating in the scram mode. This time increases to 30 seconds for the ram mode because additional iterations are required to determine the thermal choking location. This could be reduced if the MATLAB code was replaced by a C++ version.

The MASIV engine model has also been incorporated into a model for the entire vehicle called Michigan/AFRL Scramjet Trim (MASTrim), which calculates the net accelerations and angular accelerations of the vehicle and provides tools to balance the forces and moments to achieve desired accelerations. MASTrim also calculates the linearized equations

of motion to study the basic stability and controllability characteristics of the vehicle at a given flight condition.

These models are used to simulate flight of a class of vehicles throughout the entire hypersonic flight envelope from isolator unstart, which sets the lower bound on the flight Mach number (M_∞), to ram-to-scram transition, which occurs at an intermediate Mach number, to the Mach number where the vehicle no longer attains adequate thrust to maintain steady, level flight. Several significant and previously unreported trends are discussed throughout. Predictions of the flight conditions at which both unstart and ram-to-scram transition occur are made for the first time. The realization that a decreasing angle of attack at higher Mach numbers allows the inlet to operate over a wide range of conditions leads us to recommend a shift from the constant–angle-of-attack design currently advocated in the literature [10, 11].

Simultaneous optimization of a vehicle design and ascent trajectory is also presented. A new trajectory optimization technique based on lessons from optimal control allow a significant reduction in the computation required for the trajectory optimization.

The present work provides a relatively complete picture of hypersonic flight, but many questions remain, and in fact several new ones are identified. For example, a region of potential instability near ram-scram transition is identified. A jump in the thrust is also predicted when the mode transitions, but the jump is sensitive to the choice of model. In both cases, more experimental research is needed to resolve the issue, and specific recommendations are made. As a result of these and other questions, the work is able to conclude with considerable suggestions for future work.

1.1   Motivation

The case for developing hypersonic vehicles is usually made by comparing to rockets, which must carry their own oxidizer in addition to fuel [12]. Because air-breathing engines do not need to carry their oxidizer, they have the potential for much more thrust per kilogram of fuel. Acquiring the oxidizer from the air and slowing it to a speed at which combustion can occur adds considerable complexity, and the benefit is not the same for all vehicle speeds. The result of this trend is a graph like that of Fig. 1.1, which shows a sketch of vehicle performance for a range of flight Mach numbers (M_∞) and a variety of propulsion systems.

A common measure of the efficiency of a propulsion system is the specific impulse,
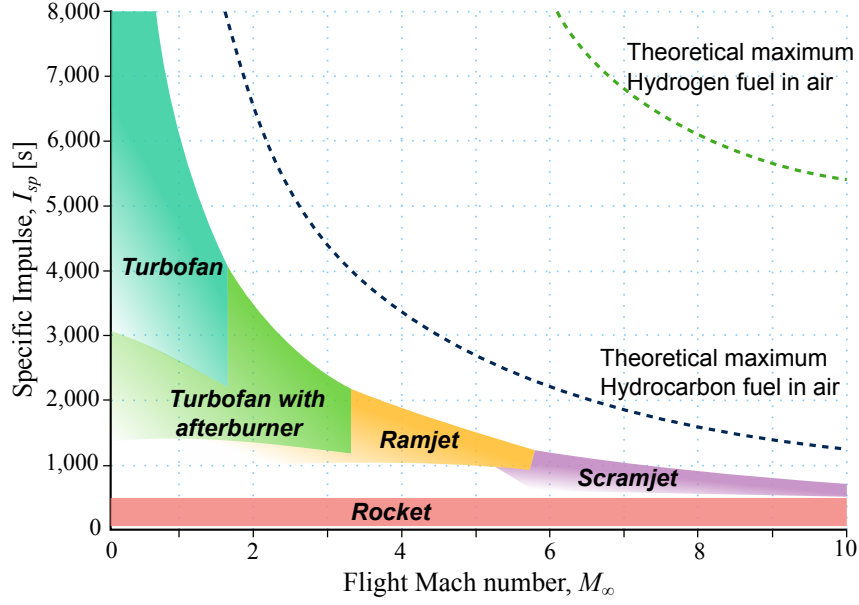
Figure 1.1: Approximate efficiency (specific impulse) as a function of Mach number for various aerospace propulsion systems.

which is defined as

$$I_{sp} = \frac{\mathcal{T}}{\dot{m}_f g} \tag{1.1}$$

where $\mathcal{T}$ is the thrust, $\dot{m}_f$ is the rate of fuel injected (fuel mass flow rate, in kg/s), and $g=9.8$ m/s^2. This measures the amount of thrust produced for each kilogram of fuel used. As Fig. 1.1 shows, air-breathing propulsion systems are more efficient than rockets, but the difference is smaller at high Mach numbers.

In air-breathing hypersonic flight, the engine has a much more complicated task than in either rocket-powered or gas-turbine–powered aircraft, and this can be demonstrated using a very simple analysis. Consider a trajectory in which the dynamic pressure remains approximately constant:

$$q_\infty = \frac{1}{2}\rho_\infty U_\infty^2 = \frac{1}{2}\gamma p_\infty M_\infty^2 \tag{1.2}$$

An increase in dynamic pressure benefits vehicle thrust up to some fixed limit imposed by the vehicle structure [11]. The mass flow captured by the inlet is then

$$\dot{m} = \rho_\infty U_\infty A = \frac{q_\infty A}{U_\infty} \tag{1.3}$$

where A is the inlet capture area, which varies slightly with Mach number and angle of attack. Eq. 1.3 shows that as the velocity increases, the mass flow goes down, and thus

there is a lower potential for thrust. The first consequence is that the engine the engine has to occupy a large fraction of the vehicle cross-section area, with the corollary being that the engine also has to provide much of the lift. Furthermore, the inlet is responsible for compressing the freestream to a sufficiently high pressure for combustion, which means that engine performance can be highly sensitive to flight conditions such as Mach number and angle of attack.

For an engine to provide adequate thrust over a wide range of flight conditions, it must address at least the following points.

- The inlet must provide adequate compression (at least 0.5 atm) to the combustor.

- The compression must not cause too high of an entropy rise, i.e., stagnation pressure loss, which would limit combustor performance.

    - The compression tends to rise with M_∞, but the efficiency tends to decrease.

    - Interactions between shock waves can cause large drops in performance at off-design conditions. A successful inlet design must limit shock interactions throughout the flight envelope.

- The engine must not cause too large of a moment on the vehicle. This will size the elevators.

- The back pressure from the combustion must not block flow from entering the engine.

- The stability derivatives must be such that the vehicle can be stabilized and controlled.

- The engine must produce a net positive acceleration.

These points mean that the design of an air-breathing hypersonic engine is a difficult engineering problem. At the same time, it also means that constructing an appropriate flight dynamics model is equally challenging. To ensure that the model is able to evaluate the engine performance with respect to each of the points in the list above, the model must capture the following phenomena.

- Shock-shock and shock-expansion interactions affecting inlet efficiency and spillage

- Fuel-air mixing

- Finite-rate chemistry for estimation of the flame length

- Accurate modeling of the nozzle exhaust plume to estimate nozzle lift and thrust

- Thermal choking

- Back pressure due to combustion and the pre-combustion shock train created by the back pressure

The MASIV and MASTrim models account for these effects, although there are other factors that may have a qualitative impact on the performance of hypersonic vehicles.

In one way, the sketch in Fig. 1.1 shows the potential importance of optimization for scramjet-powered vehicles. Because the efficiency increase relative to rockets is less at higher Mach numbers, a small improvement in performance may have a greater impact on how favorable the scramjet design is to a rocket. Figure 1.1 also demonstrates another difficulty that optimization can help address. Namely, a dual-mode ramjet-scramjet vehicle used as an accelerator must operate over a very wide range of Mach numbers–from perhaps Mach 4 to Mach 12. Even the fastest air-breathing piloted vehicle to date, the SR-71 [13] operated over a much smaller range of Mach numbers in comparison. The literature on this topic often implicitly suggests that the geometry should continuously morph to adjust to each Mach number (e.g. [14]). In this work, the difficulties associated with operating over a range of Mach numbers are addressed directly.

While hypersonic vehicles are by necessity highly integrated, future aerospace vehicles of all varieties are likely to become more integrated as well [10]. This trend toward highly integrated vehicles enables system performance and economic gains, and as a result the experience gained with necessarily integrated hypersonic vehicles will have applications for many classes of aircraft.

1.2   Background

The difficulty of air-breathing hypersonic flight is apparent from the failures of programs like the National Aerospace Plane (NASP), National Aerospace Initiative (NAI), and HTV-3X to demonstrate hypersonic flight [15]. At the same time, hypersonic flight in the form of rockets and reentry vehicles has been a reality for over fifty years; it is the nature of hypersonic propulsion that introduces special challenges [16]. Research spanning several decades [17–21] repeatedly indicates that hypersonic flight is possible and economically feasible, but after fifty years of research into air-breathing hypersonic flight, flight data is limited to a few minutes from the X-43 [22] and the X-51 [23].

This overview of the hypersonic literature focuses on the aspects of hypersonic flight that is most relevant to the present work. These include integrated propulsion systems including ram-to-scram transition; flight dynamics, with a special focus on trajectories; and

optimization. Several studies on the economic feasibility are included to put the research in perspective.

1.2.1 Applications

One application that has driven a great deal of research in the area of hypersonic propulsion and flight dynamics is highly responsive missiles. Starkey and Lewis [24] demonstrated that such missiles have combinations of range and response time that are outside the capabilities of other missile types. This result is in agreement with previous statements [25], and this is an important driver of hypersonic research.

The trajectory analysis in this thesis primarily considers the acceleration of a hypersonic vehicle. The acceleration phase is an important part of flight for most hypersonic vehicles, but it is particularly important for the application of space access. The most well-known proposal for such a concept is the NASP [26], but other programs such as Skylon [27, 28] and the Astrium spaceplane [29] are the subjects of current research. Other concepts have been developed with the backing of very interesting research but without such popular names or acronyms. A notable example is the so-called Hypersonic Space and Global Transportation System (HSGTS), which places the inlet on the top of the vehicle opposite its usual location [30].

A closely related and somewhat surprising application of hypersonic flight is high-altitude tourism [31]. Hypersonic vehicles for tourism require acceleration and ascent, and possibly the vehicle will have to return to its original airport. Compared to other tourism options such as the SpaceShipOne [32], hypersonic vehicles face more difficult technological challenges and offer much longer flights. This is one of the applications proposed for the DLR's FAST20XX concept [33] and the Astrium spaceplane.

Passenger transport at very high speeds has also gained much attention throughout the history of hypersonic research. Currently the only competing class of aerospace vehicle for transport at comparable speeds is a rocket boost plus a long-range dynamic glide phase [34]. By comparison, air-breathing hypersonic flight may actually be safer. Vehicle concepts include the LAPCAT [3] and the FAST20XX [35], but experience with supersonic transport and the difficulty of modern airlines to make a profit show that this can be a difficult proposition [36].

1.2.2 Component Analysis

An air-breathing hypersonic vehicle can be split into the following components, which are also listed with primary roles for each component.

- *Engine*, which provides the vehicle's thrust and a significant portion of the lift

    - *Inlet*, compresses freestream flow for better combustion and provides lift (depending on the configuration)

    - *Isolator*, region of internal flow for pre-combustion shock train if needed; highly coupled with combustor

    - *Combustor*, component for subsonic or supersonic combustion

    - *Nozzle*, expands flow for high thrust and may provide lift depending on design

- *Control surfaces*, trim forces on vehicle and control vehicle attitude

- *Exterior surface*, provide high lift and minimal drag

Models for each of these components are necessary for a successful vehicle trajectory analysis and optimization, which is the goal of the present work.

Developmental research into hypersonic control surface ranges from basic force and moment calculations [37–39] to aeroservothermoelastic analysis [40–42] to considerations of the actual construction of the materials and moving parts [37]. For flight dynamics research, the calculation of forces and moments is most relevant, although other considerations such as frequency limitations and thermo-structural deformations may place important limits on the flight envelope and performance of the vehicle. Calculation of forces using Computational Fluid Dynamics (CFD) dates from at least 1982 in the work of Chaussee and Rizk [43]. More recent computational studies on hypersonic control surfaces have investigated diverse situations such as canard-elevon interactions by Skujins et al. [39], aeroelastic stability boundaries by Lamorte and Friedmann [44], and aerothermoelasticity by Crowell and McNamara [45] and Falkiewicz and Cesnik [42].

An interesting report by Cole and Aroesty [46] suggests that the optimum shapes for control surfaces at hypersonic velocities may differ significantly from the diamond airfoil shapes typically assumed. Attempts to reproduce the counterintuitive shapes suggested by Cole and Aroesty for three-dimensional hypersonic wings have not been reported.

Another category relevant to the hypersonic forces and moments is the calculation of forces on an aerodynamically optimized vehicle with no propulsion system. Research into waverider designs that fit this category is extensive; examples include viscous shape optimization by Bowcutt et al. [47], stability derivative calculations by Tarpley and Lewis [48], temperature calculations by Zien [49], and experimental data from Gillum et al. [50].

Finally, research into the aerothermodynamics of reentry vehicles [51] can also be useful for air-breathing hypersonic studies, and a great deal of flight data is available [52, 53],

but some of the properties of the gas dynamics at reentry speeds and altitudes differ from the gas behavior in the flight regimes where air-breathing propulsion is practical [54].

Detailed simulation of air-breathing hypersonic propulsion systems for a wide range of flight conditions (Mach number, angle of attack, and/or sideslip angle) is relatively rare in the literature. Brown et al. [55] consider the performance of two-dimensional inlets much like those studied in this thesis. They considered varying Mach number and also discussed the formulation of the robustness properties that such an inlet must have to operate effectively over a wide range of velocities. O'Brien computed the viscous performance of a realistic streamline-traced inlet using CFD for a wide range of Mach numbers and angles of attack [56].

For idealized vehicles or idealized flow conditions, more progress has been made. Sabean and Lewis optimized the design of an axisymmetric profile launching from a tube filled with a fuel/oxidizer mixture [57]. Under such conditions, an accurate simulation is relatively easy to attain. The work of Sabean and Lewis uses the thrust coefficient at three different Mach numbers as three separate objective functions. Many inlet designs focus on optimized shapes that have unknown performance at off-design conditions [58]. Despite this, studies have shown that these streamline-traced inlets tend to have good off-design performance [56], and even different streamlined-traced designs morphed together perform well [59].

Computational techniques with reduced computation time are more desirable for control or trajectory studies, but they are also difficult to construct for complex hypersonic inlets. Bussey and Lewis developed a technique for three-dimensional inlets that uses compound compressible flow [60], but more progress is needed before it can be used to analyze generic inlet designs. In this regard, the present research (e.g. [61]) is a unique contribution, although it is limited to two-dimensional inlet designs.

Models with reduced computational time for the combustor are perhaps more common, but with some caveats. The Ramjet Performance Analysis Code (RJPA) code [62] has been used to analyze subsonic and supersonic combustion ramjets for several years, but it is a zero-dimensional analysis (that is, the flow is solved at several stations using algebraic models without using any differential equations), and RJPA also requires the user to specify the combustion efficiency. The SRGULL code [63, 64] is an engineering code for the performance of an entire integrated flowpath, and it uses an equilibrium-chemistry model for the combustor. In addition to the equilibrium-chemistry limitation, it assumes that all of the fuel mixes efficiently with the supersonic air. Despite the lack of finite-rate chemistry and mixing models, it showed a close match to the Mach 7 static pressure flight data from the Hyper-X (X-43) program [65]. That experience suggests that simpler analysis methods

are appropriate when ground testing or other testing shows that the engine meets certain criteria such as good mixing. We would not expect an equilibrium model to match pressure profiles for a case when the fuel and air do not mix or the fuel does not ignite.

The model of O'Brien et al. [66] includes finite-rate chemistry but not fuel-air mixing. As this summary implies, there are very few competing models for dual-mode ramjet-scramjet combustion. A small number of other programs have existed, such as SCCREAM [67] and RASCAL [20], but they have become obsolete or are not widely used. The work of Torrez et al. [68, 69] (used for the present thesis research) includes all these effects, but is currently limited to simple fuel injection schemes.

Peterson et al. [70, 71] have demonstrated that CFD simulation of supersonic combustion has made progress but is still not able to match experimental data with the same success as for external flows. Baurle and Eklund [72] also showed that a detailed CFD analysis of a hydrocarbon scramjet was not able to match experimental data. Note that in this case, the reduced-order methods have actually produced more accurate results, although we do not expect this to always be the case.

The literature is less extensive for hypersonic nozzles, partially because they are better understood. Nozzle designs with a free shear layer using the method of characteristics date from Nickerson and Dunn [73], while analysis of these nozzles at off-design conditions is difficult to find. A study by Sangiovanni et al. [74] showed that the recombination of postcombustion gases may have a significant effect on thrust at high flight Mach numbers. Our work [75,76] agrees with this assessment using a two-dimensional model, but the effect is largest at Mach numbers above the range where air-breathing propulsion is expected to be advantageous. In comparison, analysis of plug nozzles, which are similar in many aspects, is more extensive [77–81], and these results were used to validate the nozzle analysis used in the present research.

1.2.3   Flight Dynamics

A great deal of literature exists on many aspects of the flight dynamics of hypersonic vehicles. Analyses of hypersonic vehicles can be divided into the following rough groups, which are organized approximately from the lowest levels of integration (i.e. individual component analysis) to complete vehicles with complete trajectories.

1. Component force and moment calculations

2. Vehicle net force and moment calculations

3. Trim analysis and stability and control analysis

4. Trajectory simulation and optimization

5. Feedback control design and simulation

The items are not entirely hierarchical because research on items earlier in the list are often much more detailed than the component models used as part of tip-to-tail vehicle analyses. This scheme tends to work well when the component analyses give results that can be represented by simpler formulas with reasonable accuracy.

In the present work, the MASIV and MASTrim models are used to address points 1–4 using a unified representation of the vehicle throughout.

The first of these points was discussed in Sec. 1.2.2, and few studies address point 2 without continuing to point 3. Chavez and Schmidt [8] presented a two-dimensional model for a scramjet vehicle using a first-principles analysis along with an analysis of the linearized stability properties at a trimmed flight condition. Bolender et al. [9, 82, 83] presented a similar model for longitudinal flight with more accurate submodels. Both reports found a merged phugoid-altitude mode, which differs from the uusual results for subsonic and supersonic aircraft. The work of Chavez and Schmidt and Bolender et al. shares a common trait with Frendreis et al. [84, 85] in that it also considers the effects of flexibility on hypersonic flight. Current development is ongoing to include flexibility into the MASTrim model.

Both Chavez and Schmidt [8] and Oppenheimer and Doman [38] calculated the stability derivatives analytically using Newtonian flow [8] and first-order piston theory [38]. We also introduced a model for six-degree-of-freedom hypersonic flight [86], but without flexibility considerations.

Singular perturbation theory [87, 88] is a technique that has been used for several trajectory optimization studies involving hypersonic vehicles. A common thread in these studies is to write the fuel mass flow rate as a function of the flight condition variables, as is done in Chapter 6. Halter and Cliff [89] used singular perturbation theory to calculate optimum trajectories including change of heading. Chichka et al. [90] present a trajectory analysis using singular perturbation theory. In [90] a region of "chattering" was reported where the thrust required for trim is below the minimum value that can be attained with the engine on, and as a result the vehicle must rapidly switch the engine on and off to achieve unaccelerated flight. Since this mode of flight is impractical, it constitutes another unexpected operating limit.

The NASP trajectory work by Calise et al. was quite extensive, and utilized a technique to eliminate time from the fuel consumption calculation similar to the one presented here [91]. In their work time integration is replaced with integration with respect to specific

energy, whereas here velocity is used. Their use of singular perturbation theory also resembles the trajectory optimization formulation presented in this work, although it involves the solution of a two-point boundary value problem that in practice can be difficult to solve. That work was later extended by Corban et al. [92] to allow fuel mass flow rate to be an arbitrary function of angle of attack. However the present work goes a step further by considering trajectory optimization in which the fuel mass flow rate is an arbitrary function of both angle of attack and Mach number.

Keshmiri et al. [93] used optimal control theory directly rather than employing singular perturbation analysis. Their work did not remove time from the simulation, which can lead to computational difficulties with increasingly complex vehicle models. Gilbert et al. [94] and Lu [95] found that using traditional optimal control techniques, optimization of hypersonic trajectories has difficulty in achieving convergence because of high sensitivity of hypersonic flight. Lu [95, 96] proposes inverse dynamics as a solution to this difficulty.

Other approaches to simulate or optimize trajectories have included using a code called Program to Optimize Simulated Trajectories (POST) [97] by Olds and Budianto [11] and continuation by Grant et al. [98]. Torrez [99] used a collocation method [100] to simulate a hypersonic trajectory, and the optimization was done directly. Trajectory studies in other fields by Spangelo and Gilbert [101] discussed the potential pitfalls of using splines in the trajectory simulation.

Feedback control of hypersonic vehicles is not considered in this thesis, but it is a closely related topic. Schmidt [102] discussed important properties of the hypersonic control problem including the tendency for thrust control variables to excite structural modes. Raney and Lallman [103] considered the complex case of controlled flight during a hypersonic turn, and Parker et al. [104] developed a control law for the model of Bolender and Doman [9] using feedback linearization. Further information on this topic can be found in [105].

1.2.4 Coupling between Propulsion and Flight Dynamics

Investigations of air-breathing hypersonic vehicles consistently show a higher degree of coupling between flight conditions and engine performance than other types of air vehicles. Specific examples are myriad. Schmidt found that changes in the thrust input can excite problematic structural modes [102]. Torrez et al. [106] found that accounting for finite-rate chemistry causes a noticeable shift in the poles of the linearized system. Lewis noticed that optimized designs for both cruisers and accelerators result in higher lift-to-drag ratios than vehicles designed only to minimize drag at one condition [107].

These results justify the work presented in this thesis. Trajectory analyses such as [91] have typically assumed simple algebraic relationships such as lift that is directly proportional to angle of attack or drag as a quadratic function of lift. Experimental data has shown that these may be reasonable approximations for aerodynamic data if properly formulated, but we do not expect a similar statement to be true for the propulsion system.

Consider the following experimental research. Robinson et al. [108] measured lift, drag, and the pitching moment of a scramjet model in a shock tunnel and found that a simple theory was able to predict the thrust fairly accurately while the lift and pitching moment were less accurate. By measuring the distribution of lift, they showed that the majority of the error comes from failure to predict the lift from the nozzle. As a result, the experiment verifies that accurately predicting the lift distribution from the nozzle is critical for flight dynamics modeling. The experimental results also highlight how the lift is a strong function of equivalence ratio, which is an example of coupling between propulsion and aerodynamics not present in traditional aircraft and an example source of parametric uncertainty. In this case an increase of the thrust setting increases the lift, which cannot be modeled with an assumption like $C_L = C_{L_\alpha}\alpha$. Parker et al. [104] calculated curve fits for the longitudinal model of [9] and found several complex relationships that deviated from the classic aircraft results.

The flight data from the Hyper-X (X-43) program was used to validate the SRGULL code [65], but the data is not publicly available for other validation studies. Experimental or flight data for air-breathing hypersonic propulsion systems tends to come from individual components, but it still enables many insights necessary for accurate models. Emami et al. [109] published experimental data on a scramjet inlet that was used to validate the Supersonic Aerodynamic Model Using Riemann Interactions (SAMURI) inlet model described in Chapter 2. Other useful inlet data comes from Fernandez et al. [110]. Experimental results used to validate the combustor model come from Micka et al. [111, 112] and Fotia and Driscoll [113, 114]. Finally, the experimental linear plug nozzle data of Chutkey et al. [79] was used to validate the SAMURI model used for nozzle flows.

1.2.5 Vehicle Sizing

Flight experiments to date have been for small-scale vehicles. The most relevant test flights for this work are those of the X-43 [115]. Because the MAX-1 vehicle framework used throughout this work is based on a scaled-up X-43 design, the sizing and mass of the X-43 is useful. The length of the X-43 test vehicles is 3.63 m, and the mass is 1370 kg [22].

The X-51 flight vehicle is another test that is extremely important to research in air-

breathing hypersonic propulsion. As the first engine flowpath designed for both ram-mode and scram-mode combustion, it expands the envelope of flight data even if it does not reach speeds as high of those of the X-43. The length of the X-51 test vehicle, which uses hydrocarbon fuel while the X-43 used liquid hydrogen, is 7.63 m, and the mass is 1810 kg [116].

An approximate vehicle length of 100 ft was selected for this research [9]. This is an intermediate scale that has potential uses for all or most of the conceived applications for hypersonic vehicles. Large research programs throughout the history of hypersonic vehicles–such as the X-43, the X-51, and the NASP (or X-30) [117]–have tended to focus on either small or large vehicles. Although there are no theoretical limitations that suggest a medium-scale vehicle is less feasible than either a small vehicle or a large one, it is important to find a relatively accurate estimate for the mass of our medium-scale vehicle.

The mass estimates used for the MAX-1 come from Chudoba [118]. The scaling relationships specifically account for the vehicle's target Mach number and the fuel type. As stated by Lewis [107], detailed models for mass fraction and fuel fraction are not generally available, and scaling relationships must be used unless detailed structural analysis is considered as part of the modeling process. Since the Chudoba relationships are directed at various types of hypersonic vehicles, they are thought to be more reliable than the extrapolated weight formulas from Raymer [119].

Ardema et al. [120–122] provided mass estimates for hydrogen-fueled hypersonic vehicles using several configurations. Their work includes considerations due to structural mass, fuel tank types, and the mass of the thermal protection system. As such, it is still a highly useful study even today. The Ardema study did not suggest a scaling relationship between weight and length; instead several designs with takeoff weight of 400,000 lb are given. Assuming Chudoba's suggested scaling of

$$ W \propto (planform\ area)^{0.906} \tag{1.4} $$

the predicted weight for the MAX-1 vehicle is 41,549 kg, compared to the mass used in this work of 43,089 kg. In other words, the rough mass scaling estimates seem togive similar results for the data that are available. Furthermore, it provides a better estimate than the constant-density assumptions frequently found in the literature [123].

The X-30 (NASP) program [1] did not lead to a flight test or prototype vehicle, but it was a very large research program lasting several years nonetheless. As such, there are not concrete, fixed numbers for the mass and length, but the numbers were roughly converging toward the end of the program [1, 124].

Table 1.1: Comparison of actual weight and predicted weight using Chudoba scaling.

Vehicle	Length	Takeoff Weight	Predicted Wieght
MAX-1	28.5 m	43,089 kg	43,089 kg
X-43	3.63 m	1368 kg	1026 kg
X-51	7.63 m	1814 kg	2100 kg
NASP	48.8 m	181,400 kg	150,000 kg
XB-70	57.6 m	246,000 kg	253,000 kg

Table 1.1 shows how the predicted weights using the Chudoba mass scaling relationships compares to the actual weights of various vehicles. The XB-70, a Mach 3 strategic bomber prototype built in the 1960s, has been added to the table as an example of a large, high-speed vehicle even if Mach 3 is usually not considered hypersonic [125]. For all the vehicles, the relationships are fairly accurate, and some of the differences are expected. In particular, the X-43 had a large ballast mass in the nose of the vehicle to ensure static stability [22], and accounting for that mass would put the estimate closer to the actual weight of the vehicle. For the MAX-1 vehicle, this table means that the rough number for mass is acceptable for the purposes of basic flight dynamics research.

1.2.6 Optimization

Because of the integration among the various parts of hypersonic vehicles, optimization considering several disciplines of vehicle performance and modeling (for example propulsion and flight dynamics) is highly relevant. This technique is called multidisciplinary design optimization (MDO), and applying it to hypersonic vehicles is an idea that seems to have come after the termination of NASP [20]. This should not come as a surprise because although MDO has origins dating from the 1960s and 1970s [126], it is relatively recent as a mainstream technique [127].

Many objective functions have been used for design optimization of hypersonic vehicles. The optimization is usually tailored to the mission for which the vehicle is intended. For transport vehicles, air-breathing range is an ideal objective function [20]. Fuel consumption at a cruise condition can be used as an approximation. However, compared to low-speed aircraft, hypersonic vehicles have more fuel as a fraction of vehicle mass. As a result, the lift-to-drag ratio varies significantly throughout the mission, and varying C_L/C_D has significant impact on the range, for example [107].

Some authors [128–130] have also considered the challenging problem of multiobjective optimization. Optimization with multiple objectives is often controversial, but it can be used to identify tradeoffs in the design space.

Much of the literature on optimization in the field of hypersonics focuses on the design of individual components, often at individual operating conditions. Smart [14] demonstrated a highly useful algorithm for optimizing two-dimensional scramjet inlets under just those assumptions. With the ability to rapidly compute performance at off-design conditions, we showed that such inlet designs have very poor performance for even small perturbations from the design conditions [61, 131]. Brown et al. [55] discussed robust optimization to mitigate this result. In Chapter 2, we present an approach to the inlet design problem that addresses these issues directly with constraints on shock interactions.

Payne et al. [132] optimized a row of transverse fuel injectors of exactly the type considered in this work. Payne et al. also encountered a problem that has become familiar to us: the performance of complex hypersonic models is not always a smooth function of the design variables. Optimization of two-dimensional scramjet nozzles was addressed by Nickerson and Dunn [73], although this topic requires an update to address changes in Mach number, fueling condition, and angle of attack.

The optimization studies discussed in this section are complemented by the trajectory optimization studies discussed previously [11, 89–96, 98]. The closest research to the present cooptimization of vehicle design and trajectory was by Grant et al. [130], who considered optimization of simultaneous optimization of aerodynamic and trajectory decision variables using variational methods for the trajectory optimization.

1.2.7 Economics

The challenges associated with hypersonic flight have meant that the rate of progress has been slow. This was predicted long ago by Loftin [133].

For example, in 1972, Petersen and Waters estimate that the minimum cumulative cash flow for a fleet of 250 hypersonic transport vehicles would be around $6 billion (in 1972 USD), and this point would come 13 years after the initialization of the project [134]. It is also an inauspicious indicator that the economic performance of supersonic transports was consistently overestimated [135–138]. Adding to the potential pitfalls for hypersonic passenger transport is the difficulty that modern airlines have making a profit [36]. Unless hypersonic transports turn out to be cheaper than expected, some type of economic support, such as monopoly protection, may be needed.

For certain types of missiles, air-breathing hypersonic propulsion has advantages that other technologies cannot match, and this makes the economic argument for hypersonics much more favorable [25, 139]. For spaceplanes, the economics remains speculative [140], but the only competing technologies are rocket launch vehicles, which are very expensive

but support a multibillion dollar industry [141]. Rockets also require an extensive launch infrastructure, which may be an area where air-breathing vehicles have an advantage.

Environmental concerns are yet another potential discipline to be considered in hypersonic vehicle design. The effect of regular hypersonic flight on ozone depletion is uncertain, and noise from shock waves must not be too high [142, 143]. Noise mitigation will almost certainly include both designing a vehicle to minimize the shock signature and employing various flight planning strategies. Increasing the altitude will decrease the amount of noise at ground level, although this does not necessarily eliminate the problem. If noise restrictions mean that hypersonic flight will only be allowed over oceans, turn performance of the vehicle may be an important factor.

In summary, it is safe to say that economic and environmental concerns add to the considerable technical challenges faced by air-breathing hypersonic vehicles. Historically, hypersonics research has died off quickly from several times of relatively high activity. Yet research continues, and even revives itself following periods of relatively low activity [15]. This is a strong indicator that the future of hypersonic vehicles is bright even if some of the applications are not successful.

1.3   New Aspects

In this work, several original contributions are discussed. Many of these involve new aspects of hypersonic propulsion modeling that have not been considered in previous control-oriented or trajectory studies. In particular, a new method for rapidly analyzing two-dimensional supersonic flow was developed. This model, called SAMURI, is similar to the method of characteristics but includes oblique shock waves, expansion waves, contact discontinuities, and interactions among waves. Previous engineering models applied to hypersonic inlet and nozzle modeling have only included a subset of these phenomena.

Contributions are also made to the understanding of thermal choking in the combustor and dual-mode engine operation. This work builds on previous collaboration with Torrez [68, 69, 99], but several new aspects are described in this thesis. A more thorough description is presented for the interactions between the isolator and combustor, and the role of friction in ram-mode operation is highlighted. Rationale is presented for the first time that a discontinuity in thrust exists at ram-to-scram transition, and a region of potential instabilities near transition has been identified.

The new aspects of hypersonic modeling have also enabled several contributions to the understanding of ramjet and scramjet flight dynamics. Engine unstart and ram-to-scram transition are phenomena that have been identified by previous authors, but they have not

been plotted on the flight corridor map using a complex model. In the case of unstart, it has not been reported in terms of trimmed flight conditions at all.

Finally, the trajectory and vehicle design optimization work applies concepts that are new in the context of air-breathing hypersonic vehicles. This includes a trajectory optimization technique and its application to finding the optimum acceleration profile for an ascent trajectory, which complements previous work to select the optimum altitude profile. Although the design optimization presented here is restricted to a small set of design variables, it is the first study known to the author that includes simultaneous optimization of the trajectory and vehicle geometry.

1.4   Outline

The thesis contains several chapters that primarily describe the methodology of the MASIV/MASTrim models, and the following chapters describe applications. Chapter 2 describes the propulsion system, which includes the inlet, the isolator and combustor, and the nozzle. A description of the SAMURI model in Sec. 2.1 is a key part of the thesis. Much of the development of the combustor model was done by Torrez [68, 69, 99], and the discussion of those models is accordingly brief here.

Chapter 3 contains a brief discussion of the overall generic vehicle design used for this research, the design variables that can be used to vary it, and the models used to calculate the forces on the external surfaces. The first portion of Chapter 4, along with Appendix B, describes how the forces and moments on the MAX-1 vehicle are used to calculate accelerations and vehicle accelerations and other flight dynamics properties.

The remainder of Chapter 4 (from Sec. 4.2–4.4) discusses a first application of the combined MASIV/MASTrim models, which is to explore the flight envelope and determine performance throughout. Turning flight is also discussed in Sec. 4.3. In Chapter 5, flight in ram mode is considered. Of particular interest are ram-scram transition and combustion-induced isolator unstart, which previously have not been plotted on the flight corridor map using a complex model. Chapter 6 discusses optimization applied to the MASIV/MASTrim models. First a trajectory optimization problem with a fixed vehicle is discussed, and a computation-reducing methodology is introduced. This allows for a more complicated problem, which is simultaneously optimizing the trajectory and several vehicle design variables.

Finally, Chapter 7 summarizes the work. In addition, numerous topics for future work, including some that are currently underway, are discussed.

CHAPTER 2

Dual-Mode Ram-Scramjet Models

The subject of this chapter is the Michigan/AFRL Scramjet In Vehicle (MASIV) engine model. Air-breathing engines for hypersonic vehicles have four primary components: an inlet to compress the freestream airflow to levels acceptably high for efficient combustion, an isolator to contain any internal pressure rise driven by back pressure from the combustion, a combustor in which the heat addition from combustion occurs, and a nozzle to extract thrust by allowing the flow to expand. Because the flow is supersonic (except in the isolator and combustor during ram mode), information propagates downstream, which leads to the picture shown in Fig. 2.1. Furthermore, it must calculate the lift and moment on the inlet and nozzle surfaces, which can be affected by shock interactions and any upstream surfaces.

Ram mode produces an exception to this one-way flow of information because much of the internal flow is subsonic. The isolator produces a pressure rise, and the amount of pressure increase that must occur is the unique value that allows thermal choking to occur in the combustor. As a result, the pressure rise in the combustor becomes a dependent variable of the ram-mode solution process that must be solved for iteratively, and this feedback is represented by the dotted arrow in Fig. 2.1. A combination of ram-mode and scram-mode may also be possible, and this is usually referred to as dual-mode combustion, but such combinations are not considered in this work.

Section 2.1 discusses the supersonic solution method that is used for both the inlet and nozzle components. The supersonic model SAMURI is a substantial improvement over previous models used in hypersonic flight dynamics studies, and it is given a separate section here. The remaining sections present the components in the sequence of Fig. 2.1, but descriptions of the isolator and combustor are shortened due to more extensive discussion by Torrez [68, 69, 99] and in Chapter 5.
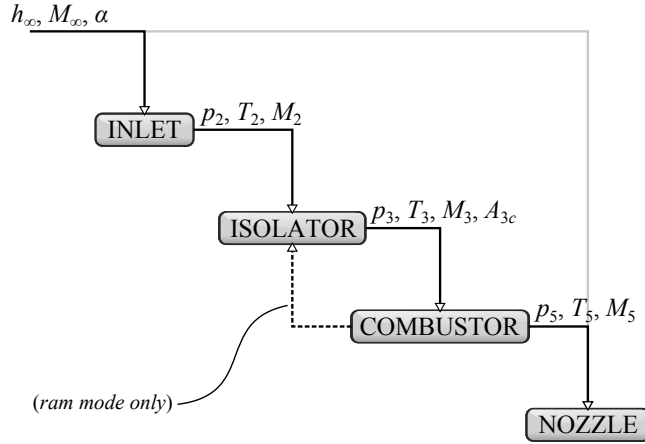
Figure 2.1: Information flow in dual-mode ramjet/scramjet. Feedback from combustor to isolator only occurs when there is thermal choking in the combustor.

2.1 SAMURI: A Method for 2D Supersonic Flow

To model the performance of a 2D scramjet inlet with a desired accuracy, a model must be able to capture certain phenomena. Since the gas state (density, pressure, temperature, velocity) at the end of the inlet is an important parameter for the performance of the combustor and thus the thrust, an inlet model must do more than predict the pressure on the inlet surfaces.

As a result, it is critical that a model for oblique shockwaves be included in the inlet analysis. This represents a significant improvement in fidelity for control-oriented modeling from the work of Chavez and Schmidt [8], which used Newtonian aerodynamics for the inlet, and Bolender and Doman [9], which considered the model as a sequence of two oblique shocks. However, except at very specific conditions, interactions between shock waves are also very important for modeling both the forces on the inlet and the exit conditions that are passed on to the combustor.

It has been shown [55, 61] that shock interactions have a significant impact on inlet performance when it is operated at off-design conditions. Furthermore, expansion fans are also present in the inlet flow at off-design conditions, and modeling them is necessary to calculate even the mass flow into the combustor correctly. Finally, the oblique shockwaves interact not only with each other but also the expansion fans.

All of these effects play an important role in the inlet, but indeed this turns out to be the entire list of important phenomena in purely supersonic inviscid flow. As a result, the model is also appropriate for other applications, including the nozzle, which is important
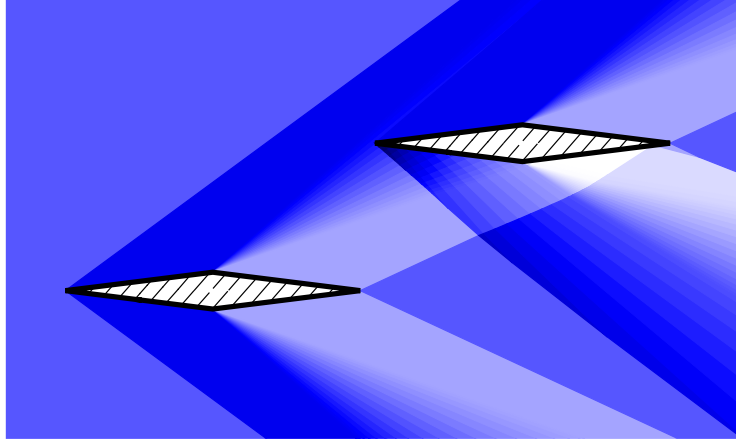
Figure 2.2: Two diamond airfoils, $M_\infty = 2$, $\alpha = 0$.

for this work. An example application to a flow not related to dual-mode ramjet/scramjet engines is shown in Fig. 2.2.

The most important contribution of SAMURI is the capability to model shock-shock, shock-expansion, and expansion-expansion interactions automatically. Compared to previous work, the discretized expansion fans are similar to the "method of waves" described in [144] but with a modification to ensure that the waves satisfy mass and momentum conservation. Many of the wave interactions are discussed individually in [145], but the unified approach presented here in terms of Riemann problems simplifies and generalizes those results. Not only are all of these effects be modeled, but the modeling is done in a computationally efficient manner.

Riemann problems can be seen in Fig. 2.2 and are the subject of Section 2.1.2. Another important topic can be found in Section 2.1.5, which discusses the range of conditions for which the SAMURI model is valid.

2.1.1 Oblique Shocks and Discretized Expansion Fans

The SAMURI model considers the flow to be a collection of oblique discrete waves. An oblique shock wave causes a (nearly) discrete change in the flow properties along a wave that has an angle β with the upstream flow. If the flow upstream of the shockwave is labeled state A, the downstream is labeled B, and the change in the flow angle across the shock is δ, the standard equation for an oblique shock is

$$\tan\delta = \cot\beta \frac{M_A^2 \sin^2\beta - 1}{1 - M_A^2 \sin^2\beta + \frac{\gamma+1}{2}M_A^2} \tag{2.1}$$

where M is the local Mach number and γ is the ratio of specific heats. Briggs [146] noticed that this equation could be solved explicitly. Although his solution was presented in 1964, it is frequently forgotten, and many researchers solve (2.1) iteratively. Using the explicit version causes a significant reduction in computational complexity, which can be significant even on a modern computer if the solution includes many oblique shocks.
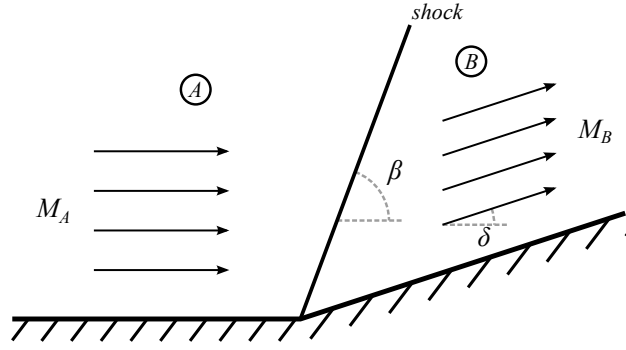
Figure 2.3: Angle and Mach number definitions for an oblique shock.

Once the shock angle β has been found, the downstream states can be found using the well-known equations from [147], for example.

$$\frac{p_B}{p_A} = \frac{2\gamma}{\gamma+1}M_A^2\sin^2\beta - \frac{\gamma-1}{\gamma+1} \qquad \frac{\rho_B}{\rho_A} = \frac{\frac{\gamma+1}{2}M_A^2\sin^2\beta}{1+\frac{\gamma-1}{2}M_A^2\sin^2\beta} \qquad (2.2)$$

$$M_B = \frac{1}{\sin(\beta-\delta)}\sqrt{\frac{1+\frac{\gamma-1}{2}M_A^2\sin^2\beta}{\gamma M_A^2\sin^2\beta - \frac{\gamma-1}{2}}} \qquad \frac{T_B}{T_A} = \frac{p_B\,\rho_A}{p_A\,\rho_B} \qquad (2.3)$$

where p is static pressure, ρ is static density, and T is static temperature.

A supersonic two-dimensional expansion wave satisfies the equations of the Prandtl–Meyer expansion fan, but it can be shown that directly discretizing the Prandtl–Meyer equations leads to at least one conservation violation. Consider the simple control volume shown by the dotted line in Fig. 2.4. The equation for conservation of mass for this control volume is

$$\rho_A u_A H = \rho_B u_B \left(1 + \frac{\tan\delta}{\tan\sigma}\right) H \cos\delta \qquad (2.4)$$

which balances the mass flux into the left edge of the control volume with the mass flux out of the right edge. If we consider the wave to be a discretization of a Prandtl-Meyer expansion, the downstream conditions p_B, ρ_B, and u_B are determined as a function of the deflection angle δ and the upstream conditions ρ_A, p_A, and u_A. Therefore, in order to
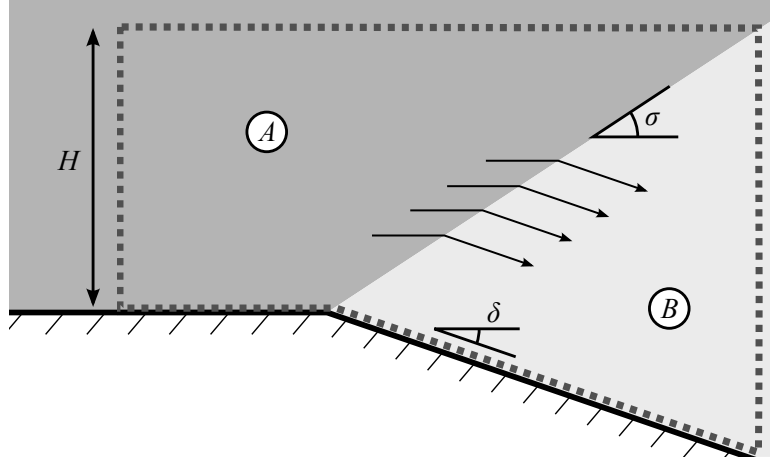
Figure 2.4: Control volume for discretized expansion with $n_{exp} = 1$.

conserve mass, the value of σ must satisfy Eq. (2.4), as was done in Eq. (26) of [61]. Now consider the conservation of momentum in the horizontal direction. This time the top and bottom surfaces cannot be ignored, and the conservation equation is

$$\rho_A u_A^2 H + p_A H = p_B H + \rho_B u_B^2 \left(1 + \frac{\tan \delta}{\tan \sigma}\right) H \cos^2 \delta + E_x \qquad (2.5)$$

where E_x is an error in the conservation of momentum. Since all of the variables in Eq. (2.5) are determined, the value of E_x will not necessarily be zero. In other words, there is no value of σ that satisfies both Eq. (2.4) and (2.5) with $E_x = 0$. This differs from a true expansion fan in which the density, pressure, etc. vary continuously, and all of the conservation equations are satisfied.

One solution to the discretization problem is to treat the conservation equations (2.4) and (2.5), along with similar ones for momentum in the vertical direction and energy, as a system of four variables: ρ_B, p_B, u_B, and σ. This will trade errors in the conservation equations for errors in the values of ρ_B, p_B, and u_B, and this leads directly to the equations for an oblique shock from above. Since the deflection angle is less than zero, the solution will be an expansion shock, which destroys entropy. Fortunately, the inaccuracy diminishes rapidly once the expansion fan is modeled as three or four expansion shocks in sequence.

The solution of the oblique shock equations are discussed in [61] for gases that cannot be assumed to be perfect gases.
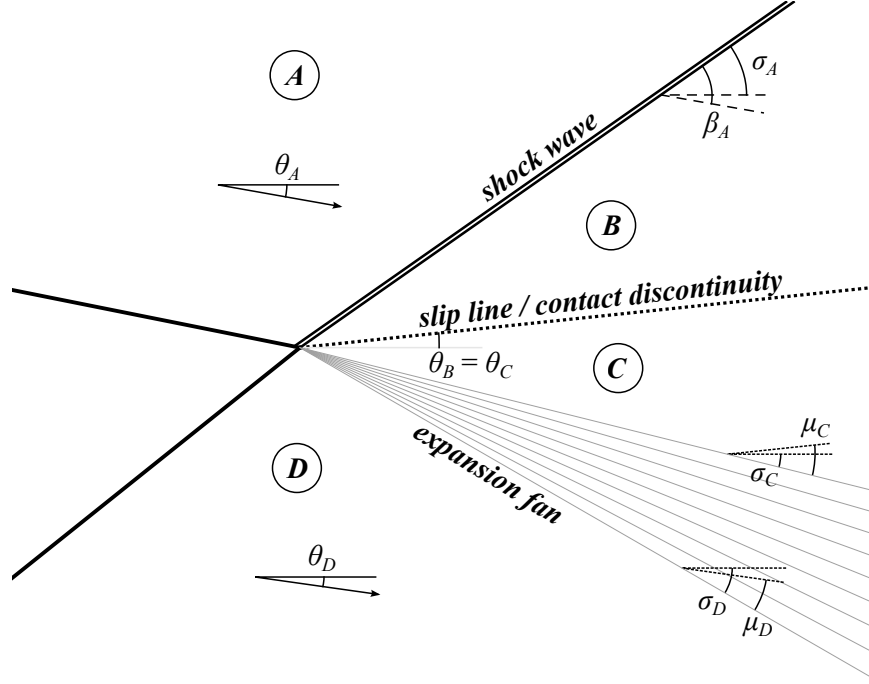
Figure 2.5: Sketch of Riemann interaction with a shock and expansion resulting. Two waves (lines on left of figure) interact to bring states *A* and *D* into contact. The flow in region *A* goes through a shock to form state *B*, and the flow in region *D* goes through an expansion to form state *C*.

2.1.2 Riemann Interactions

Figure 2.5 shows an example of the more challenging scenario where two or more waves intersect. Although many possible types of wave interactions are possible (including shock-shock, shock-expansion, expansion-expansion, multiple interactions, and others), it turns out that the type of interaction is not directly relevant to the solution. Instead, all that matters is the flow state directly above and below the interaction point. In Fig. 2.5, this refers to states *A* and states *D*, and thus we say that the solution reduces to solving the two-dimensional Riemann problem between states *A* and *D*.

A flow state is the set of parameters needed to completely define the properties of the gas at a point. Table 2.1 defines the parameters used in SAMURI. For two states *A* and *B* to be adjacent to each other at more than one point, the two states must satisfy one of two conditions:

1. the two states must satisfy Eqs. (2.1)–(2.3), or

2. the two states must have the same pressure ($p_A = p_B$) and flow direction ($\theta_A = \theta_B$).

In general, when two waves intersect, the resulting adjacent states (*A* and *D* in Fig. 2.5)

Table 2.1: List of parameters and description that define a flow state.

Symbol		Description
ρ	=	density [kg/m^3]
p	=	pressure [Pa]
T	=	temperature [K]
M	=	Mach number [1]
θ	=	flow angle [rad]
$Y_1, \ldots, Y_{n_{sp}}$	=	gas composition, species mass fractions [1]

do not satisfy either of these two conditions. To solve this seeming inconsistency, two things happen. Two new waves are introduced, which results in two new regions, B and C. Regions A and B satisfy condition 1, and the same can be said for regions C and D. In addition, states B and C must satisfy condition 2, and this becomes the primary criterion for the solution of the Riemann problem.

A simple way to describe this problem is to write a pressure–deflection function that determines the post-shock pressure given an upstream state and a deflection angle. For example if the upstream state is A, and the downstream state is B,

$$p_B = p(A, \delta_A) = \left(\frac{2\gamma}{\gamma + 1} M_A^2 \sin^2 \beta(M_A, \delta_A) - \frac{\gamma - 1}{\gamma + 1} \right) p_A \tag{2.6}$$

The pressure increases when $\delta_A > 0$ and decreases when $\delta_A < 0$. Note that the deflection angle (δ_A) is given by the difference in the flow angles:

$$\delta_A = \theta_B - \theta_A \tag{2.7}$$

The solution of the wave interaction problem then reduces to a simple equation of the form

$$p(A, \theta_B - \theta_A) = p(D, \theta_D - \theta_B) \tag{2.8}$$

which must be solved iteratively for θ_B. Eq. (2.8) can be used for all wave interaction problems. This includes trailing edges, where states A and D come into contact with each other not because of the intersection of two waves but because of the end of the physical structure that was separating them. Figure 2.5 could represent a trailing edge if the space between regions A and D on the left side of the figure is the trailing edge of an airfoil for example. Whether the solid black lines are waves or the walls of a physical structure does not change the nature of the Riemann problem that determines the flow downstream of the interaction point.
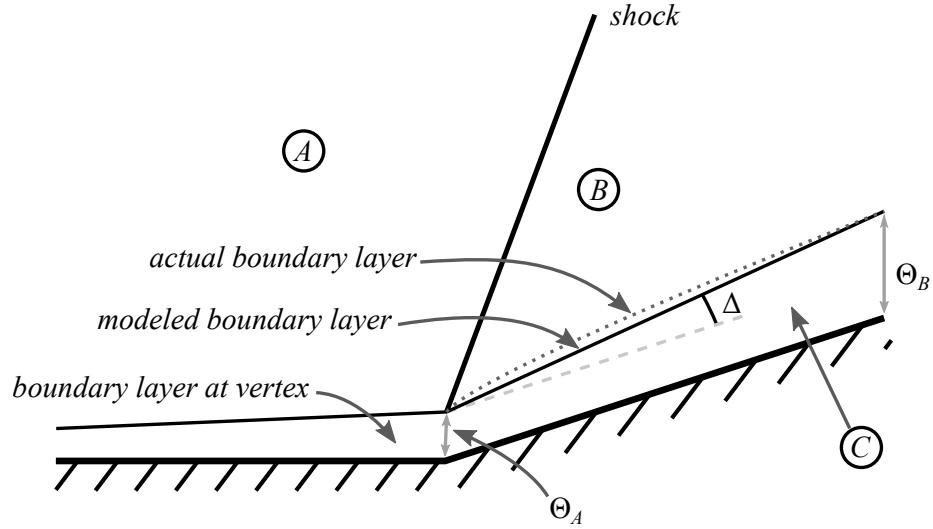
Figure 2.6: Sketch of the boundary layer model at vertices.

Assuming inviscid, two-dimensional, supersonic flow, this technique produces the exact solution to a general wave interaction problem. In a real viscous flow, there will be mixing across the slip line due to the difference in momentum between regions *B* and *C*, but this mixing tends to be small in supersonic flow. The only strong slip lines in the inlet and nozzle simulations considered for this work occur at the trailing edges of the nozzle cowl and nozzle body.

To ensure efficient computation, SAMURI also includes the capability to ignore any of the three lines emanating from a Riemann interaction (in Fig. 2.5, lines separating *A* and *B*, *B* and *C*, or *C* and *D*) if the wave or slip line is very weak. This prevents a rapid increase in the number of waves that could otherwise occur, and this introduces conservation errors that are less than 1%.

2.1.3 Compressible Boundary Layers

The current SAMURI model includes a simple modeling capability for boundary layers. In effect, the surface of the vehicle is expanded by a distance equal to the momentum thickness. Between vertices of the surface, the boundary layer is treated as a straight line connecting the momentum thickness at the upstream vertex and the momentum thickness at the downstream vertex. In reality, a boundary layer is curved, but more vertices can be added get a better approximation of the true boundary layer shape.

For the calculation of the momentum thickness, the Van Driest II method is used [5].

The friction coefficient (C_f) on a flat plate is calculated using the formulas from [148],

$$\frac{\sin^{-1} B_1 + \sin^{-1} B_2}{\sqrt{C_f(T_{aw}/T_e - 1)}} = 4.15 \ln\left(\text{Re}_{xe} C_f \frac{\mu_e}{\mu_w}\right) + 1.7 \tag{2.9}$$

where

$$B_1 = \frac{2b_1^2 - b_2}{\sqrt{4b_1^2 + b_2^2}} \qquad\qquad B_2 = \frac{b_2}{\sqrt{4b_1^2 + b_2^2}} \tag{2.10}$$

and

$$b_1 = \sqrt{\frac{\gamma - 1}{2} M_e^2 \frac{T_e}{T_w}} \qquad\qquad b_2 = \frac{T_{aw}}{T_w} - 1 \tag{2.11}$$

Momentum thickness is the preferred boundary layer metric because it is closely tied to drag. The integrated total friction coefficient for a flat plate with length L is $C_f = 2\Theta/L$ where Θ is the momentum thickness at the end of the plate. This is very convenient since we use a control volume to calculate the forces on the vehicle, although it is more common to use displacement thickness as a correction to inviscid calculations.

Figure 2.6 gives an illustration of how this boundary layer model treats vertices of the vehicle geometry. At a given vertex of the geometry, the existing boundary layer has a momentum thickness, which is marked as Θ_A in Fig. 2.6. If the vertex is a leading edge, Θ_A is zero.

The boundary layer, marked as region C in Fig. 2.6, is modeled as having a pressure equal to that of region B but with zero velocity. This does not provide a way to estimate the heat transfer or any other property that requires detailed knowledge of the boundary layer profile, but it does provide a first estimate of drag due to the momentum that is lost on account of the region in which there is no velocity.

2.1.4   Algorithm

Previous subsections discussed the models of physical phenomena in two-dimensional supersonic flows. The current subsection provides a brief description of how SAMURI uses these models to create flow solutions.

Figures 2.7 and 2.8 provide a graphical step-by-step application of the SAMURI method to a simple flow problem. The input to SAMURI consists of three parts:

1. the flow geometry, which is a set of closed polygons;

2. the flow domain, i.e., the rectangle (control volume) over which the solution is calculated; and

3. the initial flow state(s), which may or may not be uniform.

In the example of Fig. 2.7(a), the flow geometry is a simple triangular airfoil, and the initial conditions are the density, pressure, temperature, Mach number, and flow angle at the left-hand side of the rectangle. The vertical solid gray line in Figs. 2.7 and 2.8 represents the current x-coordinate, and thus the picture in Fig. 2.7(b) represents starting at the minimum x-coordinate with a uniform condition.

The next step is to determine the next x-coordinate where a new flow phenomenon occurs. In this case it is the leading edge of the airfoil, as shown in Fig. 2.7(c). A leading edge introduces two new waves–one for the upper surface and one for the lower surface. This requires SAMURI to solve two deflection equations with known deflection angles, and it initializes two waves with the resulting angles. These waves are represented by the arrows emanating from the leading edge in Fig. 2.7(c).

The second consequence of the leading-edge solution is the knowledge of the states downstream of the waves. These are labeled 3 and 4 in Fig. 2.7(d). After this point, the next step is again to find the next x-coordinate where new waves are needed. In Fig. 2.7(d), this is the vertex on the lower surface of the triangular surface. The solution at this vertex is an expansion wave, shown here discretized into three waves, which introduces new regions 5, 6, and 7.

Figure 2.8(a) repeats Fig. 2.7(d) keep consistency between the two figures. After the expansion wave solution has been calculated, the next step is to advance to the trailing edge. At the trailing edge, two inconsistent flow states (3 and 7) come into contact with each other, and so the solution is equivalent to a Riemann problem as discussed in Sec. 2.1.2. The final step is to advance to the edge of the flow domain, as shown in Fig. 2.8(c), which completes a set of polygons that represent the final flow solution. Figure 2.8(d) shows an example that plots the static temperature in each polygon.

The graphic depicts much of the SAMURI process, and a more definitive description of the algorithm is presented in Appendix A.

2.1.5   Range of Model Validity

This subsection is included to discuss the limits of applicability for the SAMURI model. The main assumptions associated with the model are listed below.

- The flow is two-dimensional and supersonic.
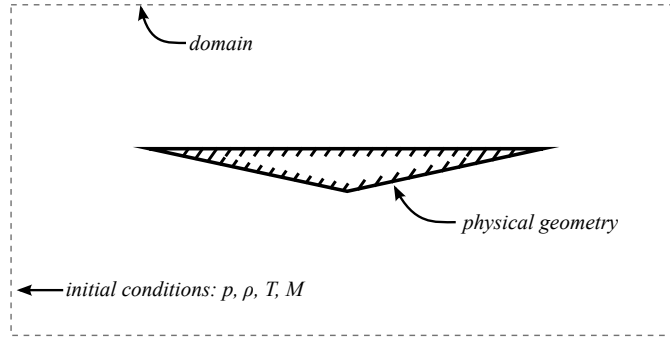
(a) Input.
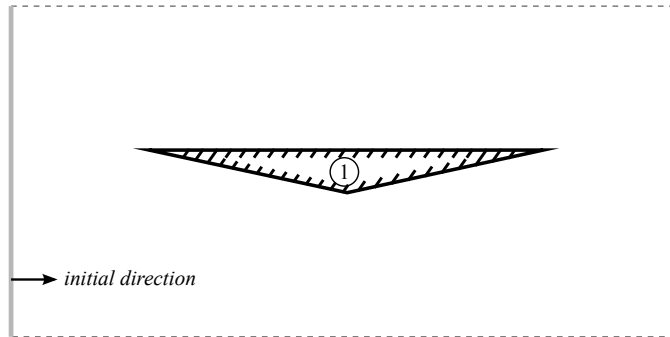
(b) Step 0: Begin at minimum x-coordinate.
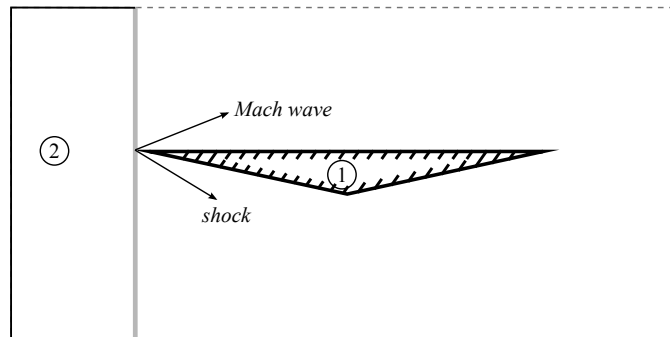
(c) Step 1: Advance to first leading edge.
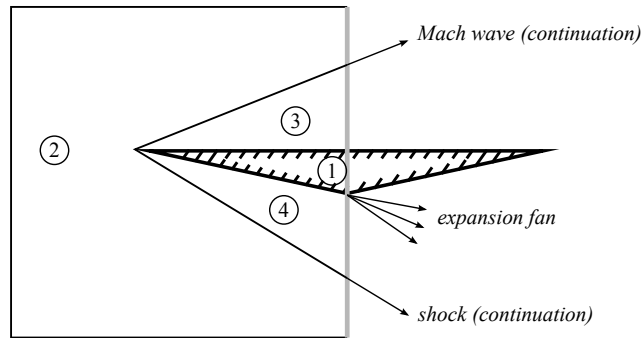
(d) Step 2: Advance to next vertex.

Figure 2.7: Step-by-step example of SAMURI algorithm: input through step 2.
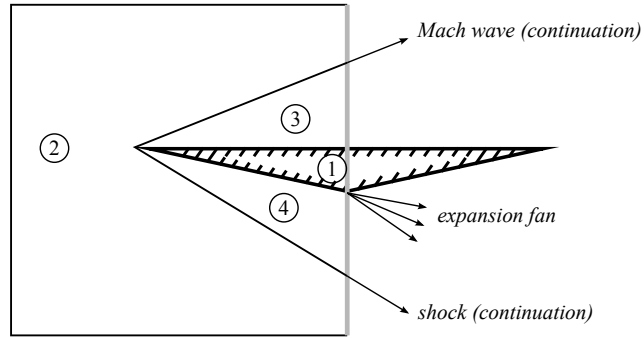
(a) Step 2: Advance to vertex.
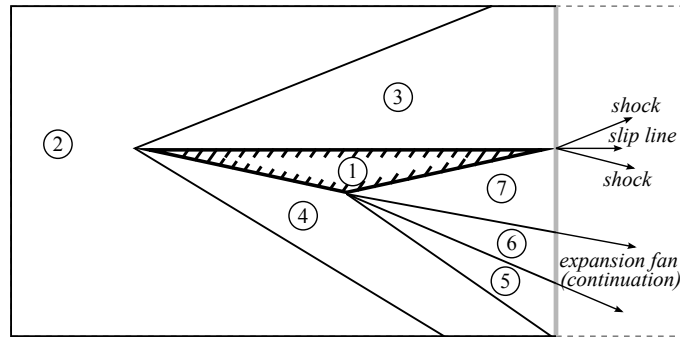
(b) Step 3: Advance to trailing edge.
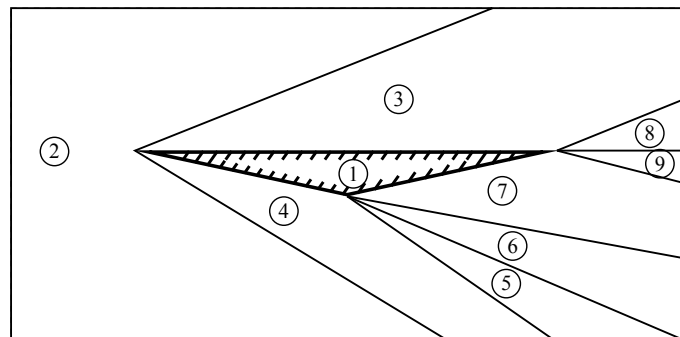
(c) Step 4: Advance to end of solution domain.
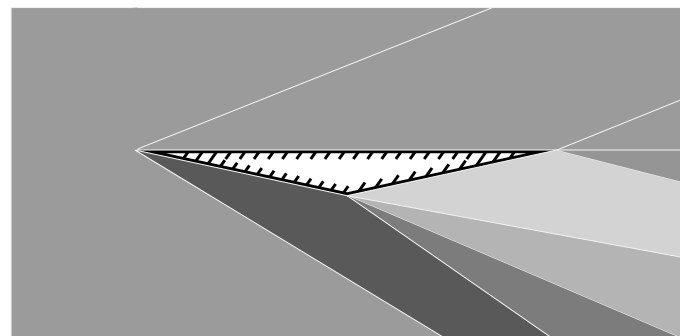
(d) Temperature plot.

Figure 2.8: Step-by-step example of SAMURI algorithm: step 2 through solution.

- The boundary layer is simulated as a wall displaced by the momentum thickness (Θ), which is calculated using an empirical formulat.

- The boundary layer is assumed to be fully turbulent.

- Separated boundary layers are not present.

- Interactions between shocks and boundary layers are not modeled.

At high Mach numbers, the shock is located partially within the boundary layer, which should create problems for the SAMURI model, but in practice the boundary layers are small enough that the effect was not significant in tests up to Mach 10.

Within the flow regime where SAMURI is valid, the dominant flow phenomena outside the boundary layer are shock waves and expansion fans. The expansion fans are modeled as several discrete expansion waves. The interactions between waves are solved using Riemann interactions, and the mixing layer along the slip line is ignored.

The model is only valid if the fuel, air, and combustion products are fully mixed. That is, SAMURI does not have a model for mixing. The chemistry is assumed to satisfy one-dimensional conservation equations along streamlines. This combination of assumptions was tested for Mach numbers up to 18, and it may be valid for even higher Mach numbers providing that the Knudsen number is low. However, the upper bound on the Mach number where SAMURI is applicable would be lower in flows with shock-boundary layer interactions. The model is also not valid for isolators, where the shock-boundary layer interactions play a critical role.

2.2   Inlet

The importance of the inlet of an air-breathing vehicle becomes greater and greater as the vehicle speed increases. For automobiles and propeller-driven aircraft, the inlet must merely provide a way for air to enter the engine. For subsonic aircraft, the inlet need not do much more except that it also must not cause too much distortion to the flow. If a gas turbine is being flown at supersonic speeds, the inlet must also efficiently slow the airflow (relative to the aircraft) to subsonic speeds.

At hypersonic speeds, it is not practical to use a compressor, so the inlet also gains the responsibility to provide the necessary compression to the rest of the engine. Further, if the assumption is made of constant dynamic pressure,

$$q_\infty = \frac{1}{2}\rho_\infty U_\infty^2 = \frac{1}{2}\gamma p_\infty M_\infty^2 \qquad (2.12)$$

the mass flow is inversely proportional to the flight speed:

$$\dot{m} = \rho_\infty U_\infty A = \frac{2q_\infty}{U_\infty} A \tag{2.13}$$

Thus the inlet must capture much of the air incident on the vehicle (i.e., the capturea rea, A, must be large). Finally, the inlet should be as short as possible. At such high speeds, the length scales tend to increase because the flow spends less time to cover a given distance. A long inlet may have good performance but add too much mass to the vehicle and have a negative effect on the overall vehicle performance.

Because of the one-way flow of information typical in a hypersonic air-breathing engine, the inlet is arguably the most important component. Poor performance in the inlet can cascade through the entire engine. For example, the inlet performance affects the inlet, the combustor, and the nozzle, while the nozzle performance affects only the nozzle. In Chapter 6, it will be shown that the total fuel consumption for an ascent trajectory may vary by a factor of two by changing nothing by the inlet design.

Figure 2.9 shows the basic parameters that define such a two-dimensional inlet design. It consists of m external ramps and n internal ramps, which leads to $m + n$ oblique shocks in the ideal case. In Fig. 2.9, in which $m = n = 2$, these shocks are represented as gray lines. In the ideal case of no shock interactions, the flow can be analyzed with only a few simple equations. The kth shock has a deflection angle δ_k, which is known from the inlet geometry, and this deflection angle enables the calculation of state $k + 1$ using the oblique shock equations of Sec. 2.1.1.

$$\beta_k = \beta(M_k, \delta_k) \qquad\qquad p_{k+1} = \left(\frac{2\gamma}{\gamma + 1} M_k^2 \sin^2 \beta_k - \frac{\gamma - 1}{\gamma + 1} \right) p_k \tag{2.14}$$

$$\theta_{k+1} = \begin{cases} \theta_k + \delta_k & \text{if } k \leq m \\ \theta_k - \delta_k & \text{if } k > m \end{cases} \qquad M_{k+1} = \frac{1}{\sin(\beta_k - \delta_k)} \sqrt{\frac{1 + \frac{\gamma - 1}{2} M_k^2 \sin^2 \beta_k}{\gamma M_k^2 \sin^2 \beta_k - \frac{\gamma - 1}{2}}} \tag{2.15}$$

This splits the flow into $m + n + 1$ regions, which are numbered in Fig. 2.9(a).

The reality is much more complicated. Instead of relying on Eqs. (2.14) and (2.15), the MASIV model uses SAMURI to solve the inlet flow. The inputs are the inlet geometry, as depicted in Fig. 2.9(b) (two polygons: one for the main inlet body and one for the cowl below), and the freestream flow condition.

Figure 2.10 shows a sample solution. The overall view shown in Fig. 2.10(a) shows the two visible external shocks and looks much like the simplified description of the inlet flow.
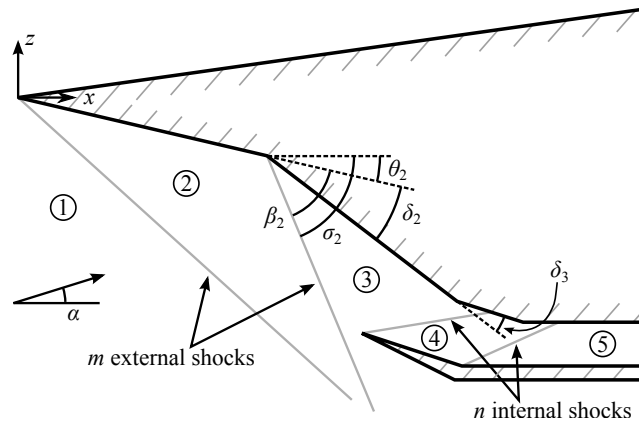
(a) Angle definitions and region numbers.
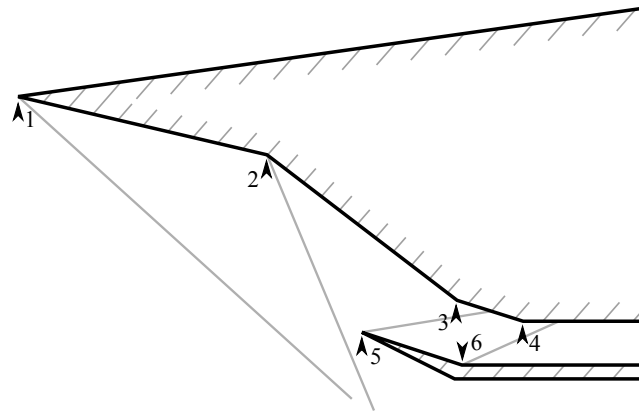
(b) Vertex indices.
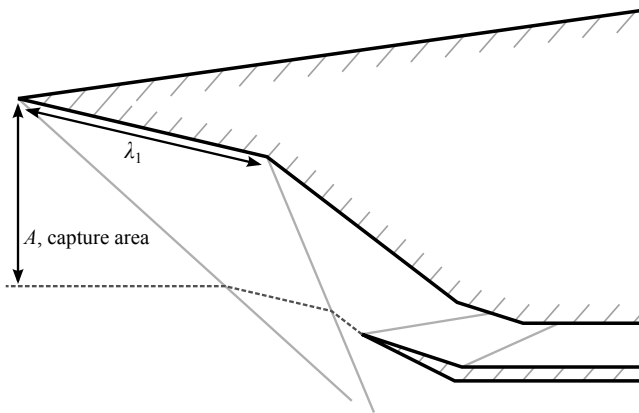
(c) Length definitions.

Figure 2.9: Definitions for inlet design methodology.
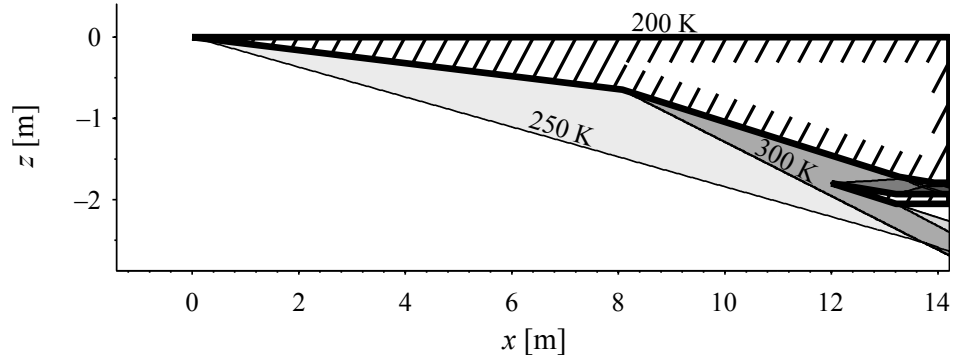
(a) Full inlet.
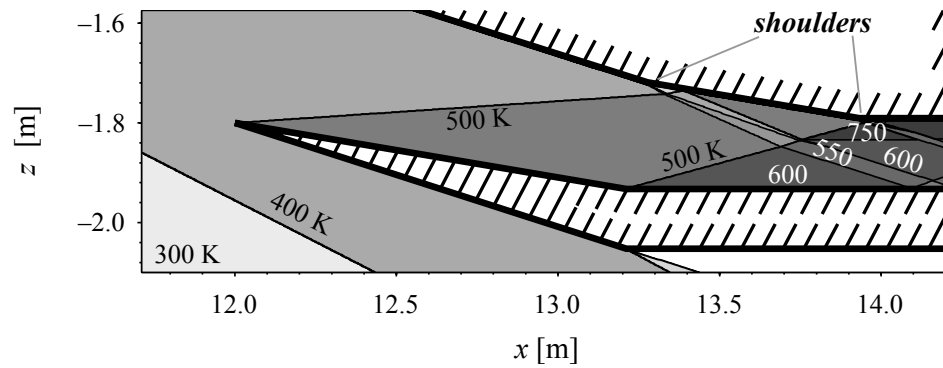
(b) Inlet cowl region.

Figure 2.10: Contours of temperature in Kelvins for a sample inlet solution.

A closer look at the inlet cowl region in Fig. 2.10(b) shows that expansion waves are also present, and these interact with the internal shocks in a complex way. The expansion fans are introduced when the internal shocks are not canceled by the change in flow direction at the inlet shoulders.

Fortunately, the shockwaves and expansions partially cancel each other in the example shown in Fig. 2.9, and the performance is likely to be quite good for this case. Note that the internal shocks intersect the inlet surface downstream of the shoulder points in Fig. 2.10(b). If these shocks change angle only slightly, they will intersect the inlet surface upstream of the shoulders, which causes a much different performance. It was shown [61, 131] that this represents a discontinuity in performance, and the reason is that the sequence matters. A shock followed by an expansion followed by another shock is different from two shocks followed by an expansion. The advantage of the MASIV inlet model using SAMURI is that it is able to distinguish these two and many other cases, which often have a dramatic effect on inlet and thus the entire inlet performance.

(a) Inlet solution using CFD++®.

(b) Inlet solution using SAMURI
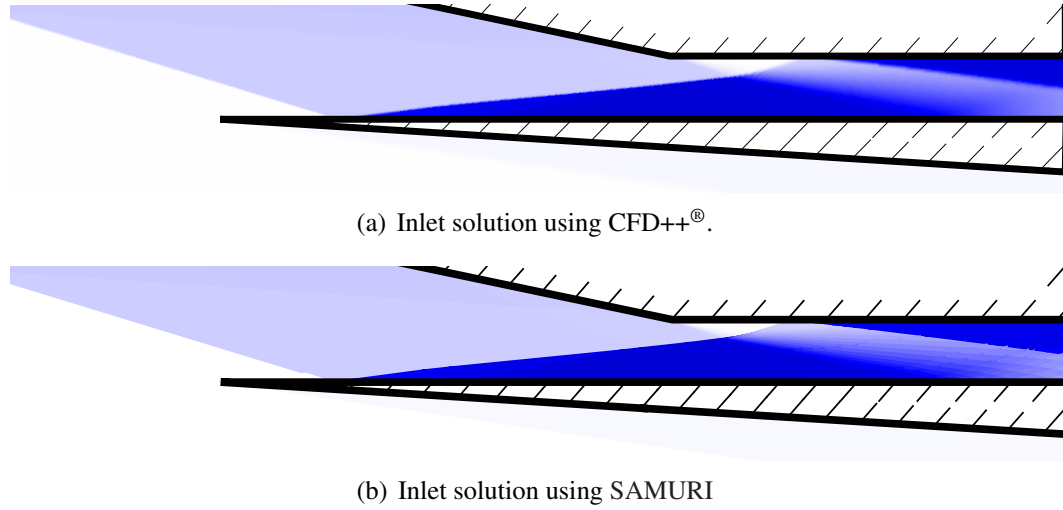
Figure 2.11: Comparison of commercial CFD package (CFD++®) and SAMURI inlet solution: temperature for $M_\infty = 10$, $\alpha = 0$.

Table 2.2: Averaged outflow properties of CFD and calorically imperfect inviscid model.

	CFD++®	SAMURI	relative error
p_2/p_∞	34.70	35.39	0.0199
T_2/T_∞	3.603	3.645	0.0156
u_2/u_∞	0.9289	0.9302	0.0013
$p_{0,2}/p_{0,\infty}$	0.3331	0.3552	0.0664

2.2.1   Comparison to 2D CFD

The first validation test that was performed for the MASIV inlet model involved a comparison to a two-dimensional CFD solution. The commercial package CFD++® [149] was selected for this purpose. An inlet design and flight condition was selected with a large amount of wave interactions to provide a difficult test to the model's capabilities.

Figure 2.11 shows the temperature solution for the two models, and the results are quite similar. The discretization of the expansion fans is visible in Fig. 2.11(b), but otherwise the two are difficult to distinguish. Table 2.2 shows the results from both models for several state variables. It was calculated that the two models predict values of the pressure recovery factor that differ by 6%, although other parameters closer. More details of this comparison are presented in [61]. What is striking about the two results and their similarity is the difference in computation time required to attain them. The CFD solution required approximately eight hours using eight processors, while the SAMURI took less than one second on a single processor using MATLAB®.
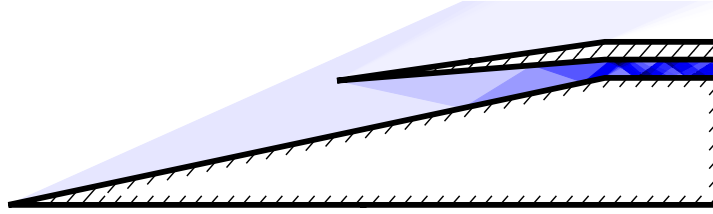
Figure 2.12: SAMURI solution for the Emami et al. geometry with $\theta_{cowl} = 6.5°$. Darker shades of blue represent regions of higher pressure; white represents freestream pressure and black represents $p/p_\infty = 40$.

2.2.2 Comparison to Experimental Data

A second validation study was performed for the MASIV inlet model by comparing its results to an experiment by Emami et al. [109]. The experimental geometry had a cowl that could be adjusted so that the angle of the cowl lower surface (θ_{cowl}) varied from 2° to 11°. Figure 2.12 shows the SAMURI solution at one condition for the geometry from that experiment with $\theta_{cowl} = 6.5°$. No flow visualization like the one in Fig. 2.12 was provided in [109], but static pressure measurements were taken at several points along the wall.

Table 2.3: Lengths for the experimental inlet geometry of Emami et al.

Surface	Length
Inlet ramp (horizontal)	24.82 cm
Inlet ramp (vertical)	4.826 cm
Isolator height	1.016 cm
Forward cowl length	11.18 cm

The relevant lengths for the experimental geometry are presented in Table 2.3. Figure 2.13 shows a comparison of the static pressure between the experimental data and the SAMURI calculation at three points along the inlet surface. Station 1 is along the bottom surface of the cowl 5.84 cm downstream of the cowl leading edge. The second pressure tap is on the bottom surface of the cowl 10.3 cm downstream of the cowl leading edge. The third pressure tap is on the inlet ramp 0.23 cm upstream of the shoulder.

The experimental geometry of [109] had a width five times greater than the height of the inlet exit, and thus three-dimensional effects might be expected to be significant. The comparisons in Fig. 2.13 show that the results are similar despite the potential for three-dimensional effects. Larger differences are present for smaller cowl deflection angles, and this is probably the result of a stronger bow shock at the cowl leading edge, which in reality
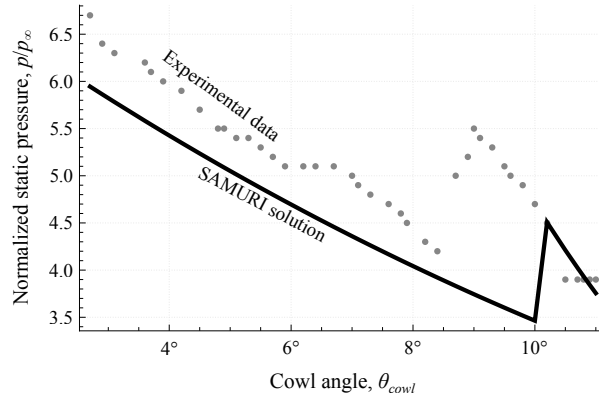
(a) Station 1.
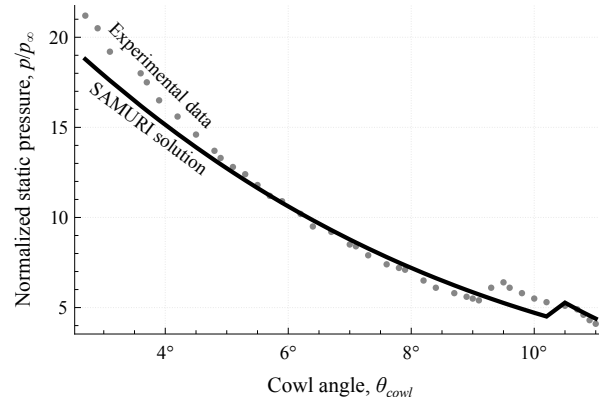
(b) Station 2.
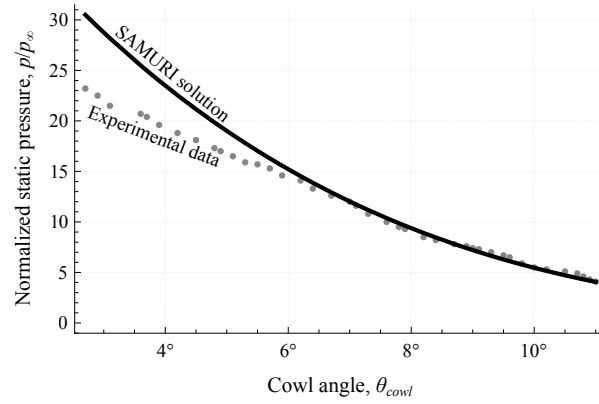
(c) Station 3.

Figure 2.13: Comparison of experiment and SAMURI inlet models.

was not infinitely sharp.

Both the experimental and SAMURI data show obvious signs of a shock in Figs. 2.13(a) and 2.13(b) in the form of a steep jump in the pressure data over a narrow range of θ_{cowl}. The model and the experiment disagree slightly on when this shock crosses over the point

Table 2.4: List of design parameters for two-dimensional hypersonic inlet. An extra design variable not listed is x_{m+n+1}, which can be used to scale the entire inlet.

Symbol(s)	Description
m	number of external ramps, integer
n	number of internal ramps, integer
z_{m+n+1}	z-coordinate of cowl leading edge, inlet aspect ratio
$\delta_1, \ldots, \delta_{m+n}$	change in angle between each pair of ramps
$\lambda_1, \ldots, \lambda_{m+2n-2}$	length of each ramp

in question, and this is likely due to the fact that no boundary layer model was used in the SAMURI calculations. Further details of this comparison can be found in [61].

2.2.3 Inlet Design Methodology

A hypersonic inlet must accomplish all of the tasks described in the beginning of this section, but one may note from Fig. 2.9 that the class of geometries considered here has a relatively small set of design parameters. For a fixed number of shocks, there are only $2m + 3n$ design variables, and existing work gives some insight on how to optimize these design parameters to maximize the efficiency of the inlet [14].

Because hypersonic inlets must operate over a wide range of Mach numbers to be practical, an important question is how changes in Mach number affect the performance. In Fig. 2.14, a performance comparison for two inlet geometries is shown, but for now we only consider the single-condition design. This inlet follows the design methodology of [14] to maximize the stagnation pressure at Mach 8. The pressure recovery factor is a measure of entropy rise, and it is defined as the ratio of the inlet exit stagnation pressure to the freestream stagnation pressure.

$$\frac{p_{0,2}}{p_{0,\infty}} = \frac{p_2}{p_\infty} \left(\frac{1 + \frac{\gamma - 1}{2} M_\infty^2}{1 + \frac{\gamma - 1}{2} M_2^2} \right)^{\frac{\gamma}{\gamma - 1}} \tag{2.16}$$

Figure 2.14 shows that the design optimized for Mach 8 flight is highly sensitive to changes in the Mach number around Mach 8. There are also many fluctuations in the curve at other Mach numbers, although these are exaggerated by the SAMURI model.

A strategy to mitigate these issues using a comparably simple design methodology was first introduced in [131] and further refined in [150]. Although the equations for this design process can become somewhat tedious, the concept is actually quite simple. Rather than designing the inlet to operate at a single flight condition, a range of Mach numbers and
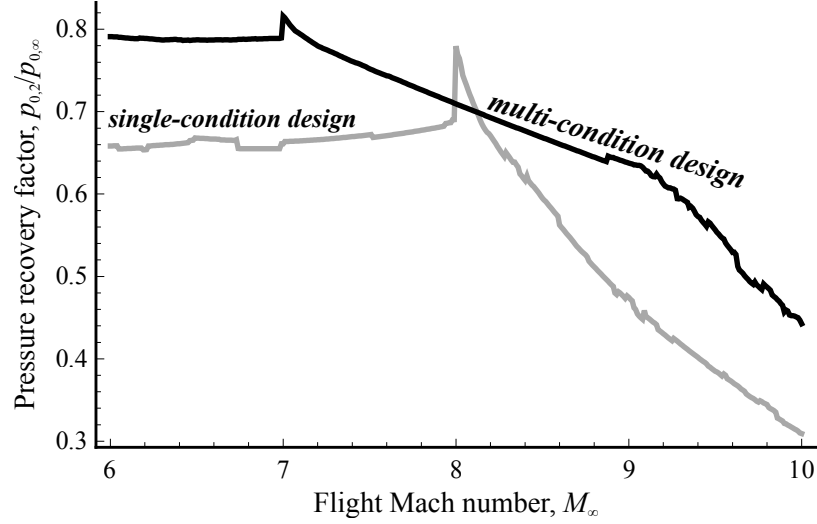
Figure 2.14: Efficiency for single-condition ($M_{min} = M_{max} = 8$) and multi-condition ($M_{min} = 7$, $M_{max} = 9$) inlet designs with $m = 3$ and $n = 1$.
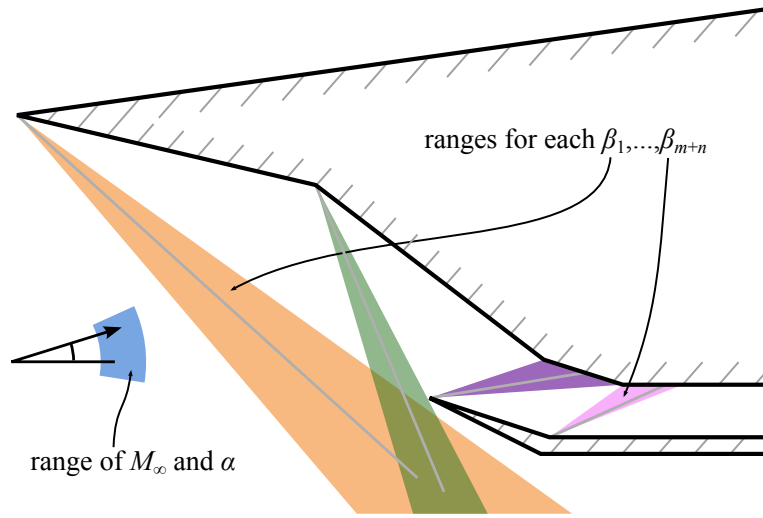
Figure 2.15: Wedges traced by inlet shockwaves over a range of M_∞ and α.

angles of attack should be taken into consideration when designing an inlet.

The process is split into two phases. First, the deflection angles $\delta_1, \ldots, \delta_{m+n}$ are determined using the single-condition process described in [14], and the second phase is to determine the lengths of each ramp, $\lambda_1, \ldots, \lambda_{m+2n-2}$. To complete this second phase, a range of both angle of attack $[\alpha_{min}, \alpha_{max}]$ and a range Mach number $[M_{min}, M_{max}]$ are selected. Using the deflection angles known from the first phase of the design, it is possible to calculate the entire range of shock angles over this two-variable set of flight conditions.

This range of shock angles is represented by the colored wedges in Fig. 2.15. Finally, the wedges make it possible to pick ramp lengths such that the following two conditions are satisfied.

1. The external shocks (orange and green wedges) remain upstream of the cowl leading edge and do not go into the interior flow region.

2. The intersection of each internal shock (purple and pink wedges) and the inlet body stays between its shoulder and the next one downstream.

The black curve in Fig. 2.14 shows that this methodology does eliminate the variations over the specified design region. However, there is a tradeoff between peak performance and the size of range of design conditions.

The following is a summary of the inlet design process.

1. Input number of external ramps (m) and number of internal ramps (n).

2. Input design Mach number (M_{design}) and angle of attack (α_{design}).

3. Input compression ratio at design condition.

$$r_p = \left(\frac{p_2}{p_\infty} \right)_{M=M_{design},\ \alpha=\alpha_{design}} \tag{2.17}$$

4. Apply design routine of [14] to get deflection angles.

$$\{ \delta_1, \ldots, \delta_{m+n} \} = f_1(m, n, M_{design}, \alpha_{design}, r_p) \tag{2.18}$$

5. Input range of flight conditions ($M_{min}, M_{max}, \alpha_{min}, \alpha_{max}$).

6. Determine ramp lengths using shock interaction constraints.

$$\{ z_{m+n+1}, \lambda_1, \ldots, \lambda_{m+2n-2} \} = f_2(M_{min}, M_{max}, \alpha_{min}, \alpha_{max}, \delta_1, \ldots, \delta_{m+n}) \tag{2.19}$$

An extension of this algorithm is given in [150] that provides a strategy for the case that the inlet cowl position can be varied in flight. In the present work, the cowl position is considered to be fixed.

Consider the range of design conditions represented by the darker gray rectangle in Fig. 2.16. The present design process ensures that strong shock interactions do not occur inside this rectangle, but that does not mean that all conditions outside the rectangle do
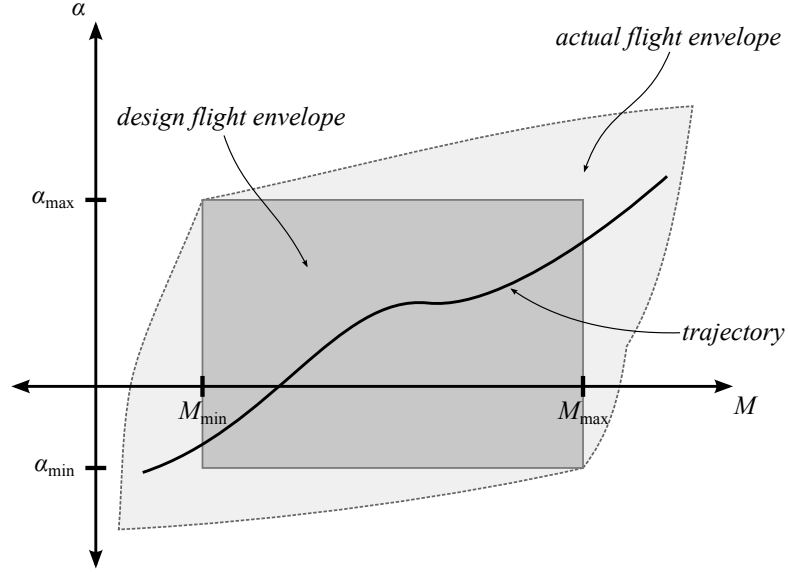
Figure 2.16: Sketch of inlet design conditions (darker gray rectangle) and envelope determined by shock interaction constraints (lighter gray).

have strong shock interactions. In practice, usually only two corners of this rectangle are active constraints, and the inlet has a wider envelope of efficient operation than expected. Furthermore, the trend has a fortunate orientation for real hypersonic vehicles.

The fact that angle of attack typically rises at higher Mach numbers has typically been viewed as a hindrance to be mitigated, but the sample trajectory (black curve) in Fig. 2.16 shows that it extends the Mach number range of the inlet. Conversely, this phenomenon could be used to reduce the size of the design rectangle, and full utilization of this effect could lead to a significant improvement in performance.

2.3 Isolator

The function of the isolator in a hypersonic air-breathing propulsion system varies between two extremes. Much of the time, it does nothing. However in ram mode it is responsible for providing part of the pressure rise to the combustor. This happens over of a sequence of shocks called a pre-combustion shock train, which is a sequence of shocks that interacts with the boundary layer. The shock train adjusts to the conditions in the combustor, which is possible because information flows upstream due to subsonic flow.

Figure 2.17 shows a sketch of the two most common isolator shock trains, which are oblique and normal shock trains. In MASIV, both types of shock trains are modeled

(a) Normal shock train.

(b) Oblique shock train.

(c) Idealized isolator flow.
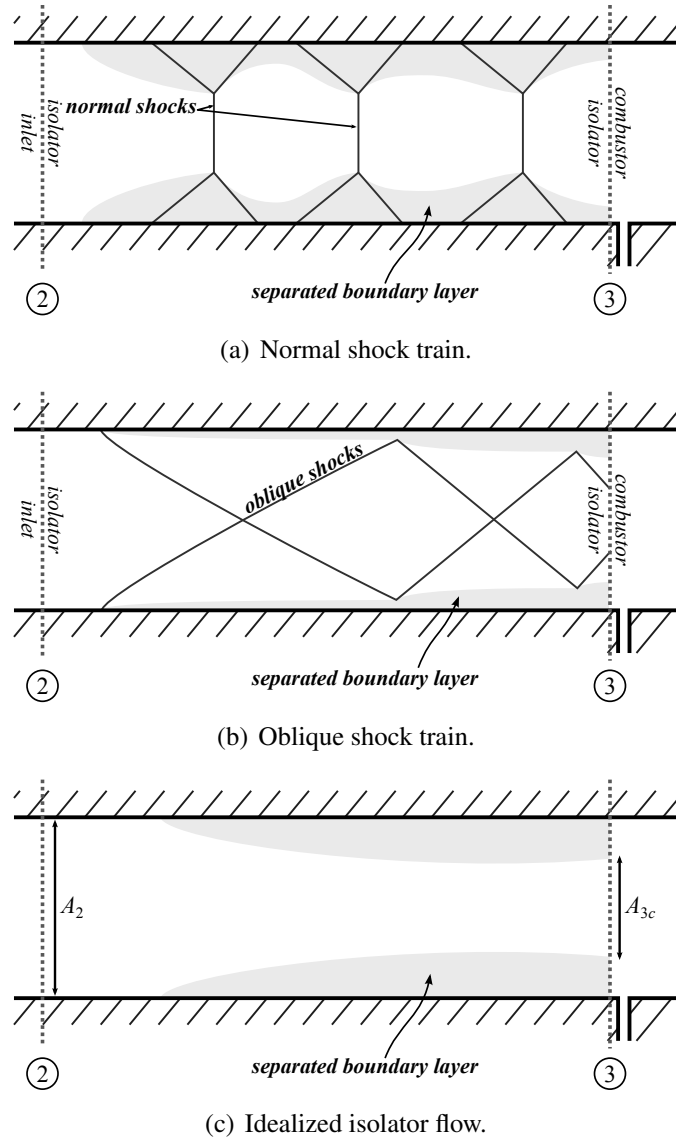
Figure 2.17: Sketch of isolator shock train types and idealization.

as a combination of uniform core flow and a separated boundary layer, as illustrated in Fig. 2.17(c). Heiser and Pratt derived the conservation equations for this model of the isolator [151], which are quite simple.

$$\rho_2 u_2 A_2 = \rho_3 u_3 A_{3c} \tag{2.20}$$

$$p_2 A_2 + \rho_2 u_2^2 A_2 = p_3 A_3 + \rho_3 u_3^2 A_{3c} \tag{2.21}$$

Here A_{3c} is the area of the flow that is outside the separated boundary layer, as shown in Fig. 2.17(c). As can be seen from these equations, the assumption of the Heiser and Pratt

model is that there is no mass flow or momentum flux in the separated region. At a given x-coordinate, the pressure is assumed to be equal in the core flow and the separated boundary layer, but the velocity in the boundary layer is zero. Solution of these two equations along with the assumption of constant stagnation temperature gives the following two equations.

$$\frac{p_3}{p_2} = 1 + \gamma M_2^2 - \gamma M_2 M_3 \sqrt{\frac{1 + \frac{\gamma-1}{2} M_2^2}{1 + \frac{\gamma-1}{2} M_3^2}} \tag{2.22}$$

$$\frac{A_{3c}}{A_2} = \frac{1}{\gamma M_3^2} \left((1 + \gamma M_2^2) \frac{p_2}{p_3} - 1 \right) \tag{2.23}$$

The length of the shock train is computed using

$$\frac{L_{ST}}{H} = \frac{1}{0.228} \ln \left(\frac{M_2^2}{M_3^2} \frac{1 + \frac{\gamma-1}{2} M_3^2}{1 + \frac{\gamma-1}{2} M_2^2} \right) \tag{2.24}$$

where H is the height of the isolator. This relationship originates from Ikui et al. [152], and has been tested experimentally [113, 114].

The primary design variable for the isolator is its length. A longer isolator will be able to contain longer (and thus stronger) shock trains, but it may also negatively affect vehicle performance by adding extra weight. The effect of variable area in the isolator may be worthy of consideration, but it has not been considered in the present work. At present, no attempt has been made to use SAMURI to model the isolator shocks; the method used is the simplified equations presented here.

2.4 Combustor

The derivation and development of the equations used in this section were first done by Torrez [99], and I have incorporated them into the MASTrim vehicle code. The MASIV combustor code was described in detail in [68] and [69]. MASIV solves the following seven ordinary differential equations, which include the conservation of mass, momentum, energy, and species. The equations simulate one-dimensional flow in a variable-area duct

with heat addition from combustion as well as wall friction and wall heat loss.

$$\frac{1}{\rho}\frac{d\rho}{dx} = \frac{1}{\dot{m}}\frac{d\dot{m}}{dx} - \frac{1}{u}\frac{du}{dx} - \frac{1}{A}\frac{dA}{dx} \tag{2.25}$$

$$\frac{1}{u}\frac{du}{dx} = -\frac{1}{\rho u^2}\frac{dp}{dx} - \frac{2c_f}{D} + \left(1 - \frac{u_F}{u}\cos\theta_F\right)\frac{1}{\dot{m}}\frac{d\dot{m}}{dx} \tag{2.26}$$

$$\frac{1}{p}\frac{dp}{dx} = \frac{1}{\rho}\frac{d\rho}{dx} + \frac{1}{T}\frac{dT}{dx} - \frac{1}{W}\frac{dW}{dx} \tag{2.27}$$

$$\frac{1}{W}\frac{dW}{dx} = -\sum_{i=1}^{n_{sp}}\frac{W}{W_i}\frac{dY_i}{dx} \tag{2.28}$$

$$\frac{d\dot{m}}{dx} = \sum_{i=1}^{n_{sp}}\frac{d\dot{m}_{i,F}}{dx} \tag{2.29}$$

$$c_p\frac{dT}{dx} = \frac{h_{0,F} - h_0}{\dot{m}}\frac{d\dot{m}}{dx} - \frac{2c_f c_p(T_{aw} - T_w)}{\text{Pr}^{2/3}D} - u\frac{du}{dx} - \sum_{i=1}^{n_{sp}}h_i\frac{dY_i}{dx} \tag{2.30}$$

$$\frac{dY_i}{dx} = \frac{\dot{\omega}_i W_i A}{\dot{m}} + \frac{1}{\dot{m}}\frac{d\dot{m}_{i,F}}{dx} - \frac{Y_i}{\dot{m}}\frac{d\dot{m}}{dx} \tag{2.31}$$

The quantities in the above equations are defined in Table 2.5, and a more complete description is given in [68]. To solve the conservation equations it is required that the profile of the chemical reaction rate ($\dot{\omega}_i(x)$) of each species be supplied to the first term on the right-hand side of Eq. (2.31). Fuel-air mixing and combustion cannot be properly simulated by a 1D model, so a 3D mixing/combustion reduced-order model was developed, and it is described in [68]. The fuel is injected as a jet in a cross-flow, and the jet centerline coordinate y_C has been measured [153, 154] to be

$$\frac{y_C}{d_F} = c_2\left(\frac{x_C}{d_F}\right)^{1/3}R^{2/3} \tag{2.32}$$

where x_C is the axial distance from the injector, d_F is the fuel jet diameter, and R is the fuel jet momentum ratio

$$R = \sqrt{\frac{\rho_F}{\rho_A}\frac{u_F^2}{u_A^2}} \tag{2.33}$$

Along this curved jet centerline, the mean fuel mass fraction has been measured to be

$$Y_{F,C} = c_3\left(\frac{\rho_F}{\rho_A}\right)^{1/3}\left(\frac{u_F}{u_A}\right)^{-1/3}\left(\frac{x_C}{d_F}\right)^{-2/3} \tag{2.34}$$

The mean fuel mass fraction also follows a Gaussian profile in the direction that is normal to the curved jet centerline. The standard deviation of fuel mass fraction fluctuations also

43

Table 2.5: List of symbols for Eqs. (2.25)–(2.34).

Symbol		Description
A	=	area [m^2]
c_f	=	friction coefficient
c_p	=	specific heat at constant pressure [J/kg·K]
D	=	hydraulic diameter [m]
d_F	=	fuel injector diameter [m]
h	=	specific enthalpy [J/kg]
$\dot{m}$	=	mass flow rate [kg/s]
n_{sp}	=	number of species
p	=	pressure [Pa]
Pr	=	Prandtl number
R	=	momentum ratio
T	=	temperature [K]
u	=	flow velocity in axial direction [m/s]
W	=	molecular weight [kg/kmol]
x	=	axial spatial coordinate [m]
y	=	transverse spatial coordinate [m]
Y	=	species fraction
θ_F	=	fuel injection angle [rad]
ρ	=	density [kg/m^3]
$\dot{\omega}$	=	chemical reaction rate [kmol/m^2·s]

Table 2.6: List of subscripts for Eqs. (2.25)–(2.34).

Symbol		Description
A	=	core flow
aw	=	adiabatic wall
C	=	fuel centerline
F	=	fuel or fuel jet
i	=	species number
w	=	wall

follows a measured scaling law [153, 154].

Large lookup tables are generated so that after the mean fuel-air ratio (and its standard deviation) are computed at each x, y, z location using Eqs. (2.32) and (2.34), the table provides the results of the previously-computed finite-rate chemistry and turbulent mixing properties. The tables are similar to those generated by Fluent [155]. Local reaction rates are integrated over the yz-plane to obtain the desired reaction rates ($\dot{\omega}_i(x)$) which are inserted into Eq. (2.31). The advantage of the reduced-order method is that once the large lookup tables for chemical reaction rates and turbulent mixing properties are generated,
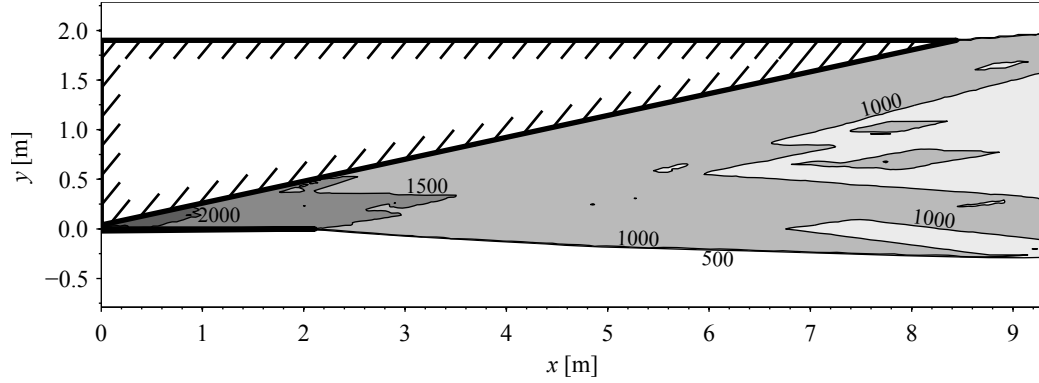
(a) Result from SAMURI.
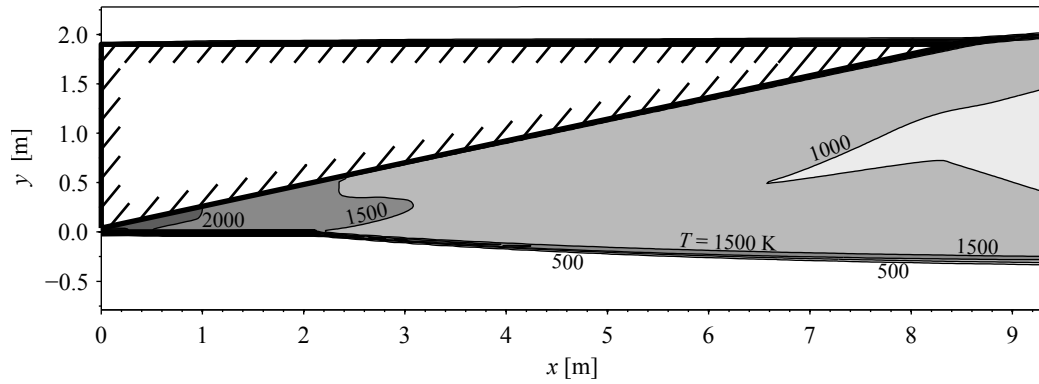
(b) Result from CFD++®.

Figure 2.18: Comparison of SAMURI results to CFD++® for the scramjet nozzle of Sangiovanni et al.

they can be rapidly accessed by MASIV. The disadvantages are that the generation of the lookup tables takes considerable time, and each fuel type requires its own table.

2.5 Nozzle

The nozzle model is the subject of [76] and has many similarities to the inlet model. It is similar in the sense that SAMURI is used for both components, but there are differences as well. While the inlet consists primarily of oblique shocks, the most important waves in the nozzle are expansion fans. This difference is important for the present modeling effort because shocks are nearly discrete while expansions are continuous.

However, shocks still play an important role in most nozzle flows, for example at the trailing edge of the cowl and the nozzle body. The nozzle model must be able to model both shocks and expansions, and thus SAMURI is preferable to the method of characteristics.

Another important phenomenon in a hypersonic nozzle occurs at the trailing edge of the cowl. For nozzles in the class of vehicle considered in this work, much of the lower boundary of the exhaust plume is a free surface that can change with atmospheric conditions and combustor heat release.

This exhaust plume can be seen in the comparison of SAMURI to CFD++® shown in Fig. 2.18, which uses the geometry and operating condition from [74]. The solution of this exhaust plume boundary begins with the solution of a Riemann problem at the cowl trailing edge, and the subsequent behavior is determined from interactions with the waves from the expanding nozzle flow.

The results of Fig. 2.18 show agreement between CFD++® and SAMURI. The SAMURI solution of Fig. 2.18(a) exhibits a more angular solution, which is the product of the expansion fan discretization. Importantly, the predictions of the exhaust plume boundary are very close, and the difference in thrust prediction is about 4%.

Experimental or flight data for a scramjet nozzle is expensive to generate, and no viable data was found for validating the MASIV nozzle model. However, linear plug nozzles have many of the same properties, and Chutkey et al. [79] provided a good data set for comparison.

Both linear plug nozzles and scramjet nozzles have a free surface so that the exhaust plume can adjust to atmospheric conditions, and the main difference is that plug nozzles also have a large deflection of flow angle. The SAMURI solution of the geometry from [79] is shown in Fig. 2.19 for two operating conditions. The conditions in the experimental apparatus of [79] were controlled by setting the stagnation pressure of the exhaust.

Although no comparable flow visualization was provided in [79], the results of Fig. 2.19 are consistent with expectations. At the design condition, the flow is essentially a single large expansion fan centered at the cowl trailing edge. In Fig. 2.19(b), the flow is underexpanded, and the surrounding air keeps the exhaust flow closer to the nozzle surface.

Static pressure measurements along the surface of the nozzle are compared to the SAMURI results in Figs. 2.20 and 2.21. Results match quite well except that the experiment shows a higher pressure in the middle portion of the nozzle surface in Fig. 2.20. Most importantly, both the experiment and computation show that the pressure begins to increase again in the underexpanded case (Fig. 2.19). This can also be seen in Fig. 2.19(b) in the form of a darker region on the nozzle surface at around $x = 3$ cm.

The MASIV engine component models have been shown here to capture a wide variety of phenomena that are important for hypersonic engine and vehicle performance. The assumptions for each of the models were discussed in Sec. 2.1.5, and the operating conditions remain within the range of validity throughout the results presented in Chapters 4–6.
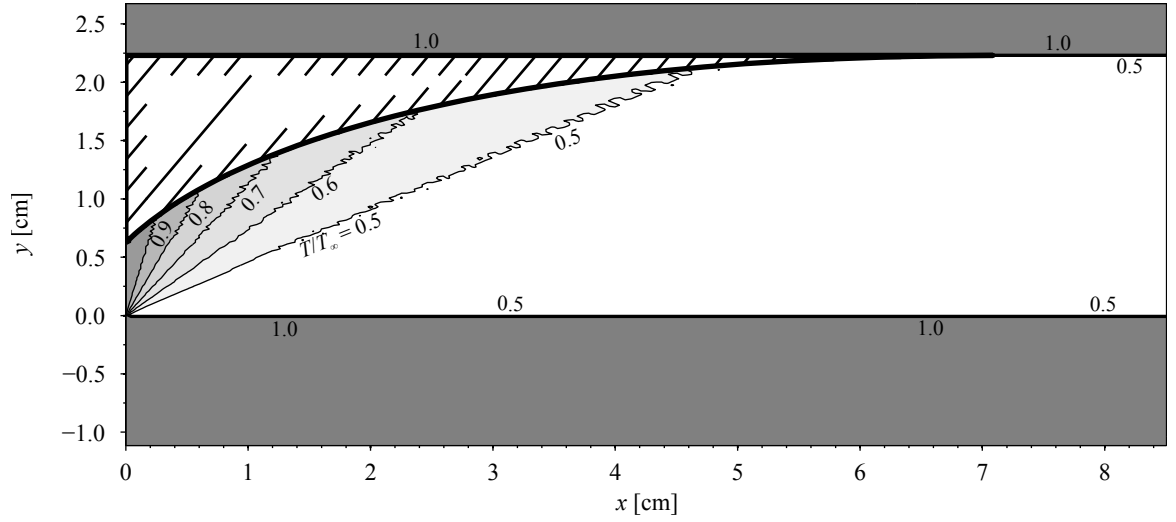
(a) Design condition ($p_{0,i}/p_\infty = 60$).
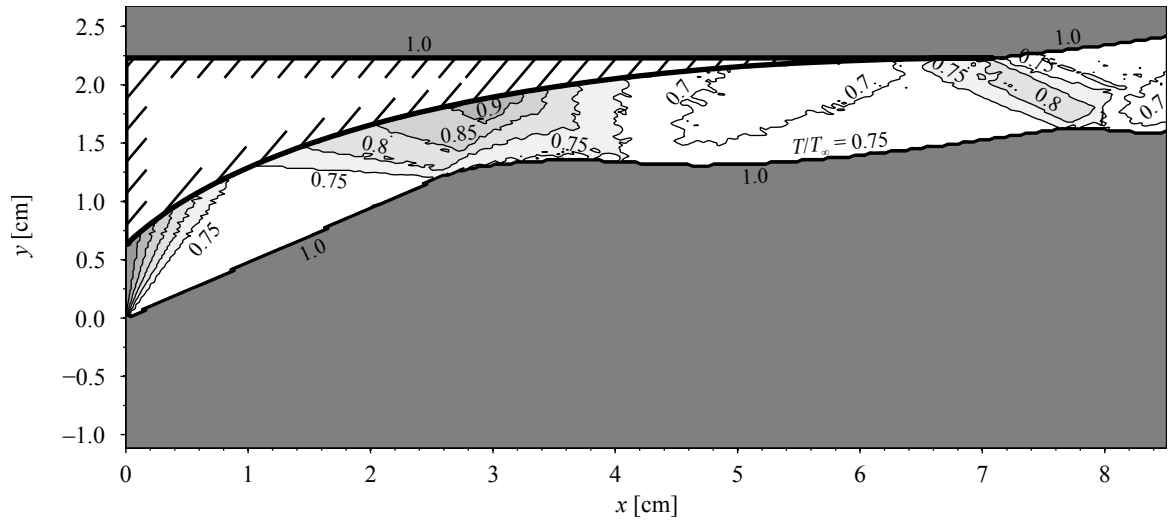
(b) Off-design condition ($p_{0,i}/p_\infty = 10$).

Figure 2.19: Contours of normalized temperature (T/T_∞) computed by SAMURI for flow in a plug nozzle at two pressure ratios.
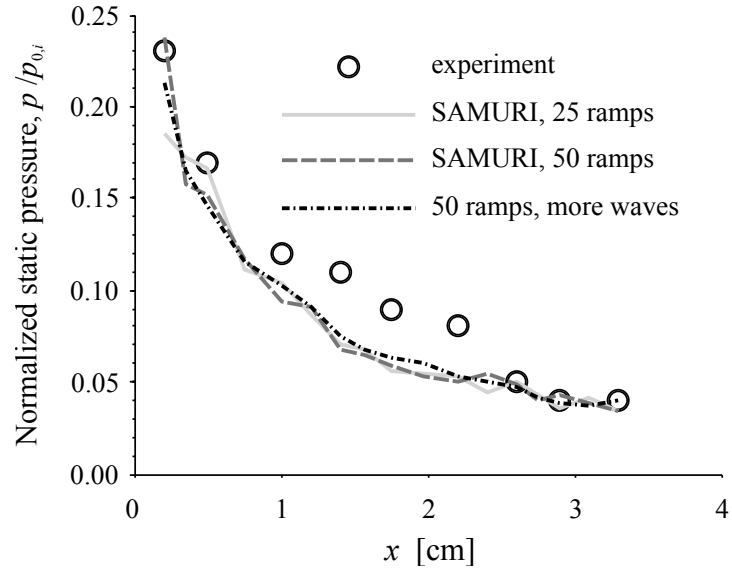
Figure 2.20: Comparison of plug nozzle surface pressure for design case ($p_{0,i}/p_\infty = 60$).
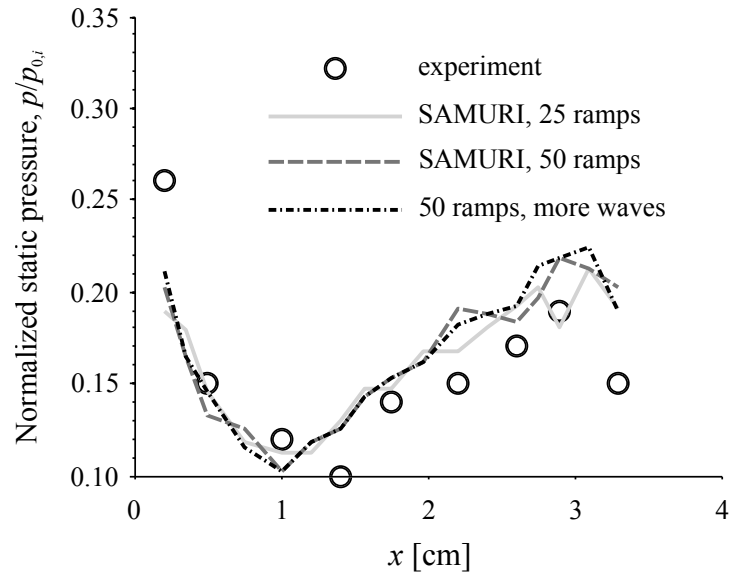
Figure 2.21: Comparison of plug nozzle surface pressure for off-design case ($p_{0,i}/p_\infty = 10$).

CHAPTER 3

Dual-Mode Ramjet-Scramjet Vehicles

The MASTrim vehicle model consists of the engine model discussed in Chapter 2, an external vehicle model that incorporates the hypersonic engine into a full tip-to-tail vehicle, and a suite of flight dynamics tools that will be discussed in Chapter 4.

A stylized view of the MAX-1 Vehicle Design (MAX-1) vehicle is shown in Fig. 3.1. The components of the propulsion system—the inlet, isolator/combustor, and nozzle—are quite visible and are on the same scale as the whole vehicle. The two main external shocks are sketched in blue, and the exhaust plume of the nozzle is sketched in orange. Modeling of the propulsion components is discussed in Chapter 2.

The subject of this chapter is to discuss how the engine is integrated into the vehicle. Because the propulsion system of an air-breathing hypersonic vehicle must be of the same scale as the vehicle, it is logical or even necessary to build the vehicle around the engine. This is exactly the approach taken in MASTrim; the engine is designed first, and the exterior is formed to fit around it. There are 21 design variables that define the engine design and 31 for the remainder of the vehicle.

In addition to the fuselage layout, some of the design variables are used to specify four surfaces for stabilization and control. These include two vertical tails and two horizontal
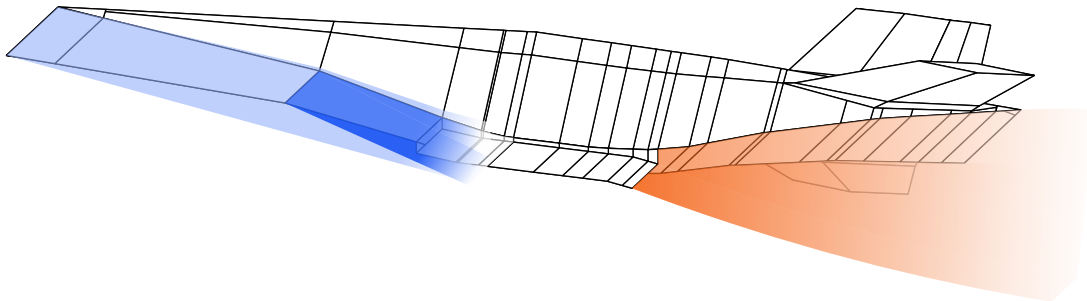
Figure 3.1: View of MAX-1 vehicle with stylized shocks and exhaust plume.
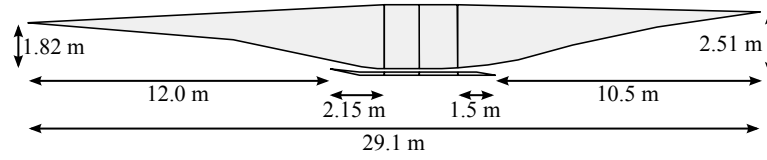
(a) Inlet and nozzle dimensions.
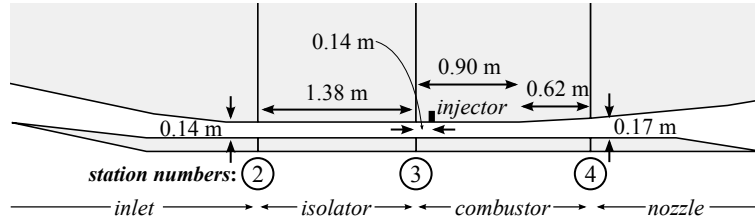
(b) Internal flowpath dimensions with station numbers.

Figure 3.2: Baseline MAX-1 flowpath dimensions. Engine width is 2.143 m.

surfaces, and each of these consists of a fixed portion and a movable surface. The horizontal control surfaces must function as pitch control devices (elevators) and roll control devices (ailerons), and so they are called *elevons*. Yaw control is performed by the vertical control surfaces (rudders).

Section 3.2 describes the remaining modeling component required for the calculation of forces and moments on the vehicle, which is the calculation of surface pressures on these exterior surfaces. The MASTrim model uses a local shock-expansion method to do this, which is similar to the approach used in [20].

Finally, the net angular accelerations on the vehicle cannot be determined without a model for the mass distribution and the location of the center of mass. In the present work, the total mass of the vehicle is determined using scaling relationships suggested by Chudoba [118], and the mass distribution is assumed to be uniform throughout the vehicle. These assumptions, which are discussed in more detail in Sec. 3.1.3, are useful to obtain a first estimate of the mass properties, but more detailed analysis would be required for later phases of design.

3.1 Vehicle Design

The MAX-1 design, which is sketched in Fig. 3.1 and shown in more detail in Fig. 3.2, demonstrates one instance of the 52 design variables used in MASTrim to construct a vehicle. This section presents an overview of how these parameters are used, and a complete description can be found in the official users' manual [156].

50
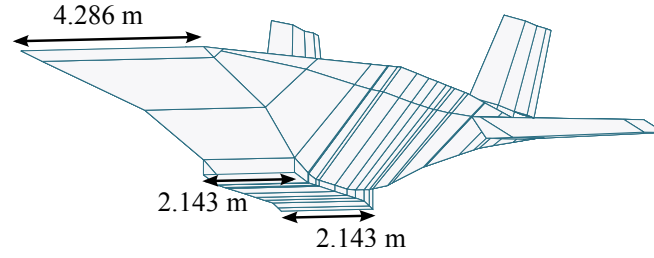
(a) Front view.
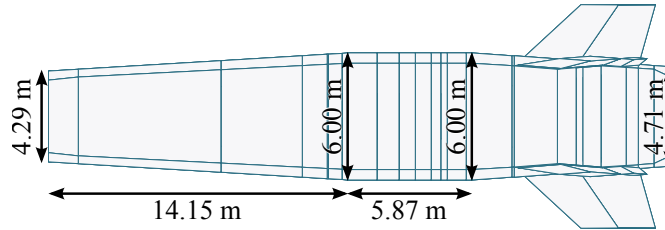
(b) Top view.

Figure 3.3: Two views of the MAX-1 vehicle showing fuselage dimensions.

3.1.1 Fuselage Design

Figures 3.2(a) and 3.2(b) show the dimensions of the engine flowpath. Many of the lengths in those two illustrations are used as design variables for the vehicle, while other lengths are determined automatically to match the specified flight conditions.

For example, the number of external ramps (two in Fig. 3.2(a)), the number of internal ramps (two in Fig. 3.2(b)), and the length in the x-direction from the leading edge of the vehicle to the leading edge of the cowl (12.0 m in Fig. 3.2(a)) are all given as inputs to the vehicle design routine. Then the length and slope of each ramp and the vertical distance between the vehicle and cowl leading edges (1.82 m in Fig. 3.2(a)), are determined using the process described in Sec. 2.2.3.

Once the two-dimensional engine flowpath has been constructed, a fuselage can be built around it. Figure 3.3 shows the main features of the fuselage shape. Once the engine width (2.143 m in Fig. 3.3(a)) is selected, the next input is the width of the leading edge (4.29 m in Fig. 3.3). This width is used as a baseline for the configuration of the rest of the top surface, which is shown in Fig. 3.3(b).

While the shape of the bottom of the fuselage is primarily determined by the engine flowpath design, the top surface is described by six design variables including the width of the leading edge. In addition to the leading edge width, the width at the trailing edge (4.71 m in Fig. 3.3(b)) is also a design variable. There is also a region of constant width

51

(a waist section, with a width of 6.00 m in Fig. 3.3(b)). The location of this waist section from the leading edge (14.15 m in Fig. 3.3(b)) and the length of the waist section (5.87 m in Fig. 3.3(b)) are the design parameters used to finish the layout of the top surface. The remaining fuselage design variable is the angle of the top surface at the leading edge, which sets a height for the vehicle. This design parametrization inherently limits the nozzle to the type used in the MAX-1 vehicle.

The MASIV/MASTrim model does not require that the vehicle is designed using the process described above to function. Any fuselage that can be discretized into a set of triangular planes can be used. An example of a very different vehicle layout used with MASTrim was presented in [157]. In addition, an interface was developed by [158] to design more generic fuselages that can be incorporated into MASTrim.

3.1.2 Control Surfaces

The final portion of the MASTrim design routine that completes the vehicle surface is the placement of stabilizing surfaces and movable control surfaces. Two vertical and two horizontal surfaces each have a movable section. Design variables for each surface include location of the center of the root, root chord length, taper ratio, span, sweep, dihedral angle, and portion of the surface that is movable.

Figure 3.4 shows all four movable surfaces. Another design variable is the fraction of the chord that is movable, and this fraction is constant from the base to the tip. For the MAX-1 control surfaces shown in Fig. 3.4, the horizontal surfaces are all-moving (100% movable), while the vertical control surfaces have a trailing-edge flap (30% of the chord is movable). A variable to control what fraction of the span is movable is not included.

The definitions of positive and negative deflection angles must also be laid out. The two horizontal control surfaces must control both the pitch, which is traditionally controlled by elevators, and roll, which is traditionally controlled by surfaces called ailerons; thus the horizontal control surfaces here are referred called *elevons*, which is a portmanteau of two control surface types. This terminology is not unique to hypersonic vehicles.

In keeping with convention for elevator angles, the individual elevon deflection angles are defined so that a positive deflection causes the trailing edge to move down and produces a negative pitching moment. If the left elevon deflection angle is δ_{LE}, and the right elevon deflection angle is δ_{RE}, then the average of the two deflection angles,

$$\delta_{CE} = \delta_e = \frac{\delta_{LE} + \delta_{RE}}{2} \tag{3.1}$$

or collective elevon angle, can also be thought of as the elevator angle, which is traditionally

52
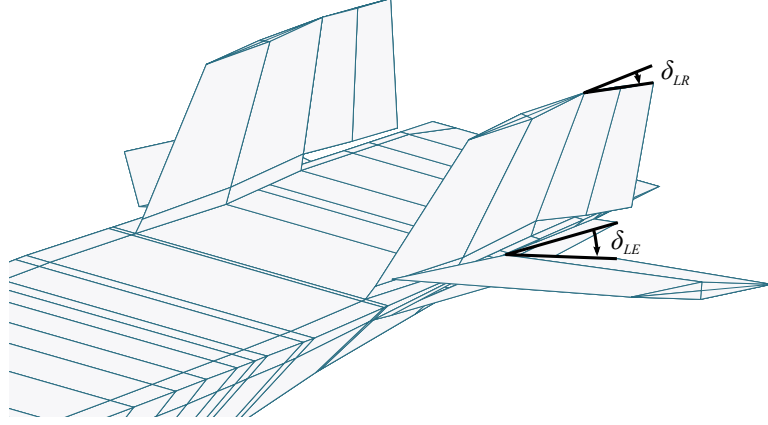
Figure 3.4: Tail region of MAX-1 vehicle showing positive control surface deflections. Left elevon deflection ($\delta_{LE} = +12°$) and left rudder ($\delta_{LR} = +25°$) are labeled.

denoted δ_e. Similarly, the difference of the two deflections serves as an aileron angle, which is traditionally denoted δ_a.

$$\delta_{DE} = \delta_a = \frac{\delta_{RE} - \delta_{LE}}{2} \tag{3.2}$$

Similar definitions are used for the rudders. For both rudders, a positive deflection moves the trailing edge to the left. The collective rudder angle is the usual rudder angle, which is often denoted δ_r.

$$\delta_{CR} = \delta_r = \frac{\delta_{LR} + \delta_{RR}}{2} \tag{3.3}$$

It is not as obvious what an intuitive application for the difference between the two deflection angles would be, but the difference is defined here as

$$\delta_{DR} = \frac{\delta_{RR} - \delta_{LR}}{2} \tag{3.4}$$

3.1.3 Mass Properties and Center of Mass

To provide a first estimate of the mass properties of a hypersonic vehicle, correlations provided by Chudoba [118] are used. These correlations give estimated weights for the vehicle and how much fuel it can carry, and the correlations are dependent on the planform area of the vehicle, design Mach number, and fuel type.

The following describes Chudoba's scaling relationships as they apply to the MASTrim hypersonic vehicle design. Specific numbers are for the MAX-1 vehicle design. The empty mass (more specifically the operating weight including payload but with no fuel) is deter-

mined by the lifting area of the vehicle, which is defined to be

$$S = L_{vehicle}w_{nose} = 125.8 \text{m}^2 \tag{3.5}$$

A more accurate approach would be to use the combined area of the vehicle projected into the *xy*-plane, and this may be a source of error in the mass estimates. Then the empty mass is given by

$$m_{owe} = (241.06 \text{ kg}) \times \left(\frac{S}{1 \text{ m}^2}\right)^{0.906} = 1.925 \times 10^4 \text{ kg} \tag{3.6}$$

The interesting thing to note here is that empty mass scales approximately with the area of the vehicle rather than the volume. The scaling relationships from [118] such as the one above is empirical and based on historical data, but this scaling could be expected. Much of the structure of the vehicle is near the exterior surface, and the surface area grows with the length of the vehicle squared. Also, the lift of a vehicle scales with the area, and so the mass should not grow much faster than the lift to ensure that larger vehicles can still fly. This may mean that larger vehicles are likely to be more flexible (and have lower natural frequencies) as they have less structural mass per volume.

The next step in the mass scaling relationships is to determine the so-called propulsive index, which is defined

$$I_p = (1701 \text{ kg})e^{-0.1877M_{design}} = 314.1 \text{ kg} \tag{3.7}$$

The propulsive index is a measure of how much fuel mass will be needed to satisfy mission objectives. The idea is that air-breathing engines are less efficient at higher Mach numbers, and more fuel mass is required for such vehicles. This number can then be used to determine how much fuel mass the vehicle will have using a weight ratio

$$WR = \frac{m_{fuel}}{m_{owe}} = 1 + \frac{\rho_{fuel}}{I_p} = 1.239 \tag{3.8}$$

where *WR* is the ratio of fuel mass to empty mass. Assuming LH2 fuel, the density is $\rho_{fuel} = 75 \text{ kg/m}^3$. The relationships of [118] are based on historical data, and although the logic of them is not always easy to follow, we showed in Sec. 1.2.5 that they match other available data for a range of hypersonic vehicles.

Once the mass of the vehicle is calculated, an inertia tensor must be constructed. For this model, we assume that the mass is distributed evenly throughout the vehicle except for some ballast placed at the nose to shift the center of mass forward. This assumption is used regardless of how much fuel is currently in the vehicle, and as a result, the inertia tensor

Table 3.1: Mass properties of vehicle.

Symbol	Description	Value
	operational empty mass	1.93×10^4 kg
	maximum fuel mass	2.38×10^4 kg
I_{xx}	specific moment of inertia	2.33 m^2
I_{yy}	specific moment of inertia	36.23 m^2
I_{zz}	specific moment of inertia	37.90 m^2
I_{xz}	specific product of inertia	0.54 m^2
x_{cg}	center of mass location	-12.88 m
z_{cg}	center of mass location	0.17 m

divided by mass is constant. The assumption that the mass distribution is approximately constant has not been verified,

The location of the center of mass is important because it affects stability and the moments on the vehicle. Moving the center of gravity forward in effect causes a nose-down moment, which the vehicle must counteract. Normally the elevator setting (δ_{CE}) decreases (that is, deflects trailing-edge up). If $\delta_{CE}>0$, this causes a reduction in drag from the elevator. However, the change in the elevator setting also causes a slight decrease in the lift, which leads to a higher trim angle of attack and thus more drag. As a result of these two competing trends, moving the center of mass forward can cause either a increase or decrease in the fuel consumption. Experience has shown that the minimum-drag center of mass location is significantly aft of the location that would cause the vehicle to be marginally stable. It should be noted that a marginally unstable design can be acceptable as long as the instability is with reason so that it can be stabilized.

For the MAX-1 vehicle, the center of gravity is shifted forward from the center of volume to help with stability. This causes an increase in fuel consumption and is a powerful design variable for many aspects of vehicle performance. The mass properties of the vehicle are summarized in Table 3.1. Unfortunately, vehicle mass studies in the literature such as [120] do not present results for moments and products of inertia for comparison and validation.

3.2   External Aerodynamics

To calculate the forces on the vehicle's exterior, we use a modification of the panel method from [20] that also incorporates viscous forces. The vehicle exterior shown in Figs. 3.1, 3.3, and 3.4 is split into a triangular surface mesh that can be seen in Figs. 3.5 and 3.6.
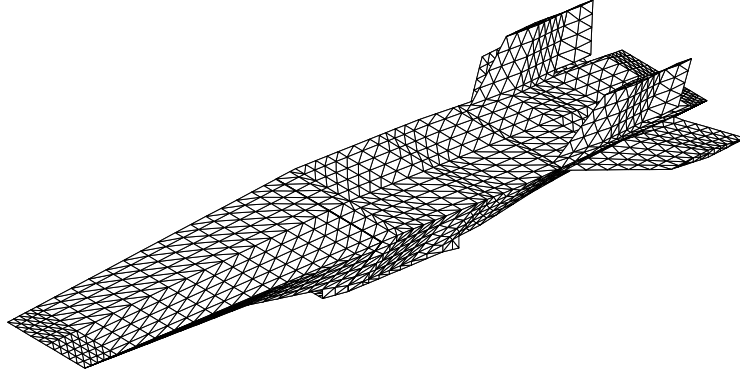
Figure 3.5: Upper surface of MAX-1 vehicle showing triangulated surface.

For each triangular surface panel, the freestream velocity is projected onto the surface, and the angle between the freestream and the projected velocity is then used to compute the thermodynamic properties behind either an oblique shock or a Prandtl-Meyer expansion, depending on the sign of the angle. This method is similar in nature to Newtonian impact theory [8] and piston theory [38] in that the pressure is calculated independently for each triangular panel. This method was shown to agree with the HABP (Hypersonic Arbitrary Body Program) to within a few percent, especially for small angles of attack [20], and recent work has also verified the present external aerodynamics model against CFD results [158].

The flow also accounts for the angular velocity of the vehicle, ω_{nb}^b, so that the "freestream" velocity for a given triangle is

$$\mathbf{u}^b = \mathbf{u}_\infty^b + \omega_{nb}^b \times (\mathbf{r}^b - \mathbf{r}_{cg}^b) \tag{3.9}$$

where the superscript b means that each vector is written in the body coordinate frame described earlier. Then the deflection angle is calculated by solving

$$\sin\delta = -\frac{\hat{\mathbf{n}}^b \cdot \mathbf{u}^b}{\|\mathbf{u}^b\|} \tag{3.10}$$

where $\hat{\mathbf{n}}^b$ is the outward-pointing unit normal vector. The pressure on the triangle is given by usual oblique shock theory using $M = \|\mathbf{u}^b\|/a_\infty$ as the local Mach number and δ as the deflection angle when δ is positive but less than a certain deflection δ_{max}. When $\delta > \delta_{max}$, Newtonian aerodynamics is used as it is known to give good results for large incidence angles. In the current vehicle, no surfaces create a detached shock as long as the vehicle is flying at an angle of attack between $-5°$ and $+5°$, although elevon deflections of about $20°$

56
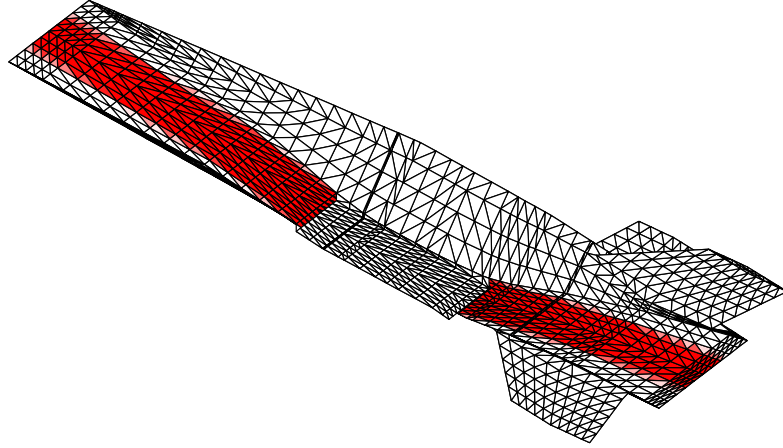
Figure 3.6: MAX-1 vehicle geometry with engine flowpath surfaces highlighted in red.

would cause detached shocks.

Boundary layer thickness and friction coefficient are computed using the Van Driest II method [5]. Since the viscous force on each triangle depends on the size of the boundary layer that exists upstream of the triangle, it is not possible to calculate the forces independently for each triangle. Considering the boundary layer to restart on each triangle would lead to a considerable overestimate of viscous drag, and to account for this, a momentum thickness is calculated for each edge of each triangle. For each edge that is part of a leading edge, this thickness is set to zero. This model provides a first estimate of the viscous drag on the exterior of the vehicle, but it does not account for shock-boundary layer interactions. The boundary layer is assumed to be turbulent on the entire surface of the vehicle. Due to this assumption, the viscous drag estimate is higher than the actual number, although transition from laminar to turbulent boundary layers causes other complications in addition to the drag force.

3.3 Engine Integration

The purpose of this section is to describe how the MASIV engine model of Chapter 2 and the external analysis described in the present chapter are combined to form the MASTrim vehicle model. First, the surface mesh of the vehicle is split into engine and non-engine portions. In Fig. 3.6, the triangular panels that are part of the engine are shown in red. For these surfaces, the external aerodynamics analysis of Sec. 3.2 is not used, and the pressure and force results from the engine analysis are applied instead.

This means that no forces are double-counted, but there may be local discontinuities in

the modeled pressure, especially on the nozzle surfaces. More importantly, it means that the complex phenomena that affect engine performance are accounted for on the relevant surfaces.

Figure 3.7 shows how information is passed to and from each component in the MASTrim code. In Fig. 3.7, there are three types of blocks and three types of arrows, and these are explained in the caption.

The inputs to the simulation consist of states ($\mathbf{x}$, also referred to as the flight condition variables) and a vector of control variables ($\mathbf{u}$). The flight condition is fed into an atmospheric model that determines the freestream air conditions needed for the inlet and external aerodynamics solvers. The four engine components on the left are shown, repeating most of the information in Fig. 2.1. The force and moment created by each of the four engine components is calculated individually, as indicated by the dashed lines in Fig. 3.7. External pressures and viscous effects naturally provide another source of forces on the vehicle, and this is represented by the fifth input to the forces & moments block.

Finally, the outputs of the model consist of accelerations and angular accelerations. Calculating these linear and angular accelerations requires applying the complex nonlinear equations of motion discussed in the next chapter.
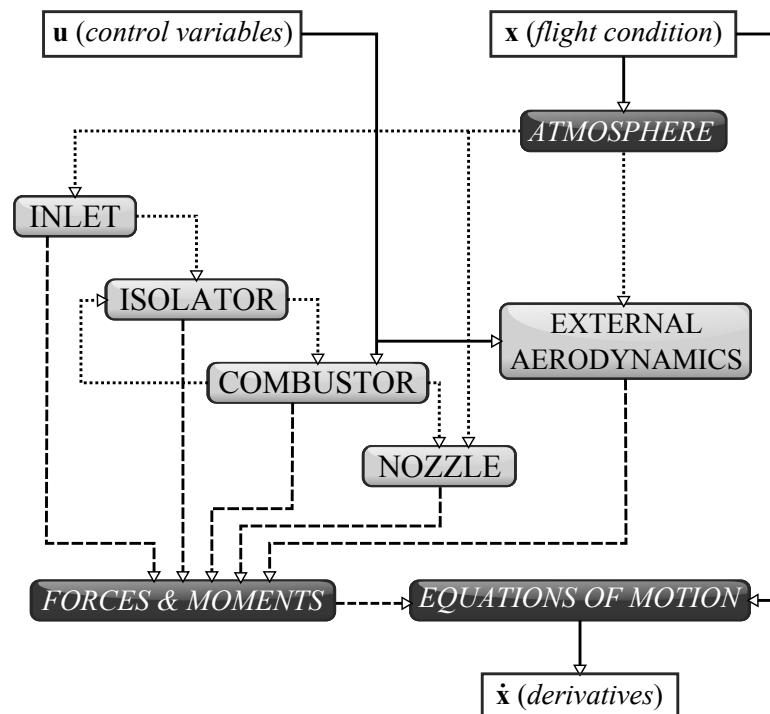
Figure 3.7: Overview of information flow within the MASTrim program. White blocks represent inputs and outputs, and solid lines show the flow of information to and from these inputs and outputs. Dark blocks represent models not specific to the vehicle, and the gray blocks represent vehicle component models. Dotted lines show information about gas states, and dashed lines show force & moment information.

CHAPTER 4

Flight Dynamics of Hypersonic Vehicles

This chapter describes the use of the MASTrim model to simulate hypersonic flight. Unlike the previous chapters, most of the variables in this chapter pertain to the vehicle as a whole. For example, the flight Mach number, M, is a variable that describes the speed of the vehicle rather than the speed of the flow at a particular point in the inlet or combustor as it would have in Chapter 2 or 3. The analysis of the individual components (inlet, isolator, combustor, nozzle, and external surface) still plays an important part in understanding the flight dynamics of a hypersonic vehicle, but these results will be expressed using only two variables: the net aerodynamic and propulsive force on the vehicle ($\mathbf{f}^b$) and the net aerodynamic and propulsive moment ($\mathbf{M}^b$).

Section 4.1 shows how these forces and moments relate to the net accelerations and angular accelerations, and then a method to balance these accelerations (i.e., trim the vehicle) is presented. In Sec. 4.1.3, some insight is given into the stability and controllability of the vehicle is given.

Section 4.2 gives a discussion of the trends in these flight variables over a range of vehicle speeds and altitudes. In so doing, the explanation frequently turns back to the detailed analysis of the previous chapters to explain the overall performance and flight dynamics of the vehicle. Finally, Sec. 4.3 shows an example application of this type of analysis to describe how the MAX-1 vehicle performs in a range of turning flight conditions. Together, it is hoped that the discussion contained in this chapter gives insight into the nature of air-breathing hypersonic flight dynamics and shows how the MASTrim model can be used to simulate a wide variety of flight conditions and maneuvers.

4.1   Equations of Motion

For hypersonic vehicles, the velocities and altitude are high enough that the assumption a flat Earth is no longer valid. For example, to maintain level flight going east over the

equator at Mach 8 and an altitude of 26 km, the required lift force would be only 87% of the weight of the vehicle. We employ a model that is consistent with a rotating WGS84 Earth [159, 160].

The purpose of this section is to briefly describe the equations of motion used throughout this work. The full system of equations is described in Appendix B, while Sec. 4.1.1 identifies the primary function of the most important variables. Section 4.1.2 describes how the forces and moments are balanced. Finally, Sec. 4.1.3 describes the linearized equations of motion, which are used to investigate the stability and controllability properties of individual flight conditions.

4.1.1   State Variables and Control Variables

The full equations of motion, derived in Appendix B, are

$$\dot{\mathbf{v}}^b = \mathbf{f}^b + C_n^b \mathbf{g}^n - C_n^b (\Omega_{ie}^n)^2 C_e^n \mathbf{r}^e - C_n^b (2\Omega_{ie}^n + \Omega_{en}^n) \mathbf{v}^n - \Omega_{nb}^b \mathbf{v}^b \tag{4.1}$$

$$\dot{\boldsymbol{\omega}}_{ib}^b = (\mathsf{I}^b)^{-1} (\mathbf{M}^b - \Omega_{ib}^b \mathsf{I}^b \boldsymbol{\omega}_{ib}^b) \tag{4.2}$$

In these equations, the net aerodynamic and propulsive forces per unit mass ($\mathbf{f}^b$) and moments per unit mass ($\mathbf{M}^b$) are the terms calculated by the methods described in Chapters 2 and 3. The inertia tensor per unit mass is I^b. An angular velocity written ω_{ab}^c describes the rotation of the b-frame with respect to the a-frame with the components calculated in the c-frame, and Ω_{ab}^c represents the same angular velocity but written in skew-symmetric matrix form. For example Ω_{ie}^n is the angular velocity of the Earth with respect to the inertial i-frame with the results written in the n-frame (navigation frame). At the equator, the angular velocity of the Earth points straight north, and at the North pole it points straight up (i.e., normal to the surface of the Earth).

For the bulk of this analysis, the above equations are treated as a black box and written in a much simpler form:

$$\dot{\mathbf{x}} = \mathbf{F}(\mathbf{x}, \mathbf{u}) \tag{4.3}$$

Here $\mathbf{x}$ is a vector of state variables that describe the position, velocity, attitude, and rotation of the vehicle; $\mathbf{u}$ is a vector of control (or input) variables that the pilot or control system can use to affect how the plane's state variables change. All the terms in the equations of motion depend on $\mathbf{x}$, while only the net forces ($\mathbf{f}^b$) and moments ($\mathbf{M}^b$) depend on the control variables.

Table 4.1: List of state variables and descriptions for the equations of motion.

Symbol	Name	Type
L	Geodetic latitude	Position
λ	Longitude	Position
h	Altitude	Position
V	Speed, or total velocity magnitude	Velocity
α	Angle of attack	Velocity
β	Sideslip angle	Velocity
ϕ	Roll angle	Attitude
θ	Pitch angle	Attitude
ψ	Yaw angle	Attitude
P	Roll rate	Angular velocity
Q	Pitch rate	Angular velocity
R	Yaw rate	Angular velocity

Table 4.2: List of state variables and descriptions for the vehicle control variables.

Symbol	Name	Primary purpose
ER	Equivalence ratio	Thrust, acceleration control
δ_{CE}	Collective elevon angle (elevator angle)	Pitch control
δ_a	Differential elevon angle (aileron angle)	Roll control
δ_{CR}	Rudder angle	Yaw control
δ_{DR}	Differential rudder	Usually not used
δ_{xc}	Horizontal displacement of the inlet cowl	Control inlet efficiency
δ_{zc}	Vertical displacement of the inlet cowl	Control inlet efficiency

There are many ways to parametrize the state; the following variables are used here.

$$\mathbf{x} = [\begin{array}{cccccccccccc} L & \lambda & h & V & \alpha & \beta & \phi & \theta & \psi & P & Q & R \end{array}]^T \tag{4.4}$$

The state variables are described in Table 4.1. The primary control variables are

$$\mathbf{u} = [\begin{array}{cccc} ER & \delta_{CE} & \delta_{DE} & \delta_{CR} \end{array}]^T \tag{4.5}$$

All but the equivalence ratio (ER) are deflection angles, which are described in more detail in Sec. 3.1.2. Only these four primary control variables were varied during the flight simulations in this work, but several more control variables can be varied in MASTrim including deflections of the inlet cowl. Table 4.2 provides a full list of the control variables that have been implemented in the MASTrim.

4.1.2 Trimmed Flight Conditions

Given a target acceleration $\dot{\mathbf{x}}$, finding a trimmed flight condition becomes a problem of finding values of $\mathbf{x}$ and $\mathbf{u}$ such that Eq. (4.3) is satisfied. In the general case, $\mathbf{x}$ has 12 components, and m is the number of control variables. This results in a system of 12 equations and $12 + m$ variables. However, the position, velocity, and angular velocity are inputs to the trim equation. This is so that we can determine the trimmed flight condition for a given velocity (V) and altitude (h), for example. This reduces the problem to 6 equations with $2 + m$ variables. It is convenient to write the trim equations

$$\dot{\boldsymbol{\xi}} = \mathbf{F}(\boldsymbol{\xi}, \boldsymbol{v}) \tag{4.6}$$

where

$$\boldsymbol{\xi} = [\, L \quad \lambda \quad h \quad V \quad \gamma \quad \chi \quad P \quad Q \quad R \,]^T \tag{4.7}$$

$$\boldsymbol{v} = [\, \alpha \quad \phi \quad ER \quad \delta_{CE} \quad \delta_{DE} \quad \delta_{CR} \,]^T \tag{4.8}$$

and the unknown derivatives are

$$\dot{\boldsymbol{\xi}} = [\, \dot{V} \quad \dot{\gamma} \quad \dot{\chi} \quad \dot{P} \quad \dot{Q} \quad \dot{R} \,]^T \tag{4.9}$$

This results in a system of 6 unknowns ($\dot{\boldsymbol{\xi}}$) and six variables ($\boldsymbol{v}$), so it can be solved as a nonlinear system of equations.

4.1.3 Linearized Equations

Let $\bar{\mathbf{x}}$ and $\bar{\mathbf{u}}$ be a particular flight condition and control setting such that $\dot{\bar{\mathbf{x}}} = \mathbf{F}(\bar{\mathbf{x}}, \bar{\mathbf{u}})$. Considering a small perturbation to both $\bar{\mathbf{x}}$ and $\bar{\mathbf{u}}$ results in the linearized equations of motion. A first-order expansion gives

$$\dot{\bar{\mathbf{x}}} + \Delta \dot{\mathbf{x}} = \mathbf{F}(\bar{\mathbf{x}}, \bar{\mathbf{u}}) + \frac{\partial \mathbf{F}}{\partial \mathbf{x}}\bigg|_{\bar{\mathbf{x}}, \bar{\mathbf{u}}} \Delta \mathbf{x} + \frac{\partial \mathbf{F}}{\partial \mathbf{u}}\bigg|_{\bar{\mathbf{x}}, \bar{\mathbf{u}}} \Delta \mathbf{u}$$

At the same time, consider an output function of states that can be measured during flight so that $\mathbf{y} = \mathbf{G}(\mathbf{x}, \mathbf{u})$ with

$$\mathbf{y} = [\, V \quad \gamma \quad \chi \quad \phi \,]^T \tag{4.10}$$

in our case. Recognizing that $\dot{\bar{\mathbf{x}}} = \mathbf{F}(\bar{\mathbf{x}}, \bar{\mathbf{u}})$, the linearized equations of motion become

$$\Delta\dot{\mathbf{x}} = \mathsf{A}\Delta\mathbf{x} + \mathsf{B}\Delta\mathbf{u} \tag{4.11}$$

$$\Delta\dot{\mathbf{y}} = \mathsf{C}\Delta\mathbf{x} + \mathsf{D}\Delta\mathbf{u} \tag{4.12}$$

where

$$\mathsf{A} = \left.\frac{\partial\mathbf{F}}{\partial\mathbf{x}}\right|_{\bar{\mathbf{x}},\bar{\mathbf{u}}} \qquad\qquad \mathsf{B} = \left.\frac{\partial\mathbf{F}}{\partial\mathbf{u}}\right|_{\bar{\mathbf{x}},\bar{\mathbf{u}}}$$

$$\mathsf{C} = \left.\frac{\partial\mathbf{G}}{\partial\mathbf{x}}\right|_{\bar{\mathbf{x}},\bar{\mathbf{u}}} \qquad\qquad \mathsf{D} = \left.\frac{\partial\mathbf{G}}{\partial\mathbf{u}}\right|_{\bar{\mathbf{x}},\bar{\mathbf{u}}}$$

Analysis of the linearized dynamics gives insight into the stability and control characteristics of the vehicle. The eigenvalues of A give the open-loop stability characteristics of the trimmed flight condition, and by selecting the controlled states and the corresponding control effectors to be used, we can also calculate the transmission zeros of the system.

4.2 Operating Maps

Operating maps, first reported in [161], show trends in vehicle performance and operation for a range of flight conditions. An example of an operating map is a function for the equivalence ratio (ER), angle of attack (α), and elevator angle (δ_{CE}) required for steady-level flight over a range of flight Mach numbers (M) and altitudes (h). Such operating maps illuminate trends in vehicle performance and operation that would be difficult to determine from individual trim conditions or time-domain simulations. Another application of such operating maps is to provide a surrogate model for optimization so that the optimizer does not have to evaluate the full model at every iteration.

Figure 4.1 shows an operating map with axes of Mach number (M) and altitude (h). This example operating map is calculated for the MAX-1 vehicle shown in Fig. 3.2 with the fuel tanks half full. The figure considers flight that is eastward ($\chi = 90°$) at the equator ($L = 0$). This type of flight condition is used as a baseline because it maximizes utilization of the Earth's rotation. Westward flight ($\chi = 270°$) requires more lift and thus has a higher fuel consumption.

Figures 4.1(a), 4.1(c) and 4.1(d) show the required values of trim variables ($\boldsymbol{\upsilon}$) to satisfy the equations of motion for steady, level flight. The MASTrim model was able to trim the vehicle at all of the flight conditions in the scram mode except at the lowest Mach numbers and highest altitudes (upper left corner; corresponds to the lowest dynamic pressures).

(a) Equivalence ratio (*ER*).

(b) Fuel mass flow rate ($\dot{m}_f$) in kg/s.

(c) Angle of attack (α) in degrees.

(d) Elevator angle (δ_{CE}) in degrees.
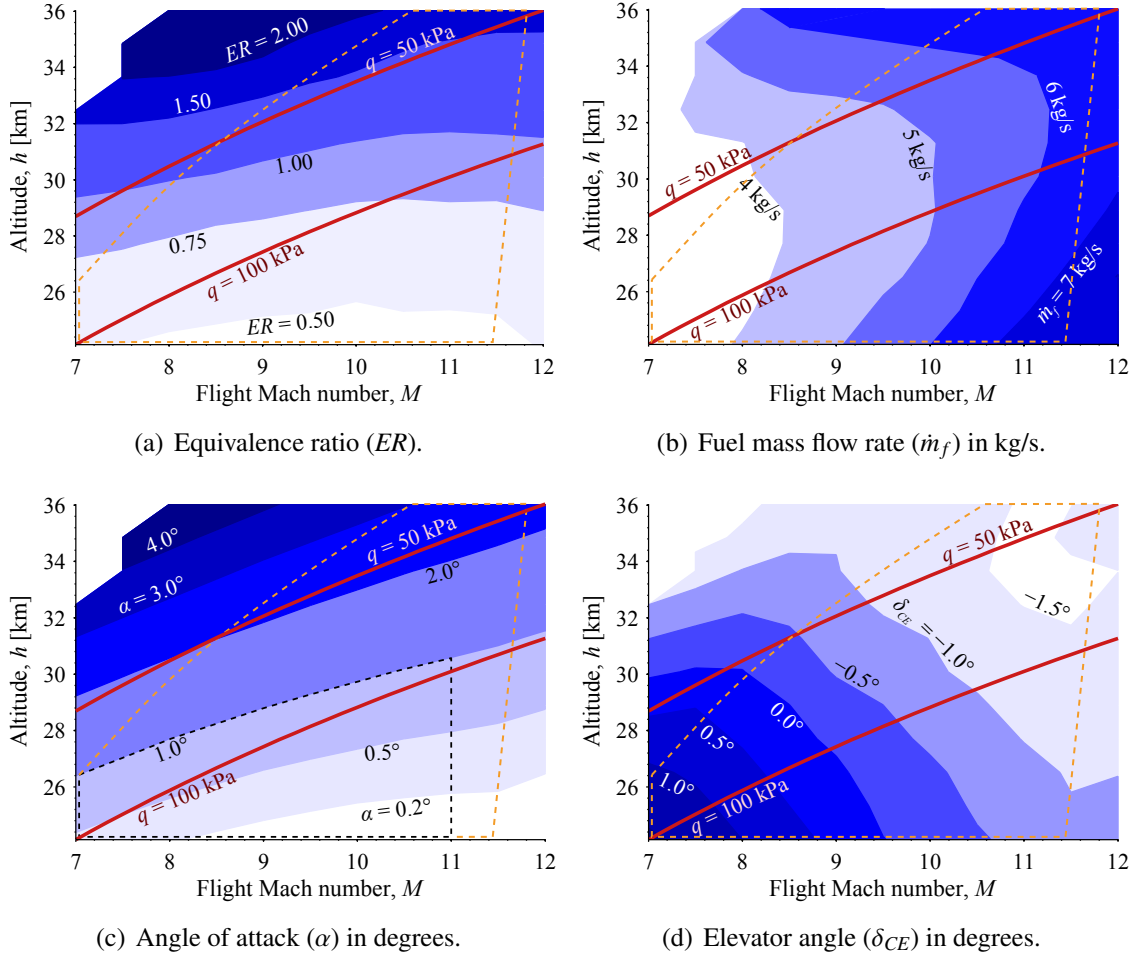
Figure 4.1: Operating map for steady, level flight for the MAX-1 vehicle assuming equatorial ($L = 0$), eastward ($\chi = 90°$) flight conditions. The red lines mark upper ($q = 100$ kPa) and lower ($q = 50$ kPa) bounds of the flight corridor. The upper left corner corresponds to conditions that could not be trimmed in the scram mode. Fig. 4.1(c) shows the boundaries of the inlet design M and α range (black dotted line) and the actual limits of strong interactions in the inlet (orange dotted line). These limits would be affected by unmodeled effects such as shock–boundary-layer interactions and blunted leading edges.

However, structural and heating constraints (which are not modeled in this work) typically limit the dynamic pressure (q) to about 100 kPa. A minimum dynamic pressure of about 50 kPa is usually used to ensure adequate pressure in the combustor. Lower combustor pressures are possible, but operability suffers at such low pressures. The range of flight conditions between these dynamic pressures is called the flight corridor.

Interestingly, Fig. 4.1(b) shows that for a fixed Mach number (vertical line), the fuel consumption is lowest within the flight corridor. This demonstrates that even neglecting other constraints, the flight corridor is the region with ideal engine performance.

One important trend is that the trim angle of attack decreases as the Mach number increases and the altitude is constant (horizontal lines in Fig. 4.1(c)). This is due to the increasing dynamic pressures at higher Mach numbers, which means that a lower lift coefficient is needed. If the altitude is increased while keeping the Mach number constant (vertical lines in Fig. 4.1(c)), the angle of attack must increase. The higher altitude entails a lower dynamic pressure, which means that a higher lift coefficient is needed. Both of these trends can be seen from the definition of lift and drag coefficients.

$$L = q_\infty S C_L = q_\infty S (C_{L_0} + C_{L_\alpha} \alpha) \tag{4.13}$$

$$D = q_\infty S C_D = q_\infty S (C_{D_0} + K C_L^2) \tag{4.14}$$

For a fixed Mach number, the parameters C_{L_0}, C_{L_α}, C_{D_0}, and K are approximately constant. From these equations, it can be seen that increasing q_∞ while holding L constant results in a lower angle of attack and a lower drag force.

The angle of attack analysis also explains many of the trends in the equivalence ratio operating map (Fig. 4.1(a)). Increasing the Mach number while holding the altitude constant (horizontal lines in Fig. 4.1(a)) tends to increase the drag on the vehicle but also increase the mass flow to the engine. In addition, the angle of attack decreases along this line, which tends to lower the drag coefficient. The result is that the equivalence ratio (*ER*) may actually decrease, although Fig. 4.1(b) shows that the actual fuel consumption increases with Mach number. Now consider an increasing altitude with a fixed Mach number (vertical lines in Figs. 4.1(a) and 4.1(b)). The angle of attack must increase to trim the vehicle, which results in a higher drag coefficient. At the same time, the dynamic pressure is decreasing, which tends to lower the actual drag force. Therefore as the altitude increases, the equivalence ratio consistently increases while the fuel mass flow rate first decreases and then increases again.

Decreases in angle of attack do not always lead to improved performance, however. A lower angle of attack means that the inlet capture area is smaller, and at a certain point this

limits the performance of the engine.

The final trend to discuss from Fig. 4.1 is the effect of leaving the range operating conditions for which the inlet was designed. Recall from Chapter 2 that the present inlet design method finds the ramp angles that minimize the stagnation pressure loss when the flight Mach number equals the design Mach number ($M = M_{design}$) subject to a compression constraint. The ratio of the static pressure at the end of the inlet (p_2; see Fig. 3.2) to the freestream pressure (p_∞) is fixed at the design Mach number, and this value is also a design variable called r_p:

$$r_p = \left.\frac{p_2}{p_\infty}\right|_{M=M_{design}} \tag{4.15}$$

Second, the lengths of the inlet ramps (e.g. L_1-L_4 in Tables 5.1 and 5.2) are selected so that certain shock interactions do not occur when the flight Mach number is in a certain window $M_{min} < M < M_{max}$, and the angle of attack is in another window $\alpha_{min} < \alpha < \alpha_{max}$. Specifically, the external shocks must remain upstream of the cowl leading edge so that the shocks do not go into the combustor, and the internal shocks must remain downstream of "shoulders" on the inlet body.

The MAX-1 inlet used to calculate the results in Fig. 4.1 was designed for Mach numbers $M \in [7, 11]$ and angles of attack $\alpha \in [-0.5°, 1.0°]$ with a design compression ratio of $r_p = 70$. In the angle of attack operating map (Fig. 4.1(c)), the flight conditions that stay within this rectangle of Mach numbers and angles of attack are inside the shape marked with a dotted black line. However the shock interactions of the inlet design routine are not active on the entire boundary marked with the black dotted line. The orange dotted lines in Fig. 4.1(c) denote the contours of where the shock interaction constrains are active. The two boundaries share exactly two points, which are the lowest Mach number and highest angle of attack (top left corner of black dotted region) and the highest Mach number and lowest angle of attack (not pictured; would be at $M = 11$ and $h = 24.2$ km).

The operating maps of Fig. 4.1 show noticeable changes at the boundary marked by this orange dotted line. The upper Mach-number constraint (right, vertical orange line) shows the point where the first external shock hits the cowl leading edge, and this boundary has a noticeable effect in the equivalence ratio plot (*ER*, Fig. 4.1(a)), the angle of attack plot (α, Fig. 4.1(c)), and the elevator angle plot (δ_{CE}, Fig. 4.1(d)). Going outside this boundary has the tendency to increase the forces on the inlet, which results in a lower angle of attack and higher equivalence ratio. The upper angle-of-attack boundary (left diagonal dotted orange curve in Fig. 4.1(c)) is visible in the elevator angle map (Fig. 4.1(d)) as a sharp change in slope of the contours.

It is a predictable result that the trim angle of attack increases with increasing Mach

number along a constant–dynamic-pressure trajectory. The reason is that lift coefficients tend to be lower at larger supersonic Mach numbers [147]. Current literature [11, 30] appears to identify this as a detrimental result to be minimized, but our results suggest otherwise. The lower angles of attack at low Mach numbers help keep the internal shocks downstream of the shoulder points, and the higher angles of attack at high Mach numbers help keep the external shocks upstream of the cowl leading edge. The result is that the inlet region of efficient operation (orange dotted lines in Fig. 4.1(c)) extend well beyond the design Mach number range, and this coupling between Mach number and angle of attack is a favorable result for two-dimensional inlets.

By considering a trajectory with constant dynamic pressure, it is possible to draw operating maps that show sensitivities to other variables, as well. In terms of the operating map shown in Fig. 4.1, an example is to consider only values of M and h that are along the red $q = 100$ kPa curve. The altitude is then determined for a given Mach number, and another variable can be varied on the vertical axis.

Fig. 4.2 contains an example that shows how the trim variables and performance vary with vehicle mass. Specifically, the mass of the vehicle is altered using the amount of fuel in the tanks. The total mass of the vehicle is then

$$m = m_{owe} + r_f m_{fuel} \qquad (4.16)$$

where m_{OWE} is the mass of the vehicle with no fuel, m_{fuel} is the mass of fuel with the fuel tanks completely full, and r_f represents how full the tanks are. Figure 4.2 shows that the effect of increasing the mass of the vehicle is to increase the lift coefficient (by increasing the angle of attack, α), which increases the drag and requires more fuel. There is also an effect on the elevator angle (δ_{CE}), which is caused only by changes in angle of attack because the MASTrim model assumes that the center of gravity is in the same location regardless of how much fuel is in the tanks.

This is just one example of a variable to use on the vertical axis of the operating map. Other useful examples include vehicle acceleration (which can be used for trajectory design and optimization), climb rate, or design variables. Section 4.3 contains another example that shows the trim variables as a function of turn rate.

4.3 Turning Flight

In this section we discuss turning flight. The equations of motion derived in previous sections are valid for a variety of flight conditions including turning, but the specifics of turn-

(a) Equivalence ratio (*ER*).

(b) Fuel mass flow rate ($\dot{m}_f$) in kg/s.

(c) Angle of attack (α) in degrees.

(d) Elevator angle (δ_{CE}) in degrees.
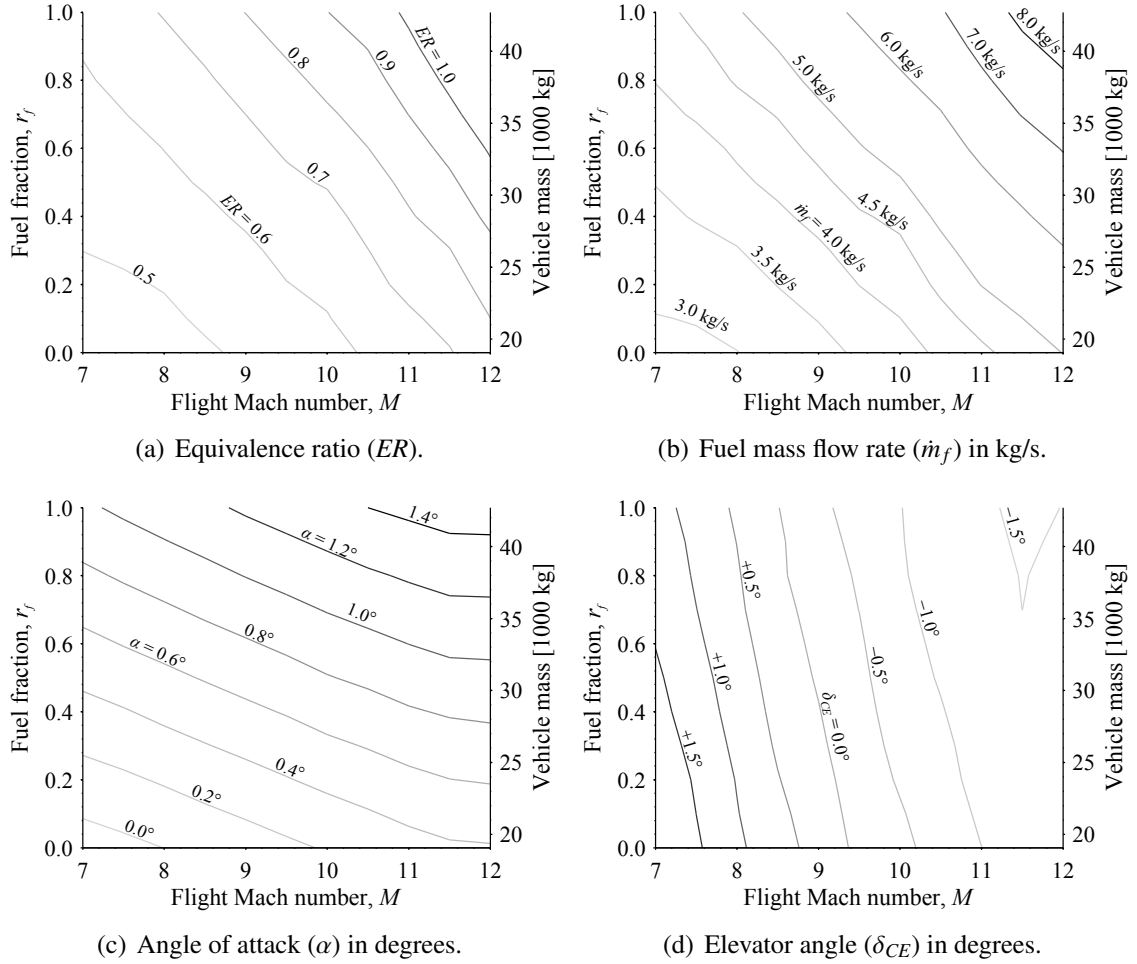
Figure 4.2: Operating map for steady, level flight for the MAX-1 vehicle assuming constant dynamic pressure ($q = 100$ kPa) and equatorial ($L = 0$), eastward ($\chi = 90°$) flight conditions. The red $q = 100$ kPa curve in Fig. 4.1 corresponds to $r_f = 0.5$ in these plots.

ing are discussed. The typical method for an air vehicle to turn is to roll the vehicle, which points the lift vector laterally, which means that the total lift must increase to maintain level flight. The drag increases as a result. For hypersonic vehicles, the turn radius is very large even for turns with a high lateral acceleration due to the high velocities. Finally, turning has a tendency to put the engine into ram mode both because of the increase in required thrust to maintain airspeed and the changed shock pattern in the inlet due to higher angles of attack.

Turning flight for hypersonic vehicles has been studied in detail in the past, particularly as it applies to reentering spacecraft [162–164]. The dependence of performance on flight condition adds considerably more complexity to the air-breathing version of hypersonic turning. In this realm, Mooij [165] developed and documented the performance of an

algorithm to control the heading angle and bank angle of a hypersonic vehicle, but the reference trajectory was not for turning flight. Schöttle and Hillesheimer [166] considered trajectories that included turning, but a very simple aerodynamics and engine models were used. Halter and Cliff [89] used singular perturbation theory to optimize trajectories that included both ascent and change of heading. The most relevant work was done by Raney and Lallman [103] who considered a control law for a hypersonic vehicle trajectory with several different phases, including a change of heading. Much of the framework by Raney and Lallman is applicable to the present work, although control laws are not considered here.

The relevant trim equations for turning flight can be written as

$$
\begin{bmatrix} \dot{V} \\ \dot{\gamma} \\ \dot{\chi} \\ \dot{P} \\ \dot{Q} \\ \dot{R} \end{bmatrix} = \mathbf{F} \left(\begin{bmatrix} V \\ \gamma \\ \chi \\ h \end{bmatrix}, \begin{bmatrix} ER \\ \alpha \\ \delta_{CE} \\ \phi \\ \delta_{DE} \\ \delta_{CR} \end{bmatrix} \right)
\tag{4.17}
$$

This situation is no different from any other application of the trim equations. Since MASTrim solves the trim equations for given linear and angular accelerations, the specific challenge is to determine what values to use for the targets on the right-hand side. Consider as an example a flight condition that is initially flying east ($\chi = 90°$) over the equator ($L = 0$) and turning to the north ($\dot{\chi} < 0$). To maintain the (initially eastward) velocity, $\dot{v}_E$ must equal zero. In general,

$$
\dot{V} = \dot{v}_N \cos\gamma \cos\chi + \dot{v}_E \cos\gamma \sin\chi - \dot{v}_D \sin\gamma
\tag{4.18}
$$

so for level ($\gamma = 0$), eastward flight, $\dot{V} = \dot{v}_E$. Next, $\dot{v}_D$ must equal zero to maintain the current altitude. The rotational accelerations must all be zero, $\dot{P} = \dot{Q} = \dot{R} = 0$. What remains is to quantify the lateral acceleration, which in Eq. 4.17 corresponds to $\dot{\chi}$.

Using the traditional flat-Earth equations of motion, a 2g-turn refers to a maneuver in which the pilot experiences a force that is twice as strong as gravity. In this case we would write $n = \|\mathbf{f}^b\|/g$ where the load factor n would be 2 for a 2g-turn. We could use the same definition for hypersonic flight, but it would give the unusual result that a 1g-maneuver would still have some component of turning, and steady-level flight would be described as a less-than-1g maneuver. Instead we define the turning coefficient so that the component of the acceleration normal to the velocity is the same as it would be for the flat-Earth equations. Thus for a vehicle that is flying directly eastward, the acceleration to the north
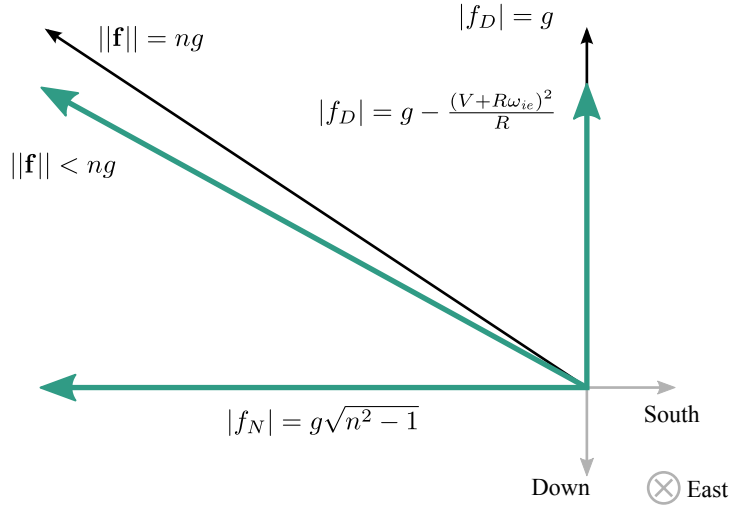
Figure 4.3: Definition of load factor for flat-Earth (black) and hypersonic (green) equations of motion assuming eastward flight.

is given by

$$\dot{v}_N = g\sqrt{n^2 - 1} \tag{4.19}$$

Figure 4.3 demonstrates the definition of load factor and shows how the lateral component is the same for both flat-Earth and general equations of motion.

In Eq. (4.17), the total acceleration is isolated into $\dot{V}$, the altitude is controlled by $\dot{\gamma}$, and the turning has been consolidated into the parameter $\dot{\chi}$. The formula for it is

$$\dot{\chi} = \pm \frac{\sqrt{n^2 - 1}}{V\cos^2\gamma} g \tag{4.20}$$

with the sign determining whether the aircraft turns to the left ($-$) or the right ($+$). The six variables to be determined by the trim routine roughly serve the following purposes: the equivalence ratio (ER) controls the acceleration; the angle of attack (α) determines the climb rate ($\dot{\gamma}$); the collective elevon angle (δ_{CE}) controls the pitch rate ($\dot{Q}$); the rudder angle (δ_{CR}) controls the yaw rate ($\dot{R}$); the differential elevon (δ_{DE}, for traditional aircraft this would be the aileron angle) controls the roll rate ($\dot{P}$); and the roll angle (ϕ) controls change of heading ($\dot{\chi}$). The variables are of course more coupled than that list would suggest. For example, more turning (that is, higher $\dot{\chi}$) requires more lift and thus a higher angle of attack, which also increases the required equivalence ratio. However, the roll rate and yaw rate are almost entirely isolated, meaning that we can usually set $\delta_{CR} = \delta_{DE} = 0$, and this will be enough to ensure that $\dot{P} = \dot{R} = 0$.

71

(a) Equivalence ratio, *ER*.

(b) Angle of attack, α (degrees).

(c) Elevator angle, δ_{CE}.

(d) Roll angle, ϕ (degrees).
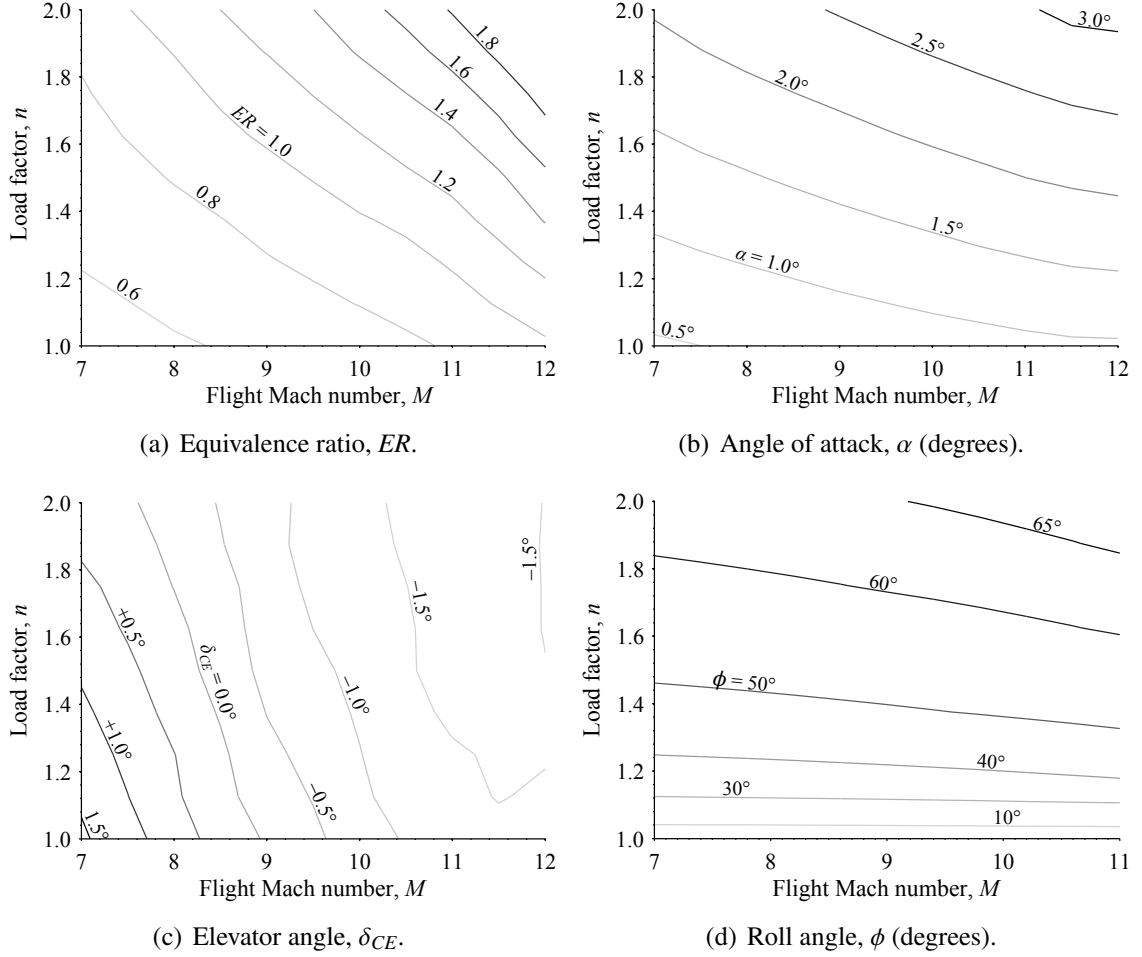
Figure 4.4: Operating map for various turning conditions. The dynamic pressure is constant at 1 atm.

Figure 4.4 shows the operating map for four trim variables for a range of Mach numbers and turning load factors. The remaining trim variables (sideslip angle and rudder angle) are zero for all trim conditions. A constant dynamic pressure of 1 atm is assumed, and the total acceleration is set to $\dot{V} = 0$. Most of the trends are intuitive. Increasing the velocity means that the lift coefficient can be reduced, and so the angle of attack decreases. The result that the angle of attack increases with Mach number is due to the well-known result that the lift coefficient decreases with Mach number, although this trend stops at the upper end of the inlet design Mach range (in this case at $M = 9$). At the same time, more turning (higher n) requires more lift (hence higher α) and thus more fuel (higher *ER*).

The elevon angle (δ_{CE}) does not vary much with n, despite the higher angles of attack. As the angle of attack increases and the equivalence ratio increases to maintain airspeed, the higher pressure on the nozzle counteracts the expected nose-up moment from an increased

(a) Longitudinal dynamics.

(b) Lateral dynamics.
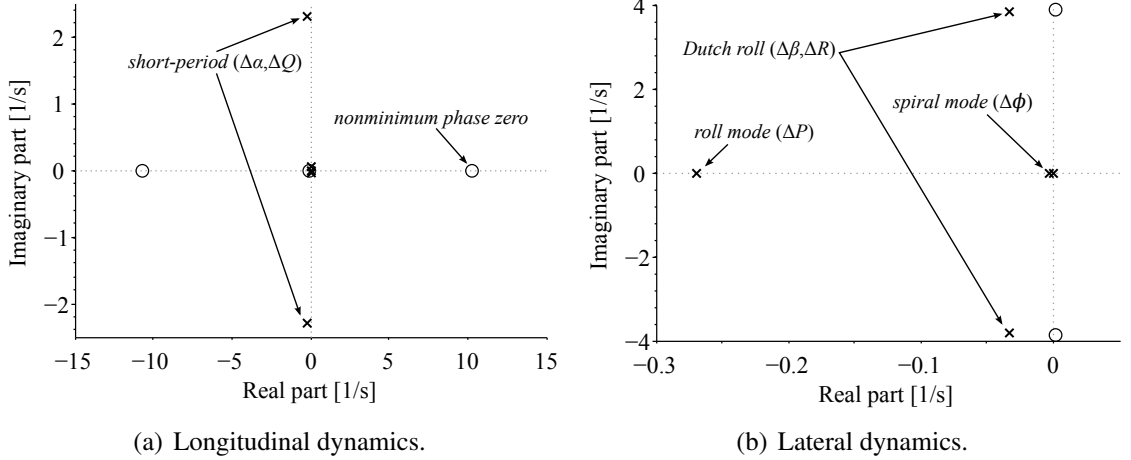
Figure 4.5: Pole/transmission zero maps of the Jacobian linearization about a steady, level Mach 8 flight condition with $n = 1$, $M = 8$, and $h = 26$ km. Dominant poles are labeled with their names and participating variables.

angle of attack. Finally, the roll angle (ϕ) is higher for higher values of n, but it is not constant for a given value of n. This is because the vertical component of the lift decreases with higher speed due to the higher centrifugal acceleration.

A linear perturbation analysis was calculated at two flight conditions. The two flight conditions correspond to correspond to $n = 1$ and $n = 2$ at $M = 8$ from Fig. 4.4. The altitude ($h = 25.8$ km) comes from the Mach number and dynamic pressure of $q = 1$ atm. The first case, for which the pole/transmission zero maps are shown in Fig. 4.5, is for nonturning flight while Fig. 4.6 shows the maps for turning flight. To determine which states are associated with each pole, the process in Appendix C was used. The two flight conditions, about which the linear systems are obtained, are tabulated in Table 4.3.

For the linearization analysis,

$$\mathbf{x} = [\, h \quad V \quad \alpha \quad \beta \quad \phi \quad \theta \quad \psi \quad P \quad Q \quad R \,]^T \tag{4.21}$$

is the full set of state variables, and the full set of inputs is

$$\mathbf{u} = [\, ER \quad \delta_{CE} \quad \delta_{DE} \quad \delta_{CR} \,]^T \tag{4.22}$$

Finally, the outputs were selected to be

$$\mathbf{y} = [\, V \quad \gamma \quad \chi \quad \phi \,]^T \tag{4.23}$$

73

(a) Longitudinal dynamics. (b) Lateral dynamics. A zero at -723 is not plotted.
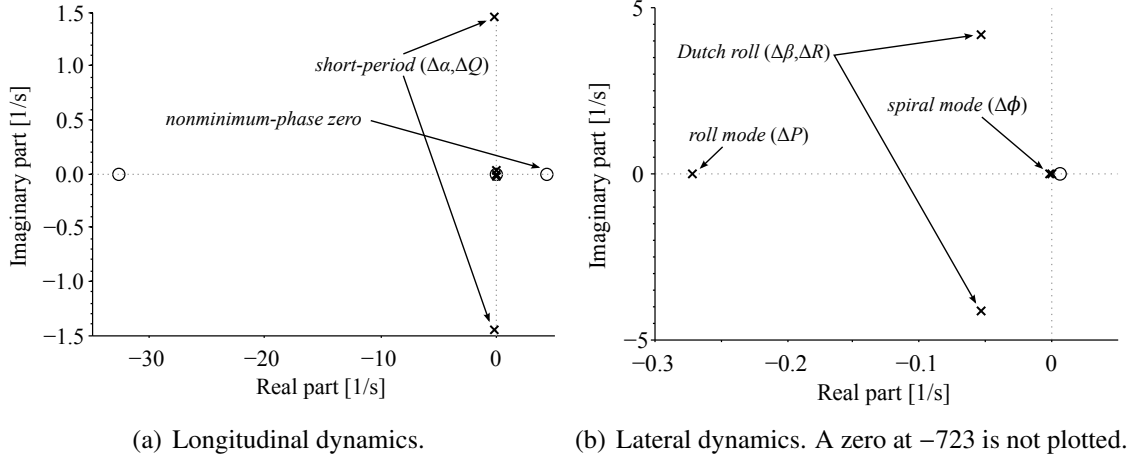
Figure 4.6: Pole/transmission zero maps of the Jacobian linearization about the turning Mach 8 flight condition with $n = 2$, $M = 8$, and $h = 26$ km. Dominant poles are labeled with their names and participating variables.

The states were split into longitudinal states of h, V, α, θ, and q and lateral states of β, ϕ, ψ, p, and r. The longitudinal inputs are ER and δ_{CE}, and the lateral inputs are δ_{DE} and δ_{CR}. The outputs are split into longitudinal outputs, V and γ, and lateral outputs, χ and ϕ.

The longitudinal dynamics, shown in Figs. 4.5(a) and 4.6(a), are quite similar between the two cases while the lateral dynamics, shown in Figs. 4.5(b) and 4.6(b), show more notable differences. According to the modal participation analysis discussed in Appendix C, the dynamics can be split into longitudinal and lateral/directional dynamics for the turning case, which would not necessarily be expected. Specifically, all participation values of longitudinal states in lateral/directional modes or vice versa are below 0.02. One change, however, is that the roll and Dutch roll modes are somewhat coupled for the $n = 2$ case (crossover participation values of about 0.09).

In both cases, the poles are similar (with stable Dutch roll, roll, and spiral modes), but the zeros have moved. For the $n = 1$ case, both zeros are on the imaginary axis, while both are on the real axis for $n = 2$. Actually, a zero at -723 is not shown in Fig. 4.6(b) because it would give the plot too large of a range of scales. The main reason for the difference in linearization zeros is that the roll state, ϕ, is not zero in the turning case. The result is increased control authority of the heading output, χ. Since roll is the most effective way to control heading, the response of the system to small changes in roll is important in determining how easily the velocity heading (χ) can be controlled. However, when ϕ is zero, small changes in ϕ result in only small changes in the lateral force.

For both configurations, one of the zeros of the pitch dynamics is non-minimum phase,

Table 4.3: Trimmed flight conditions for two detailed linear analysis examples.

State or input	**Fig.** 4.5, $n = 1$	**Fig.** 4.6, $n = 2$
h	26 km	26 km
V	2394 m/s	2394 m/s
α	0.583°	2.37°
β	0°	0°
ϕ	0°	63.55°
ψ	90°	92.12°
θ	0.583°	1.05°
ER	0.586	1.12
δ_{CE}	0.728°	−0.244°
δ_{DE}	0°	0°
δ_{CR}	0°	0°

which is consistent with the results in [104]. This is expected because of the actions the vehicle needs to take to increase γ. In order to increase the climb rate, the vehicle needs to deflect the elevators upward to increase the angle of attack, but deflection of the elevators decreases the lift instantaneously, which causes the aircraft to plunge and drop altitude before it begins to pitch nose-up and increase α and thus lift. These non-minimum phase dynamics affect the control design, and are important in this case because the vehicle is open-loop unstable, and the transmission zeros effectively limit the amount of bandwidth in the system.

A final point to discuss is the radius of curvature. By considering centrifugal acceleration during a turn, the turn radius can be found to be

$$R = \frac{V^2}{g\sqrt{n^2 - 1}} \tag{4.24}$$

Figure 4.7 shows the turn radius over the full range of hypersonic conditions. At Mach 10, even a 2-g turn results in a turn radius of over 500 km. Flight at such conditions would give a strange feeling, because the vehicle would have a roll angle of greater than 60°, and the apparent acceleration really would be almost twice the strength of gravity, but the horizon would barely be moving.

It was learned from this work that turns of up to 2g do not have an unacceptably adverse impact on the engine performance even at high Mach numbers. As a general rule of thumb, a 2-g turn will approximately double the fuel consumption compared to steady, level flight. For most hypersonic flight conditions, the maximum turn rate will be limited by structural
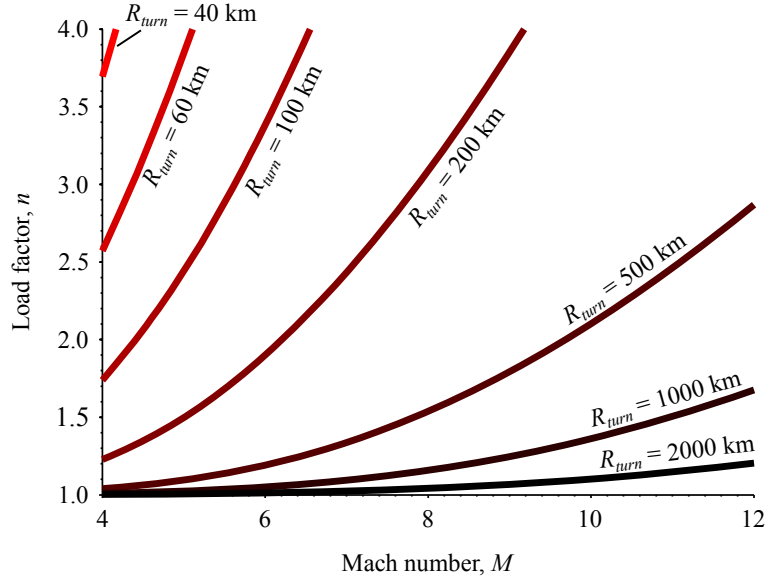
Figure 4.7: Turn radius for various hypersonic conditions.

concerns, much like for lower-speed aircraft. Exceptions will occur when the when the vehicle is near a maximum-acceleration boundary. It is possible that increasing the turn rate could unstart the engine, cause thermal choking, or simply consume all of the oxygen available to the engine.

Compared to other high-speed vehicles, the ability to sustain a turn is an advantage for air-breathing hypersonic vehicles. However, at very high Mach numbers, even a large load factor represents a very small turn rate, and so the trajectory should be aligned with the proper direction before accelerating above Mach 6.

4.4 Summary

This chapter has discussed how the MASTrim model can be used to understand individual flight conditions. Together with Appendix B, it shows how a vector of state variables (which describe the position, velocity, orientation, and angular velocity of the vehicle) combined with a set of input variables (which can be determined by a pilot or control system), can be used to determine the acceleration of the vehicle. This incorporates all of the results from the previous sections to determine the forces and moments, and a framework is described for balancing the forces and moments to achieve desired performance such as acceleration or rate of turn.

A tradeoff between angle of attack and Mach number on trajectories with constant dynamic pressure was identified to be a favorable rather than unfortunate result. Because large

76

design Mach number windows have been shown to decrease performance (See Sec. 2.2.3 and also [150, 167]), it is favorable to have an inlet with a relatively narrow design range. The coupling between angle of attack and Mach number allows this to be possible.

The operating maps of Sec. 4.2 provide a useful tool for understanding flight in any regime. Many of the trends are smooth and monotonic, but the complex interactions of hypersonic flight often lead to changes in performance that are only visible in such operating maps. Figure 4.1 shows an example that describes a wide variety of speeds and altitudes that the MASTrim model can solve. However, Fig. 4.2 shows a more practical performance chart that focuses on a realistic set of flight conditions (such as a dynamic pressure of 100 kPa) and uses the other axis to show the sensitivity to some other design variable. This is a useful technique that can be used to investigate the effect of both trajectory and design variables. The utility of these operating maps can be seen in Chapter 6, where we discuss the analysis and design of trajectories and couple this to the vehicle design problem for an accelerating vehicle.

CHAPTER 5

Unstart and Ram-Scram Transition

A dual-mode ramjet-scramjet engine has the advantage that it can produce positive thrust for a wide range of flight Mach numbers. The challenge is that the pilot or flight control system does not directly control which mode the engine is in. Instead, the mode is primarily determined by the vehicle speed, altitude, and throttle setting. Because the forces and moments on the vehicle can change abruptly when the engine switches from one mode to the other, understanding and predicting this ram-scram transition boundary is critical for the flight dynamics of air-breathing hypersonic vehicles.

Operation of the engine in ram mode has another potential pitfall: unstart. In ram-mode operation, a pre-combustion shock train slows the airflow to subsonic conditions in the isolator region of the engine, which is upstream of the fuel injector. If this shock train becomes too long, it can move upstream of the inlet cowl and block some of the airflow into the engine. Unstart conditions are associated with performance that is both undesirable and more difficult to predict. Accurate predictions for both unstart and ram-scram have not been reported in the open literature previously because they require a first-principles model of the thermal choking process.

5.1   Introduction

Figure 5.1 is presented to explain how several tradeoffs were explored in the present work. It was decided to only consider trajectories along which two parameters are held constant: the vehicle acceleration (a) and the dynamic pressure ($q_\infty = \frac{1}{2}\rho_\infty U_\infty^2$). The bottom curve in Fig. 5.1 represents a dynamic pressure of $q_\infty = 100\,\text{kPa}$. For a vehicle acceleration of 0 m/s^2 (steady, level flight), ram-scram transition is predicted to occur at the labeled curve on the right of Fig. 5.1. At each point the vehicle has been trimmed, so that all forces and moments are balanced to provide the desired acceleration. The amount of engine fueling cannot be selected *a priori*; the fueling must be set to the proper value that provides the
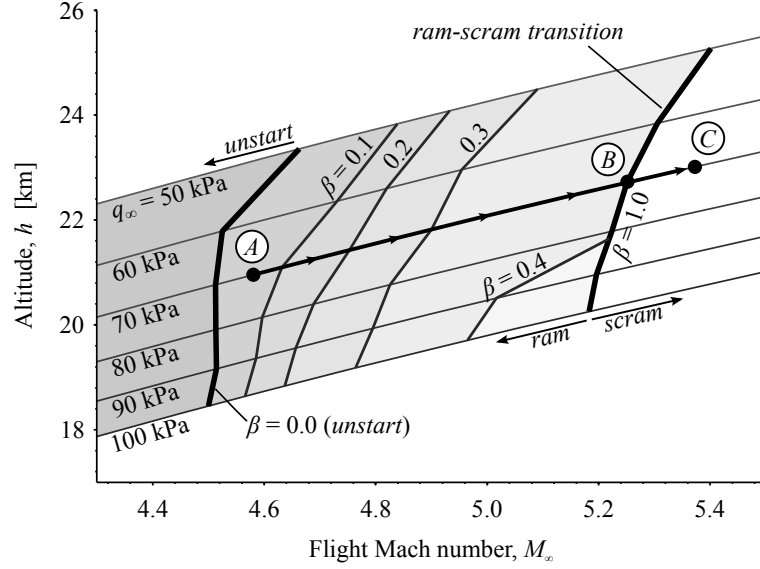
Figure 5.1: Contours of unstart margin and ram-scram transition for trimmed steady level flight for dynamic pressures between 50 kPa and 100 kPa. Unstart occurs when the unstart margin (β) equals zero. For example a ramjet could be ignited at point A and transition to scram mode at point B.

correct thrust to trim the vehicle. If this amount of fueling is excessive, unstart will occur. This corresponds to the black curve on the left in Fig. 5.1 labeled $\beta = 0.0$. Unstart margin is defined to be

$$\beta = \frac{L_{ISO} - L_{ST}}{L_{ISO}} \tag{5.1}$$

where L_{ISO} is the length of the isolator section (which is fixed for a given vehicle), and L_{ST} is the length of the shock train. The downstream end of the shock train has been found to remain anchored very close to the downstream end of the isolator, so the distance $(L_{ISO} - L_{ST})$ in the numerator of Eq. (5.1) is the distance between the entrance to the isolator and the upstream edge of the shock train. When $\beta = 0$, the leading edge of the shock train moves upstream into the inlet, and unstart occurs.

Figure 5.1 shows that if our ramjet engine is ignited at condition A ($h = 20.7$ km, $M_\infty = 4.55$), unstart will occur if conditions move to the left of the solid line marked $\beta = 0.0$, for example if M_∞ is decreased to be less than 4.5 or the altitude is increased to more than 22 km. However, if instead the Mach number is increased such that conditions move to the right along the $q_\infty = 70$ kPa contour toward point C, the unstart margin (β) increases, which is desirable. At point B, a ram-scram transition is predicted to occur. Between points B and C, the engine is in the scram mode, and the unstart margin is 1.0 (no shock train).

Previously there has been no first-principles model available to compute unstart and

ram-scram transition curves such as those in Fig. 5.1. Work by the Billig group [168] and by Rodriguez et al. [169] discuss unstart but rely on unproven empirical relations and do not trim the vehicle. Therefore one goal of this work is to use a newly developed Michigan/AFRL model to compute a series of curves, such as those in Fig. 5.1, that represent the boundaries at which unstart or ram-scram transition occurs. The geometry of the vehicle has been selected to be the MAX-1 vehicle that is shown in Fig. 3.2.

The present chapter computes where unstart and ram-scram transition occur along an ascent trajectory. This type of information has not been published before. Chichka et al. [90] and Rodriguez et al. [169] plotted thermal choking boundaries on the flight corridor map using simplified combustor models, but there was no ram-mode model and thus no ram-scram transition. Another step that was taken was to assess the method by comparing predictions to available ram-scram transition measurements [113, 114] in Sec. 5.3.2. Results show the effects of varying the following governing parameters: dynamic pressure, the vehicle acceleration, and the inlet compression ratio. Engine unstart and the length of the isolator shock train are discussed in Sec. 5.3.1. This work represents an extension of previous reduced-order models of hypersonic vehicles that were developed by Bolender and Doman [9], Starkey and Lewis [170], and others [8, 48, 66, 171–173]. In all previous studies the unstart limits and ram-scram transition boundaries were not considered.

Reduced-order models, such as those described in [8, 9, 48, 61, 66, 68, 69, 76, 161, 167, 170–173], are essential for this type of research. Suppose that it is desired to compute the vehicle properties along the six trajectories plotted in Fig. 5.1. Vehicle thrust and aerodynamic forces must be computed approximately 1800 times, which is unacceptable if a high-fidelity CFD code is employed. That is, for each of the six trajectories, the vehicle must be trimmed at approximately twenty different altitudes. At each altitude the thrust and aerodynamic forces have to be computed about fifteen times to determine by iteration what angle of attack, equivalence ratio, and elevator setting trims the vehicle. The MASIV/MASTrim reduced-order model computes the thrust and all aerodynamic forces in approximately three seconds on a single 2.6-GHz processor for the scram mode. This time increases to 30 seconds for the ram mode because additional iterations are required to determine the thermal choking location. Thus the computational time to generate Fig. 5.1 was approximately eight hours.

Because the code is written in MATLAB, the time could be greatly reduced if a C++ version were implemented. If higher accuracy is required, the reduced-order model can be used along with high-fidelity CFD; MASIV is useful in that it indicates the small subset of conditions for which CFD runs should be attempted. The CFD would have to find a viscous solution to capture the boundary layer effects, which adds yet more computational expense
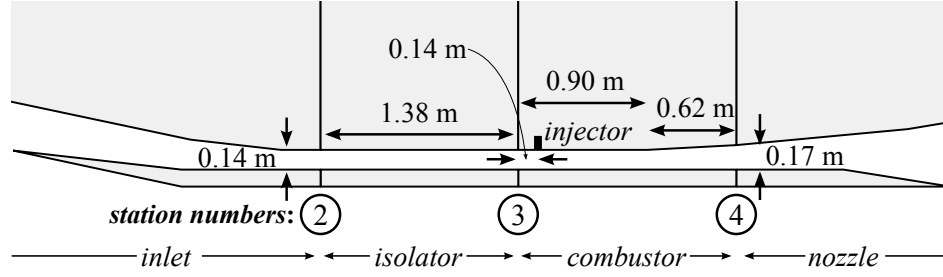
Figure 5.2: Internal flowpath of MAX-1 with dimensions and station numbers. Engine width is 2.143 m. Same as Fig. 3.2(b).

and complexity. The simplifying assumptions associated with the reduced-order model are summarized in Sec. 5.3.

5.2 Ram-Scram Transition and Unstart

Engine unstart occurs only in the ram mode, and in the ram mode thermal choking must occur at some location since there is no physical throat. When the amount of fueling is increased, the (subsonic) Mach number M_3 at the combustor entrance must decrease (note: location 3 is marked in Fig. 3.2). This causes the pressure p_3 to increase, and p_3 represents the back pressure on the isolator. The only way that the static pressure can increase from the given value of p_2 at the isolator entrance to the back pressure p_3 is for a shock train to exist in the isolator. For sufficiently large fueling rates, the imposed pressure ratio p_3/p_2 increases. To meet these boundary conditions, the number of shocks as well as the length of the shock train also must increase. The rear edge of the shock train is experimentally found to be anchored at the downstream end of the isolator (where fuel is injected). Thus the leading edge of the shock train moves upstream until it enters the inlet and unstart begins. The inlet shocks are perturbed, the boundary layer separates, and spillage occurs, which leads to a rapid loss of thrust.

To compute the unstart limit, one must start with the known downstream boundary condition at the thermal choking location ($M = 1$) and work backward. The first step is to compute M_3, the Mach number at the point where fuel is injected (see Fig. 5.2). First consider the simplified case of a constant-area combustor that is thermally choked at its downstream end ($M_4 = 1$). The value of M_3 at the combustor entrance is easily computed using a simple Rayleigh line method, since the heat addition ($\Delta T_0 = T_{04} - T_{03}$) and M_4 are known. However, this approach is not realistic since area change must be considered, and the location of thermal choking is not known. Shapiro describes a more general method to

predict M_3 for the simplified case of heat added to pure air flowing in a variable-area duct with no friction. Shapiro's equation [21, 174] is

$$\frac{1}{M^2}\frac{\mathrm{d}M^2}{\mathrm{d}x} = -\frac{2\left(1+\frac{\gamma-1}{2}M^2\right)}{1-M^2}\frac{1}{A}\frac{\mathrm{d}A}{\mathrm{d}x} + \frac{\left(1+\gamma M^2\right)\left(1+\frac{\gamma-1}{2}M^2\right)}{1-M^2}\frac{1}{T_0}\frac{\mathrm{d}T_0}{\mathrm{d}x} \tag{5.2}$$

A singularity occurs in Eq. (5.2) at the location where M approaches one due to the $(1 - M^2)$ terms in the denominators. Shapiro explains that the x-location of thermal choking is determined by the following equation, which is derived by applying L'Hospital's rule to Eq. (5.2).

$$\frac{1}{A}\frac{\mathrm{d}A}{\mathrm{d}x} = \frac{\gamma+1}{2}\frac{1}{T_0}\frac{\mathrm{d}T_0}{\mathrm{d}x} \tag{5.3}$$

After the x-location of choking is determined (from the given values of $\frac{\mathrm{d}A}{\mathrm{d}x}$ and $\frac{\mathrm{d}T_0}{\mathrm{d}x}$), then Eq. (5.2) should be solved in the negative x-direction to obtain the Mach number $M(x)$ throughout the combustor. This method predicts the (subsonic) value of M_3 for any given amount of heat addition for any area profile $A(x)$.

Torrez [69] determined that Shapiro's approach could be extended to combustion in a generic duct. This work required further extension [175] to properly account for the role of the separated boundary layer in the combustor. Shapiro's equations, (5.2) and (5.3), were not used in the present work because they are limited to non-reacting, single-component gas (air) with constant heat capacity. Instead the differential equations that are listed in Secs. 2.4 and 5.3 were solved to consider reacting gas mixtures with real gas properties and finite-rate chemistry. Eqs. (2.25)–(2.31) were derived and developed by Torrez, and the modifications present in Eqs. (5.10) and (5.11) represent original contributions of the present work. The next section also describes the shooting method used to simultaneously compute the x-location of thermal choking and the proper value of M_3.

After the value of M_3 has been computed, the next step is to compute the pressure p_3 at the combustor entrance. Heiser and Pratt [151] have derived the following relation using the equations for conservation of mass and momentum across the isolator.

$$\frac{p_3}{p_2} = 1 + \gamma M_2^2 - \gamma M_2 M_3 \sqrt{\frac{1+\frac{\gamma-1}{2}M_2^2}{1+\frac{\gamma-1}{2}M_3^2}} \tag{5.4}$$

The isolator contains complex shock patterns and boundary layer separation, but these processes do not have to be modeled because Eq. (5.4) relates the upstream conditions (p_2, M_2) to the downstream conditions (p_3, M_3).

Next, the length of the shock train, L_{ST}, is computed using

$$\frac{L_{ST}}{H} = \frac{1}{0.228} \ln \left(\frac{M_2^2 \, 1 + \frac{\gamma-1}{2} M_3^2}{M_3^2 \, 1 + \frac{\gamma-1}{2} M_2^2} \right) \tag{5.5}$$

Eq. (5.5) is an empirical relation that has been experimentally verified numerous times [113, 114, 152]. The final step is to compute the unstart margin β by inserting the value of L_{ST} into Eq. (5.1).

The ram-scram limit was computed using a separate method that does not require a ram-mode solution. Ram-scram transition is defined as follows [69]. If a fully supersonic solution to the governing equations exists, then the engine will operate in the scram mode. If no supersonic solution exists, the engine must operate in the ram mode, and the appropriate shock structure forms in the isolator to decelerate the air to subsonic velocities. Therefore to compute the ram-scram transition point, it is only necessary to start with the nearly zero fueling case and then compute a fully supersonic (scram) solution. Then the fueling is increased until the local Mach number decreases to unity at some location. This defines the ram-scram boundary; no ram solution is necessary to calculate it.

To illustrate this idea, consider the simplified case of pure air flowing in a duct with no friction. We define $(\Delta T_0)_{RS}$ to be the amount of heat addition (divided by c_p) that causes the supersonic flow to thermally choke at some location. Figure 5.3 shows the values of $(\Delta T_0)_{RS}$ for the case of a constant-area duct. The standard Rayleigh line equations were used to show that increasing the combustor entrance Mach number M_3 causes an increase in the required value of $(\Delta T_0/T_{03})_{RS}$ that causes choking. If the area of the duct is not constant, the standard 1D relations between M, $\frac{dA}{dx}$, and $\frac{dT_0}{dx}$ must be solved instead of the Rayleigh line equations [68]. For example, if the pressure varies linearly between stations 3 and 4, and $\frac{dA}{dx}$ is constant,

$$\left(\frac{\Delta T_0}{T_{03}} \right)_{RS} = \frac{\frac{\gamma+1}{2}}{\left(1 + \frac{\gamma-1}{2} M_3^2 \right) M_3^2} \left(\frac{1 + \frac{A_4}{A_3} + 2\gamma M_3^2}{1 + \frac{A_3}{A_4} + 2\gamma} \right)^2 - 1 \tag{5.6}$$

Now consider the entire engine flowpath. The goal is to replace the vertical axis of Fig. 5.3 with the engine equivalence ratio ER and to replace the horizontal axis of Fig. 5.3 with the flight Mach number M_∞. The result is Fig. 5.4, which is another way to represent the lines in Fig. 5.3. To generate Fig. 5.4, the transition equivalence ratio is

$$ER_{RS} = \frac{c_p (\Delta T_0)_{RS}}{r_{st} Q_R} \tag{5.7}$$
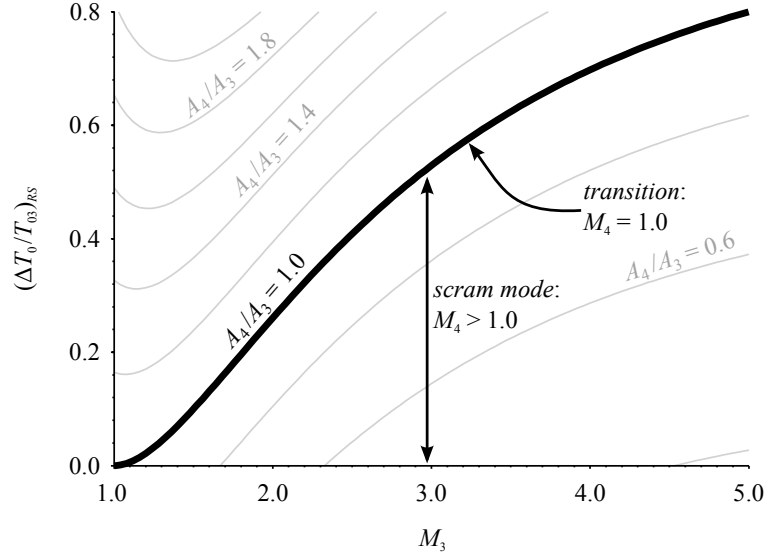
Figure 5.3: Simplified (Rayleigh line) analysis showing the ram-scram transition curve for a constant-area combustor ($A_4/A_3 = 1$) and several other area ratios (gray lines). The thick black curve represents the heat addition that drives the Mach number M_4 to unity. The Mach number at the inlet to the combustor is M_3.

where Q_R is the heating value of the fuel and r_{st} is the stoichiometric fuel-air ratio. Heat losses are neglected so $T_{03} = T_{0\infty}$. Also, since only the scram mode is considered, the shock train in the isolator is weak so that $M_3 = M_2$. The stagnation temperature $T_{0\infty}$ is determined from the flight Mach number (M_∞) and the known dynamic pressure (q_∞), which then determines the altitude and thus the ambient static temperature T_∞. To convert M_3 in Fig. 5.3 to flight Mach number M_∞ in Fig. 5.4, it is assumed that the inlet consists of two oblique shocks, which gives M_2 as a function of M_∞. In Sec. 5.3 these many assumptions are replaced with a more realistic analysis.

Figure 5.4 shows that a ram-scram transition occurs along line A→B. In this case the flight Mach number is increased, and *ER* is held constant. Increasing the flight Mach number increases the combustor inlet stagnation temperature T_{03} while *ER* and thus ΔT_0 remain constant. Thus $\Delta T_0/T_{03}$ decreases, and M_3 increases. This movement downward and to the right in Fig. 5.3 means that another way to cross the transition curve is to start at point A and decrease *ER*, which also reduces $\Delta T_0/T_{03}$ but holds M_3 constant. A more likely result is that a trimmed vehicle will follow a path such as C→D such that both the flight Mach number and the equivalence ratio are increasing. To summarize, the transition curve (i.e., the thick line in Fig. 5.4) is determined by three non-dimensional governing
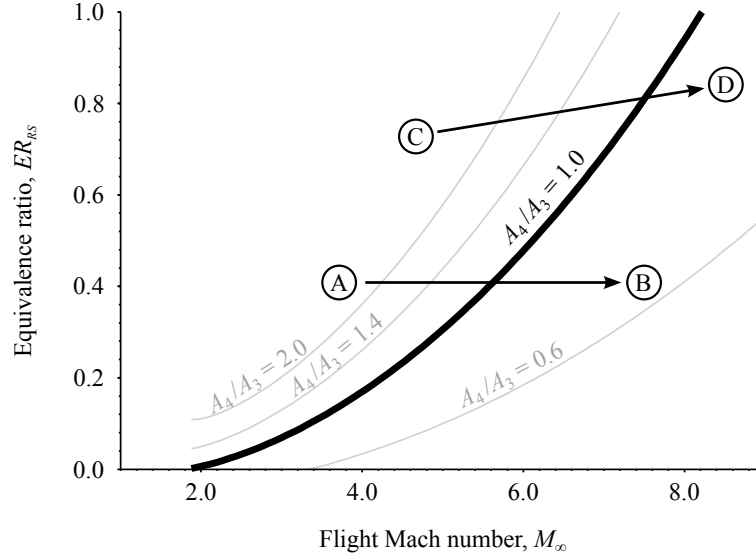
Figure 5.4: Simplified analysis showing the equivalence ratio required for ram-scram transition. This line is equivalent to the line from Fig. 5.3, but the vertical axis was converted to equivalence ratio, and the horizontal axis was converted to flight Mach number. Lines A→B and C→D represent possible vehicle trajectories.

parameters:

$$ER_{RS} = f\left(M_3, \frac{c_p T_{0\infty}}{r_{st} Q_R}, \frac{A_4}{A_3}\right) \tag{5.8}$$

The final step is to convert Fig. 5.4 to the axes used in Fig. 5.1 (the Flight Corridor Map). For one selected value of dynamic pressure (q_∞), the MASTrim trim code will compute the line C→D in Fig. 5.4. This is the equivalence ratio required to trim the vehicle as a function of flight Mach number. Where the line C→D crosses the black transition line, transition occurs, and the point at which this occurs is the transition Mach number. This transition Mach number is one point plotted in Fig. 5.1. The procedure is repeated for different values of q_∞, and the transition Mach numbers form the dashed line in Fig. 5.1.

While the above simplified analysis is instructive, it has several assumptions that must be relaxed. The location of thermal choking is not known. The heat capacity of the gas is not constant. Different gas species are present due to combustion. The heat release distribution along the length of the combustor is not known, and it depends on mixing, finite-rate chemistry, and gas dissociation and recombination. To improve the analysis, the MASIV model from Chapters 2 and 3 is used. Aspects relevant to ram-scram transition and unstart are described in Sec. 5.3.

85

5.3 Ram Mode and the MASIV Combustor Model

For calculation of unstart margin and ram-to-scram transition, several details that were not discussed in Sec. 2.4 become important. In particular, the treatment of the separated boundary layer created in the isolator must be addressed. Section 5.3.2 also contains a comparison between the ram-scram transitions using MASIV calculations and a lab-scale experiment.

5.3.1 The MASIV Engine Unstart Method

MASIV relies on the same concepts as discussed in Sec. 5.2 but solves Eqs. (2.25)–(2.31) in order to compute $M(x)$. A shooting method is required to first guess the x-location of choking and guess a value of M_3 (at the combustor entrance; see Fig. 3.2). Several iterations are required before the correct value of M_3 and the choking location are determined. The resulting predicted wall static pressure profiles $p(x)$ were found to agree (to within 15%) with the measurements of Fotia and Driscoll [69, 113, 114]. This level of uncertainty was considered to be acceptable for a reduced-order model.

Once the value of M_3 is determined, Eq. 5.4 is used to compute p_3. This equation is derived in Heiser and Pratt [151] for a constant-area isolator with negligible friction. Conservation of mass and momentum are applied, and it is assumed that the shock train separates the flow into two separate streams: the central core flow and the low-speed separated boundary layer. Eq. 5.4 has been verified by experimental results [176]. Given a pressure value from Eq. 5.4, the core area of the flow at the combustor inlet is

$$r_{A3} = \frac{A_{3c}}{A_2} = \frac{1}{\gamma M_3^2}\left((1 + \gamma M_2^2)\frac{p_2}{p_3} - 1\right)$$
(5.9)

The remainder of the geometric area at the combustor inlet, $A_3 - A_{3c}$, is a separated boundary layer with pressure but no momentum. The values of p_2 and M_2 (at the isolator entrance; see Fig. 3.2) are determined by the inlet model; they depend on the altitude, flight Mach number, angle of attack, and the geometry of the inlet.

When there is a separated boundary layer at the combustor inlet, the conservation equations (2.25)–(2.31) must be modified. A new variable $r_A = A_c/A$ is introduced to express the fraction of the area that is outside the separated boundary layer. The conservation of

mass and momentum from Eqs. (2.25) and (2.26) become

$$\frac{1}{\rho}\frac{d\rho}{dx} = \frac{1}{\dot{m}}\frac{d\dot{m}}{dx} - \frac{1}{u}\frac{du}{dx} - \frac{1}{A}\frac{dA}{dx} - \frac{1}{r_A}\frac{dr_A}{dx} \tag{5.10}$$

$$\frac{1}{u}\frac{du}{dx} = -\frac{1}{\rho u^2 r_A}\frac{dp}{dx} - \frac{2c_f}{D} + \left(1 - \frac{u_F}{u}\cos\theta_F\right)\frac{1}{\dot{m}}\frac{d\dot{m}}{dx} \tag{5.11}$$

The new term in Eq. (5.10) comes from the fact that the mass flow is constrained to the core area, and thus $\dot{m} = \rho u A_c = \rho u r_A A$. The change in the momentum equation comes from the fact that the pressure flux acts over the entire area A even when there is a separated boundary layer. The initial value of r_A is determined from Eq. (5.9), and a method is needed to determine how r_A evolves within the combustor. Based on experimental wall pressure profiles [114], the decision was made to choose $\frac{dr_A}{dx}$ so that the combustion occurs at constant pressure whenever the boundary layer is separated ($r_A < 1$). The flow reattaches when $r_A = 1$, and in this case $\frac{dr_A}{dx}$ is set to be 0 so that Eqs. (2.25), (2.26) are identical to Eqs. (5.10), (5.11).

An interesting aspect of the MASIV model is that it predicts the flame length, which normally is longer than the distance required to thermally choke the flow. Thus heat normally is added downstream of the choking point. A good combustor design must have a value of $\frac{dA}{dx}$ that is sufficiently large to prevent the Mach number from returning back to unity downstream of the choking location. The required value of $\frac{dA}{dx}$ can be estimated using Eq. (5.3).

5.3.2   Ram-Scram Predictions for a Lab-Scale Geometry

Before the MAX-1 vehicle in Fig. 3.2 was considered, the MASIV model was assessed using the small lab-scale geometry shown in Fig. 5.5(b). Assessment requires measurements of the conditions at which ram-scram transition occurs, and there are few such measurements available. This serves as an important validation of the model and code, and it is fortunate that some experimental data on transition is available.

Fotia and Driscoll [113] have made such measurements for the geometry in Fig. 5.5(b), which has an isolator with a height of 25.4 mm, a width of 38.1 mm, and a length of 358 mm. The combustor consists of a 115 mm long constant-area section (that is also 25.4 mm high and 28.1 mm wide) followed by a diverging section. The diverging section is 38.1 mm wide and 329 mm long, and its lower wall diverges at 4 degrees from the tunnel centerline. Fuel is injected from a single 0.249 mm diameter wall port located at the entrance to the combustor. The Mach number M_2 at the isolator entrance is 2.1, and the stagnation temperature prior to combustion was varied from 900 K to 1400 K. Stagnation
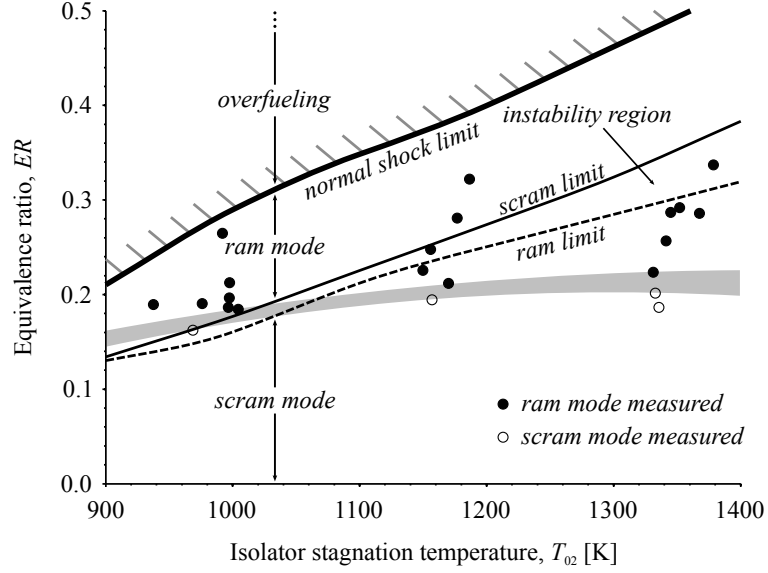
(a) Measured and calculated ram-scram transition.
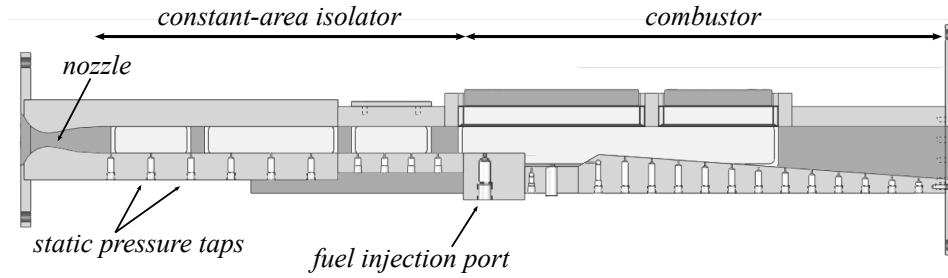
(b) Lab-scale geometry.

Figure 5.5: Assessment of the predicted ram-scram transition. Gray region is measured limit of [113, 114]. The instability region is discussed in Sec. 5.4.4.

pressure (p_{02}) was maintained at 549.2 kPa.

The gray area in Fig. 5.5(a) represents the measured ram-scram boundary reported in [113]. It represents the range between the highest equivalence ratio (*ER*) for which a scram condition was observed and the lowest equivalence ratio for which a ram condition was observed. Note that the simple analysis in Sec. 5.2 predicts that the transition curve should be a straight line in Fig. 5.5(a). That is, the heat required to cause transition, $(\Delta T_0)_{RS}$, should be directly proportional to T_{02} when M_3 and A_4/A_3 are held fixed, as they are in the experiment.

Two boundary lines are marked for the computational results. The solid line (labeled "scram limit") shows the highest equivalence ratio for which a scram-mode solution can be found, and this is the definition of ram-scram transition used throughout the rest of the

dissertation. The dotted line ("ram limit") shows the lowest equivalence ratio for which a ram-mode solution can be found. Between these two lines is a region of potential instabilities, and it is discussed in Sec. 5.4.4. Experimental evidence [113] shows that ram-mode solutions with the isolator exit Mach number (M_3) just less than one are not usually observed. Furthermore, other authors have speculated that the combustor and isolator naturally adjust so that entropy rise is minimized [151, 168]. Both of these results suggest that the scram mode is preferred. Throughout this work, the scram limit is used to determine ram-scram transition.

The thick line above the ram-scram transition boundaries in Fig. 5.5(a) marks the normal shock limit. Above this equivalence ratio, no solution can exist because the required pressure rise in the isolator would exceed the physical limit. This limit is predicted by previous models as well [62, 168]. Going to an equivalence ratio above the normal shock limit would most likely cause a type of unstart as stated in [151].

5.4 Vehicle results

This section discusses the unstart margin and ram-scram transition for the MAX-1 vehicle shown in Fig. 3.2. The fuel is hydrogen, and the combustor divergence angle is 3.11°. In all cases the vehicle is trimmed as it follows a trajectory along which two quantities are held constant: the dynamic pressure (q_∞) and the vehicle acceleration (a). Section 5.4.1 shows how the length of the shock train is affected by Mach number (M_∞) and acceleration (a), and this leads to a prediction of where unstart occurs. Section 5.4.2 discusses ram-scram transition and how it is affected by the following parameters: the dynamic pressure (q_∞), the vehicle acceleration (a), the inlet design Mach number (M_{design}), the inlet compression ratio (r_p), and the combustor divergence angle (θ_c). Finally, Section 5.4.3 shows how the engine flow and vehicle performance change on either side of ram-scram transition.

5.4.1 Unstart margin for the MAX-1 vehicle

Figure 5.6 shows the effect of Mach number and acceleration (a) on the unstart margin assuming a constant dynamic pressure of $q_\infty = 100$ kPa. Seven constant-acceleration trajectories are shown. Several prevalent trends are visible, and this type of information has not been reported before.

Consider the trajectory with $a = 1$ m/s². The minimum Mach number at which the ramjet can be ignited with an unstart margin $\beta \geq 0.05$ is labeled point A ($M_\infty = 5.05$) in Fig. 5.6. If the $a = 1$ m/s² trajectory is followed, ram-scram transition occurs at point B
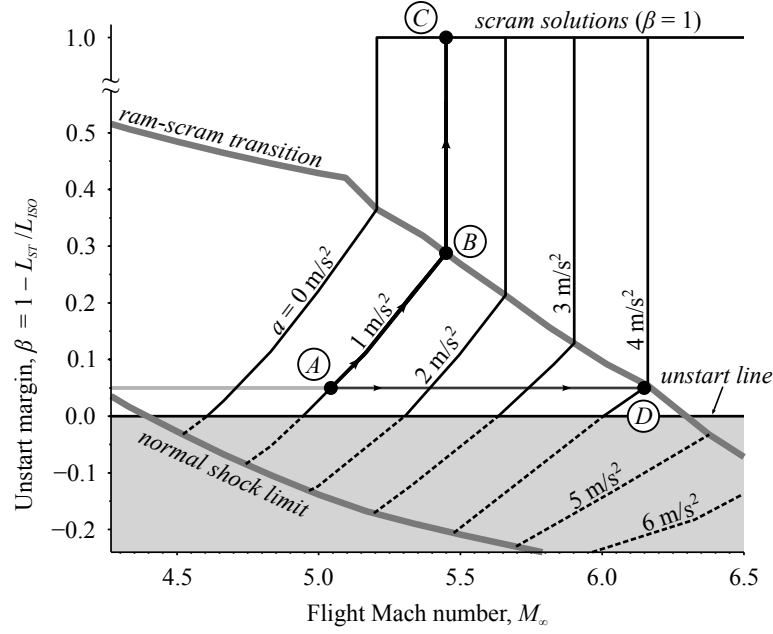
Figure 5.6: Unstart margin for constant-acceleration, constant–dynamic-pressure (q_∞=100 kPa) trajectories. When β<0 (gray area), the isolator is unstarted. The gray line (β=0.05) represents a nonzero cutoff for unstart margin. Two trajectories are highlighted: a constant-acceleration trajectory ($A{\to}B{\to}C$) and a maximum-acceleration trajectory ($A{\to}D$).

($M_\infty = 5.45$). The solution then jumps to point C, which is a scram-mode solution with no isolator shock train ($\beta = 1.0$).

Ram-mode solutions that are farther from transition have longer shock trains, and hence lower unstart margin. Therefore understanding unstart margin is simply an extension of understanding the trends that are important for ram-to-scram transition. As discussed in Section 5.2, increasing the flight Mach number increases M_3 and T_{03}. Although the equivalence ratio has to increase as a result of the decreased mass flow at higher Mach numbers (assuming constant dynamic pressure), the trend as M_∞ increases is to transition from ram mode to scram mode. In fact, for sufficiently high flight Mach numbers, it is not possible to burn enough fuel to choke the flow.

The effect of acceleration is also shown in Fig. 5.6. Increasing the acceleration at a fixed Mach number forces the operating condition to move downward along a vertical line in Fig. 5.6, and thus toward unstart. This is because larger acceleration requires more thrust, and thus the equivalence ratio increases. This raises the back pressure on the isolator (p_3) as well as the length of the shock train.

The horizontal gray line in Fig. 5.6 is the maximum-acceleration trajectory assuming a value of $\beta_{\min} = 0.05$. At $M_\infty = 5.05$ (point A), this acceleration is $a = 1$ m/s^2; when
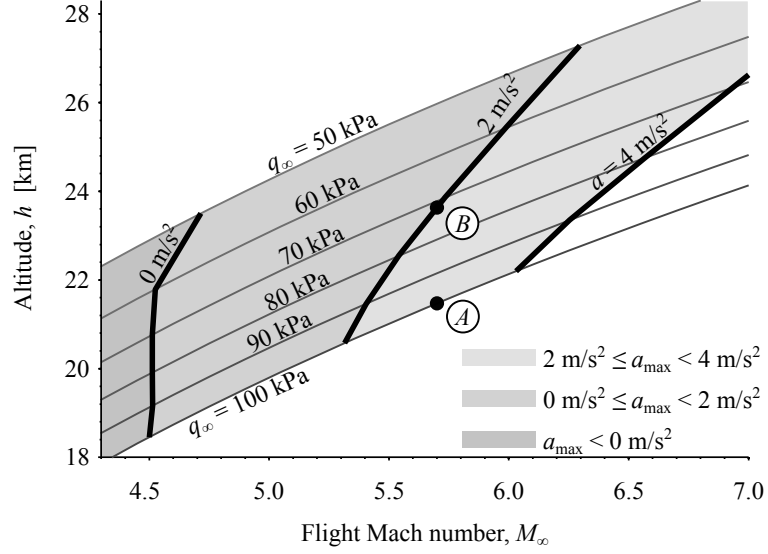
Figure 5.7: Unstart boundaries (thick black lines) plotted on the Flight Corridor Map for varying vehicle acceleration (a). Unstarted flight conditions are to the left of the thick black lines.

$M_\infty = 5.7$, the acceleration can be increased to 3 m/s^2; and at $M_\infty = 6.15$ (point D), the maximum acceleration is 4 m/s^2.

Figure 5.7 shows the lines where unstart margin is zero on the Flight Corridor Map for contours of constant acceleration. There are two factors that give the unstart curves a positive slope. Consider points A and B in Fig. 5.7 and assume an acceleration of $a = 2$ m/s^2 at both points. The Mach number is the same ($M_\infty = 5.7$), but point B is at a higher altitude. At point B, this is the maximum acceleration before unstart occurs, while at point A the unstart margin is greater than zero at an acceleration of 2 m/s^2.

Assuming the weight of the vehicle is constant, the lower dynamic pressure at point B means that a higher lift coefficient is needed. The result is a higher drag coefficient at point B, and thus a higher equivalence ratio (ER). A larger equivalence ratio increases the back pressure on the isolator and thus a longer shock train, which causes unstart at point B.

The second reason for the positive slope of the unstart curves is only true for nonzero accelerations, which is also the reason that the unstart curves have lower slopes for higher accelerations. Both thrust and drag are approximately proportional to dynamic pressure when the Mach number, angle of attack, and equivalence ratio are held constant. Thus the acceleration is given approximately by

$$ma \approx q_\infty S (C_T - C_D) \qquad (5.12)$$

where C_T is the thrust coefficient and S is a reference area. The previous argument showed that C_D increases when q_∞ decreases, and so a higher thrust coefficient is needed. If thrust is greater than drag, a fixed value of $C_T - C_D$ results in a lower acceleration for a lower value of q_∞. This means that the thrust coefficient has to be increased even more than the increase in C_D when the acceleration is greater than zero.

5.4.2 Ram-scram Transition

In this section ram-scram transition boundaries are shown for several variations on the vehicle design. For all trajectories, the acceleration (a) and dynamic pressure (q_∞) are held constant. Dynamic pressures from 50 kPa to 100 kPa are used. The first subsection shows the location of ram-scram transition for the MAX-1 vehicle as presented in Fig. 3.2 but with varying values of acceleration. The remaining subsections consider slight modifications to several design parameters: inlet compression ratio, inlet design Mach number, and combustor divergence angle.

5.4.2.1 Acceleration

Figure 5.8 shows the flight condition at which the MAX-1 vehicle transitions from ram mode to scram mode as a function of acceleration and dynamic pressure. For example, if the Mach number is 6, the dynamic pressure is 100 kPa, and the acceleration is 2 m/s^2, the vehicle is in scram mode because the condition is to the right of the line labeled "2 m/s^2" in Fig. 5.8.

The gray lines show trajectories with constant dynamic pressure. A higher acceleration increases the transition Mach number because the thrust required is larger. With the resulting increased equivalence ratios and corresponding heat release, the engine remains in ram mode longer. This analysis matches the unstart discussion from Section 5.4.1.

One thing to note is that the transition curves in Fig. 5.8 are closer to their unstart counterparts in Fig. 5.7 at higher accelerations. Another way to look at this is to say that acceleration has a larger effect on the unstart limits than on the transition boundaries. Either way, the result is a narrower ram-mode region at higher accelerations. This can be explained in terms of Fig. 5.6, which shows that unstart occurs for weaker isolators at higher flight Mach numbers. Specifically, the cause is that the shock train becomes longer as M_2, the Mach number at the start of the isolator, increases. If M_2 is high enough, then even an isolator with $M_3 = 1$ will be unstarted, with the result that no ram-mode solution is possible.
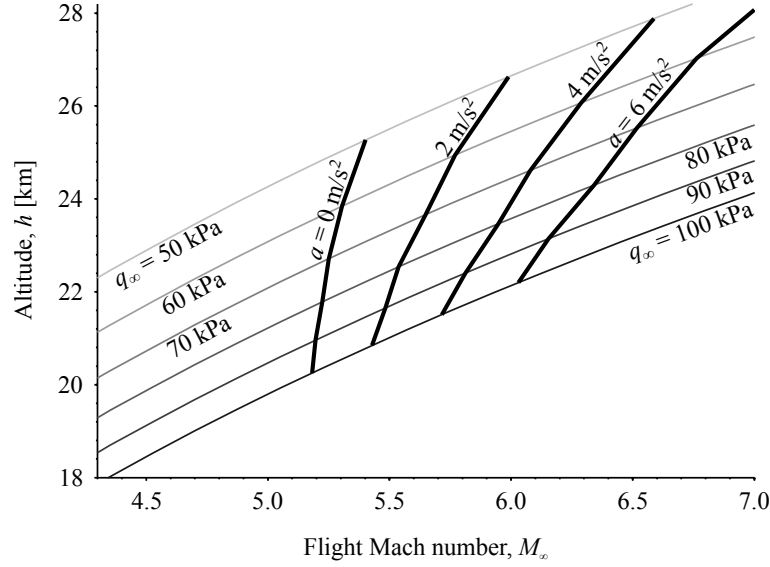
Figure 5.8: Ram-scram transition flight conditions for the MAX-1 vehicle for various constant-acceleration and dynamic pressure trajectories. For a selected acceleration, ram mode is to the left of the black line, and scram mode is to the right.

5.4.2.2 Inlet Design

Figures 5.10 and 5.11 show the effects of a changing inlet design on the ram-scram transition. This differs from the previous subsection in that it involves slight changes to the vehicle shown in Fig. 3.2. Throughout this subsection and the next, the acceleration is always $a = 0$ m/s^2, corresponding to steady, level flight.

An important parameter used to design the inlets is the design Mach number (M_{design}). The design Mach number is an input to the inlet design algorithm as described in Sec. 2.2.3. Since the shock angles vary with Mach number and angle of attack, it is not possible to construct an inlet that works equally well for all flight conditions, but a good inlet design can avoid detrimental shock interactions for an appreciable range of Mach numbers. While initial work on such inlet designs addressed this problem by designing an inlet while considering only a single flight condition [14, 61], more recent work has resulted in design methods that work for a prespecified range of flight conditions [55, 131, 150].

The present inlet design method finds the ramp angles that minimize the stagnation pressure loss when the flight Mach number equals the design Mach number ($M_\infty = M_{design}$) subject to a compression constraint. The ratio of the static pressure at the end of the inlet (p_2; see Fig. 3.2) to the freestream pressure (p_∞) is fixed at the design Mach number, and
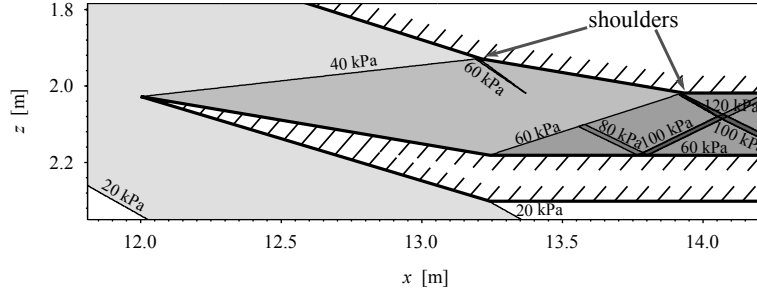
(a) Inlet cowl region for $M_{design} = 8$ design.
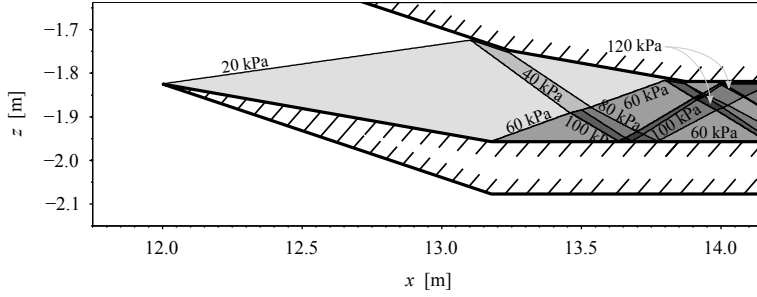
(b) Inlet cowl region for $M_{design} = 9$ design.

Figure 5.9: Pressure contours for two vehicles at a trimmed flight condition with q_∞=100 kPa, M_∞=5.8, and a=2 m/s^2. The M_{design}=8 vehicle is in scram mode while the M_{design}=9 is in ram mode.

this value is also a design variable called r_p:

$$r_p = \left.\frac{p_2}{p_\infty}\right|_{M_\infty=M_{design}} \tag{5.13}$$

Values of r_p are listed in Tables 5.1 and 5.2. Second, the lengths of the inlet ramps (L_1-L_4 in Tables 5.1 and 5.2) are selected so that certain shock interactions do not occur when the flight Mach number is in a certain window $M_{min} < M_\infty < M_{max}$. Specifically, the external shocks must remain upstream of the cowl leading edge so that the shocks do not go into the combustor, and the internal shocks must remain downstream of "shoulders" on the inlet body. These shoulder points are the points on the internal portion of the inlet where the slope of the wall changes. These shoulders, which are labeled in Fig. 5.9(a), are the two vertices of the wall in the upper right portion of the figures. The shock-interaction constraints are not satisfied in Fig. 5.9(b) because the internal shocks (labeled 20 kPa and 60 kPa) hit the wall upstream of these shoulder points. See Sec. 2.2.3 for more details on the inlet design methodology.

In the present work, this range of Mach numbers is defined to go from 2.0 less than

the design Mach number to 2.0 greater than the design Mach number. Thus the baseline MAX-1 vehicle ($M_{design} = 9$) is designed for operation from $M_\infty = 7$ to $M_\infty = 11$. Table 5.1 describes the geometry of the inlet for a range of inlet design Mach numbers (M_{design}).

Inlets often have acceptable performance outside their design range, especially if the trimmed angle of attack is lower at lower flight Mach numbers [167]. Furthermore, the performance metric used for inlet design was stagnation pressure loss, which may not correlate perfectly with overall vehicle performance.

Figure 5.10 shows that lowering the design Mach number results in a lower ram-scram transition Mach number. At a given M_∞, inlets with M_{design} close to M_∞ have less drag. Because the drag is lower, the equivalence ratio is lower, and there is a higher chance of being in scram mode. Figure 5.9 illustrates an example. Pressure contours are shown for two vehicles at the same dynamic pressure, flight Mach number, and acceleration, but with different inlet design Mach number. The primary difference between the two cases is that the $M_{design} = 9$ design in Fig. 5.9(b) has more shock interactions.

Figure 5.11 shows the effect of the inlet compression ratio (r_p) on the ram-scram transition boundary, and Table 5.2 gives inlet geometry for various values of r_p. In Fig. 5.11, the acceleration was kept at 0 m/s^2, and the design Mach number is 9. The design with an inlet compression ratio of 70 corresponds to the MAX-1 vehicle. The effect of this design parameter on ram-scram transition is very slight, with the tendency for higher compression ratios to delay ram-scram transition to higher Mach numbers.

5.4.2.3 Combustor Divergence Angle

Figure 5.12 shows the effect of an important combustor design parameter, which is the divergence angle in the expanding region of the combustor. The divergence angle cannot directly affect whether the engine is in ram mode or scram mode because that is determined by the heat release in the constant-area region. However, if the divergence angle has a large effect on thrust within scram mode, it could change the equivalence ratio required for trim, which would change the transition Mach number as a result. The results in Fig. 5.12 are for divergence angles ranging from 2.11° to 5.11°, with the $\theta_c = 3.11$° curve corresponding to MAX-1 from Fig. 3.2. The results show that the effect of the combustor divergence angle is small, and the computed trends are not monotonic. Too large a value for θ_c could reduce the thrust, while too low of a divergence angle would allow the flow to thermally choke in the diverging section. Both of these would cause the transition Mach number to increase, which may be the explanation for the smallest and largest divergence angles being to the right in Fig. 5.12.

Table 5.1: Ramp angles (θ), ramp lengths (L), and area ratio (A_1/A_2) for various inlet design Mach numbers. Compression ratio is r_p=70. The baseline vehicle has M_{design}=9.

Parameter	$M_{design} = 6$	$M_{design} = 7$	$M_{design} = 8$	$M_{design} = 9$
θ_1	9.28°	7.81°	6.73°	5.90°
θ_2	22.62°	19.12°	16.59°	14.67°
θ_3	12.30°	10.34°	8.94°	7.89°
L_1	8.58 m	8.40 m	8.30 m	8.24 m
L_2	5.62 m	5.62 m	5.60 m	5.57 m
L_3	0.07 m	0.07 m	0.08 m	0.08 m
L_4	0.97 m	0.95 m	0.93 m	0.92 m
A_1/A_2	13.84	15.17	16.01	16.58
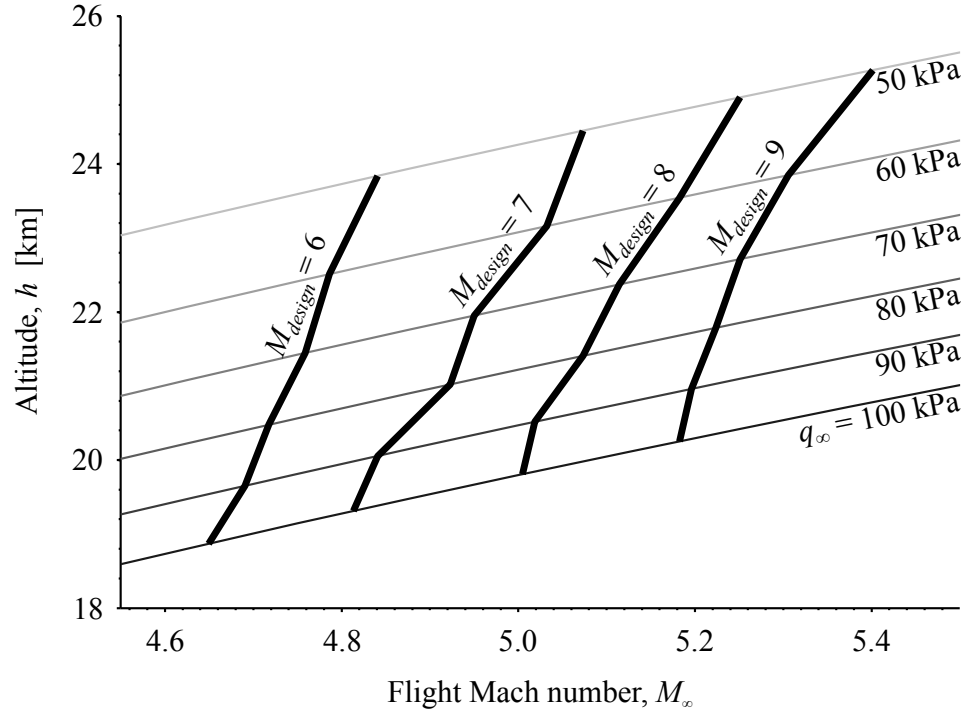
Figure 5.10: Ram-scram transition flight conditions for varying inlet design Mach number assuming steady, level flight.

Table 5.2: Ramp angles (θ), ramp lengths (L), and area ratio (A_1/A_2) for various inlet compression ratios. Design Mach number is $M_{design}=9$. The baseline vehicle has $r_p=70$.

Parameter	$r_p = 50$	$r_p = 60$	$r_p = 70$	$r_p = 80$	$r_p = 90$
θ_1	5.23°	5.59°	5.90°	6.17°	6.42°
θ_2	12.96°	13.86°	14.67°	15.40°	16.07°
θ_3	6.93°	7.44°	7.89°	8.30°	8.68°
L_1	7.84 m	8.06 m	8.24 m	8.39 m	8.52 m
L_2	6.18 m	5.84 m	5.57 m	5.34 m	5.15 m
L_3	0.10 m	0.09 m	0.08 m	0.08 m	0.07 m
L_4	1.02 m	0.96 m	0.92 m	0.88 m	0.84 m
A_1/A_2	13.83	15.28	16.58	17.77	18.86
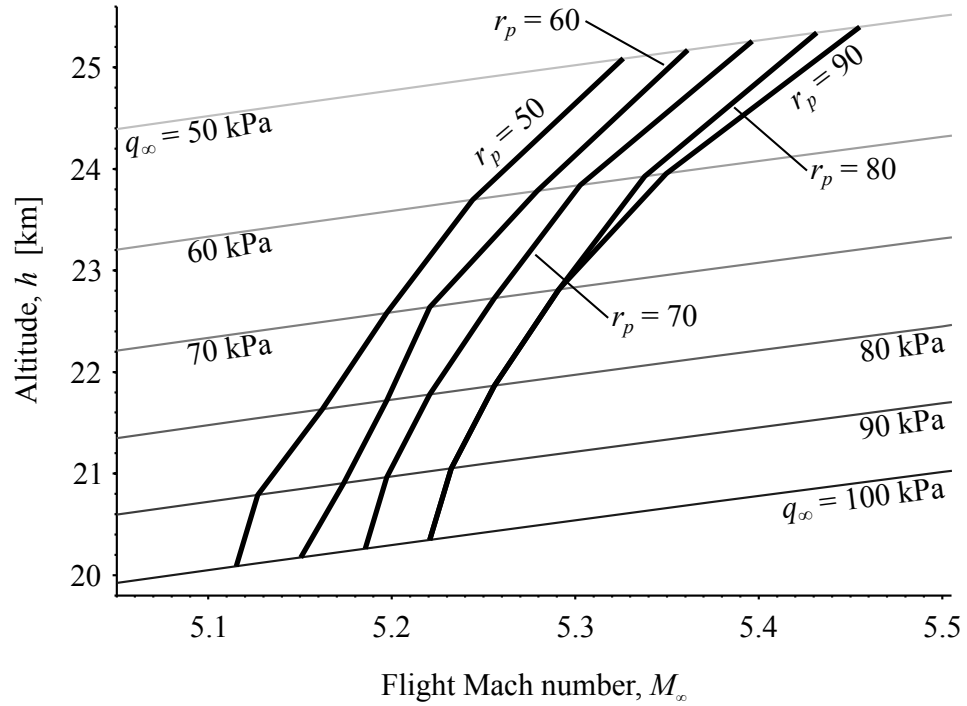
Figure 5.11: Ram-scram transition flight conditions for varying inlet compression ratio, which is the pressure ratio at the design Mach number, $r_p=p_2/p_\infty(M_{design})$.
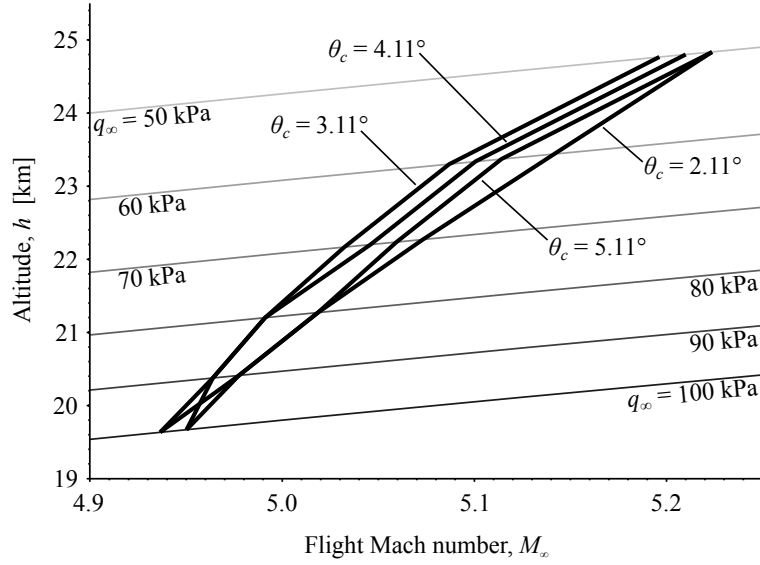
Figure 5.12: Ram-scram transition flight conditions for varying combustor divergence angle.

5.4.3 Jumps at the Ram-Scram Boundary

One undesirable aspect of the ram-scram transition is that sudden changes in the wall pressure can occur. These changes have been measured in the lab-scale experiments of [113, 114]. The reason for the sudden change in wall pressure is that the engine has a downstream thermally-choked boundary condition while it operates in the ram mode, but this boundary condition is suddenly removed. The Mach number profiles undergo the significant change that is plotted in Fig. 5.13.

The jump in wall pressure leads to corresponding rapid changes in thrust, lift, and drag forces, and if severe enough this could lead to loss of vehicle control. For this reason, improved predictions of the wall pressure jump at transition can be of value to the design of a fast-response control system.

Figure 5.13 shows the jump in the static pressure and Mach number profiles for one example of ram-scram transition. To generate the conditions in Fig. 5.13, a ram-mode solution near the boundary of ram-scram transition was found. The acceleration was selected to be $a = 2$ m/s^2, and the dynamic pressure was selected to be $q_\infty = 100$ kPa. From Fig. 5.8, this leads to the flight Mach number of $M_\infty = 5.72$. Then, after finding the trimmed equivalence ratio for those flight conditions, the equivalence ratio was lowered by 0.002 to cause transition to scram mode. As shown in Fig. 5.13, this causes a large change in both the pressure and Mach number profiles in the isolator and combustor. Although this jump in internal flow conditions is worthy of study, we are mostly interested in the changes in the
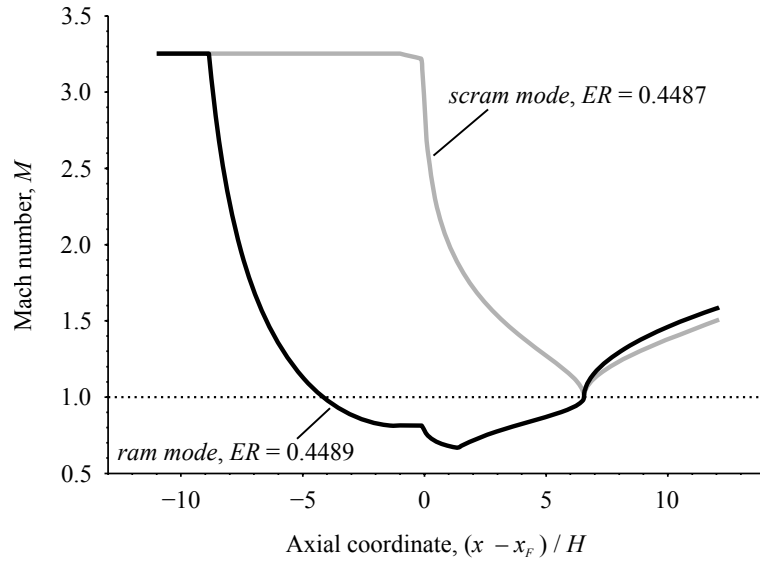
(a) Mach number profile.
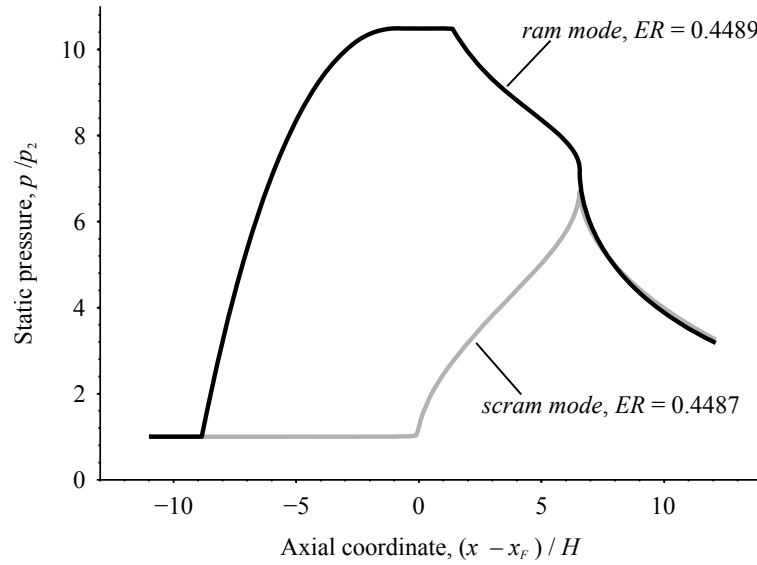
(b) Static pressure profile.

Figure 5.13: Mach number and static pressure profiles for the isolator and combustor of the MAX-1 vehicle under two conditions. The flight Mach number is M_∞=5.72, the dynamic pressure is q_∞=100 kPa. The acceleration for the ram case is a=2.00 m/s^2, and for the scram case it is a=0.53 m/s^2.

exit conditions, the forces, and the moments. The computations indicate that there is a corresponding jump in the thrust; the vehicle acceleration drops by about 1.47 m/s^2 when the engine goes into scram mode. Fortunately, corresponding change in net moments causes a change of only 0.02 rad/s^2. The reason for this small change is that the change in thrust and change in pressure on the nozzle surface pressure tend to counteract each other. The primary causes for the jumps seen in this simulation are that the separated boundary layer reduces friction in ram mode (i.e. $c_f = 0$ in Eq. (5.11)), and the combustion is more complete due to the slower airflow.

5.4.4 Region of Potential Instabilities

In the above analysis, the vehicle is ascending and increasing its Mach number, so the engine is first ignited in the ram mode. Our fundamental assumption in the previous analysis is that the engine operates in the scram mode whenever possible. However, it was found that there is a region in which both ram and scram solutions are mathematically possible. This region is shown in Fig. 5.5. In the ram mode, the combustor is thermally choked, and relatively strong shocks occur in the isolator. In the corresponding scram mode, the isolator shocks are weak, and thermal choking does not occur.

When two solutions are mathematically possible, the system may become unstable and jump to the other solution. More experimental research is needed to determine if the engine becomes unstable as ram-scram transition is approached.

Another possibility is that ram-scram transition occurs at a different condition than scram-ram transition. If this is the case, there will be conditions for which an engine can operate in either ram mode or scram mode depending on whether the equivalence ratio was increased or decreased to get to that condition. Other authors have recently modeled hysteresis relating to ram mode and scram mode in a similar engine [177]. Experimental research has not identified any hysteresis phenomenon, but more evidence is needed.

5.5 Conclusions

Ram-scram transition and engine unstart limits were computed along ascent trajectories and plotted on the Flight Corridor Map. It was shown that a dual-mode combustor will unstart if the vehicle flies too high, too slow, or at too great of an acceleration. This places limits on the flight envelope. Actions that will cause a vehicle to transition from ram mode to scram mode include increasing the Mach number, decreasing the altitude, and decreasing the acceleration. These boundaries were calculated using a reduced-order model, and

the length of the shock train was computed throughout the ram-mode flight envelope. Unstart and ram-scram transition are well-known phenomena, but previously have not been calculated in terms of flight condition variables for a trimmed vehicle.

It was found that two important design parameters, inlet compression ratio and combustor divergence angle, had little effect on ram-scram transition. The effect of the inlet design Mach number is larger. Maximum acceleration in the ram mode, which is limited by unstart, was found to be larger at higher flight Mach numbers. Finally, for the largest accelerations, the unstart limit was found to be close to the ram-scram transition boundary.

The ram-scram transition prediction was compared to experimental results, and reasonably good agreement was found. A discontinuity in the thrust at ram-scram transition was predicted by the model due to the sudden disappearance of a separated boundary layer when the thermal choking boundary condition no long applies. A region of possible instability or hysteresis in the engine was identified near ram-scram transition. These results highlight the need for more experimental data describing ram-scram transition including force measurements.

CHAPTER 6

Trajectory and Design Optimization

This chapter introduces the topic of design optimization that incorporates the coupling between flight dynamics and the propulsion systems. Focus is placed on the acceleration phase of flight, which introduces two distinct types of decision variables: parameters that affect the geometry of the vehicle and variables that determine the trajectory.

Following a summary of the relevant equations of motion in Sec. 6.1, the chapter follows a three-part approach. First, in Sec. 6.2, a simple fixed trajectory is selected, and the effects of perturbations to several design variables are investigated. Then Sec. 6.3 investigates what is essentially the converse problem of optimizing a trajectory for a fixed vehicle. Finally, in Sec. 6.4, the two are considered simultaneously. In this case, the optimum trajectory will be different for each vehicle design, and it is shown that the total fuel consumption for a trajectories varies by a factor of more than 2.5 throughout the design space.

6.1   Accelerating Trajectories

We define an altitude profile in the velocity in the velocity-altitude plane as a function

$$h = h(V) \tag{6.1}$$

such that the altitude is determined as a function of V, the magnitude of the velocity of the vehicle (alternatively, $h = h(M)$). In this work, the function $h(V)$ is selected so that the dynamic pressure,

$$q = \frac{1}{2}\rho V^2 = \frac{\gamma}{2}pM^2 \tag{6.2}$$

is held constant, but other functions $h(V)$ could be selected. The red constant-dynamic pressure curves in Fig. 4.1 show examples of such trajectories. This function $h(V)$ does not uniquely determine a trajectory because other variables, such as acceleration (a) can still

vary. In other words, there is a function

$$a = a(V) \tag{6.3}$$

that prescribes the acceleration for each velocity. The altitude profile leads to a relationship between acceleration and flight path angle (γ), as we will show. Differentiating $h(V)$ with respect to time using the chain rule gives

$$\dot{h} = \frac{\mathrm{d}h}{\mathrm{d}V}\frac{\mathrm{d}V}{\mathrm{d}t} = h'(V)a \tag{6.4}$$

Since $\dot{h} = V\sin\gamma$, we can solve for the flight path angle.

$$\sin\gamma = \frac{\mathrm{d}h}{\mathrm{d}V}\frac{a}{V} \tag{6.5}$$

This means that the flight path angle (or climb rate) is determined by our two functions $h(V)$ and $a(V)$. There is also a question of $\dot{\gamma}$, which we can find by taking another derivative of the altitude.

$$\begin{aligned}
\ddot{h} &= \frac{\mathrm{d}}{\mathrm{d}t}(V\sin\gamma) = a\sin\gamma + V\dot{\gamma}\cos\gamma \\
&= \frac{\mathrm{d}}{\mathrm{d}t}\left(\frac{\mathrm{d}h}{\mathrm{d}V}\frac{\mathrm{d}V}{\mathrm{d}t}\right) = \frac{\mathrm{d}^2h}{\mathrm{d}V^2}a^2 + \frac{\mathrm{d}h}{\mathrm{d}V}\frac{\mathrm{d}a}{\mathrm{d}t}
\end{aligned}$$

Equating the two expressions for $\ddot{h}$ and solving for $\dot{\gamma}\cos\gamma$ gives

$$\dot{\gamma}\cos\gamma = \frac{1}{V}\left[\frac{\mathrm{d}^2h}{\mathrm{d}V^2}a^2 + \frac{\mathrm{d}h}{\mathrm{d}V}\frac{\mathrm{d}a}{\mathrm{d}t} - a\sin\gamma\right]$$

Noting that

$$\frac{\mathrm{d}a}{\mathrm{d}t} = \frac{\mathrm{d}a}{\mathrm{d}V}\frac{\mathrm{d}V}{\mathrm{d}t} \qquad\qquad \sin\gamma = \frac{a}{V}\frac{\mathrm{d}h}{\mathrm{d}V}$$

this equation can be simplified to

$$\dot{\gamma}\cos\gamma = \left[\frac{\mathrm{d}^2h}{\mathrm{d}V^2}a + \left(\frac{\mathrm{d}a}{\mathrm{d}V} - \frac{a}{V}\right)\frac{\mathrm{d}h}{\mathrm{d}V}\right]\frac{a}{V} \tag{6.6}$$

Each of the terms in Eq. (6.6) is very small, and we usually just set $\dot{\gamma} = 0$ during trajectory simulation. Exceptions include very steep climbs ($\cos\gamma \approx 0$ and $\mathrm{d}h/\mathrm{d}V \gg 0$) and sharp changes in the altitude profile ($\mathrm{d}^2h/\mathrm{d}V^2 \gg 0$).

103

An important example of an altitude profile is one that maintains a constant dynamic pressure, e.g. the red curves in Fig. 4.1. The dynamic pressure is $q = \frac{1}{2}\rho V^2$ where ρ is given as a function of altitude ($\rho(h)$) given by an atmosphere model, e.g. [178]. Differentiating the dynamic pressure with respect to altitude allows one to solve for the derivative of altitude with respect fo velocity:

$$\frac{\mathrm{d}h}{\mathrm{d}V} = -\frac{2\rho}{V\frac{\mathrm{d}\rho}{\mathrm{d}h}} = -\frac{2\rho}{V\rho'(h)} \tag{6.7}$$

Substituting this into Eq. (6.5) gives

$$\sin\gamma = -\frac{2\rho a}{V^2\rho'(h)} \tag{6.8}$$

The result is a relationship between acceleration (a), climb rate (γ), and atmospheric model (ρ and $\rho'(h)$) that describes the ascent in a self-consistent manner. In other words, it gives a practical method for accelerating from one velocity to another.

It is possible to parametrize a generic ascent trajectory directly in terms of the dynamic pressure.

$$\sin\gamma = \frac{2a}{V^2\rho'(h)}\left(\frac{1}{V}\frac{\mathrm{d}q}{\mathrm{d}V} - \rho\right) \tag{6.9}$$

This yields Eq. (6.8) when q is constant, and we will only consider constant-q trajectories in the remainder of this work.

6.1.1 Trajectory Objective Functions

For a fixed vehicle, an intuitive choice of objective function for the trajectory optimization problem is the total fuel consumed during the duration of the trajectory, which can be written

$$m_f(t_2) = \int_{t_1}^{t_2} \dot{m}_f\left(V(t), a(t), m_f(t)\right)\, \mathrm{d}t \tag{6.10}$$

where t_1 is the time at which the trajectory starts, and t_2 is the time at which it finishes. Since we would like to specify the initial and final velocities (V_1 and V_2), the duration of the ascent ($t_2 - t_1$) is not known a priori. A simple change of variables makes V the variable of integration,

$$m_f(V_2) = \int_{V_1}^{V_2} \frac{\dot{m}_f(V, a, m_f)}{a}\, \mathrm{d}V \tag{6.11}$$

Using this formulation, the trajectory parametrization (acceleration given as function of velocity, $a(V)$) from Sec. 6.3 can be used directly.

When the geometry of the vehicle is allowed to change, simply using the total fuel con-

sumption for an objective function may lead to problems. For example, a smaller vehicle will naturally use less fuel, but it may not use less fuel for the same payload. One way to alleviate this issue would be to minimize fuel consumption for a given payload mass. In this work, we are more interested in fundamental tradeoffs that will be useful to future vehicle designers, and so an objective function that highlights the effects of changes to the geometry is preferred.

Because this work considers acceleration trajectories, an interesting approach is to calculate what the efficiency would be of a rocket that produced the same acceleration using the same total mass of propellant. This can be done using the rocket equation (often called the Tsiolkovsky rocket equation, named after Konstantin Tsiolkovsky [179], but now known to have been derived 44 years before his birth by William Moore [180]). The rocket equation states that the change in velocity can be given in terms of the rocket's efficiency, the initial mass, and the mass of fuel used,

$$\Delta V = g I_{sp} \ln \frac{m_1}{m_1 - m_f} \qquad (6.12)$$

Here $g = 9.8$ m/s^2, m_1 is the mass of the vehicle at the start of the trajectory, and m_f is the total fuel consumed during the trajectory. The specific impulse, I_{sp} is a measure of efficiency, and for a rocket $g I_{sp}$ is just the exhaust velocity. In this work, we use this formula as a measure of efficiency, and the objective function of choice is

$$I_{sp} = \frac{V_2 - V_1}{g \ln(m_1/(m_1 - m_f))} \qquad (6.13)$$

This value is a function of both fuel consumption (m_f) and vehicle mass (m_1), and it also has the advantage that it allows the performance to be directly compared to rocket efficiencies.

An example that shows the utility of this objective function is shown in Sec. 6.2. Increasing the mass of the vehicle (while holding the geometry constant) leads to a dramatic increase in total fuel consumption, but the value of the trajectory specific impulse decreases only slightly.

6.1.2 Optimal Control of Accelerating Trajectory

This subsection describes how classical optimal control theory can be applied to the trajectory optimization as described in the preceding sections. Although all of the trajectory results presented in this work use a discretized trajectory simulation and direct optimization, a theoretical analysis is useful for understanding and explaining the later results.

Let $\mathcal{J}$ be the functional that calculates the fuel consumption for a trajectory,

$$\mathcal{J}(a) = m_f = \int_{V_1}^{V_2} \frac{\dot{m}_f(V, a, m_f(V, a))}{a} \, dV \tag{6.14}$$

The calculus of variations then states that the optimum acceleration function, a^* is found when

$$\frac{\partial}{\partial \varepsilon} \mathcal{J}(a^* + \varepsilon \delta a)\Big|_{\varepsilon=0} = 0 \tag{6.15}$$

where δa is a small perturbation to the optimum acceleration [181]. Evaluating this expression assuming that the mass of the vehicle does not change leads to the following integral:

$$\int_{V_1}^{V_2} \left(\frac{\partial \dot{m}_f}{\partial a} - \frac{\dot{m}_f}{a^*} \right) \frac{\delta a}{a^*} \, dV$$

This must be zero for *all* perturbations δa. The only way for this to be true is if

$$\frac{\partial \dot{m}_f}{\partial a} - \frac{\dot{m}_f}{a} = 0 \tag{6.16}$$

Eq. (6.16) is useful because it says the optimum trajectory can be solved for each point individually. Specifically, we can solve Eq. (6.16) for each velocity in $V \in [V_1, V_2]$. It turns out accounting for the change in the mass of the vehicle, i.e.

$$\frac{\partial \dot{m}_f}{\partial m_f} \neq 0$$

leads to the same result, Eq. (6.16), and this is shown in Appendix D.

However, there may not always be a feasible solution to Eq. (6.16) because it does not account for constraints on the acceleration. In such cases, the maximum feasible acceleration is the best choice, which is consistent with the predictions of bang-bang control. Figure 6.1 shows two examples of the mass flow rate required for trim ($\dot{m}_f$) as a function of acceleration (a). In the first case, Fig. 6.1(a), the function has a constant slope, and Eq. (6.16) is never satisfied. The optimal acceleration is simply the maximum acceleration.

The second case, Fig. 6.1(b), shows diminishing returns near the maximum acceleration. At the maximum acceleration, the slope of the curve is near infinite, which means that the *marginal* efficiency is very low. In other words, it takes a large amount of extra fuel to increase the acceleration only a little bit. As a result, there is an optimum acceleration that satisfies Eq. (6.16), and this optimum is at an acceleration below the maximum. Graphically, this solution is at the point where the line connecting the origin and that point is tangent to the curve. This is shown by the dotted line in Fig. 6.1(b).

(a) Linear case; a_{max} optimal.   (b) Nonlinear case; optimum from Eq. (6.16).
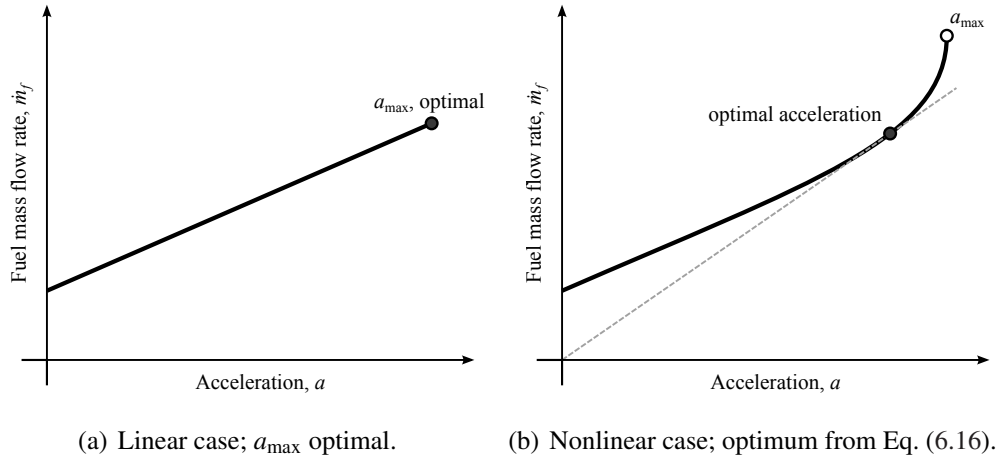
Figure 6.1: Sketch of acceleration (a) and fuel mass flow rate ($\dot{m}_f$) for two cases.

In the case of scram-mode operation, both cases are possible. When the maximum acceleration corresponds to ram-scram transition, there is no occurrence of diminishing returns, and the fuel curve looks like Fig. 6.1(a). When the maximum acceleration is determined by using up all of the oxygen available to the engine, the curve looks much like Fig. 6.1(b), and the optimum acceleration is slightly below the maximum.

The following algorithm qualitatively describes how to find the optimum acceleration profile for a continuous trajectory.

1. Begin with $V = V_1$.

2. Increase V to the next velocity.

3. Find $a(V)$ such that Eq. (6.16) is satisfied.

4. Evaluate $m_f(V)$ using Eq. (6.11).

5. Return to step 2 until $V = V_2$.

The following section describes how to discretize this approach so that it can be used for a trajectory parametrized by a finite set of variables.

6.1.3 Numerical Calculation of Fuel Consumption

Suppose that a trajectory is split into segments so that there are n pairs of flight conditions $(V_1, a_1), \ldots, (V_n, a_n)$. In this section, we show that time can be eliminated from the fuel

consumption calculation even in this discretized formulation. Using trapezoidal numerical integration, the total fuel consumption from Eq. (6.11) can be discretized to be

$$m_f(V_n) = \sum_{i=1}^{n-1} \frac{1}{2} \left(\frac{\dot{m}_{f,i}}{a_i} - \frac{\dot{m}_{f,i+1}}{a_{i+1}} \right) (V_{i+1} - V_i) \tag{6.17}$$

Taking the derivative with respect to a_i and setting it equal to zero gives

$$\frac{\partial m_f}{\partial a_i} = \left(\frac{\partial \dot{m}_{f,i}}{\partial a_i} - \frac{\dot{m}_{f,i}}{a_i} \right) \frac{V_{i+1} - V_{i-1}}{2a_i} = 0 \tag{6.18}$$

Setting this equal to zero gives the same result as Eq. (6.16).

This formulation allows the total fuel consumption to be calculated with a time-domain simulation, but it may still be useful to calculate the time spent on each trajectory segment so that a time history of the trajectory can be reconstructed a posteriori. This is somewhat complicated in the present situation because the two relevant variables, a and V, are related to each other by a time derivative. For each segment (from V_i to V_{i+1}) we can write

$$V(t) = V_i + (V_{i+1} - V_i)\zeta(t)$$
$$a(t) = a_i + (a_{i+1} - a_i)\zeta(t)$$

where $\zeta(t_i) = 0$ and $\zeta(t_{i+1}) = 1$. A time derivative of the first of these two equations gives

$$a(t) = (V_{i+1} - V_i)\dot{\zeta}(t)$$

Equating the two expressions for $a(t)$ gives a differential equation for $\zeta(t)$ whose solution is

$$\zeta(t) = \frac{a_i}{a_{i+1} - a_i} \left(\exp\left(\frac{a_{i+1} - a_i}{V_{i+1} - V_i} (t - t_i) \right) - 1 \right) \tag{6.19}$$

The utility of Eq. (6.19) is to solve for t when $\zeta = 1$, because this is the information required to calculate the amount of time spent on segment i of the trajectory, i.e. Δt_i:

$$\Delta t_i = t_{i+1} - t_i = \frac{V_{i+1} - V_i}{a_{i+1} - a_i} \ln \frac{a_{i+1}}{a_i} \tag{6.20}$$

Eq. (6.20) has a singularity in the case of constant acceleration, i.e. $a_{i+1} = a_i$. In this case,

$$\Delta t_i = \frac{V_{i+1} - V_i}{a_i} \tag{6.21}$$

The methods described in this section allow for the calculation of the relevant properties

along a discretized trajectory, and the conditions for the optimal acceleration are explained. In the sections that follow, these techniques are used to calculate the fuel consumption and time histories, but the optimization is done directly on the trajectory variables $a_1, \ldots, a_N$.

6.2 Sensitivities to Design Parameters

Two aspects of hypersonic vehicle performance are investigated in this section: the dynamic stability of the aircraft throughout trajectories and the sensitivity of total fuel consumption to changes in the vehicle design. Much of this work was presented in [167], and the results were used to guide the decision of what design variables to use for the optimization in Sec. 6.4.

In addition to the technological challenges, these vehicles also have a tendency to be unstable [8, 9, 84, 182]. This is largely because the lift-producing inlet pulls the center of pressure forward, and because the nozzles are shorter than the inlets, they tend to push the center of gravity aft. It is of course possible to add ballast to the nose to pull the center of gravity forward and thus make the vehicle more stable, but doing so may have negative effects on the fuel efficiency if it causes higher trim drag.

The trajectory used in this section includes a wide range of flight conditions from Mach 5 to Mach 12. This wide range was selected so that the effects of ram-to-scram transition on the vehicle stability, if any, could be investigated. The dynamic pressure is held constant at 100 kPa, and the acceleration is fixed at 2 m/s^2. Trajectory optimization results in subsequent sections show that accelerations higher than 2 m/s^2 are more favorable; a low acceleration was selected for this work to ensure a wider range of feasible vehicle designs.

The results are split broadly into two parts. Secs. 6.2.1–6.2.5 describe how changes to the design from the MAX-1 baseline vehicle design affect two modes of the open-loop linearized dynamics. The methodology used for this stability analysis is described in Sec. 4.1.3, and the focus will be on the short-period and Dutch-roll modes. The short-period mode describes the relatively fast pitching motion of the vehicle, and the primary participating variables (see Appendix C) are angle of attack (α) and pitch rate (Q). The Dutch-roll mode is usually the dominant mode of the lateral-directional flight dynamics, and its primary participating variables are sideslip angle (β) and yaw rate (R). Figures 4.5 and 4.6 and Sec. 4.3 give a more detailed description of the modes of the linearized flight dynamics.

The second part of the results, contained in Sec. 6.2.8, describes how these changes to the design affect the fuel efficiency. One interesting aspect of this is the tradeoff between stabilization and fuel consumption. Any change to the design that both stabilizes the ve-

hicle and reduces fuel consumption would be a particularly useful result, but none were found among the changes considered here. Also of importance is to identify a small set of design variables that have a large impact on the fuel consumption to be used in a design optimization in Sec. 6.4.

6.2.1 Center of Mass

Moving the center of gravity is the most obvious way to affect the stability of an air vehicle. In this section, the position of the center of gravity is changed without any change in the mass or other properties of the vehicle. The usual method to move the center of gravity for a real vehicle is to add ballast mass at the nose of the vehicle (which also changes the moments and products of inertia), but changes in mass and shifting the center of gravity are isolated as separate variables in this work.

Figure 6.2 shows the poles of the linearized open-loop dynamics for three designs in which Δx_{cg} corresponds to a forward shift of the center of gravity from the center of volume measured in vehicle lengths. Each vehicle design has a separate symbol ($\times$, $\square$, or o), and the pole for several flight conditions along the trajectory is shown for each vehicle design. Poles with a negative real part (to the left of the vertical dotted line) are stable, and poles with a nonzero imaginary part are oscillatory.

The baseline MAX-1 vehicle has a center of gravity that is shifted forward of the center of volume by 5% of the length of the vehicle. Not surprisingly, removing this center-of-gravity offset is destabilizing. For the short-period modes shown in Fig. 6.2(a), the vehicle is stable for all Mach numbers for MAX-1 ($\Delta x_{cg} = 0.05$) and unstable for all Mach numbers for the vehicle whose center of gravity is located at the center of volume ($\Delta x_{cg} = 0$). For a vehicle with a shift halfway in between these two vehicles ($\Delta x_{cg} = 0.025$), the short-period mode transitions from stable to unstable between Mach 9 and Mach 9.5. The pole stays to the left of the 3 rad/s controllability limit throughout the trajectory as long as $\Delta x_{cg} \geq 0.02$.

The Dutch-roll poles, shown in Fig. 6.2(b), are stable and oscillatory for all three vehicles and all flight conditions on the trajectory. The vehicles with less forward shift have longer times to half and a slightly longer oscillation period. Interestingly, all of the vehicle designs in this work show a reversal in the trend of the Dutch-roll modes at around Mach 11. The fact that this flight condition is associated with a change is consistent with expectations as the inlet was designed for conditions between Mach 7 and 11, but it would be difficult to predict the nature of the change. In Chapter 4, the most notable change was in the angle of attack (see Fig. 4.1(c)), and indeed the increasing stability in the Dutch-roll mode at Mach numbers higher than 11 comes from the lower angles of attack when the
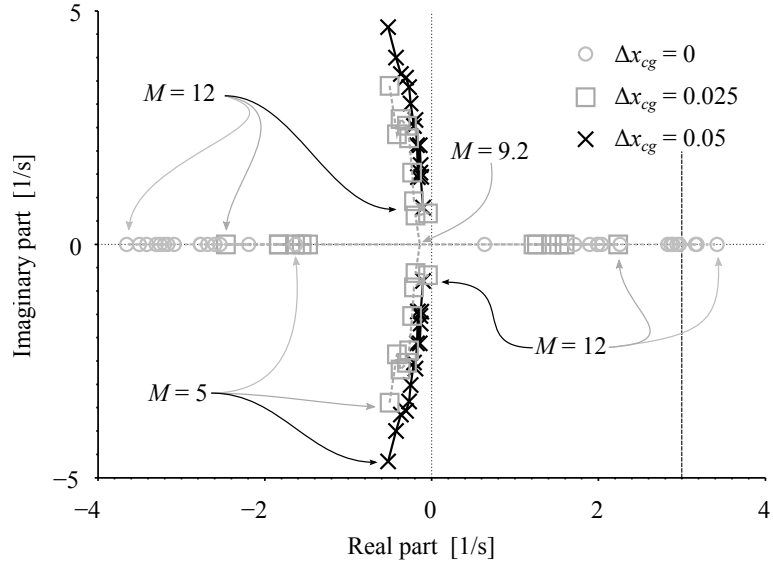
(a) Short-period modes. An approximate controllability limit of 3 1/s is marked with the vertical dashed line.
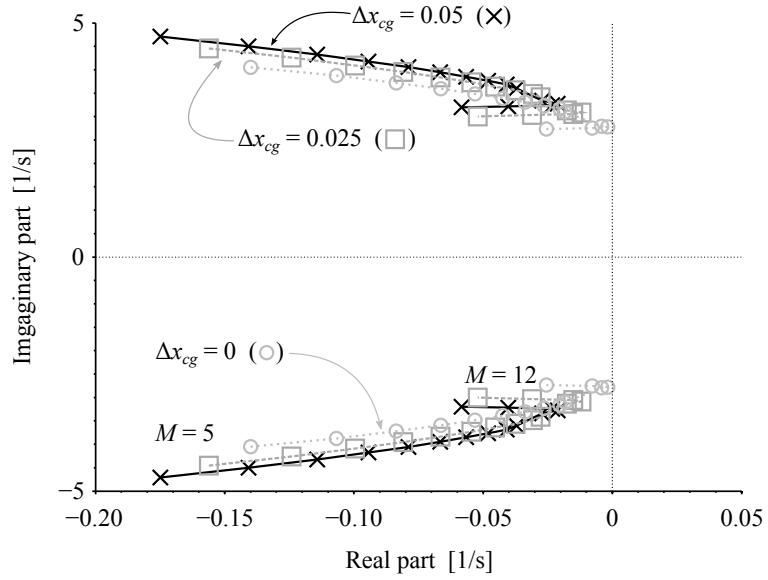
(b) Dutch-roll modes.

Figure 6.2: Plot of poles of linearized dynamics for MAX-1 (Δx_{cg}=0.05) and otherwise identical vehicles with half (Δx_{cg}=0.025) the center-of-gravity shift and no shift (Δx_{cg}=0).

inlet is operated outside its design range.

Some effects of the center of gravity location on the trim variables are shown in Fig. 6.3. The location of the center of gravity has a significant effect on both the trim angle of attack and the elevator deflection angle; both effects are primarily due to the changing net moment caused by moving the center of gravity because both the mass and the surface of
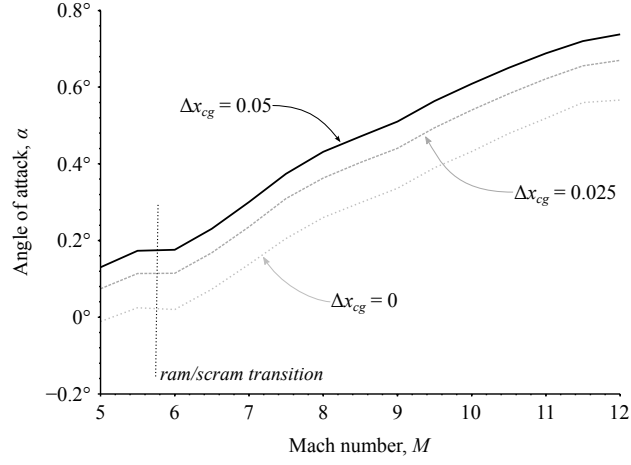
(a) Angle of attack (α)
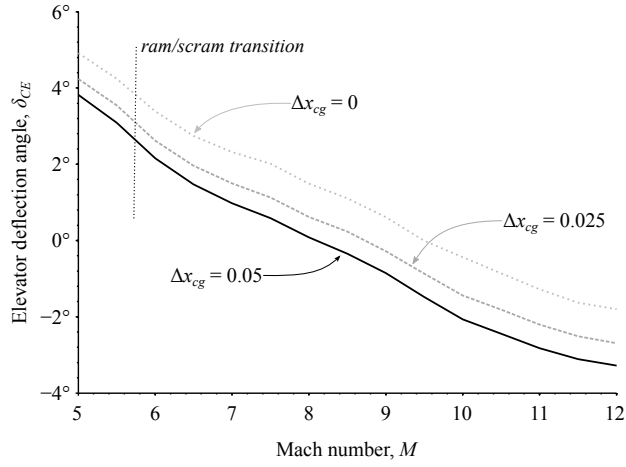
(b) Elevator deflection angle (δ_{CE}).
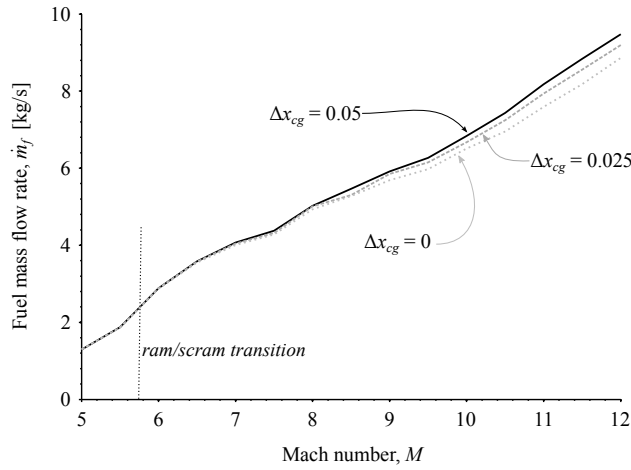
(c) Fuel mass flow rate ($\dot{m}_f$).

Figure 6.3: Plot of state and control variables for MAX-1 (Δx_{cg}=0.05) and otherwise identical vehicles with half (Δx_{cg}=0.025) the center-of-gravity shift and no shift (Δx_{cg}=0).

the vehicle are unchanged between the two designs. When the center of gravity is farther back, the elevators need to do more to counteract the nose-up moment on the vehicle, and thus an increase in the deflection angle is required, as shown in Fig. 6.3(b). Note that a positive deflection angle moves the trailing edge down, which creates a negative (nose-down) pitching moment. The fact that the lever arm of the elevators is reduced by moving the center of gravity closer also helps exaggerate the differences in the deflection angle. However, the tendency to reduce drag will reverse at some point because $|\delta_{CE}|$ will start increasing after its value goes through zero.

A change in the elevator deflection angle also cause slight shift in the lift, and so a change in the angle of attack is also required. The change in angle of attack also affects the pitching moment, so the two changes (elevator deflection angle and angle of attack) must be considered simultaneously.

Figure 6.3(c) shows that the fuel usage is only slightly affected by the location of the center of gravity. Apparently the combination of decrease in angle of attack and increase in the elevator deflection angle is such that the drag stays about the same. However, the fuel mass flow rate decreases slightly as the center of gravity moves backward, and the difference is more noticeable at higher Mach numbers. This indicates that, at least for some flight conditions, moving the center of mass forward can increase the total fuel consumption even without accounting for the mass of the ballast.

6.2.2 Change in Mass

The baseline specification for MAX-1 in Sec. 6.2 has its fuel tanks half full ($r_f = 0.5$). Therefore a simple way to change the mass of the vehicle is to add or remove some of the fuel. In the MASTrim model, the fuel mass is considered to be distributed evenly throughout the vehicle so that the center of gravity position remains fixed and the inertia tensor scales linearly with the mass.

Figure 6.4 shows that the additional mass tends to destabilize the vehicle; however, neither mode goes unstable for a 2300 kg in mass. The first result of increasing the mass is to increase the trim angle of attack. If the weight increases without changing the dynamic pressure, a larger lift coefficient is needed in order to satisfy

$$mg \approx C_L q S$$

where S is the reference lifting area of the vehicle. An increase in angle of attack tends to affect the pressure on the inlet more than other parts of the vehicle, which moves the center of pressure forward and thus destabilizes the vehicle. For any air vehicle, an increase in the
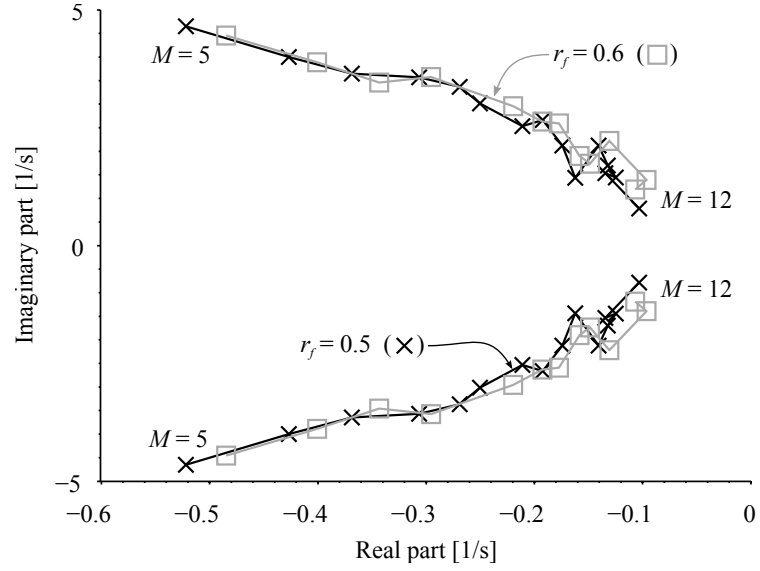
(a) Short-period modes.
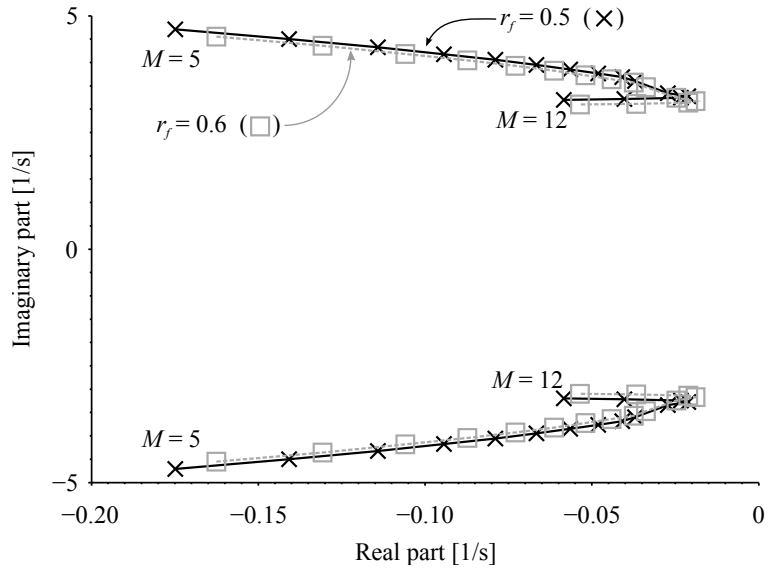
(b) Dutch-roll modes.

Figure 6.4: Plot of poles of linearized dynamics for MAX-1 (r_f=0.5) and an otherwise identical vehicle with more fuel on board (r_f=0.6).

lift coefficient increases the drag coefficient as well, and as a result, this is a case where a destabilizing change also increases the fuel usage.

114

6.2.3 Dihedral Angle

Although the MAX-1 vehicle does not have much wing area, the dihedral angle of the horizontal stabilizers and elevators can affect the lateral-directional stability. The MAX-1 vehicle has a dihedral angle of $\psi_E = 2.86° = 0.05$ radians, and the results were compared to a vehicle with twice the dihedral angle ($\psi_E = 5.73° = 0.1$ radians) and a vehicle with the opposite (anhedral) angle ($\psi_E = -2.86° = -0.05$). As shown in Fig. 6.5(b), increasing the dihedral angle makes the Dutch-roll mode more stable for each flight condition in the trajectory, while the short-period mode is mostly unaffected. The slanted sides of the vehicle keep the Dutch-roll mode stable even with a slight anhedral angle for the elevators. Of course, the slant of the vehicle slides is another geometry design variable, but it is not altered in this work. Furthermore, the trim variables are almost completely unchanged; an example is shown in Fig. 6.6. Thus the dihedral angle is an example of a design variable that can be used to alter the lateral-directional stability without much effect on any other aspect of performance. The Dutch-roll mode would be more sensitive to the dihedral angle for a vehicle with larger wings, and in that case there may be more coupling between dihedral angle and other performance metrics.

6.2.4 Design Mach Number

The performance of the inlet has been closely tied to the flight condition or range of flight conditions it was designed [14, 61, 131, 150]. However, in each of those works, the inlet was considered in isolation from the rest of the vehicle. The MAX-1 inlet design algorithm described in Sec. 2.2.3 specifies a range of Mach numbers for which the inlet should have good performance. It does this by satisfying certain constraints on the shock locations and maximizing the pressure recovery factor at a single Mach number within that range [150].

In this work we define the range of Mach numbers as a center Mach number and a width (Mach number range) so that the bounds of the range are

$$M_{\min} = M_{design} - \frac{1}{2} M_{range} \qquad\qquad M_{\max} = M_{design} + \frac{1}{2} M_{range} \qquad (6.22)$$

The values of M_{design} and M_{range} are given as inputs to the inlet design algorithm. The inlet then calculates the ramp angles so that the compression ratio (p_2/p_∞) equals a given value at M_{design} using the highest possible pressure recovery factor ($p_{02}/p_{0\infty}$). For the last step of the design routine, inlet ramp lengths are selected so that certain types of shock interactions do not occur when the Mach number is between $M_{\min}$ and $M_{\max}$.

When an inlet is operating outside its design range ($M \notin [M_{\min}, M_{\max}]$), various adverse
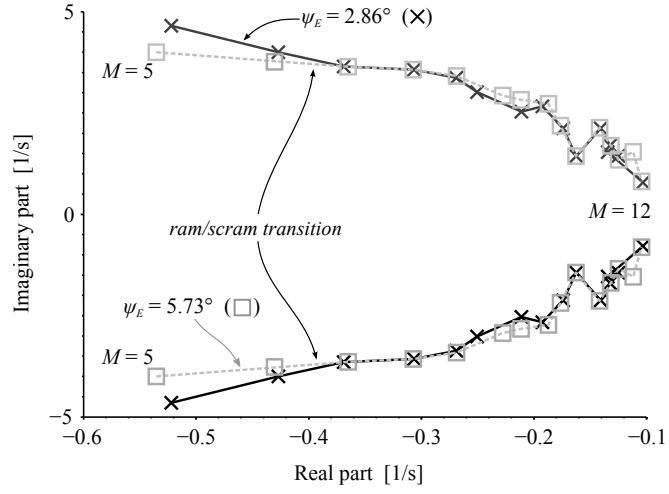
(a) Short-period modes.
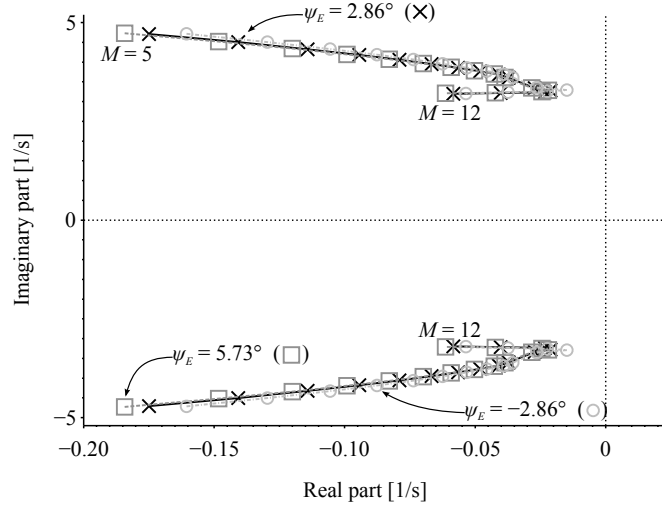
(b) Dutch-roll modes.

Figure 6.5: Plot of poles of linearized dynamics for MAX-1 (ψ_E=2.86°), and two other values of dihedral angle (ψ_E=5.83° and ψ_E=−2.86°).
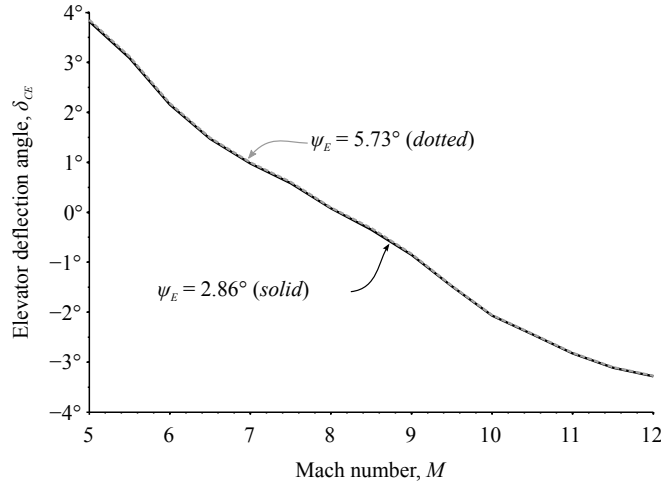
Figure 6.6: Elevator angle (δ_{CE}) for MAX-1 (ψ_E=2.86°), and two other values of dihedral angle (ψ_E=5.83° and ψ_E=−2.86°).

effects are predicted due to strong shock interactions, and some of these have been shown to affect the overall performance of the vehicle [161]. However, the direct effect on fuel consumption has not been studied. In addition, there is a tradeoff between the size of the design envelope (i.e., M_{range}) and the peak performance [131]. The trajectory used here, which accelerates from Mach 5 to Mach 12, has a large range of Mach number that goes both below and above the MAX-1 design range of Mach 7 to Mach 11. The object of this section is to investigate how operating outside the design range affects performance and stability. In particular, it seeks to answer how wide the design envelope should be compared to the trajectory and whether the inlet should be designed for the lower Mach numbers in the trajectory range or the higher Mach numbers. However, effects that are not considered here (in particular, boundary layer separation) may narrow the range over which the inlet delivers satisfactory performance.

Figure 6.7 shows the short-period and Dutch-roll poles for ($M_{min} = 7, M_{max} = 11$) with a vehicle designed for lower Mach numbers but with the same design envelope size ($M_{min} = 6, M_{max} = 10$). As shown in Fig. 6.8(a), this design change has very little effect on the short-period mode. Increasing the design Mach number appears to be slightly destabilizing for this mode, but this may be a result of the higher compression ratio that results from the way the inlets were designed. Namely, both inlets were designed to have a compression ratio (the ratio of static pressure at the end of the inlet to the freestream static pressure) of 70 at M_{design}. As a result, MAX-1 has a lower compression ratio at Mach 8 than the other design. The Dutch-roll mode, as shown in Fig. 6.7(b), is slightly more stable for the inlet designed for higher Mach numbers.

117
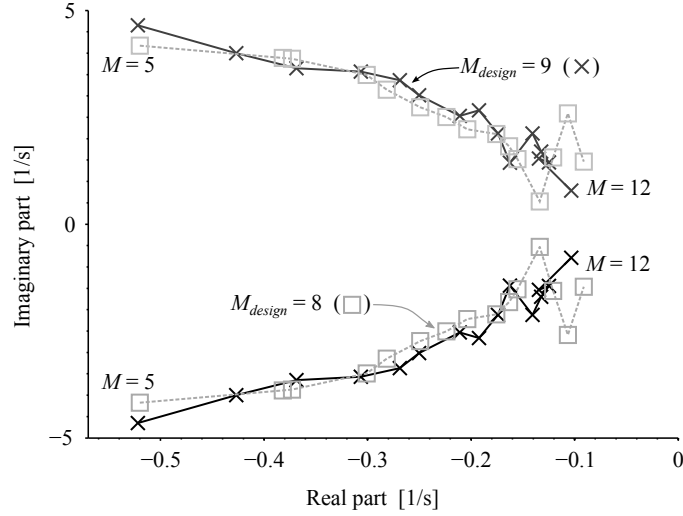
(a) Short-period modes.
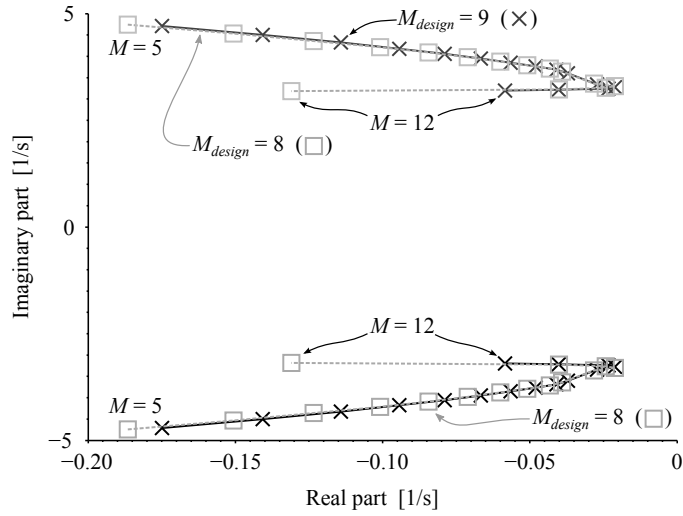
(b) Dutch-roll modes.

Figure 6.7: Plot of poles of linearized dynamics for MAX-1 (M_{design}=9) and an otherwise identical vehicle with a lower design Mach number (M_{design}=8).

The results shown in Fig. 6.8 compare MAX-1 to a vehicle with an inlet designed for a narrower range of Mach numbers ($M_{min} = 8, M_{max} = 10$). The description of these results is strikingly similar to those of the previous paragraph. The primary difference is that the poles get somewhat more chaotic at the higher Mach numbers for the inlet designed for a narrower range of conditions. This is not surprising in that the inlet has a lower upper bound for the design range than the other designs, but it is perhaps surprising that the apparent randomness is noticeable for the case where $M_{max} = 10$ but not for the case that $M_{max} = 11$. In both cases, the shock from the second external ramp goes inside the inlet,
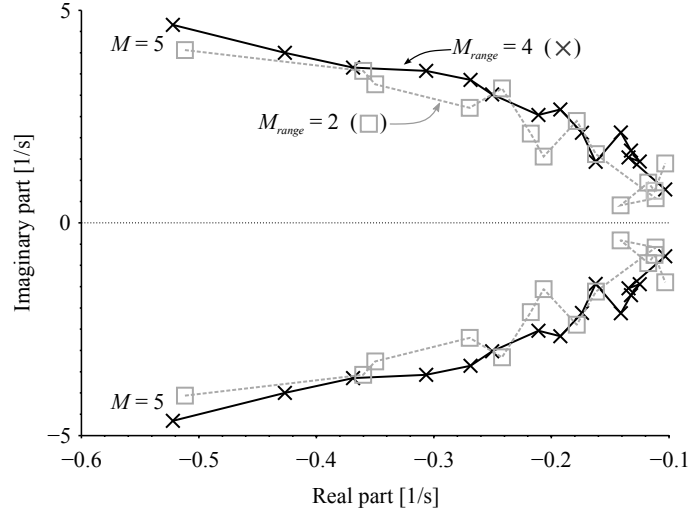
(a) Short-period modes.
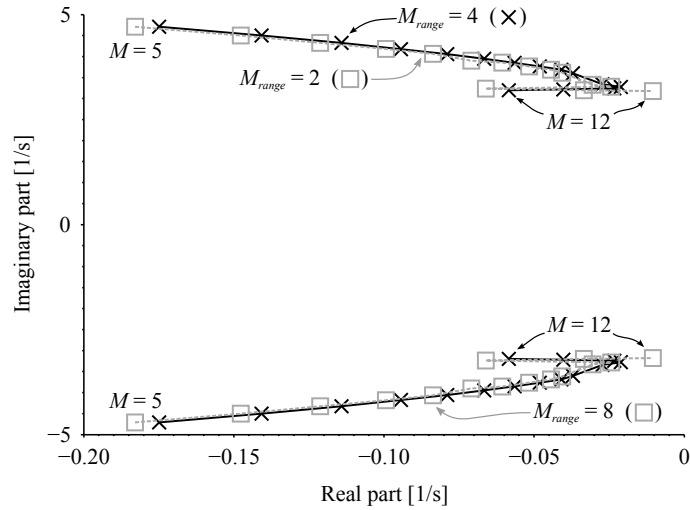
(b) Dutch-roll modes.

Figure 6.8: Plot of poles of linearized dynamics for MAX-1 (M_{range}=4) and an otherwise identical vehicle with a lower design Mach number (M_{range}=2).

but there are more shock interactions that result in the case of the $M_{range} = 2$ design.

The result can be explained in terms of actual inlet conditions and design conditions. The inlet is specified to avoid the worst shock interactions for a rectangular area in Mach number/angle of attack space. Since the design algorithm does this by satisfying constraints at the corners of this rectangle, the actual flight envelope might include a wider range of conditions. The sketch in Fig. 6.9 gives an example of how this works. In fact, only two of the four corners of the design envelope (shown in darker gray in Fig. 6.9) are actively constrained. Near the other two corners, shock interactions might not occur for a range of
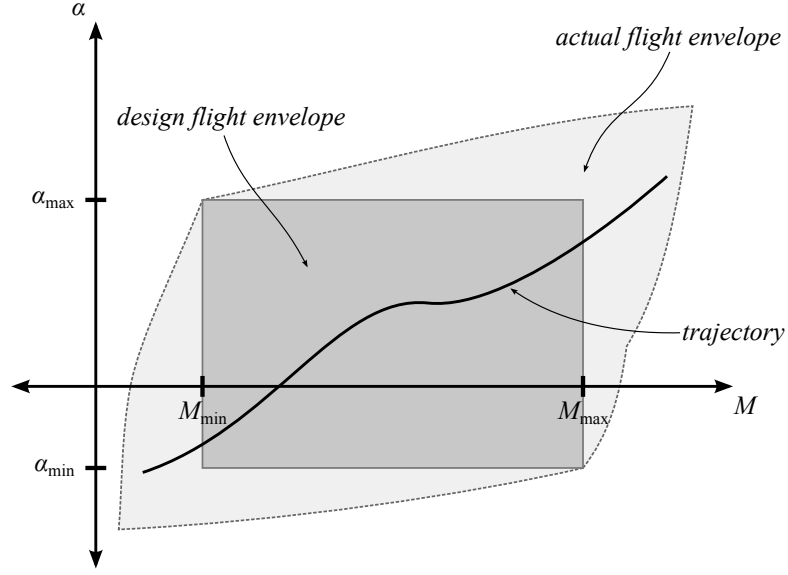
Figure 6.9: Sketch of inlet design conditions (darker gray rectangle) and envelope determined by shock interaction constraints (lighter gray).

flight conditions outside the design set. In short, the inlet design methodology specifies where shock interactions must not occur; it does not imply that the deleterious interactions occur for all conditions outside the design rectangle. Finally, the example trajectory in Fig. 6.9 (solid black curve) shows an example of a trajectory that goes outside the design range of conditions yet does not experience strong shock interactions. This appears to be the case for MAX-1 flying along the trajectory used in this work, but the alternative design ($M_{range} = 2$) does go outside the actual envelope.

6.2.5   Inlet Compression Ratio

Apart from the design range of flight conditions discussed in the previous subsection, another inlet design variable is the compression ratio of the inlet. The compression ratio, r_p, is the ratio of the static pressure at the end of the inlet (p_2) to the freestream static pressure (p_∞) when the vehicle is flying at a Mach number equal to M_{design}. Altering the compression ratio is accomplished by changing the deflection angles of each shock, and a side effect is that the height of the inlet exit decreases with a higher inlet compression ratio. The effect on combustion and thrust of increasing the inlet compression beyond the minimum level is not fully understood.

Figure 6.10 shows the effect of increasing r_p on the short-period and Dutch-roll modes. The short-period mode shows relatively small changes with no recognizable pattern. The
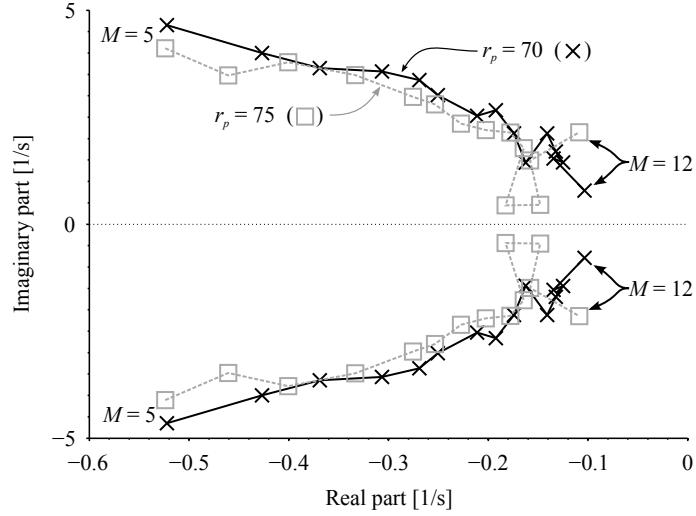
(a) Short-period modes.
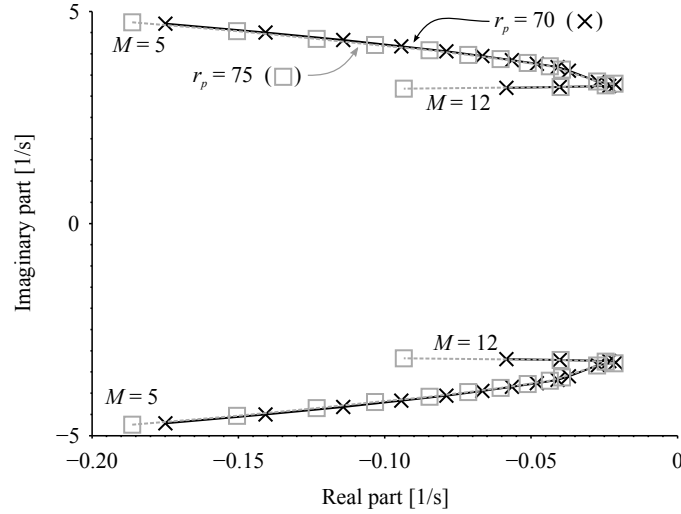
(b) Dutch-roll modes.

Figure 6.10: Plot of poles of linearized dynamics for MAX-1 (r_p=70) and an otherwise identical vehicle with a higher inlet compression ratio (r_p=75).

Dutch-roll poles in Fig. 6.10(b) show a consistently stabilizing effect from increasing r_p, which is caused by a decrease in the trim angle of attack. The decreased angle of attack is also probably responsible for the neutral effect on the short-period mode, because the increased pressure on the surface of the inlet would be expected to shift the center of pressure forward and thus destabilize the longitudinal dynamics. This also explains why the trim angle of attack decreases; the raised pressure on the inlet surface would tend to increase the lift coefficient, so there must be some other change to keep the lift coefficient unchanged.
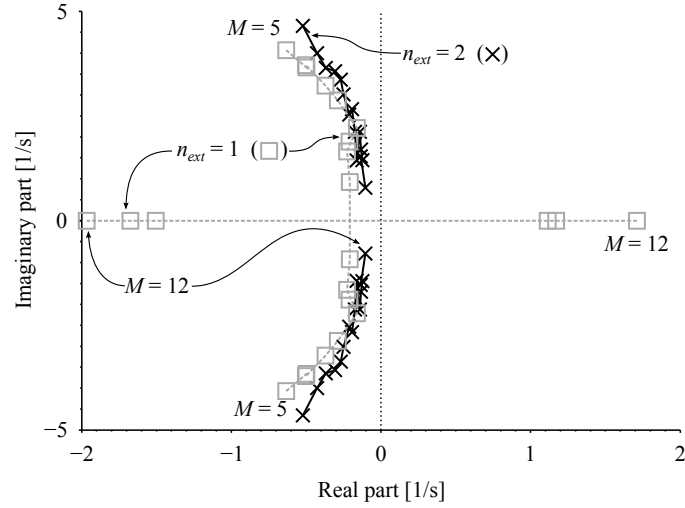
(a) Short-period modes.
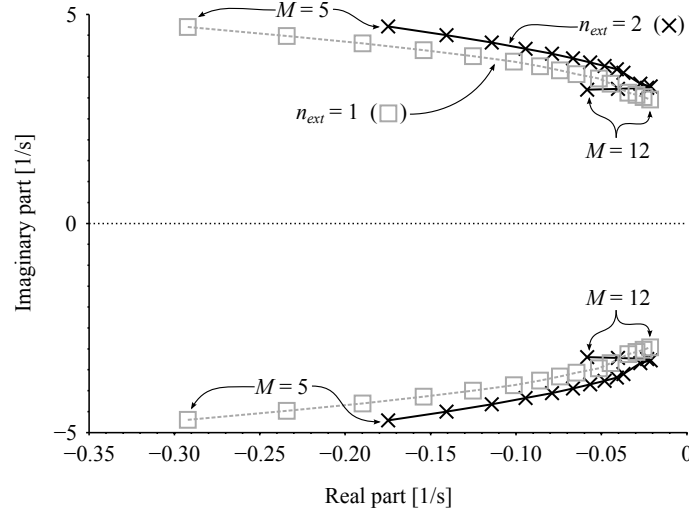
(b) Dutch-roll modes.

Figure 6.11: Linearized dynamics for MAX-1 (n_{ext}=1) and a vehicle with one external ramp (n_{ext}=1).

6.2.6 Number of Inlet Ramps

Two design variables that have a very important effect on performance is the number of internal and external inlet ramps. The baseline MAX-1 vehicle has two external ramps (n_{ext} = 2) and two internal turns (n_{int} = 2). These variables are different from the other design parameters in that they are not continuous. As such changes to these design variables do not result in "sensitivities," but understanding the effects of these variables is quite important.

Figure 6.11 shows the short-period and Dutch-roll modes for a vehicle in which the

number of external inlet shocks has been reduced to 1 ($n_{ext} = 1$) from the default value of 2. Both Chavez and Schmidt [8] and Bolender and Doman [9] analyzed a vehicle with a single external ramp, so the results here are useful for comparison. It should be noted that other combinations of number of inlet shock did not result in a vehicle that could be trimmed throughout the baseline trajectory.

The stronger pressure near the nose of the vehicle for a single-external-ramp vehicle should destabilize the vehicle because it moves the center of pressure forward. In Fig. 6.11(a), it can be seen that the short-period mode transitions to unstable between Mach 10.5 and 11. Both the low-speed short-period modes and all the Dutch-roll modes actually increased in stability margin. The cause is that the single-ramp design has a dramatically lower angle of attack (a difference of about 2° at each Mach number), which counteracts the forward shift of the center of pressure.

6.2.7   Conclusions from Stability Analysis

Throughout the stability analysis, it was found that for many design variables (r_f, r_p, M_{design}, M_{range}, α_{range}), the primary effect was to change the trimmed angle of attack. Perturbations that increased the lift of the vehicle tended to decrease the trim angle of attack, which had a stabilizing influence. Conversely, adding mass to the vehicle increased the trim angle of attack, which had a destabilizing influence.

Not surprisingly, it was found that shifting the center of gravity has a significant impact on stability. In addition, the expected result was confirmed that changing the dihedral angle affects lateral-directional stability without having much impact on any other trim variables or the longitudinal stability. Finally, it was found that changing inlet to have only one external ramp shifted the center of pressure forward dramatically. Such a change to the vehicle design is highly unfavorable because it both destabilizes the vehicle and increases fuel requirements, as will be shown in the next section.

6.2.8   Performance

This subsection investigates the effects of the various alterations to the design of MAX-1 on the trim variables and fuel consumption throughout the trajectory. In addition to most of the design perturbations discussed in Secs. 6.2.1–6.2.6, an additional design with a limited range of design angle of attack is considered here. The MAX-1 vehicle has an inlet designed using

$$\alpha_{\min} = -0.5° \qquad\qquad \alpha_{\max} = +1.0°$$
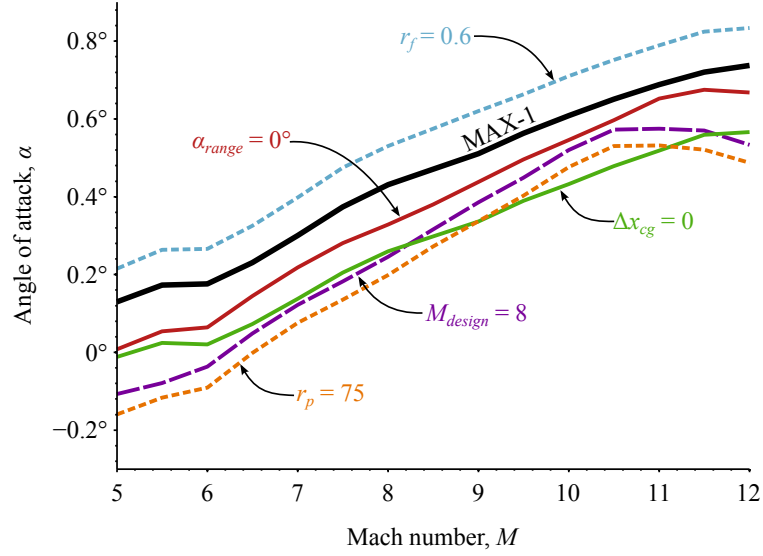
Figure 6.12: Trim angle of attack for several vehicle designs and an accelerating trajectory.

so $\alpha_{range} = 1.5°$. A contrasting design with $\alpha_{min} = \alpha_{max} = 0°$ (or $\alpha_{range} = 0°$.) is considered here. The effect should be similar to decreasing the range of design Mach numbers (M_{range}), but there may also be differences. Finally, a comparison of the total fuel consumption for the trajectory is given for all of the designs, and these results are used to determine which design parameters should be used for a first design optimization study.

The first of the three trim variables plotted is the angle of attack in Fig. 6.12. The angle of attack for the single-ramp inlet is between $-2°$ and $-1°$ and is not shown in Fig. 6.12. One of the most notable results is that the vehicle with an increased mass, labeled $r_f = 0.6$, has a mostly uniform increase in the angle of attack. All of the other design alterations lower the trim angle of attack. A decrease in the angle of attack tends to decrease drag and increase stability, so the angle of attack is a very important parameter for understanding vehicle performance. A consequence of this trend is that features normally associated with poor performance, shock interactions, could indirectly cause a net decrease in fuel consumption by lowering the trim angle of attack.

Figure 6.13 shows the rate of fuel consumption ($\dot{m}_f$) for the various vehicle designs at each point along the trajectory. The heavier vehicle ($r_f = 0.6$) requires extra fuel compared to the other vehicles, which is an expected result, and the single-ramp design ($n_{ext} = 1$) requires even more fuel than that. The remaining designs have similar fuel requirements, and this is especially true at the lower Mach numbers. The differences are more pronounced at higher Mach numbers. As explained before, many of the trends in Fig. 6.13 can be explained in terms of angle of attack. All of the designs except for the single-ramp vehicle
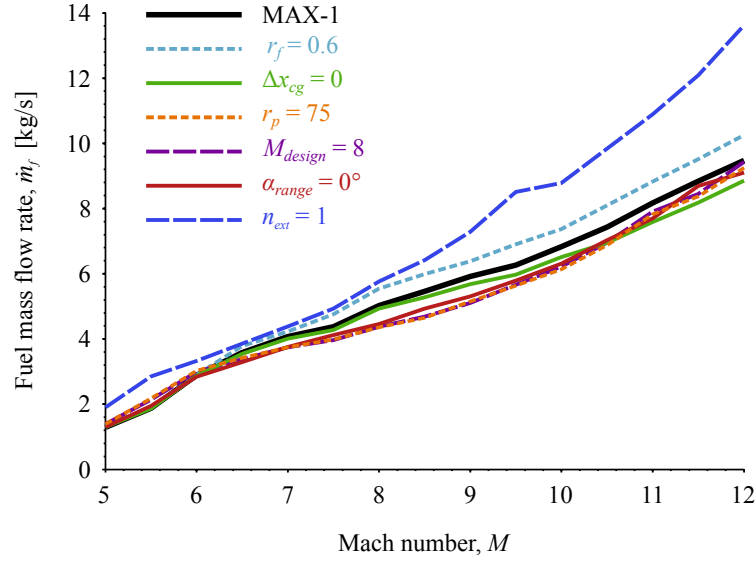
Figure 6.13: Fuel mass flow rate for several vehicle designs and an accelerating trajectory.

have very similar geometry, and so the angle of attack is the primary variable that changes the drag on the vehicle.

The cause of the reduced fuel consumption of the $\alpha_{range} = 0°$ vehicle is the tradeoff between the size of the design envelope and peak performance initially reported in [131]. The trajectory for the $\alpha_{range} = 0°$ vehicle shown in Fig. 6.12 does not have any points within the design envelope ($7 \leq M \leq 11$, $\alpha = 0°$), but performance is not degraded by strong shock interactions due to the phenomenon demonstrated in Fig. 6.9. This means at least two things about the inlet design. Since the actual high-performance envelope is much larger than the design envelope, it is difficult to know what values of M_{min}, M_{max}, α_{min}, and α_{max} are most appropriate for a given trajectory. Second, it seems that some of the shock interactions that the inlet design algorithm of [150] seeks to prevent do not have much adverse impact on overall vehicle performance.

The vehicle with a single-ramp inlet has the highest fuel consumption at all of the flight conditions along the trajectory. Because the bow shock at the leading edge of the vehicle must be much stronger for a single-ramp inlet, the drag coefficient is higher, and the fuel increase is notable despite the sizable decrease in angle of attack.

In the case of the shifted center of gravity ($\Delta x_{cg} = 0$), fuel savings comes at the expense of decreased stability. That strategy is somewhat problematic as Fig. 6.2(a) shows that this change in the center of gravity makes the short-period mode unstable throughout the trajectory. To make matters worse, there is a non-minimum phase zero in the longitudinal dynamics that interferes with the possibility of controlling the unstable short-period mode
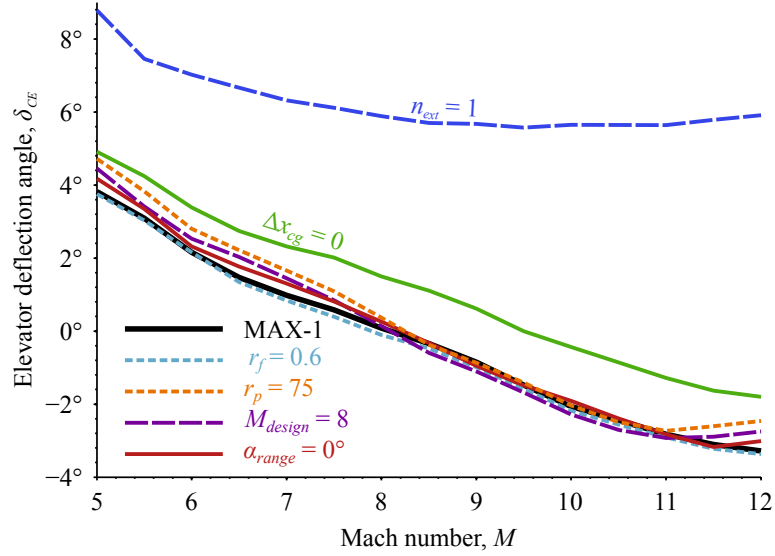
Figure 6.14: Trim elevator deflection angle for several vehicle designs.

(see Fig. 4.5).

Using the velocity flight path angle (γ) and the total velocity (V) as outputs, this non-minimum-phase zero results from the actions needed to increase the altitude of the vehicle. To increase altitude, the vehicle must pitch up, but to do that it must deflect the elevator trailing edges up, which decreases lift and causes a momentary decrease in altitude. At Mach 5, the short-period pole is 0.63 while the zero is at 5.49, which is plenty of separation. However, by Mach 12, the pole has moved to 3.42 while the zero is at 4.06. This indicates that a vehicle configuration in which the center of gravity shifts forward as fuel is used may be ideal. Using ballast in the nose will have this effect; as the fuel is burned and the mass of the vehicle decreases, the fixed-mass ballast will become a larger percentage of the mass of the vehicle so that the center of mass shifts forward.

In most cases, any design change that decreases the trim angle of attack both decreases fuel consumption and stabilizes the vehicle. This indicates that lighter vehicles and vehicles that get more lift from the inlet tend to have superior performance in terms of both stability and fuel consumption. However, it should be noted that this analysis has considered only a fixed trajectory with a constant acceleration. In reality, an air-breathing hypersonic vehicle would also be able to choose an acceleration at each Mach number. As a result, a change that reduces fuel consumption when the acceleration is 2 m/s^2 may result in a lower maximum acceleration in such a way that increases the fuel consumption after trajectory optimization has been performed.

The plots of elevator deflection angle (δ_{CE}) in Fig. 6.14 show that most of the design

Table 6.1: Trajectory fuel consumption and efficiency for several vehicle designs.

Vehicle	Initial mass	Initial fuel mass	Fuel used	Trajectory I_{sp}
MAX-1	30355 kg	11610 kg	5881 kg	1021 s
$r_f = 0.6$	32677 kg	13932 kg	6349 kg	1017 s
$\Delta x_{cg} = 0$	30355 kg	11610 kg	5617 kg	1074 s
$\Delta x_{cg} = 0.025$	30355 kg	11610 kg	5617 kg	1041 s
$r_p = 75$	30246 kg	11569 kg	5462 kg	1103 s
$M_{design} = 8$	30434 kg	11400 kg	5500 kg	1102 s
$M_{range} = 2$	30213 kg	11556 kg	5347 kg	1128 s
$\alpha_{range} = 0°$	30844 kg	11797 kg	5517 kg	1115 s
$\psi_E = 5.73°$	30355 kg	11610 kg	5872 kg	1022 s
$n_{ext} = 1$	37204 kg	14230 kg	8081 kg	897 s

alterations do not have much effect on the trimmed elevator deflection angle. The two exceptions are the shifted center of gravity ($\Delta x_{cg} = 0$), which causes a change of about $+2°$ throughout the trajectory, and the single-ramp inlet, which causes a much larger positive change. This matches expectations because the shift in position causes a direct change in the net moment about the center of gravity, and a constant shift in the elevator deflection would be expected to cancel the change in moment. Also, the single-ramp inlet moves the center of pressure forward substantially because the entire underside of the inlet experiences a high surface pressure rather than just the second half as is the case when $n_{ext} = 2$. Adding lift near the nose of the vehicle has a very significant effect on the net moment on the vehicle, so a large elevator deflection is needed to counter it. Also, this large increase in elevator deflection is a contributor to the higher fuel consumption for the single-ramp inlet vehicle due to higher trim drag.

Table 6.1 gives a summary of the mass properties and total fuel usage of each of the vehicle designs from this section. Several of the vehicles have a slightly different mass from the baseline MAX-1 design because the correlations used by the MASTrim model to estimate the mass of a vehicle and the amount of fuel it can carry depend on the exact size (volume) of the vehicle. Because of these differences in mass, the total mass of fuel consumed along the trajectory may not be the most objective measure of efficiency. Instead, the trajectory specific impulse of Eq. (6.13) is probably a more effective measure, and both numbers are reported in Table 6.1.

The results show that the heavier vehicle uses substantially more fuel but almost as efficiently as MAX-1 in terms of mass ratios. The most effective changes to the rocket-equivalent specific impulse were those that narrowed the range of the inlet design flight envelope ($M_{range} = 2$ and $\alpha_{range} = 0°$), and the design Mach number (M_{design}) was also
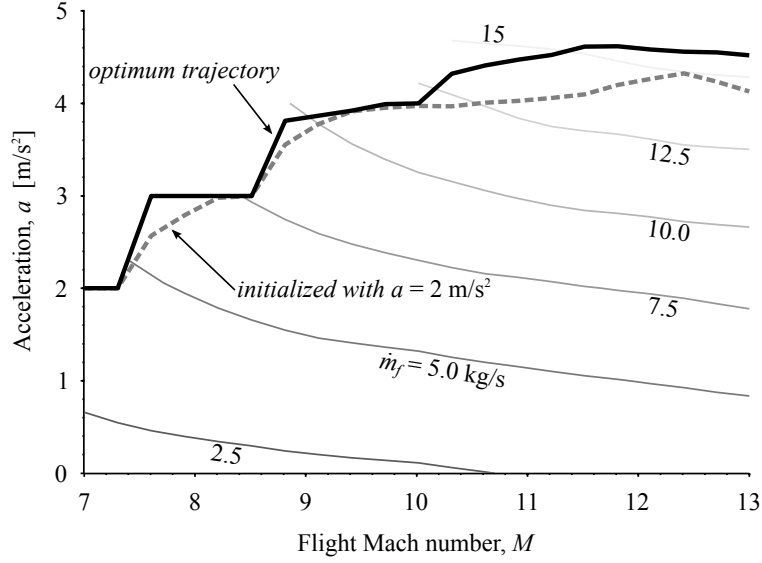
Figure 6.15: Minimum-fuel trajectory and fuel mass flow rate contours (q=100 kPa).

an effective parameter. Because α_{range} and M_{range} are such similar parameters, the two variables selected for the design study in Sec. 6.4 were M_{design} and M_{range}.

6.3 Trajectory Optimization

This section takes an approach that is complementary to Sec. 6.2. Instead of using a fixed trajectory and perturbing the vehicle design, a fixed vehicle design is applied, and the trajectory is optimized. In this section and the one that follows, the acceleration trajectory is from Mach 7 to Mach 13. These conditions were selected so that the flight conditions could be limited to the scram-mode.

Several interesting challenges are introduced by the ram-to-scram transition problem, including the abrupt change in thrust discussed in Sec. 5.4.3, but the topic of trajectories that go through this transition are left to future work.

Like in Sec. 6.2, the dynamic pressure is held fixed, although the optimization is repeated for several different (fixed) values of the dynamic pressure. The trajectory optimization problem, then, becomes a matter of selecting the acceleration (a) at each point along the trajectory, and the techniques discussed in Sec. 6.3 can be applied.

The rule of thumb usually used for design of a minimum-fuel trajectory is to select the highest dynamic pressure that the structure can withstand because higher dynamic pressure is favorable for the engine [11]. In Chapter 4, we showed that an increase in the dynamic pressure does not always reduce the fuel consumption required to maintain steady, level

128

flight, but the maximum pressure is increases. As a result, for a problem such as this in which the optimum acceleration will be different for each dynamic pressure, the highest dynamic pressure is indeed best. The optimization study is repeated for three different dynamic pressure to illustrate this point.

6.3.1   Minimum-Fuel Acceleration Profile

Figure 6.15 shows the optimum acceleration profile for the MAX-1 vehicle flying at a constant dynamic pressure of $q = 100$ kPa starting with full fuel tanks at Mach 7. The results show that the optimum trajectory nearly exactly follows the maximum acceleration, as expected from Sec. 6.3. To understand what constrains the maximum acceleration for each flight condition and what causes the optimum acceleration to be sometimes lower than the maximum, we look at the equivalence ratio (*ER*) and exhaust oxygen mass fraction ($Y_{O_2,5}$).

The equivalence ratio in Fig. 6.16(a) starts below 1.0 at Mach 7 and then increases throughout the trajectory until the equivalence ratio is nearly 2.5 at Mach 13. Many hypersonic trajectory studies [91, 92] assume that the optimum equivalence ratio is 1.0, but there are two reasons that might not be true. The first case is if an equivalence ratio of 1.0 would thermally choke the flow, as is the case in this trajectory from Mach 7 to Mach 8.

The second reason is essentially that not all of the fuel burns. The equivalence ratio is defined as the ratio of fuel mass flow rate injected into the combustor to the largest mass rate of fuel that could possibly burn given the oxygen available. The equivalence ratio in Fig. 6.16(a) goes notably higher than unity, which means that more fuel is being injected than could possibly burn in the combustor due to the stoichiometric limit. Because not all the fuel burns, the amount of fuel that burns is lower than the stoichiometric limit and much of the fuel remains unburned in the exhaust. This means that the molecular weight of the fuel can also affect thrust; a lighter fuel such as hydrogen will tend to have more thrust in this case because lower molecular weights increase the speed of sound.

A simple parameter that indicates how much more fuel can be burned is the mass fraction of molecular oxygen in the combustor exhaust ($Y_{O_2,5}$). If there is no oxygen available in the combustor exhaust, then it is not possible to burn more fuel, and this condition determines the maximum acceleration for cases where the maximum acceleration is not determined by thermal choking.

Looking at Figs. 6.16(a) and 6.16(b), one can see that the combustion is efficient (i.e. burns most of the fuel) at lower Mach numbers but quite inefficient at higher Mach numbers. For instance, at Mach 9 with $a = 3$ m/s^2, the equivalence ratio is about 1.0, and
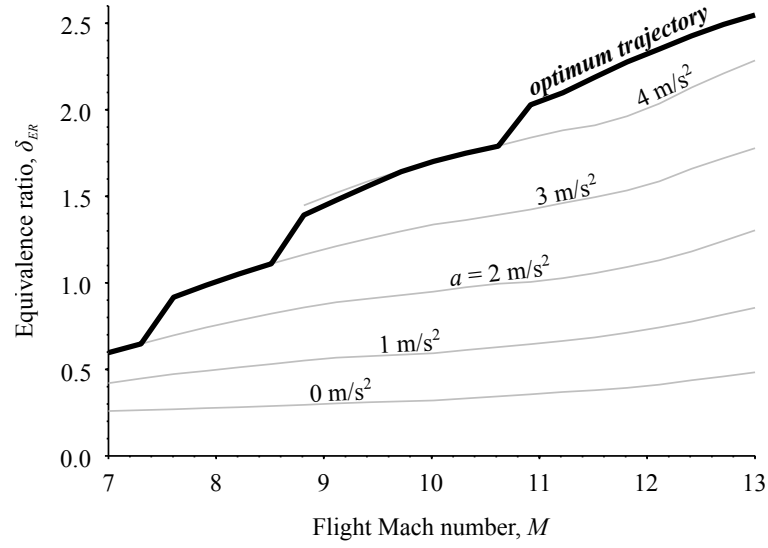
(a) Equivalence ratio (*ER*).
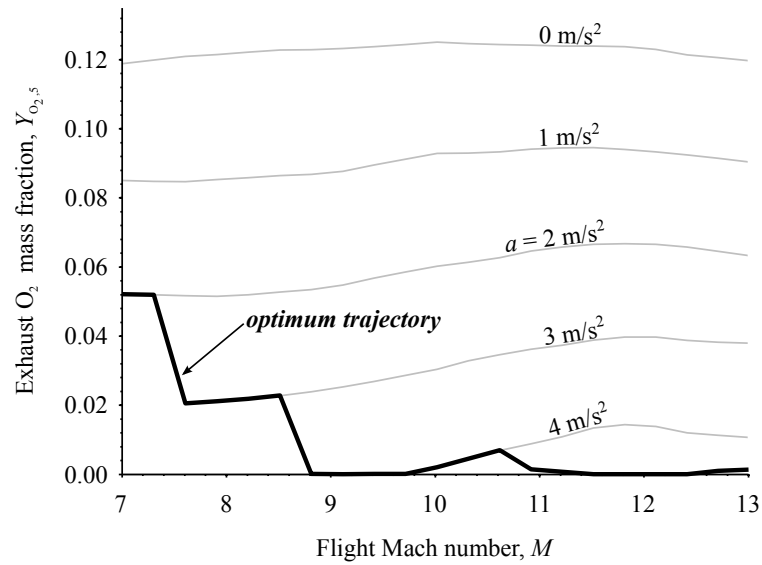
(b) Combustor exhaust O_2 mass fraction ($Y_{O_2,5}$).

Figure 6.16: State variables along minimum-fuel trajectory and constant-acceleration trajectories.

the mass fraction of oxygen remaining is 0.02, which indicates a combustion efficiency of about 90%. At Mach 13 with an $a = 3$ m/s^2, the equivalence ratio is about 1.6 while there is still O_2 remaining (a mass fraction of about 0.035).

For flight conditions with the Mach number below $M = 10$, there were no accelerations in the flight envelope that satisfied the discrete optimality condition from Eq. (6.18), and the maximum acceleration was selected. At the higher Mach numbers, the optimality condition is sometimes met slightly below the maximum acceleration, which can be explained in terms of the example in Fig. 6.1.

At zero acceleration, there is a positive amount of fuel consumption that is needed to trim the forces on the vehicle, and so the right-hand side, $\dot{m}_{f,i}/a_i$, is infinite. As the acceleration is increased, it reaches a point where it can no longer increase, and so the term $\partial \dot{m}_{f,i}/\partial a_i$ goes to infinity. This corresponds to the vertical portion of the curve in Fig. 6.1(b). Somewhere in between, assuming that $\dot{m}_{f,i}$ is a smooth function of a_i, these two terms ($\dot{m}_{f,i}/a_i$ and $\partial \dot{m}_{f,i}/\partial a_i$) will meet, and this will usually occurs slightly below the maximum acceleration.

This will not be the case if $\partial \dot{m}_{f,i}/\partial a_i$ is not smooth or does not go to infinity near the maximum acceleration. For example, if the acceleration increases linearly with fuel consumption until the equivalence ratio is unity and then the acceleration is constant above that point, Eq. (6.18) is not satisfied by any value of a_i, and the optimum acceleration will be exactly at the maximum acceleration. Similarly, if adding more fuel at the maximum acceleration would cause more heat release in the engine but also thermally choke the flow, the optimum will also be at the maximum acceleration.

In Fig. 6.16, it can be seen that both types of optimality conditions are used. For the lower Mach numbers, the maximum acceleration is limited by thermal choking, which causes the situation to look like Fig. 6.1(a), and the maximum acceleration is optimal. At the higher Mach numbers, the maximum acceleration is limited by the oxygen available in the engine, which causes the situation to look like Fig. 6.1(b) and leads to an optimum slightly below the maximum acceleration. As it turns out, this can be used as a general rule for selecting the optimum acceleration profile, and it is applicable to a wide variety of ascent trajectories.

6.3.2 Effect of Dynamic Pressure

Figure 6.17 shows the optimized trajectories for dynamic pressures of 50 kPa and 75 Pa. The MAX-1 vehicle does not perform well at a dynamic pressure of 50 kPa. In fact, it was not possible to trim the vehicle with a positive acceleration with full fuel tanks, so the
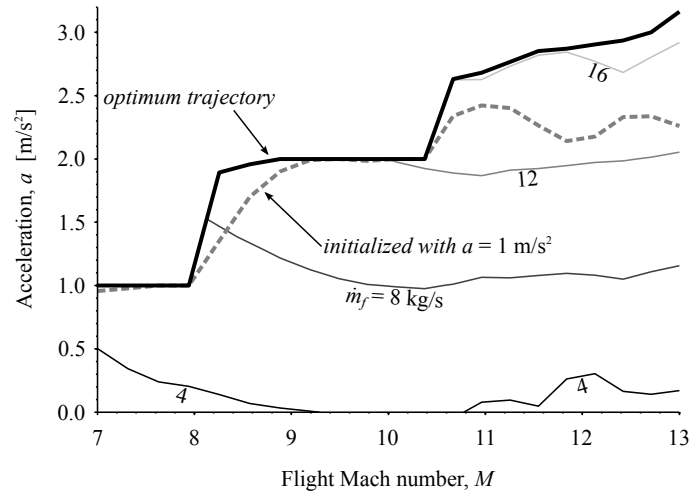
(a) Lowest dynamic pressure, $q = 50$ kPa.
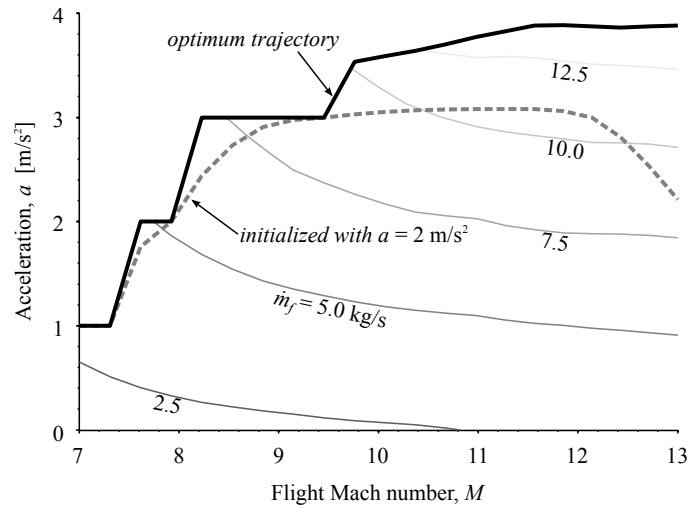
(b) Intermediate dynamic pressure, $q = 75$ kPa.

Figure 6.17: Minimum-fuel trajectories for two different dynamic pressures with contours of the fuel mass flow rate. Optimization result initialized with a low acceleration shown by dotted curve.

trajectories in Fig. 6.17(a) assume that the fuel tanks are only 70% full at Mach 7. This was the highest vehicle mass for which an acceleration of at least 1 m/s^2 could be maintained in scram mode, and incidentally may be a more realistic starting condition for Mach 7.

The primary difference among the three values for dynamic pressure is that the vehicle can accelerate faster at higher dynamic pressures. There are two main reasons for this. For a fixed vehicle mass, a lower dynamic pressure means that a higher lift coefficient is needed to satisfy trim. The result is a higher drag coefficient, and thus a lower maximum

acceleration.

The thrust is also affected by dynamic pressure. Increasing the dynamic pressure also implies an increase in the freestream pressure and thus the static pressure in the combustor. Although higher pressures are usually helpful for combustion, high densities can inhibit fuel-air mixing, and the lower trim angle of attack associated with high dynamic pressure decreases the mass flow into the engine. The result is that there is usually an ideal dynamic pressure even without considering structural or heating constraints.

The second reason that the maximum acceleration is lower for lower dynamic pressures is that the net force on the vehicle is basically proportional to the dynamic pressure. The acceleration of the vehicle is given approximately by

$$ma \approx qS\left(C_T - C_D\right) \tag{6.23}$$

where C_T is the thrust coefficient and S is a reference area. The previous argument showed that C_D increases when q decreases, and so a higher thrust coefficient is needed. If thrust is greater than drag, a fixed value of C_T-C_D results in a lower acceleration for a lower value of q. So even if the thrust and drag coefficients were unaffected by dynamic pressure, we would expect a higher maximum acceleration at higher dynamic pressures.

In Figs. 6.13 and 6.17, a dotted curve is shown in addition to the thick black optimum acceleration curve. This dotted gray curve represents the result of applying direct optimization to the trajectory starting with an initial condition of $a = 2$ m/s^2 throughout the trajectory. In all three cases, this failed to converge to the true optimum, although in some cases it did better than others. In this work, the trajectory was checked for optimality using Eq. (6.18), but a simple solution that should always give good results is to initialize with a maximum-acceleration trajectory.

6.3.3 Sensitivity of Total Fuel Consumption to Acceleration Profile

To see how much the choice of trajectory affects the total fuel consumption, Table 6.2 gives a comparison of the minimum-fuel trajectories and several constant-acceleration trajectories for four dynamic pressures. A dynamic pressure of 125 kPa is included to show the effect on the engine of further dynamic pressure increases outside the flight corridor.

As mentioned in the previous discussion, the MAX-1 vehicle was not able to sustain a positive acceleration with full fuel tanks for the q=50 kPa case, so those trajectories are initialized with the tanks 70% full. This causes a drag reduction compared to the other trajectories because the vehicle is lighter, and this is the reason that the q=50 kPa fuel consumption numbers are lower than the q=75 kPa numbers.

Table 6.2: Fuel usage for several trajectories at four dynamic pressures.

Trajectory	50 kPa[a]	75 kPa	100 kPa	125 kPa
minimum fuel	5654.1 kg[a]	6055.0 kg	5375.1 kg	5065.6 kg
maximum a	5654.1 kg[a]	6056.5 kg	5384.0 kg	5070.3 kg
$a = 1$ m/s^2	6794.3 kg[a]	7836.9 kg	7142.7 kg	7288.4 kg
$a = 2$ m/s^2	5772.2 kg[ab]	6424.1 kg[c]	5938.1 kg	5719.4 kg
$a = 3$ m/s^2	–	6049.1 kg[d]	5553.8 kg[c]	5311.7 kg
$a = 4$ m/s^2	–	–	5380.7 kg[e]	5162.4 kg[c]

[a]These trajectories are initialized 70% of the maximum fuel mass at Mach 7.
[b]Acceleration attained at $M = 8.5$. Lower accelerations used for lower Mach numbers.
[c]Acceleration attained at $M = 7.5$. Lower accelerations used for lower Mach numbers.
[d]Acceleration reached at $M = 9.0$.
[e]Acceleration reached at $M = 9.5$.

It is known that the trajectory design has a significant effect on the total fuel consumption because choosing a low acceleration causes the total fuel consumption to go to infinity. This can be seen from Eq. (6.17), for example. However, the effect of finding an optimized trajectory compared to a simpler choice such as a constant acceleration remains to be seen. As expected, increasing the dynamic pressure reduces the total fuel consumption, and a low acceleration of $a=1$ m/s^2 requires significantly more fuel than higher-acceleration trajectories. However, a further increase of the acceleration from 2 m/s^2 to 3 m/s^2 only reduces the fuel consumption a relatively small amount.

Table 6.2 also shows that the optimized trajectory saves very little fuel compared to the much simpler maximum-acceleration trajectory. For the lowest dynamic pressure, the optimized trajectory was the maximum-acceleration trajectory. This indicates that simply using the maximum acceleration is a good substitute for true trajectory optimization.

A maximum-acceleration trajectory has an equivalence ratio such that the Mach number at the end of the constant-area section is just above unity ($M_4 = 1$, see Fig. 3.2(b)) when the maximum acceleration is limited by thermal choking and an equivalence ratio so that the oxygen is almost completely burned ($Y_{O_2,5} = 0$) otherwise. Finding such a trajectory will still require preflight calculations because both of these quantities (M_4 and $Y_{O_2,5}$) are difficult to measure in flight.

The highest dynamic pressure ($q=125$ kPa) was included despite the fact that it is higher than the 100 kPa limit that is used here as a structural constraint. Interestingly, the fuel usage at $a=1$ m/s^2 is actually higher at a dynamic pressure of 125 kPa than it is at 100 kPa. This shows that even without structural constraints, the engine prefers a limited dynamic pressure at low accelerations. At higher accelerations, however, the effect of dynamic

pressure on Eq. (6.23) dominates, and a higher dynamic pressure is advantageous. The same effect also means that the maximum acceleration is higher, so indeed using the highest dynamic pressure allowed is a good choice for ascent trajectories.

6.4 Cooptimization of Inlet and Trajectory

Using the insight from Sec. 6.2, the two design variables selected for optimization were design Mach number (M_{design}) and the width of the design envelope (M_{range}). The set of design variables was kept small so that there could be a high degree of confidence of achieving an optimum result.

6.4.1 Optimization Methodology

A surrogate-optimization approach was employed for this work. Specifically, a list of design variables (M_{design} and M_{range}) was selected, and the minimum-fuel trajectory was calculated for each pair of parameters. In Fig. 6.18, these reference points are marked as purple dots. Simple spline interpolation is used for other points in the design space.

At each reference point, the trajectory optimization analysis of Sec. 6.3 is used to calculate the optimum acceleration profile. The reference trajectory has a constant dynamic pressure of $q = 100$ kPa and accelerates from Mach 7 to Mach 13. The trajectory optimization portion of the analysis plays an important role in determining the relative merits of each possible vehicle design. Total fuel consumption, which is defined in Eq. (6.17), is highly dependent on the acceleration profile, and each vehicle design will have a different optimum acceleration.

It was shown in Sec. 6.2.8 that changes to the two design variables considered in this optimization study both have a significant impact on the trajectory specific impulse (I_{sp}) even for a trajectory with a fixed acceleration, but another important consequence of changing the design is to raise or lower the maximum acceleration. When these two factors are considered simultaneously, the change in total fuel consumption may be even more pronounced than the examples shown in Table 6.1.

Once the optimum acceleration profile and resulting total fuel consumption were calculated for the 48 vehicle designs represented by purple dots in Fig. 6.18, it was realized that many of the vehicles could not successfully fly the ascent trajectory. For the vehicles in the lower left-hand region of the design space (low M_{design} and low M_{range}), the inlet simply would not operate at the higher Mach numbers. For these vehicle designs, contours of the maximum number at which the inlet operated (M_{upper}) are shown in red. Clearly this value
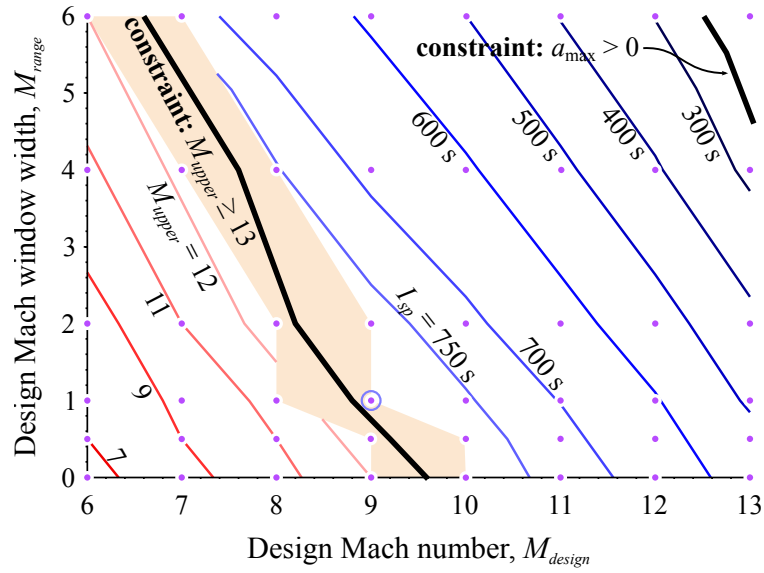
Figure 6.18: Contours of rocket-equivalent specific impulse (I_{sp}) in blue. Points used for surrogate are shown in purple, and contours of the maximum trim Mach number (M_{max}) are shown in red for designs that could not complete the trajectory. No information is available about the orange region. The optimum feasible design (M_{design}=9, M_{range}=1) is circled.
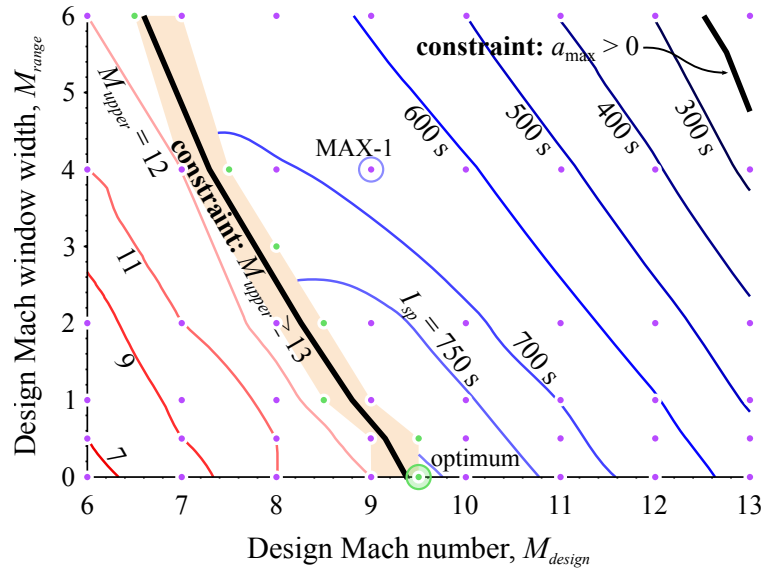
Figure 6.19: Contours of rocket-equivalent specific impulse (I_{sp}) in blue after several more points were added to the surrogate. Additional points used for surrogate are shown in green. The optimum feasible design (M_{design}=9.5, M_{range}=0) is circled.

MAX-1

Optimized design, $M_{design} = 9.5$, $M_{range} = 0$
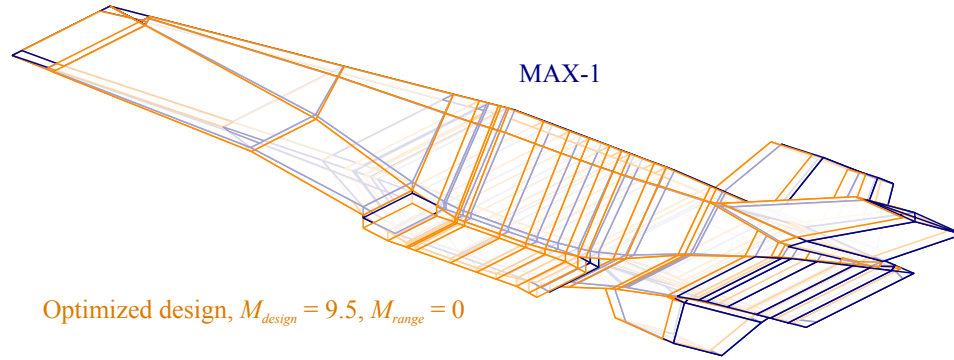
Figure 6.20: Optimized vehicle result overlayed with MAX-1.

must be at least 13, or the vehicle will not be able to fly the trajectory.

At the same time, the upper right corner of the design space ($M_{design} = 13$, $M_{range} = 6$) was also an infeasible design, although for a different reason. For that condition, the vehicle was not able to produce enough thrust to maintain positive acceleration at Mach 7 with full fuel tanks. Without a positive acceleration, there is no increase the Mach number, and so the design was infeasible.

From Fig. 6.18 it is clear that the highest-performing designs are near the lower left constraint (i.e. $M_{upper} \geq 13$). However, it is not possible to estimate the performance very close to the constraint due to the resolution of the surrogate. One option would be to use extrapolation and estimate the location of the boundary, but a more reliable approach would be to simply increase the resolution in the neighborhood of the constraint in question.

Figure 6.19 shows that by evaluating the optimum acceleration for only seven more designs (green dots), the uncertainty near the feasibility constraint was substantially reduced. The resulting optimum happens to be at the corner of two constraints, namely $M_{range} \geq 0$ and $M_{upper} \geq 13$, and the trajectory specific impulse has been increased from 687 s for MAX-1 ($M_{design} = 9$, $M_{range} = 4$) to 811 s for the resulting optimum vehicle ($M_{design} = 9.5$, $M_{range} = 0$).

6.4.2 Discussion

The importance of these two design variables, M_{design} and M_{range}, is demonstrated by Figs. 6.18 and 6.19. Not only did the analysis enable an 18% increase in the trajectory specific impulse, but it also showed that the performance could be far worse than the MAX-1 design.

Figures 6.20 and 6.21 show overlays of the baseline MAX-1 design with the result
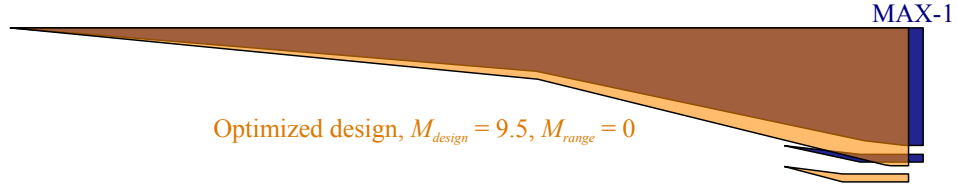
Figure 6.21: Comparison of MAX-1 and optimized inlet designs.
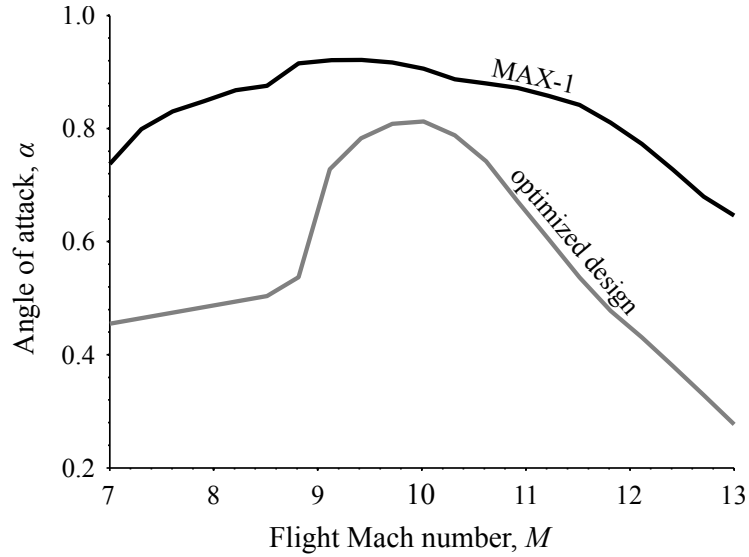
Figure 6.22: Angle of attack along optimized trajectory for MAX-1 and optimized vehicle.

from the trajectory-design cooptimization study. In Fig. 6.20, the two vehicles are difficult to distinguish except that the improved design is slightly thicker in the vertical direction. Since both of the design variables are inlet parameters, it is perhaps more informative to look at the comparison of inlet geometries in Fig. 6.21. Again the differences are relatively subtle, but the change in the vertical height of the inlet is more noticeable.

This is one demonstration of how important the inlet geometry can be for vehicle performance. Relatively small changes to the design resulted in an 18% improvement of the performance of the entire vehicle. Since the optimized result was near the constraint $M_{upper} \geq 13$, further changes in the same direction (i.e. making the inlet thicker in the vertical direction) would result in a vehicle that cannot fly the required trajectory. Further, changes in the nature of the trajectory would yield different vehicle designs.

It is a somewhat unexpected result that the optimum result was an inlet designed for a single Mach number in the middle of the trajectory Mach number range. However, the resulting design was not quite the single-condition design of [14] because it was still designed for a range of angle of attack ($-0.5° \leq \alpha \leq 1°$. This is a narrow range of conditions,

so it would be interesting to know if the design has the high sensitivities reported in [131] and discussed in Sec. 2.2.3 and Fig. 2.11.

Figure 6.22 shows the angle of attack along the optimized trajectories of MAX-1 (M_{design} = 9, M_{range} = 4) and the improved design (M_{design} = 9.5, M_{range} = 0). The optimized design does show more abrupt changes than MAX-1, but at least there is no point-like peak. Fig. 6.22 also appears to show the reason that the alternate design was preferred; although the inlet may be performing worse when considered in isolation, it is producing more lift and thus allowing the vehicle to fly at a lower angle of attack.

Considering a trajectory that includes ram-to-scram transition may lead to different conclusions. Even if a trajectory with a narrower range of Mach numbers (for example, Mach 4 to Mach 7) introduces an interesting aspect in that the design affects the Mach number at which transition occurs. A design that allows the vehicle to remain in the ram mode longer is likely to have lower total fuel consumption, but this may lead to very high surface temperatures in the combustor.

6.5   Conclusions

This chapter provided an incremental study of the effects of two types of decision variables (geometric parameters and trajectory variables) on the performance of an air-breathing hypersonic vehicle. By considering the two types of optimization first individually and then simultaneously, it was possible to uncover several important results.

It was found that small changes to the inlet design had a dramatic effect on total fuel consumption for an ascent trajectory. For the case considered, it was possible to reduce the fuel consumption by 14% (corresponding to an 18% increase in trajectory specific impulse) from the baseline MAX-1 design. Throughout the design space, the range of performance included infeasible designs, trajectory specific impulses as low as 280 s, and values as high as 810 s. Subtle changes to the design of a hypersonic vehicle can have very large effects on performance for an ascent trajectory.

The angle of attack was identified as an important factor in explaining the differences in performance, and as a result the inlet compression ratio (r_p), which was not used in the present optimization study, could increase performance by lowering the angle of attack without the negative side effects associated with designing the inlet for a narrow range of conditions.

It was found that the trajectory with minimum total fuel consumption is close to the maximum acceleration at all times, but the maximum acceleration was not found to be associated with a fuel-air equivalence ratio of unity. Instead, the maximum acceleration

corresponds to either the equivalence ratio that causes thermal choking or the equivalence ratio such that the available oxygen is consumed—whichever is lower.

Flying at a higher dynamic pressure leads to lower trim angle of attack, which lowers the drag coefficient and thus total fuel consumption for an ascent trajectory. Since acceleration is proportional to the dynamic pressure times the difference of the thrust and drag coefficients, dynamic pressure also raises the maximum acceleration, which is favorable for an ascent trajectory.

Perturbations to the MAX-1 design in several important design variables were also discussed. In most cases, there is a direct tradeoff between stability and fuel consumption. Finally, the sensitivity study identified the relative effectiveness of each design variables to reduce the fuel consumption for a fixed trajectory. Altering the mass of the vehicle proved to increase the fuel consumption as expected, but the trajectory specific impulse was almost unaffected. A fuel consumption is only modestly sensitive to the location of the center of mass, and inlet design variables were identified as the most effective parameters.

CHAPTER 7

Conclusions and Future Work

7.1 Summary

The figures and tables in this dissertation represent the results of approximately 650,000 tip-to-tail hypersonic vehicle simulations. Performing so many simulations in a reasonable time required the development of a model that could be evaluated with a single processor in a few seconds.

The development of such a model is a primary contribution of the present work. The SAMURI model was developed for two-dimensional supersonic flows, and it was used to model both the inlet and the nozzle. It marks an improvement to both simple algebraic models and the method of characteristics because of its ability to handle shocks, expansion waves, wave interactions, and boundary layer thickness.

A new ram-mode solver was created that furthers the understanding of dual-mode air-breathing propulsion systems. This model is a major contribution and captures the tight coupling between the isolator and combustor that occurs via the pre-combustion shock train and its associated pressure rise. The change in friction due to the presence of a separated boundary layer was a new contribution that led to the discovery of a potential thrust discontinuity at transition.

Next, a framework was described for discussion of the flight dynamics of the MAX-1 and related vehicles. The framework included the six-degree-of-freedom equations of motion for a rotating, ellipsoidal Earth model and a toolkit to trim the forces and moments on the vehicle to attain a desired climb rate, acceleration, and turn rate.

These equations of motion were then tied back to the ram-mode model through the phenomena of ram-scram transition and isolator unstart. Both occurrences were known phenomena from previous research, but the present work demonstrated progress in the form of relating these effects to the flight dynamics of the vehicle. For example, it was shown that increasing the acceleration tends to unstart the engine in the low-Mach region

of the ram-mode flight envelope, and it also tends to delay ram-scram transition to higher Mach numbers.

The final topic discussed in the main content of this dissertation was the sensitivity of performance to various decision variables. This included variables that affected the mass distribution of the vehicle, the inlet geometry, and parameters for the trajectory. For the variables that were considered, the results could largely be explained in terms of the acceleration and angle of attack. For the trajectory optimization, an approach was used that replaced time with velocity as the integration for the trajectory simulation, and this reduced the number of computations required.

The primary contributions of this work are listed below.

- Creation and implementation of two-dimensional supersonic flow solver (SAMURI)

    - New method of discretization for expansion fans

    - Inclusion of real-gas effects

    - General and fast Riemann solution for wave interactions

    - Implementation of automated SAMURI code

    - Validation against both CFD and experimental data

- Reduced-order model for isolator–combustor coupling in ram mode

- Constructed tip-to-tail vehicle code that has been distributed to several other collaborators in industry, government, and academic institutions

- Investigated ram-to-scram transition on the flight corridor map

- Investigated isolator unstart on the flight corridor map

- Identified effects of many changes to design variables on fuel consumption and stability

- Performed trajectory optimization to minimize fuel consumption and identified fuel-air mixing as a primary limiter on performance

- Introduced a framework for optimization simultaneously considering geometry design and trajectory design variables

7.2 Future Work

Several aspects of the present work have natural continuations that are both interesting and useful for future engineers. An extension to more diverse vehicle types is one such example. Including fuels other than hydrogen should be included to make the work more relevant to practical vehicles. A more detailed mass and structural model should be developed so that the interactions of flight dynamics and flexibility can be investigated.

In addition, there are several smaller projects to be completed that will contribute valuable insight into the couplings of flight dynamics and hypersonic air-breathing propulsion systems. For example, a time-domain simulation of the transition from ram mode to scram mode would help identify how much of a problem is caused by the change in thrust and pitching moment that occurs at the transition. A trajectory optimization that includes the transition point would also be interesting, particularly as the choice of acceleration affects when the transition occurs.

The simultaneous cooptimization of geometry and trajectory variables in this work included only two geometric parameters. Future work should generalize the approach used here, or select a different approach, so that a larger set of design variables can be used. The possibility of varying dynamic pressure should also be considered. Stability and control considerations should be considered directly as disciplines in the optimization analysis.

In the present work, the design variables that had the most impact on total fuel consumption were all related to the inlet geometry. However, it is possible that additional aspects of the design that were not considered here could also have a significant effect. The possibility of having injectors at multiple axial locations would introduce a new control variable (what fraction of the fuel is injected at each location) that could improve performance, especially in the neighborhood of ram-scram transition or unstart.

Several proposed research topics address extensions to the modeling capabilities demonstrated in this dissertation. Those that are the most important and most likely to be addressed in future research efforts are given subsections below.

7.2.1 Three-Dimensional Extension to SAMURI

A critical limitation of the current MASIV propulsive model is that the inlet and nozzle components must be two-dimensional designs. In recent years there has been a trend toward complex inward-turning inlet designs that cannot be approximated using two-dimensional methods.

To address this limitation, an approach based on a technique related to compound compressible flow [60,183] is currently under development. The technique is based on a system
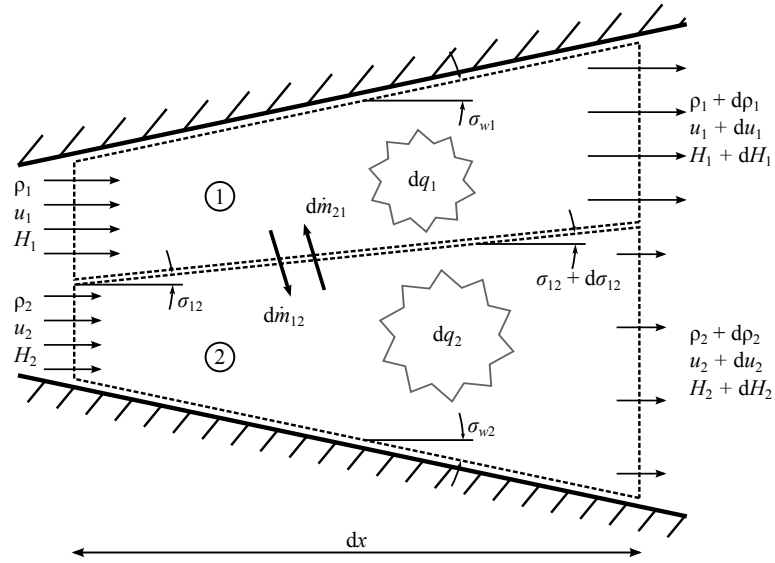
Figure 7.1: Control volume for two adjacent stream tubes in two dimensions.
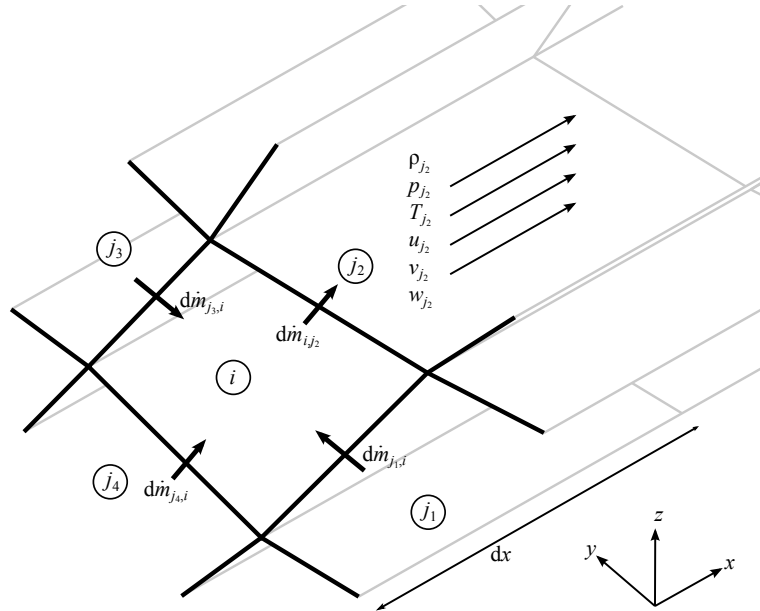
Figure 7.2: Sketch of stream tube i that borders four regions j_1, j_2, j_3, j_4.

of quasi-1D stream tubes, and it also should be useful for modeling non-uniform flow in the combustor, as sketched in Fig. 7.1. Figure 7.2 shows the graphical version of approximately how the method works. Preliminary work indicates that this may be a powerful method that has applications to three-dimensional flows other than inward-turning inlets.

7.2.2 Improved Injection and Mixing Modeling

The current MASIV combustor model is limited to a row of fuel injectors at a single axial location. Potentially there are important advantages to having multiple rows of injectors, especially to avoid unstart during ram-mode operation. The pre-combustion shock train is anchored at the fuel injection point, so injecting the fuel further downstream means that a longer (and thus stronger) shock train can be maintained without unstarting the isolator.

Meanwhile, scram-mode operation has the opposite preference. Injecting the fuel as far upstream as possible allows the fuel more time to burn, which is significant given the very high flow speeds that can be present in supersonic combustion. Because this and other possibilities when the fuel can be injected at least two axial locations (such as the ability to mimic a combustor with a controllable area profile [62]), it would be worthwhile to create this capability in the MASIV model.

The primary challenge is that the conditions at the second injector are affected by the first injector, and thus the model requires a much larger lookup table. Fortunately, the subject of the following subsection should mean that this problem can be alleviated without having to distribute large data files with the MASIV code.

7.2.3 Flamelet Table Reduction

For each different fuel, the MASIV combustor model relies on a large lookup table to generate the reaction rates throughout the internal flow. Currently, each such table is very large, and for more complex fuels it would be much larger. Approaches to reduce the size of these tables have been discussed, but no work has progressed. A recent approach developed for similar situations is to use artificial neural networks [184]. It is also hope that the use of these networks will result in substantially faster lookup times as it will eliminate the need to extract data from very large arrays.

7.2.4 Generic Vehicle Generation and Integration

Currently work is in progress to integrate the MASIV model with a much more generic vehicle generation scheme [158]. The approach will be more consistent with traditional computer-aided design tools whereas the current design routine described in Chapter 3 is entirely within MATLAB®. This work will be important in expanding the MASIV model to more practical applications, but it also means that future extensions to the propulsion system models must fit within the new framework. In particular, it would be less than ideal if the extensions in the previous subsections—three-dimensional inlet modeling, multiple

injector locations, reduced chemistry tables—were implemented but did not work with the existing MASIV interfaces. To ensure that a usable and effective program is the product, it is hoped that as many users as possible will provide feedback on their own needs and preferences for how the code should behave.

7.3 Conclusions

By creating an advanced, tip-to-tail model for air-breathing hypersonic vehicles that can evaluate the forces and moments on a vehicle in a few seconds, it was possible to investigate many aspects of hypersonic flight and make several new contributions.

It is concluded that the MASIV and MASTrim models are a significant improvement over previous reduced-order models of air-breathing hypersonic vehicles. It was shown to be possible to add finite-rate chemistry, isolator-combustor coupling, shock-shock and shock-expansion interactions, and fuel-air mixing to a tip-to-tail vehicle model that can be evaluated on a single contemporaneous processor in about 5 seconds or less, although this time increases to 30 seconds for a ram-mode solution.

Predictions of unstart and ram-to-scram transition were plotted on the Flight Corridor Map for the first time. A dual-mode combustor will unstart if the vehicle flies too high, too slow, or at too great of an acceleration. Actions that will cause a vehicle to transition from ram mode to scram mode include increasing the Mach number, decreasing the altitude, and decreasing the acceleration. Unstart and ram-scram transition are well-known phenomena, but previously have not been calculated in terms of flight condition variables for a trimmed vehicle. At ram-to-scram transition, the possibility of a discontinuity in thrust was identified, and this has serious implications for vehicles that must fly through this boundary.

Strategies for scram-mode trajectory optimization were proposed, which complements the work of previous authors. The recommendation to fly at the highest dynamic pressure allowable to minimize fuel consumption was verified, but the recommendation for maximum acceleration was shown to be in need of slight modification. Instead of flying at an equivalence ratio of unity, the maximum acceleration for a scram-mode trajectory is limited by thermal choking at lower Mach numbers and oxygen availability at higher Mach numbers. In many cases the optimum acceleration will correspond to an equivalence ratio greater than unity. In addition, it was explained how situations could occur where the optimum acceleration is slightly below the maximum.

The effects of changes to the baseline MAX-1 geometry were also investigated. The Mach number for which the engine inlet is designed was shown to have a significant impact on the ram-scram transition Mach number, and the other design variables had only a

146

minimal effect. With regards to fuel consumption along a scram-mode ascent trajectory, all of the inlet design variables were shown to have a large impact. To the author's knowledge, this was the first air-breathing hypersonic vehicle optimization study that simultaneously considered trajectory and geometric design variables. Although only two geometry variables were considered, the optimization study was able to reduce the fuel consumption by 14% from the baseline design.

7.4 Closing

The MASTrim/MASIV model has been used throughout this work and in the research of several other authors. One of the persistent risks of such a project is that the code becomes obsolescent when the primary authors graduate or move on to other topics. In this case, active work continues on many of the components, and there will be important extensions. Consider it as a suggestion to future workers and collaborators that a high level of usability and generality should be kept as a priority. If these efforts are successful, it can become a tool for future preliminary designers in addition to the role it has already played in the fundamental understanding of air-breathing hypersonic vehicles.

APPENDIX A

Full Algorithm for SAMURI

The Supersonic Aerodynamic Model Using Riemann Interactions (SAMURI) model was the subject of Sec. 2.1, but some the details of the algorithm were not presented such that the efforts might be easy to duplicate. This appendix gives a reasonably complete picture including how the key information is stored during the solution process.

The output of SAMURI consists of two parts. The first is a set of N polygons

$$\mathbf{Z} = \{\mathbf{z}_1, \ldots, \mathbf{z}_N\} \qquad \mathbf{z}_k = \left\{(x_{k,1}, y_{k,1}), \ldots, (x_{k,m_k}, y_{k,m_k})\right\} \qquad (A.1)$$

such that the kth polygon has m_k points. The second output is a matrix of states

$$\mathbf{S} = [\, \mathbf{s}_1 \quad \cdots \quad \mathbf{s}_N \,] \qquad \mathbf{s}_k = \begin{bmatrix} \rho_k \\ p_k \\ T_k \\ M_k \\ \theta_k \end{bmatrix} \qquad (A.2)$$

such that $\mathbf{s}_k$ describes the gas properties inside polygon $\mathbf{z}_k$. The first n_{surf} polygons are the physical structures that are input into the program, and the "states" of these polygons are set to non-numeric values (NaN) to keep them separate from true flow solution polygons.

During a SAMURI solution, the process goes from left to right, and the program keeps track of which states intersect the vertical line at the current x-coordinate. Figure A.1(a) shows an intermediate view of the solution such that the current x-coordinate matches that of the airfoil's lower vertex. The vertical line there intersects eight polygons, although three of them only intersect at a single point. SAMURI keeps a running tally of the indices of these polygons in a variable called $\mathbf{k}$, and it also keeps track of the angles of the separating boundaries (waves, slip lines, surfaces, or edges of the flow domain) in a variable σ and
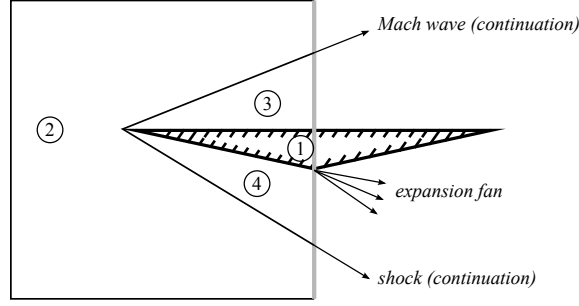
(a) Intermediate point of SAMURI solution.
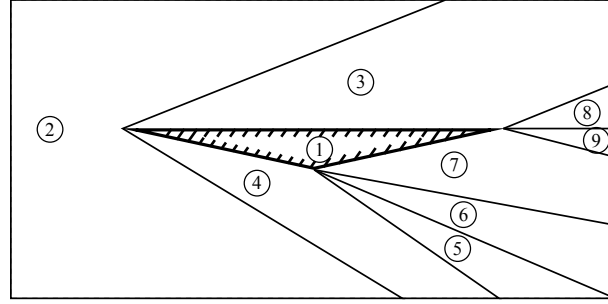
(b) Region numbers and boundaries for full solution.

Figure A.1: Intermediate point and completed solution of SAMURI process.

the y-coordinates of those boundaries in $\mathbf{y}$. Thus for the x-coordinate shown in Fig. A.1(a),

$$\mathbf{k} = \begin{bmatrix} k_1 \\ k_2 \\ k_3 \\ k_4 \\ k_5 \\ k_6 \\ k_7 \\ k_8 \end{bmatrix} = \begin{bmatrix} 2 \\ 4 \\ 5 \\ 6 \\ 7 \\ 1 \\ 3 \\ 2 \end{bmatrix} \qquad \mathbf{y} = \begin{bmatrix} y_1 \\ y_2 \\ y_3 \\ y_4 \\ y_5 \\ y_6 \\ y_7 \\ y_8 \\ y_9 \end{bmatrix} = \begin{bmatrix} y_{\min} \\ y_2 \\ y_3 \\ y_3 \\ y_3 \\ y_3 \\ y_7 \\ y_8 \\ y_{\max} \end{bmatrix} \qquad \boldsymbol{\sigma} = \begin{bmatrix} \sigma_1 \\ \sigma_2 \\ \sigma_3 \\ \sigma_4 \\ \sigma_5 \\ \sigma_6 \\ \sigma_7 \\ \sigma_8 \\ \sigma_9 \end{bmatrix} = \begin{bmatrix} 0 \\ \sigma_2 \\ \sigma_3 \\ \sigma_4 \\ \sigma_5 \\ \sigma_6 \\ 0 \\ \sigma_8 \\ 0 \end{bmatrix} \qquad \text{(A.3)}$$

It is always the case that $\boldsymbol{\sigma}$ has one more entry than $\mathbf{k}$ because σ_j separates regions k_{j-1} and k_j. The current number of entries in $\mathbf{k}$ is defined to be K. As new regions are introduced, the value of K changes, and the other variables are also dynamically updated. Figure A.2 describes the algorithm used to introduce a new region.

The bulk of the work is done by the subroutine described in Fig. A.3. Although the Riemann problem equations discussed in Sec. 2.1.2 are the same for shock-shock, shock-

A. Inputs: new wave angle (σ) and new state ($\mathbf{s}_{N+1}$).

A.1. Add a copy of the current y-coordinate to the list.

$$\mathbf{y} = [\, y_1 \quad \cdots \quad y_j \quad y_j \quad y_{j+1} \quad \cdots \quad y_K \,]^T$$

A.2. Add the new wave angle σ to the list.

$$\boldsymbol{\sigma} = [\, \sigma_1 \quad \cdots \quad \sigma_j \quad \sigma \quad \sigma_{j+1} \quad \cdots \quad \sigma_K \,]^T$$

A.3. Add the index in the same location.

$$\mathbf{k} = [\, k_1 \quad \cdots \quad k_{j-1} \quad N+1 \quad k_j \quad \cdots \quad k_K \,]^T$$

A.4. Add the current state to the matrix: $\mathbf{s} = [\, \mathbf{s} \quad \mathbf{s}_{N+1} \,]$.

A.5. Increase number of regions: $N = N + 1$.

A.6. Increase the number of active regions: $K = K + 1$.

A.7. Initialize the polygon for the new region: $z_{k_{cur}} = \{(x, y_j)\}$.

Figure A.2: Subroutine to add a new region.

expansion, and expansion-expansion interactions, the conservation equations of Sec. 2.1.1 must be applied directly if the interaction is a shock hitting a surface. Subroutine B in Fig. A.3 then has two primary tasks: determine which type of solution method is appropriate, and store the results accordingly in variables so that they can be inspected later.

Finally, the full algorithm is given in Fig. A.4. In the end, it works in a very simple way. It solves the flow from left to right by considering one x-coordinate at a time. At each x-coordinate, it sweeps through the y-coordinates from bottom to top. This separation of directions is possible in most supersonic flows as long as deflection angles are not too large and the x-axis is approximately aligned with the flow direction.

Upon completing the solution up to a given x-coordinate, SAMURI searches for the next x-coordinate where at least one interaction will occur. As a result, there is no grid in either direction, and the resolution is set only by the nature of the waves in the flow.

B. Main inputs: updated region indices ($\mathbf{k}$), boundaries ($\mathbf{y}$ and $\boldsymbol{\sigma}$) and y-index (j).

B.1. If $j = 1$ and $y_2 = y_{\min}$ (wave hitting bottom of solution domain):

B.1.1. Delete k_1, y_2, and σ_2. Set $K = K - 1$ and $J = 0$.

B.2. If $j = K$ and $y_j = y_{\max}$ (wave hitting top of solution domain):

B.2.1. Delete k_K, y_K, and σ_K. Set $K = K - 1$ and $J = 0$.

B.3. If point (x, y_j) is a leading edge:

B.3.1. Find the angles of the lower ($\theta_{low} = \sigma_j$) and upper ($\theta_{upp} = \sigma_{j+1}$) surfaces.

B.3.2. Solve wave equations using $\mathbf{s}_{k_{j-1}}$ and θ_{low} to find states $\mathbf{s}_{N+1}, \ldots, \mathbf{s}_{N+J_{low}}$.

B.3.3. Use state $\mathbf{s}_{k_{j+1}}$ and θ_{upp} to find states $\mathbf{s}_{N+J_{low}+1}, \ldots, \mathbf{s}_{N+J_{low}+J_{upp}}$.

B.3.4. Introduce states for lower surface; apply subroutine A for $\ell = 1, \ldots, J_{low}$.

B.3.5. Increase j so remaining states are added above the surface: $j = j + J_{low} + 2$.

B.3.6. Set $J = J_{upp}$.

B.4. Else if point (x, y_j) is a trailing edge or wave interaction:

B.4.1. Delete k_j, y_{j+1} and σ_{j+1}. Set $K = K - 1$. Update indices.

B.4.2. Riemann problem using $\mathbf{s}_{k_{j-1}}$ and $\mathbf{s}_{k_j}$; find new states $\mathbf{s}_{N+1}, \ldots, \mathbf{s}_{N+J}$.

B.4.3. Replace σ_j with angle of bottom wave of Riemann solution.

B.5. Else if flow adjacent to lower surface:

B.5.1. If $y_{j+1} = y_j$, delete k_j, y_j, σ_j and set $K = K - 1$.

B.5.2. Find surface angle downstream of vertex θ_{low}; replace σ_j with θ_{low}.

B.5.3. Use $\mathbf{s}_{k_{j-1}}$ and θ_{low} to find J new states $\mathbf{s}_{N+1}, \ldots, \mathbf{s}_{N+J}$.

B.6. Else if flow adjacent to upper surface:

B.6.1. If $y_{j+1} = y_j$, delete k_j, y_{j+1}, σ_{j+1} and set $K = K - 1$.

B.6.2. Find surface angle downstream of vertex θ_{upp}; replace σ_j with θ_{upp}.

B.6.3. Use $\mathbf{s}_{k_j}$ and θ_{upp} to find J new states $\mathbf{s}_{N+1}, \ldots, \mathbf{s}_{N+J}$.

B.7. Else:

B.7.1. No interactions; set $J = 0$.

B.8. End if.

B.9. Add new regions; apply subroutine A for $\ell = 1, \ldots, J$.

Figure A.3: Subroutine to test interaction type and solve flow equations.

0. Input and initialization.

    0.1. Input surface polygons: $\mathbf{Z} = \{\, \mathbf{z}_1, \ldots, \mathbf{z}_{n_{surf}} \,\}$; set $N = n_{surf} + 1$.

    0.2. Input flow domain ($x_{\min}$, $x_{\max}$, $y_{\min}$, and $y_{\max}$).

    0.3. Input initial state $\mathbf{s}_N = [\, \rho_N \quad p_N \quad T_N \quad M_N \quad \theta_N \,]^T$.

    0.4. Initialize list of states: $\mathbf{S} = \begin{bmatrix} \mathbf{s}_1 & \cdots & \mathbf{s}_{n_{surf}} & \mathbf{s}_N \end{bmatrix}$.

    0.5. Initialize coordinates and region boundaries.

$$x = x_{\min} \qquad \mathbf{k} = [\, N \,]^T \qquad \mathbf{y} = [\, y_{\min} \quad y_{\max} \,]^T \qquad \boldsymbol{\sigma} = [\, 0 \quad 0 \,]^T$$

    0.6. Initialize first flow polygon, append to list $\mathbf{Z}$.

$$\mathbf{z}_N = \{(x_{\min}, y_{\min}), (x_{\min}, y_{\max})\}$$

1. While $x < x_{\max}$.

    1.1. Initialize $j = 1$, $y_j = y_{\min}$.

    1.2. While $j \le K$ and $y_j \le y_{\max}$:

        1.2.1. Find the largest L such that $y_{j+L} = y_j$.

        1.2.2. Add the point (x, y_j) to polygon $\mathbf{z}_{k_\ell}$ for $\ell = j, \ldots, j + L$.

        1.2.3. Apply subroutine B to analyze point (x, y_j) and introduce J new states.

        1.2.4. Increase y-index: $j = j + J + 1$.

    1.3. Search for next x-coordinate.

        1.3.1. Find leading edge with the lowest x-coordinate $x_{LE} > x$.

        1.3.2. Find intersection point for each adjacent pair of waves for $j = 1, \ldots, K$.

$$x_j = x + \frac{y_{j+1} - y_j}{\tan \sigma_j - \tan \sigma_{j+1}}$$

        1.3.3. Pick $x^* = \min \{x_{LE}, x_{\max}, x_1, \ldots, x_K\}$.

        1.3.4. Update wave locations for $j = 1, \ldots, K$.

$$y_j = y_j + (x^* - x) \tan \sigma_j$$

        1.3.5. Update $x = x^*$.

        1.3.6. If leading edge option was used, add the coordinates to $\mathbf{k}$, $\mathbf{y}$, and $\boldsymbol{\sigma}$.

2. Finish regions when $x = x_{\max}$.

    2.1. For $j = 1, \ldots, K$: Add points (x, y_j) and (x, y_{j+1}) to polygon $\mathbf{z}_{k_j}$.

Figure A.4: Outer algorithm for SAMURI.

APPENDIX B

Rotating-Earth Equations of Motion

In order to apply Newton's second law directly, an inertial frame is required. In this case, the Earth-Centered Inertial (ECI) frame will be used, and we label it the *i*-frame. In such a frame,

$$\ddot{\mathbf{r}}_{ib}^{i} = \mathbf{f}^{i} + \mathbf{g}^{i} \tag{B.1}$$

where **f** is the net aerodynamic and propulsive force on the vehicle divided by the mass and **g** is the specific gravity force. The superscript *i* means that the vector is written in the inertial (*i*) frame. The subscripts on $\mathbf{r}_{ib}^{i}$ means that this vector goes from the origin of the *i*-frame to the origin of the *b*-frame (body frame), and it is the position of the vehicle in the inertial frame.

We also require a way to transform a vector from coordinate system to another. This is done with a transformation matrix, for which the following notation is utilized.

$$\mathbf{f}^{i} = \mathsf{C}_{b}^{i}\mathbf{f}^{b} \tag{B.2}$$

The *b*-frame (body frame) is attached to the vehicle such that the x^{b} axis points forward, the y^{b} axis points to the right, and the z^{b}-axis points downward. The notation of Eq. (B.2) is saying that pre-multiplying a vector that is resolved in the *b*-frame by C_{b}^{i} results in the same vector resolved in the *i*-frame.

B.1   Coordinate Frames and Angle Definitions

For this description of the equations of motion, five coordinate systems are needed. Furthermore, many angles are defined based on the rotations between pairs of coordinate systems.

The exact orientation of the inertial frame is not needed here. The reason that the inertial frame is needed is merely as a place to take derivatives, and thus we only need to define the angular velocities of the other frames with respect to it.

Table B.1: List of coordinate systems, origins, and rotations.

Coordinate system	Label	Origin	Orientation and rotation
Inertial, ECI	i	Center of Earth	Inertial, "no" rotation
ECEF	e	Center of Earth	Rotates with Earth
Navigation	n	Vehicle	Plane tangent to Earth surface
Velocity	v	Vehicle	Fixed to velocity vector
Body	b	Vehicle	Fixed to vehicle

B.1.1 Earth-Fixed (e) Frame

Since the Earth is rotating, and the atmosphere more or less rotates with it (neglecting weather patterns), we describe the motion of the vehicle in a coordinate system where each point on the surface of the Earth has constant coordinates. For this purpose, we use the Earth-Centered, Earth-Fixed (ECEF) frame, in which the z^e axis points from the center of the Earth toward the north pole, the x^e axis points toward the intersection of the equator and the prime meridian, and the y^e-axis completes a right-handed system. The angular velocity between the ECEF and ECI frames is

$$\omega_{ie}^e = \begin{bmatrix} 0 \\ 0 \\ \omega_{ie} \end{bmatrix} \qquad \omega_{ie} \approx 7.262 \times 10^{-5} \text{ rad/s} \qquad (B.3)$$

B.1.2 Navigation (n) Frame

next, we introduce a local coordinate system called the navigation frame (n-frame). The x^n-axis points toward the local north (note that this means parallel to the plane that is tangent surface of the Earth directly below the aircraft), the y^e-axis points to the local east, and the z^e-axis points downward, normal to the surface of the Earth. This frame rotates and moves with the location of the vehicle, but it does not take into account the attitude of the vehicle. The transformation matrix between the navigation and ECEF frames is

$$\mathsf{C}_n^e = \begin{bmatrix} -\sin L \cos \lambda & -\sin \lambda & -\cos L \cos \lambda \\ -\sin L \sin \lambda & \cos \lambda & -\cos L \sin \lambda \\ \cos L & 0 & -\sin L \end{bmatrix} \qquad (B.4)$$

where L is the geodetic latitude and λ is the longitude. Graphical demonstrations of L and λ are given in Fig. B.2. Altitude does not affect the transformation. Figure B.1 gives a visual demonstration of the relationship between the ECEF and navigation coordinate frames for
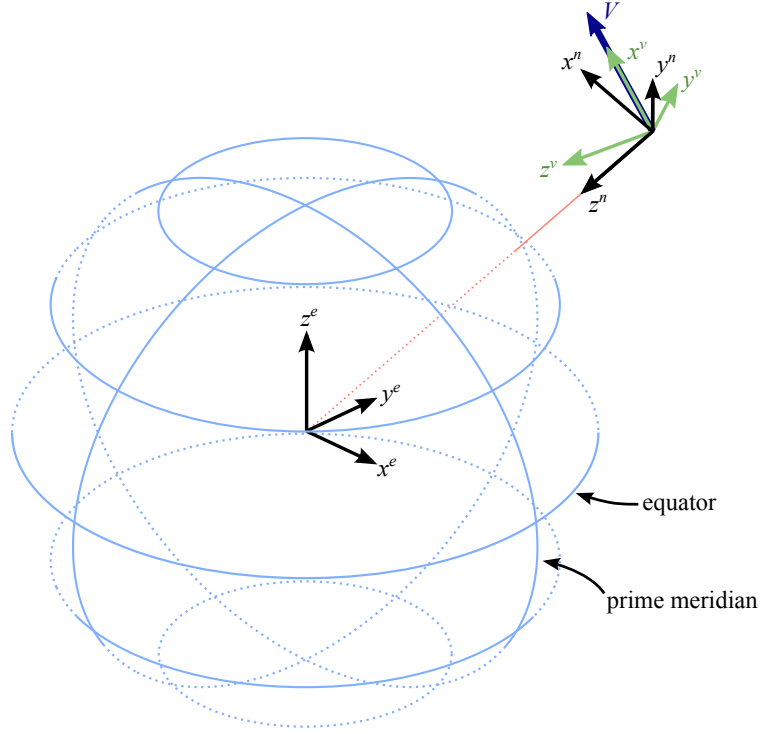
Figure B.1: ECEF and navigation coordinate frames.

an example point. The components of the vehicle velocity in the n-frame are

$$\mathbf{v}_{eb}^n = C_e^n \dot{\mathbf{r}}_{eb}^e = \begin{bmatrix} v_N \\ v_E \\ v_D \end{bmatrix} \tag{B.5}$$

These components are then the northward, eastward, and downward components of the vehicle's velocity. This equation contains an implicit assumption made with this notation; derivatives that are shown with a dot are always taken in the resolving (superscript) frame. This means, for example that $\mathbf{v}_{eb}^n \neq \dot{\mathbf{r}}_{eb}^n$ because the n-frame is rotating with respect to the e-frame, and that would conflict with the definition in Eq. (B.5). Throughout this work, the velocity ($\mathbf{v}$) and position ($\mathbf{r}$) vectors are always measured from the ECEF origin to the body origin, so the two subscripts will be dropped in the following references and equations. The subscripts are also not written in Chapter 4.

B.1.3   Velocity (v) Frame

The velocity frame is defined so that the x^v-axis points in the direction of the velocity, and the y^v-axis remains in the $x^n y^n$-plane. That is, the y^v-axis is parallel to the plane tangent

(a) View from geodetic west.

(b) View from celestial north.
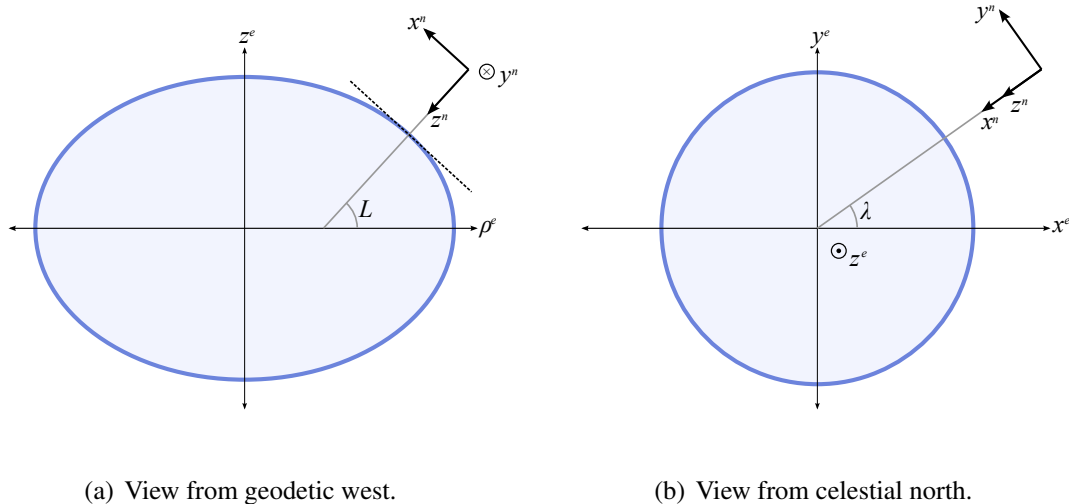
Figure B.2: Two views of the navigation frame relative to the Earth. In (a), the geodetic east direction points into the page. In (b), celestial north points out of the page.
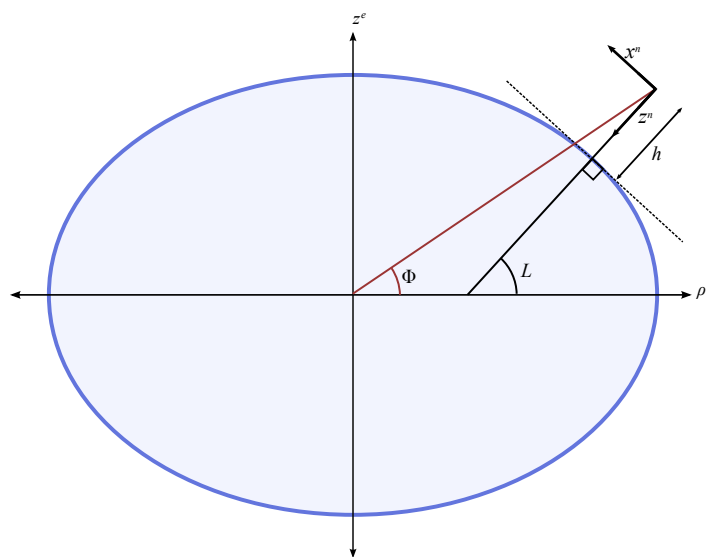
Figure B.3: Demonstration of difference between spherical and geodetic latitude.

(a) Heading angle.

(b) Flightpath angle.
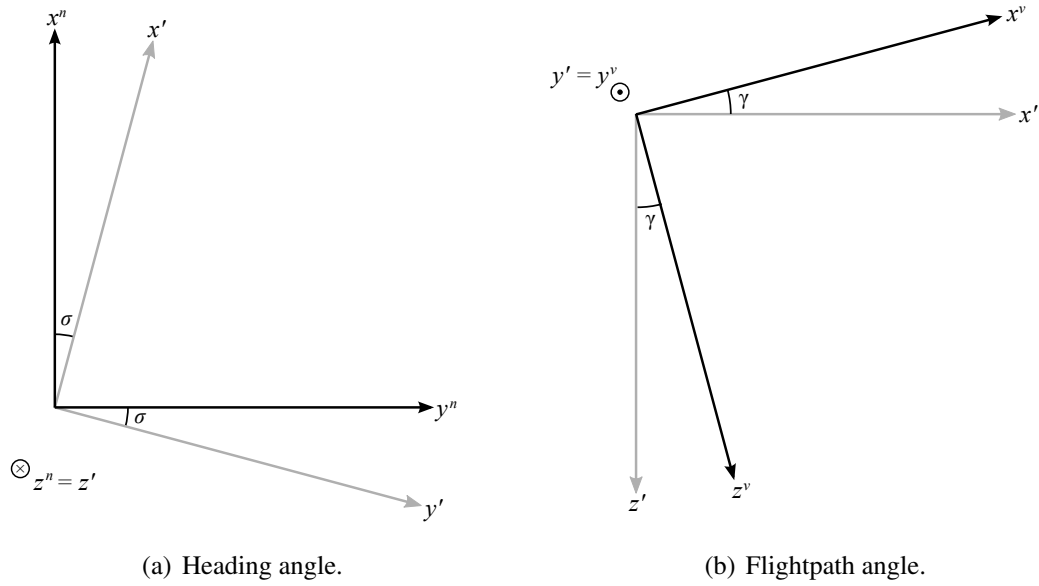
Figure B.4: The two rotations that relate the navigation frame to the velocity frame.

to the surface of the Earth. Figure B.4 shows the two rotations that are used to relate the velocity and navigation frames.

The transformation between the two coordinate frames is

$$
\mathbf{v}^n = \mathsf{C}_v^n \mathbf{v}^v = \begin{bmatrix} \cos\gamma\cos\chi & -\sin\chi & \sin\gamma\cos\chi \\ \cos\gamma\sin\chi & \cos\chi & \sin\gamma\sin\chi \\ -\sin\gamma & 0 & \cos\gamma \end{bmatrix} \mathbf{v}^v \tag{B.6}
$$

Because of the way the v-frame is defined, the velocity has a very simple definition: $\mathbf{v}^v = V\hat{\mathbf{x}}^v$. This allows us to write the velocity in the navigation frame in terms of the flight path angle (γ) and velocity heading angle (χ).

$$
\mathbf{v}^n = \mathsf{C}_v^n \begin{bmatrix} V \\ 0 \\ 0 \end{bmatrix} = \begin{bmatrix} v_N \\ v_E \\ v_D \end{bmatrix} = \begin{bmatrix} V\cos\chi\cos\gamma \\ V\sin\chi\cos\gamma \\ -V\sin\gamma \end{bmatrix} \tag{B.7}
$$

B.1.4   Body (b) Frame

The final coordinate system is the body frame, whose axes were defined earlier. The transformation matrix that defines the body frame is usually written in relation to the body

157
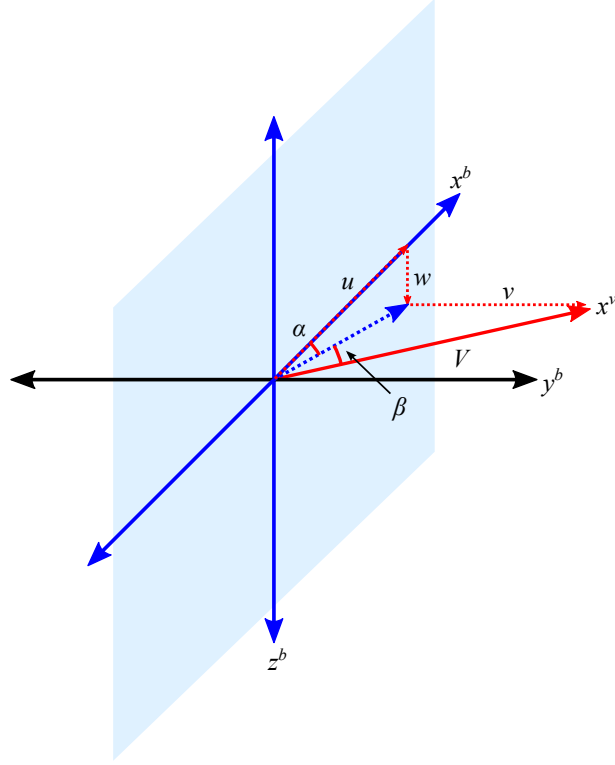
Figure B.5: Aerodynamic angles: angle of attack (α) and sideslip angle (β).

frame, and it carries the navigation frame to the body frame.

$$
C_n^b = \begin{bmatrix} 1 & 0 & 0 \\ 0 & \cos\phi & \sin\phi \\ 0 & -\sin\phi & \cos\phi \end{bmatrix} \begin{bmatrix} \cos\theta & 0 & -\sin\theta \\ 0 & 1 & 0 \\ \sin\theta & 0 & \cos\theta \end{bmatrix} \begin{bmatrix} \cos\psi & \sin\psi & 0 \\ -\sin\psi & \cos\psi & 0 \\ 0 & 0 & 1 \end{bmatrix} \tag{B.8}
$$

These angles are the standard aircraft Euler angles, and they are called the roll (ϕ), pitch (θ), and yaw (ψ). The components of the velocity in this frame are

$$
\mathbf{v}^b = C_e^b \dot{\mathbf{r}}^e = \begin{bmatrix} u \\ v \\ w \end{bmatrix} = \begin{bmatrix} V\cos\beta\cos\alpha \\ V\sin\beta \\ V\cos\beta\sin\alpha \end{bmatrix} \tag{B.9}
$$

This coordinate frame is commonly used and can be found in many texts, for example [185].

The angles defining the velocity in the body frame are angle of attack (α) and sideslip angle (β). These are sketched in Fig. B.5. The coordinate transformation between velocity

158

frame and the body frame is given by

$$
C_v^b = \begin{bmatrix} \cos\alpha & 0 & -\sin\alpha \\ 0 & 1 & 0 \\ \sin\alpha & 0 & \cos\alpha \end{bmatrix} \begin{bmatrix} \cos\beta & -\sin\beta & 0 \\ \sin\beta & \cos\beta & 0 \\ 0 & 0 & 1 \end{bmatrix} \begin{bmatrix} 1 & 0 & 0 \\ 0 & \cos\sigma & \sin\sigma \\ 0 & -\sin\sigma & \cos\sigma \end{bmatrix} \tag{B.10}
$$

where σ is a roll-like angle that completes the transformation matrix and is sometimes called the bank angle.

B.2   The WGS84 Earth Model

Instead of using a spherical Earth, we have chosen to use the WGS84 ellisoidal reference datum [159]. This is the same model used for the Global Positioning System (GPS) [160], and thus it provides an accurate reference for navigation. In this model, each curve of constant latitude is a circle, but each meridian is an ellipse with an eccentricity of

$$
e = 0.0818191908426 \tag{B.11}
$$

and a semi-major axis of

$$
R_Q = 6378137 \text{ m} \tag{B.12}
$$

One result of using an ellipsoidal Earth is the possibility of ambiguously defined latitude and altitude. In this paper, we use geodetic latitude, which has the property that moving normal to the reference ellipsoid does not change the latitude. As a result, the ECEF coordinates in terms of latitude, longitude, and altitude are

$$
x_{en}^e = \left(\frac{R_Q}{\sqrt{1 - e^2 \sin^2 L}} + h \right) \cos L \cos \lambda
$$

$$
y_{en}^e = \left(\frac{R_Q}{\sqrt{1 - e^2 \sin^2 L}} + h \right) \cos L \sin \lambda
$$

$$
z_{en}^e = \left(\frac{R_Q(1 - e^2)}{\sqrt{1 - e^2 \sin^2 L}} + h \right) \sin L \tag{B.13}
$$

Figure B.3 shows the definition of the geodetic latitude and how it compares with the latitude that one would get using the line that connects the vehicle and the center of the Earth. Note that $\rho^e = \sqrt{(x^e)^2 + (y^e)^2}$ is a definition used in that figure.

We also need the rotation rate and the angular acceleration of the n-frame with respect

to the e-frame, which are

$$\omega_{en}^n = \begin{bmatrix} \dot\lambda \cos L \\ -\dot L \\ -\dot\lambda \sin L \end{bmatrix} \qquad\qquad \dot\omega_{en}^n = \begin{bmatrix} \ddot\lambda \cos L - \dot\lambda \dot L \sin L \\ -\ddot L \\ -\ddot\lambda \sin L - \dot\lambda \dot L \cos L \end{bmatrix} \tag{B.14}$$

where

$$\dot\lambda = \frac{v_E}{R_E} \qquad\qquad \ddot\lambda = \left(\frac{\dot v_E}{v_E} - \frac{\dot R_E}{R_E}\right)\dot\lambda$$

$$\dot L = \frac{v_N}{R_N} \qquad\qquad \ddot L = \left(\frac{\dot v_N}{v_N} - \frac{\dot R_N}{R_N}\right)\dot L \tag{B.15}$$

Here R_E refers to the radius of curvature in the east-west direction and R_N is the radius of curvature in the north-south direction. Their formulae are

$$R_E = \left(\frac{R_Q}{\sqrt{1 - e^2 \sin^2 L}} + h\right)\cos L \qquad \dot R_E = -v_N \sin L - v_D \cos L$$

$$R_N = \frac{R_Q(1 - e^2)}{(1 - e^2 \sin^2 L)^{3/2}} + h \qquad \dot R_N = \frac{3}{2}\frac{(R_N - h)e^2 \sin 2L}{1 - e^2 \sin^2 L}\frac{v_N}{R_N} - v_D \tag{B.16}$$

B.3   Transport Theorem

A method is needed to calculate derivatives in non-inertial frames. The transport theorem, for example

$$\dot{\mathbf{r}}^b = C_n^b(\dot{\mathbf{r}}^n + \omega_{nb}^n \times \mathbf{r}^n) = C_n^b\dot{\mathbf{r}}^n + \omega_{nb}^b \times \mathbf{r}^b) \tag{B.17}$$

is usually used for this purpose. A simple way to write the transport theorem is to write the relation between the two non-differentiated vectors,

$$\mathbf{r}^b = C_n^b\mathbf{r}^n \tag{B.18}$$

and then differentiate:

$$\dot{\mathbf{r}}^b = C_n^b\dot{\mathbf{r}}^n + \dot C_n^b\mathbf{r}^n$$

The key to using this approach is the simple formula

$$\dot C_n^b = C_n^b\Omega_{nb}^n \qquad\qquad \Omega = \begin{bmatrix} 0 & -\omega_3 & \omega_2 \\ \omega_3 & 0 & -\omega_1 \\ -\omega_2 & \omega_1 & 0 \end{bmatrix} \tag{B.19}$$

160

The skew-symmetric matrix Ω is a matrix version of an angular velocity so that matrix multiplication takes the place of a cross product. A skew-symmetric matrix has the property that $\Omega = -\Omega^T$. Using this view of the transport theorem reduces the problem of finding the equations of motion to repeated applications of the chain rule.

B.4   Net Accelerations

Beginning with Newton's second law in the inertial frame,

$$\ddot{\mathbf{r}}^i = \mathbf{f}^i + \mathbf{g}^i$$

we can apply the transport theorem twice. First introduce the position in the ECEF frame, $\mathbf{r}^e$, and then differentiate.

$$
\begin{aligned}
\mathbf{r}^i &= C_e^i \mathbf{r}^e \\
\dot{\mathbf{r}}^i &= C_e^i \dot{\mathbf{r}}^e + C_e^i \Omega_{ie}^e \mathbf{r}^e \\
\ddot{\mathbf{r}}^i &= C_e^i \ddot{\mathbf{r}}^e + 2 C_e^i \Omega_{ie}^e \dot{\mathbf{r}}^e + C_e^i \dot{\Omega}_{ie}^e \mathbf{r}^e + C_e^i \Omega_{ie}^e \Omega_{ie}^e \mathbf{r}^e \\
&= C_e^i \left(\ddot{\mathbf{r}}^e + 2 \Omega_{ie}^e \dot{\mathbf{r}}^e + \dot{\Omega}_{ie}^e \mathbf{r}^e + (\Omega_{ie}^e)^2 \mathbf{r}^e \right)
\end{aligned}
$$

It is most convenient to calculate the aerodynamic forces on the vehicle in the body frame. The gravity points downward locally, so $\mathbf{g}^n$ is the easiest to write. Finally, $\dot{\Omega}_{ie}^e = 0$ because the Earth rotates at a constant rate. Combining these gives

$$C_e^i \ddot{\mathbf{r}}^e + 2 C_e^i \Omega_{ie}^e \dot{\mathbf{r}}^e + C_e^i (\Omega_{ie}^e)^2 \mathbf{r}^e = C_b^i \mathbf{f}^b + C_n^i \mathbf{g}^n \tag{B.20}$$

Note that we define $\mathbf{v}^e = \dot{\mathbf{r}}^e$. This means that the velocity is the rate of change of the position of the vehicle in the Earth-fixed frame, which matches intuition. However, this means that $\mathbf{v}^n \neq \dot{\mathbf{r}}^n$ and $\mathbf{v}^b \neq \dot{\mathbf{r}}^b$. Using this definition of velocity in Eq. (B.20),

$$\dot{\mathbf{v}}^e = C_b^e \mathbf{f}^b + C_n^e \mathbf{g}^n - 2 \Omega_{ie}^e \mathbf{v}^e - (\Omega_{ie}^e)^2 \mathbf{r}^e \tag{B.21}$$

This is almost a satisfactory set of equations because it gives an acceleration (the left-hand side) in terms of things we can calculate on the right-hand side. However, steady, level flight does not correspond to $\dot{\mathbf{v}}^e = 0$ because the direction of the velocity vector changes as the vehicles latitude and longitude change. The velocity in the navigation frame can be

introduced using $\mathbf{v}^e = C_n^e \mathbf{v}^n$, so the transport theorem gives

$$\dot{\mathbf{v}}^e = C_n^e \dot{\mathbf{v}}^n + C_n^e \Omega_{en}^n \mathbf{v}^n$$

Substituting this into Eq. (B.21) gives

$$\dot{\mathbf{v}}^n = C_b^n \mathbf{f}^b + \mathbf{g}^n - (\Omega_{ie}^n)^2 C_e^n \mathbf{r}^e - (2\Omega_{ie}^n + \Omega_{en}^n)\mathbf{v}^n \qquad (B.22)$$

Eq. (B.22) describes the evolution of the velocity in the navigation frame, and this is known as the inertial navigation equation [160]. This is convenient because we can differentiate Eq. (B.7) to get

$$\dot{\mathbf{v}}^n = \begin{bmatrix} \dot{V}\cos\gamma\cos\chi - V\dot{\chi}\cos\gamma\sin\chi - V\dot{\gamma}\sin\gamma\cos\chi \\ \dot{V}\cos\gamma\sin\chi + V\dot{\chi}\cos\gamma\cos\chi - V\dot{\gamma}\sin\gamma\sin\chi \\ -\dot{V}\sin\gamma - V\dot{\gamma}\cos\gamma \end{bmatrix} \qquad (B.23)$$

which means that $\dot{\mathbf{v}}^n$ can be determined in terms of variables that intuitively define the velocity and acceleration.

It is also useful to write the accelerations in the body frame. Putting the body-frame acceleration into the inertial navigation equation gives

$$\dot{\mathbf{v}}^b = \mathbf{f}^b + C_n^b \mathbf{g}^n - C_n^b(\Omega_{ie}^n)^2 C_e^n \mathbf{r}^e - C_n^b(2\Omega_{ie}^n + \Omega_{en}^n)\mathbf{v}^n - \Omega_{nb}^b \mathbf{v}^b \qquad (B.24)$$

By definition,

$$\dot{\mathbf{v}}^b = \begin{bmatrix} \dot{u} \\ \dot{v} \\ \dot{w} \end{bmatrix} \qquad \qquad \omega_{ib}^b = \begin{bmatrix} P \\ Q \\ R \end{bmatrix} \qquad (B.25)$$

B.5 Net Angular Accelerations

The previous section derived the equations for the position and velocity of the vehicle, but that is only half of the story; equations for the attitude and rotation are also needed. The specific angular momentum (angular momentum divided by mass, used so that the inertia tensor can be constant even while the mass of the vehicle changes) of the vehicle in the inertial frame is

$$\mathbf{h}_{ib}^i = \mathsf{I}^i \omega_{ib}^i \qquad (B.26)$$

where I is the inertia tensor of the vehicle divided by mass. Like in Sec. B.4, we begin with an inertial frame so that Newton's second law can be applied.

$$\mathbf{M}^i = \dot{\mathbf{h}}_{ib}^i = \frac{d\mathbf{I}^i}{dt}\omega_{ib}^i + \mathbf{I}^i\dot{\omega}_{ib}^i$$

with $\mathbf{M}$ as the net moment on the vehicle divided by the mass. This is inconvenient because $\mathbf{I}^i$ is not constant even for a rigid body, whereas $\mathbf{I}^b$ is under the assumption that fuel is evenly distributed throughout the vehicle or that the change in mass has a long time scale. The change of coordinates for a matrix gives the following result.

$$\mathbf{I}^i = C_b^i \mathbf{I}^b C_i^b$$

$$\frac{d\mathbf{I}^i}{dt} = C_b^i \Omega_{ib}^b \mathbf{I}^b C_i^b + C_b^i \dot{\mathbf{I}}^b C_i^b + C_b^i \mathbf{I}^b C_i^b \Omega_{bi}^i$$

For a rigid body with constant mass, $\dot{\mathbf{I}}^b = 0$, as mentioned before.

Putting this result into Newton's second law and transforming into the body frame gives

$$\mathbf{M}^b = \Omega_{ib}^b \mathbf{I}^b \omega_{ib}^b + \mathbf{I}^b C_i^b \dot{\omega}_{ib}^i = \Omega_{ib}^b \mathbf{I}^b \omega_{ib}^b + \mathbf{I}^b \dot{\omega}_{ib}^b \tag{B.27}$$

noting that $\Omega_{bi}^i \omega_{ib}^i = 0$ because it is the cross product of two parallel vectors. This equation can be used to solve for

$$\dot{\omega}_{ib}^b = \begin{bmatrix} \dot{P} \\ \dot{Q} \\ \dot{R} \end{bmatrix} = (\mathbf{I}^b)^{-1}\left(\mathbf{M}^b - \Omega_{ib}^b \mathbf{I}^b \omega_{ib}^b\right) \tag{B.28}$$

To calculate the derivatives of the Euler angles, we calculate

$$\omega_{nb}^b = \begin{bmatrix} p \\ q \\ r \end{bmatrix} = \omega_{ib}^b - C_n^b(\omega_{ie}^n + \omega_{en}^n) \tag{B.29}$$

Then the time rate of change for each Euler angle can be calculated using the equations

$$\dot{\phi} = p + q\sin\phi\tan\theta + r\cos\phi\tan\theta \tag{B.30}$$

$$\dot{\theta} = q\cos\phi - r\sin\phi \tag{B.31}$$

$$\dot{\psi} = q\sin\phi\sec\theta + r\cos\phi\sec\theta \tag{B.32}$$

163

APPENDIX C

Modal Participation Analysis for Linear Systems

The following appendix describes a method to determine which state variables participate in each mode of a linear system. This is important for aircraft when investigating the stability and controllability characteristics of a known flight condition. The full nonlinear equations of motion are linearized in the neighborhood of that flight condition as described in Sec. 4.1.3. In order to determine what actions can be taken to control the vehicle or redesign it to improve the stability, there must be some way to determine which states participate in stable and unstable modes.

A sample linear system has the form

$$\dot{\mathbf{x}} = A\mathbf{x} \tag{C.1}$$

with $\mathbf{x} \in \mathbb{R}^n$ a vector of state variables and $A \in \mathbb{R}^{n \times n}$:

$$\mathbf{x} = \begin{bmatrix} x_1 \\ x_2 \\ \vdots \\ x_n \end{bmatrix} \qquad A = \begin{bmatrix} a_{11} & a_{12} & \cdots & a_{1n} \\ a_{21} & a_{22} & \cdots & a_{2n} \\ \vdots & \vdots & \ddots & \vdots \\ a_{n1} & a_{n2} & \cdots & a_{nn} \end{bmatrix} \tag{C.2}$$

Typically the eigenvectors are used to determine the primary variables for a given mode, but this can have several problems, which are listed below.

1. Since $x_1, x_2, \ldots, x_n$ can each have different units, the entries of the eigenvectors also have different units.

2. Eigenvectors may contain negative or complex values, which are difficult to interpret.

3. Both eigenvalues and eigenvectors come in complex-conjugate pairs.

4. It is possible for one state to dominate several modes while other states do not play a significant role in any mode.

Consider as an example the states as described in Sec. 4.1.

$$\mathbf{x} = [\, L \quad \lambda \quad h \quad V \quad \alpha \quad \beta \quad \phi \quad \theta \quad \psi \quad P \quad Q \quad R \,]^T \tag{C.3}$$

Variously, these states have units of radians (L, λ, α, β, ϕ, θ, ψ), meters (h), meters per second (V), or radians per second (P, Q, R). Thus the norm of $\mathbf{x}$, $\|\mathbf{x}\| = (x_1^2 + \cdots + x_n^2)^{1/2}$, makes no sense because it would require adding terms with different units. Now consider a right eigenvector $\mathbf{v}_k$. It has the property that

$$\mathsf{A}\mathbf{v}_k = p_k \mathbf{v}_k \tag{C.4}$$

where p_k is a complex number that is an eigenvector of A, which we will call a "pole" here. A typical process for determining which variables participate in each mode is to look at the n right eigenvectors $\mathbf{v}_1, \ldots, \mathbf{v}_n$, normalize each of them so that $\|\mathbf{v}_k\| = 1$, and look at the resulting values. It is clear that multiplying $\mathbf{v}_k$ by a constant does not affect Eq. (C.4). However, it is just as meaningless to say that $\|\mathbf{v}_k\| = 1$ as it was to say that $\|\mathbf{x}\| = 1$. In fact, even if all the states do have the same units, this may be a poor choice if they vary on different time scales (for example longitude (λ), which varies very slowly and roll angle (ϕ), which can vary quickly).

We propose a new technique based on Durham [186, 187] that is still based on the information contained in the eigenvectors but has fewer undesirable properties. In addition to the right eigenvectors $\mathbf{v}_1, \ldots, \mathbf{v}_n$, we introduce the left eigenvectors, which satisfy

$$\mathbf{u}_k^T \mathsf{A} = p_k \mathbf{u}_k^T \tag{C.5}$$

We can compile both sets of eigenvectors into matrices

$$\mathsf{U} = \begin{bmatrix} \mathbf{u}_1^T \\ \vdots \\ \mathbf{u}_n^T \end{bmatrix} \qquad\qquad \mathsf{V} = \begin{bmatrix} \mathbf{v}_1 & \cdots & \mathbf{v}_n \end{bmatrix} \tag{C.6}$$

and the poles into a diagonal matrix

$$\mathsf{P} = \begin{bmatrix} p_1 & 0 & \cdots & 0 \\ 0 & p_2 & \ddots & \vdots \\ \vdots & \ddots & \ddots & 0 \\ 0 & \cdots & 0 & p_n \end{bmatrix} \tag{C.7}$$

Then we may write

$$A = VPU \tag{C.8}$$

which is known as a similarity transformation. Assuming that the eigenvalues are unique,

$$\mathbf{u}_\ell^T \mathbf{v}_k = \delta_{\ell k} = \begin{cases} 1 & \text{if } k = \ell, \\ 0 & \text{if } k \neq \ell \end{cases} \tag{C.9}$$

or more succinctly $U = V^{-1}$. Writing $\mathbf{q} = U\mathbf{x}$ and taking a time derivative yields

$$\dot{\mathbf{q}} = U\dot{\mathbf{x}} = UA\mathbf{x} = P\mathbf{q} \tag{C.10}$$

It turns out that this is just another way to write the eigenvalue decomposition. If we decompose an initial condition to Eq. (C.1) as

$$\mathbf{x}(0) = c_1 \mathbf{v}_1 + c_2 \mathbf{v}_2 + \cdots + c_n \mathbf{v}_n \tag{C.11}$$

the solution to the linear system of equations is simply

$$\mathbf{x}(t) = c_1 e^{p_1 t} \mathbf{v}_1 + c_2 e^{p_2 t} \mathbf{v}_2 + \cdots + c_n e^{p_n t} \mathbf{v}_n \tag{C.12}$$

Then

$$\mathbf{q}(0) = \begin{bmatrix} c_1 \\ \vdots \\ c_n \end{bmatrix} \qquad \mathbf{q}(t) = \begin{bmatrix} c_1 e^{p_1 t} \\ \vdots \\ c_n e^{p_n t} \end{bmatrix} \tag{C.13}$$

To see which state variables participate in each mode, we calculate $c_1, \ldots, c_n$ for an initial condition of $\mathbf{x}(0) = \hat{\mathbf{e}}_i$. Here $\hat{\mathbf{e}}_i$ is a unit vector with a one in the ith entry and a zero in all other entries. Since $\mathbf{q} = U\mathbf{x}$, c_j is just the ith component of the jth row eigenvector, u_{ji}. However, using just the row eigenvectors alone would of course have the same problems as using the column eigenvectors. Instead, we use the ith component of each term in Eq. (C.11) (that is, the ith component of $c_j \mathbf{v}_j$), so that the participation of mode j in a perturbation to variable i is

$$s_{ij} = u_{ji} v_{ji} \tag{C.14}$$

We can write these participation values as a matrix

$$S = U^T * V \tag{C.15}$$

where the $*$ operator means that the matrices are applied entry-by-entry rather than using matrix multiplication. The entries of S have various useful properties, which are discussed in the following sections.

C.1 Unit Analysis

Suppose the ith component of the state variable vector, x_i, has units of ξ_i and a value of X_i. In other words

$$\mathbf{x} = \begin{bmatrix} X_1\xi_1 \\ \vdots \\ X_n\xi_n \end{bmatrix} \tag{C.16}$$

This automatically determines the units for each entry of the state linearization matrix A. Specifically,

$$a_{ij} = A_{ij}\alpha_{ij} = A_{ij}\frac{\xi_i}{\xi_j}\frac{1}{\mathrm{s}} \tag{C.17}$$

where the "s" just represents units of seconds, which is required because the left-hand side of Eq. (C.1) is a time derivative. This also means that the eigenvalues have the expected units of 1/s by comparing the equation $A\mathbf{v}_k = p_k\mathbf{v}_k$ to Eq. (C.1). Another way to see this is by looking at Eq. (C.17) and noting that the diagonal entries of A all have units of 1/s, and the characteristic equation for A is only consistent if the eigenvalues have the same units as the diagonal entries of A.

The eigenvectors have a slightly more complicated situation with respect to units. However, since we are able to write $\mathbf{x}$ as a linear combination of the right column eigenvectors as we did in Eq. (C.11), the units of $\mathbf{v}$ must have at least something in common with the units of $\mathbf{x}$. Write

$$\mathbf{v}_j = \begin{bmatrix} V_{j1}\nu_1 \\ \vdots \\ V_{jn}\nu_n \end{bmatrix} \qquad\qquad \mathbf{u}_j = \begin{bmatrix} U_{j1}\eta_1 \\ \vdots \\ U_{jn}\eta_n \end{bmatrix} \tag{C.18}$$

Consider the equation $\mathbf{u}_j^T A = p_j\mathbf{u}_j^T$. The left-hand side is

$$\begin{bmatrix} U_{j1}\eta_1 & \cdots & U_{jn}\eta_n \end{bmatrix} \begin{bmatrix} A_{11}\xi_1/\xi_1 & \cdots & A_{1n}\xi_1/\xi_n \\ \vdots & \ddots & \vdots \\ A_{n1}\xi_n/\xi_1 & \cdots & A_{nn}\xi_n/\xi_n \end{bmatrix} 1/\mathrm{s}$$

The first component of the vector that results from this vector-matrix multiplication is

$$U_{j1}A_{11}\eta_1\frac{\xi_1}{\xi_1} + \cdots + U_{ji}A_{i1}\eta_i\frac{\xi_i}{\xi_1} + \cdots + U_{jn}A_{n1}\eta_n\frac{\xi_n}{\xi_1}$$

Because each of the terms in this expression must have the same units,

$$\eta_i \sim \frac{\xi_1}{\xi_i}\eta_1 \tag{C.19}$$

Similarly, the unit consistency of the multiplication

$$\begin{bmatrix} A_{11}\xi_1/\xi_1 & \cdots & A_{1n}\xi_1/\xi_n \\ \vdots & \ddots & \vdots \\ A_{n1}\xi_n/\xi_1 & \cdots & A_{nn}\xi_n/\xi_n \end{bmatrix} \begin{bmatrix} V_{j1}v_1 \\ \vdots \\ V_{jn}v_n \end{bmatrix}$$

implies that

$$v_i \sim \frac{\xi_i}{\xi_1}v_1 \tag{C.20}$$

Since both η_i and v_i have an extra degree of freedom (i.e. we can multiply each side of Eqs. (C.4) and (C.5) by a constant), we can scale the units of either the left or right eigenvector. The additional constraint that comes from Eq. (C.9) is

$$v_1\eta_1 \sim 1 \tag{C.21}$$

For this work we will assume that $v_1 \sim \eta_1 \sim 1$, that is, that both are non-dimensional. The important conclusion is that each entry of the modal participation matrix is non-dimensional

$$s_{ij} = u_{ji}v_{ji} = U_{ji}V_{ji}\eta_i v_i = U_{ji}V_{ij} \sim 1 \tag{C.22}$$

C.2 Normalization

We have shown that the modal participation matrix contains unitless entries, but there are other nice properties. One of these is that each row and column add up to 1. Typically eigenvectors are normalized so that

$$V_{j1}^2 + V_{j2}^2 + \ldots + V_{jn}^2 = 1$$

but does not actually mean that the norm of $\mathbf{v}_j$ is 1 because we have ignored the units.

From Eq. (C.11), the sum of each row of S is automatically 1. This is because we

defined the entries of the ith row of S to be the ith component of each term in Eq. (C.11) when $\mathbf{x}(0) = \hat{\mathbf{e}}_i$. Since the ith entry of $\hat{\mathbf{e}}_i$ is exactly 1, we must have that the sum of the ith row of S must also be 1.

This is a somewhat surprising property, but it gives an indication that the modal participation matrix S automatically has a good normalization. However, there are two possible complications. First, there can be complex numbers in S, but we will show later that this is not really a problem. A much more difficult situation to interpret is that entries of S may be negative.

Before we go on to address those issues, we can show that the sum of each column of S is also 1. Each column of S corresponds to an element-by-element multiplication of a left eigenvector and a right eigenvector. In other words,

$$\sum_{i=1}^{n} s_{ij} = \sum_{i=1}^{n} u_{ji} v_{ji} = \mathbf{u}_j^T \mathbf{v}_j \qquad (C.23)$$

Since $\mathbf{u}_j^T \mathbf{v}_j$ is the ith entry of the diagonal of UV, and U and V are inverses, the sum is 1.

The next step is to show that s_{ij} can only be complex if p_j is also complex assuming A is a real-valued matrix. Actually the task is quite simple given that both $\mathbf{u}_j$ and $\mathbf{v}_j$ already have the same property. Clearly if both $\mathbf{u}_j$ and $\mathbf{v}_j$ are real, then the jth column of S is also real.

We also can show that the scaling of the eigenvector does not affect the entries of S. Since $\mathbf{u}_j^T \mathbf{v}_j = 1$ for any properly matched left and right eigenvectors, we can determine what happens to the left eigenvector if we consider a right eigenvector of $c_1 \mathbf{v}_j$. The corresponding left eigenvector will become $c_2 \mathbf{u}_j$, but we must still have $(c_2 \mathbf{u}_j^T)(c_1 \mathbf{v}_j) = 1$, so $c_2 c_1 = 1$ even if c_1 and c_2 are complex. The value of s_{ij} goes from $u_{ji} v_{ji}$ to $c_1 c_2 u_{ji} v_{ji}$, so the value of s_{ij} does not change. This is a useful property that can be contrasted with the various options for eigenvector normalization for which the merits continue to be debated [188].

It is also important to realize that the transpose in Eq. (C.15) is a pure transpose and not a conjugate transpose. In other words, the imaginary part of each element remains the same after transposing. If the conjugate transpose were used, the sum of each column involving complex entries would be 0 instead of 1.

C.3   Interpretation

The insight provided in [186] is that each row of S shows how much a given state variable participates each of the modes. Since the columns of S have the same normalization prop-

erties as the rows, it is reasonable to say that the columns represent how much each of the state variables participates in a given mode. The remaining issues to interpret lie with the possibility of complex values in S and entries with negative real values.

We showed in the previous section that s_{ij} can only be complex if p_j is also complex. In this case, there is a matching complex eigenvalue, which we can call p_{j+1} for convenience, that is the complex conjugate of p_j. Fortunately, we also know that $\mathbf{v}_{j+1}$ is the complex conjugate of $\mathbf{v}_j$, which means that the $(j+1)$st column of S is the complex conjugate of column j. It is not surprising that the corresponding columns of S are complex conjugate considering that each row must have a sum of $1+0i$. Our practice is to consider the complex-conjugate pairs as a single mode and use the real parts to determine participation.

Another important task is to determine what a negative real value of s_{ij} actually means. To start, consider the extreme case that $s_{ij} = -1$. An example is the 2×2 matrix

$$\mathsf{A} = \begin{bmatrix} 2 & -\frac{1}{9} \\ 2 & 1 \end{bmatrix} \tag{C.24}$$

The eigenvalues for this matrix are

$$\mathsf{P} = \begin{bmatrix} \frac{5}{3} & 0 \\ 0 & \frac{4}{3} \end{bmatrix} \qquad\qquad \mathsf{V} = \begin{bmatrix} 0.3162 & 0.1644 \\ 0.9487 & 0.9864 \end{bmatrix}$$

The sensitivity matrix for this system is

$$\mathsf{S} = \begin{bmatrix} 2 & -1 \\ -1 & 2 \end{bmatrix}$$

which means essentially that an excitation of either $\hat{\mathbf{e}}_1$ or $\hat{\mathbf{e}}_2$ excites both modes but in opposite directions.

This example points to a few clear problems. The most obvious concern is that the eigenvectors are close to each other (i.e., almost parallel), which naturally suggests that there may be some amount of coupling between the modes. Figure C.1 shows how the eigenvector with the larger eigenvalue tends to dominate solutions for this linear system. All of this can be interpreted in a few different ways. The first is that both variables really do participate in both modes, and the participation matrix should use the absolute values of the entries. A second interpretation is that negative entries should be completely disregarded, but that would imply that the system has two modes that are controlled by only one variable. Thirdly, the modes could be interpreted as combined. Modes are universally considered to be combined when they have a complex conjugate pair of eigenvalues, but there are

170
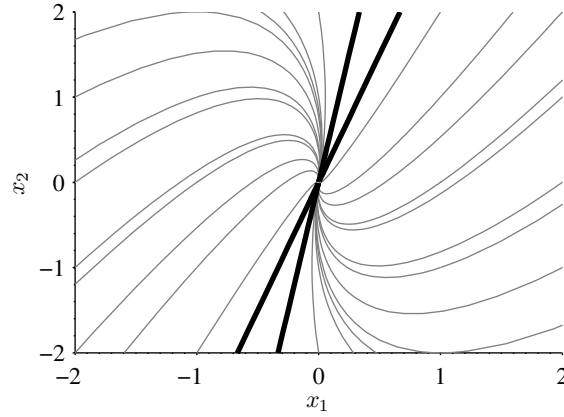
Figure C.1: Sample solutions to linear system from Eq. (C.24).
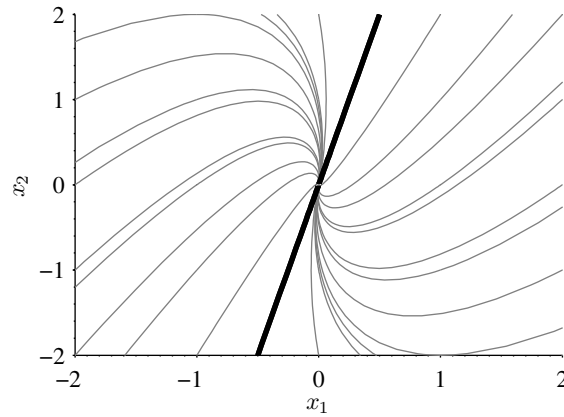
Figure C.2: Sample solutions to linear system from Eq. (C.25), which has a repeated eigenvalue.

many occasions (such as the two real eigenvalues corresponding to an unstable short-period mode) where modes are considered to be combined despite not being a complex-conjugate pair. An important aim of this method is to provide a standard for determining when modes are combined and the degree to which they are coupled.

The previous example indicated that an entry of -1 in the modal participation matrix is not that extreme at all. If we consider the linear system defined by

$$A = \begin{bmatrix} 2 & -\frac{1}{8} \\ 2 & 1 \end{bmatrix} \tag{C.25}$$

This has a single repeated eigenvalue of $\frac{3}{2}$ and a repeated eigenvector of $\mathbf{v} =$

$[0.2425 \quad 0.9701]^T$. As $a_{21} \rightarrow -\frac{1}{8}$, the entries of S diverge to $\pm\infty$. In this case, the modal participation is quite simple to analyze because there is only one mode, and both variables obviously participate in it. Figure C.2 shows some sample solutions to this system, which shows obvious similarity to Fig. C.1.

All of this suggests an interpretation for negative entries in S. The absolute value should be used to determine participation, but negative values indicate a level of coupling between modes. We can see from the definition of S that whenever A does not have a repeated eigenvector, S can be calculated, and all entries are non-infinite real or complex numbers. Then, by contrapositive, if S is undefined, there is at least one repeated eigenvector. Suppose that A has at least one repeated right eigenvector. Then V exists, but it is a singular matrix.

This leaves the question of procedure when A does indeed have a repeated eigenvector. We can avoid the problem of inverting V by calculating the left eigenvectors directly, for example as the transpose of the right eigenvectors of A^T. Then normalize each row of U so that $\mathbf{u}_j^T \mathbf{v}_j = 1$ except for the repeated eigenvectors, for which $\mathbf{u}_j^T \mathbf{v}_j = 0$. For those rows and columns, normalize $\mathbf{u}_j$ so that the maximum absolute value of $\mathbf{u}_j * \mathbf{v}_j$ is 1.

C.4 Summary

The following is a summary of the method to compute the modal participation matrix S given an initial linear system matrix A. Also, the algorithm assumes that it is easy to calculate right eigenvectors but not left eigenvectors.

1. Calculate the eigenvalues and right eigenvectors of A. This gives us V and P such that $AV = VP$.

2. Calculate the left eigenvectors using A^T. This gives us U such that $A^T U^T = U^T P$ with the same matrix P as from step 1.

3. Noramlize each row eigenvector for $j = 1, \ldots, n$. Here $\mathbf{u}_j$ is the jth column of U^T and $\mathbf{v}_j$ is the jth column of V.

   (a) If $\mathbf{u}_j^T \mathbf{v}_j \neq 0$, normalize $\bar{\mathbf{u}}_j = \mathbf{u}_j / (\mathbf{u}_j^T \mathbf{v}_j)$.

   (b) If $\mathbf{u}_j^T \mathbf{v}_j = 0$, normalize $\bar{\mathbf{u}}_j = \mathbf{u}_j / \max|\mathbf{u}_j * \mathbf{v}_j|$.

4. Combine the normalized vectors $\bar{U} = \begin{bmatrix} \bar{\mathbf{u}}_1 & \cdots & \bar{\mathbf{u}}_n \end{bmatrix}^T$.

5. Calculate $S = V * \bar{U}^T$.

Now that we have nominally calculated S, we have a $n \times n$ matrix of numbers that may be complex and that may have negative real parts. The sum of each row is 1 unless A has a repeated eigenvector. In that case the sum of each row is not predictable because of the choice of normalization in step 3.b. The sum of column j is 1 unless $\mathbf{v}_j$ is a repeated eigenvector, in which case the sum of column j is 0.

Since we will be ignoring the complex parts, we can calculate

$$\bar{\mathsf{S}} = \operatorname{Re} \mathsf{S} = \begin{bmatrix} \mathbf{s}_1 & \cdots & \mathbf{s}_n \end{bmatrix} = \begin{bmatrix} \mathbf{r}_1^T \\ \vdots \\ \mathbf{r}_n^T \end{bmatrix}$$

The following list gives useful interpretations of the matrix $\bar{\mathsf{S}}$.

- Each row $\mathbf{r}_i^T$ represents one state variable x_i. The value of r_{ij} represents what fraction of the total participation of x_i goes into mode j.

- Each column $\mathbf{s}_j$ represents one mode, which corresponds to the eigenvalue p_j. The sum of the entries in $\mathbf{s}_j$ is 1 unless p_j is a repeated eigenvalue. Thus the ith entry in $\mathbf{s}_j$, represents how much the state variable x_i participates in mode j relative to other variables.

- Negative entries in $\mathbf{s}_j$ indicate closeness of mode j with another mode. Unfortunately, the location of the negative entry does not seem to indicate which pair of modes are the close ones.

- When deciding if a variable x_i is important to mode j, use the absolute value of the corresponding entry of $\mathbf{s}_j$.

APPENDIX D

Optimal Control for Accelerating Trajectory with Varying Vehicle Mass

The total fuel mass consumed over a trajectory that accelerates from V_1 to V is

$$m_f(V) = \int_{V_1}^{V} \frac{\dot{m}_f(V,a,m_f)}{a}\, dv \tag{D.1}$$

Let $\mathcal{J}$ be the functional that calculates the fuel consumption for a trajectory,

$$\mathcal{J}(a) = \int_{V_1}^{V_2} \frac{\dot{m}_f(V,a,m_f(V,a))}{a}\, dV \tag{D.2}$$

Eq. (D.1) has the complicating factor that the fuel mass at a certain velocity V depends on the fuel mass at all previous velocities $v \in [V_1, V)$. In other words, it is an integral equation, although it is a relatively simple one.

Calculus of variations [181] states that the optimum acceleration a^* satisfies

$$\frac{\partial}{\partial \varepsilon}\, \mathcal{J}\left(a^* + \varepsilon \delta a\right)\Big|_{\varepsilon=0} = 0 \tag{D.3}$$

for any perturbation δa to the optimal acceleration. Evaluating this for Eq. (D.2) gives

$$\begin{aligned}
0 &= \int_{V_1}^{V_2} \frac{\partial}{\partial \varepsilon} \frac{\dot{m}_f(V,a^* + \varepsilon\delta a, m_f)}{a^* + \varepsilon\delta a}\, dV \Bigg|_{\varepsilon=0} \\
&= \int_{V_1}^{V_2} \frac{1}{a^* + \varepsilon\delta a}\left(\frac{\partial \dot{m}_f}{\partial a}\delta a + \frac{\partial \dot{m}_f}{\partial m_f}\frac{\partial m_f}{\partial \varepsilon}\right) - \frac{\dot{m}_f \delta a}{(a^* + \varepsilon\delta a)^2}\Bigg|_{\varepsilon=0} dV \\
&= \int_{V_1}^{V_2} \left(\frac{\partial \dot{m}_f}{\partial a} - \frac{\dot{m}_f}{a^*}\right)\frac{\delta a}{a^*} + \frac{1}{a^*}\frac{\partial \dot{m}_f}{\partial m_f}\left(\frac{\partial m_f}{\partial \varepsilon}\right)_{\varepsilon=0} dV
\end{aligned}$$

The integrand of this last equation must be zero for all perturbations δa. This means that at

174

every velocity V and for every perturbation δa,

$$\left(\frac{\partial \dot{m}_f}{\partial a} - \frac{\dot{m}_f}{a^*}\right)\delta a + \frac{\partial \dot{m}_f}{\partial m_f}\left(\frac{\partial m_f}{\partial \varepsilon}\right)_{\varepsilon=0} = 0 \tag{D.4}$$

Expanding the term $(\partial m_f/\partial \varepsilon)$, we see

$$\left(\frac{\partial \dot{m}_f}{\partial a} - \frac{\dot{m}_f}{a^*}\right)\delta a = \frac{\partial \dot{m}_f}{\partial m_f}\int_{V_1}^{V}\left(\frac{\partial \dot{m}_f}{\partial a} - \frac{\dot{m}_f}{a^*}\right)\frac{\delta a}{a^*} + \frac{1}{a^*}\frac{\partial \dot{m}_f}{\partial m_f}\left(\frac{\partial m_f}{\partial \varepsilon}\right)_{\varepsilon=0} dv$$

but from Eq. (D.4), the right-hand side is identically zero. This means that the optimal acceleration must satisfy

$$\frac{\partial \dot{m}_f}{\partial a} = \frac{\dot{m}_f}{a} \tag{D.5}$$

at each velocity.

This result does not imply that the mass plays no role in the trajectory optimization. Instead, it means that the dependence on the mass is relatively simple. At each velocity, the mass of the vehicle will have a certain value, which affects the performance ($\dot{m}_f$), but the sensitivity of the performance to the mass ($\partial \dot{m}_f/\partial m_f$) has no effect.

One way to interpret the results of this appendix is to say each subset of an optimal acceleration trajectory is also an optimal trajectory. This is a case were Bellman's principle, known in dynamic programming [189], can be applied. In other words, an acceleration $a(V)$ that minimizes the acceleration from $V = V_1$ to $V = V_3$. Then this trajectory must contain the optimum acceleration from $V = V_1$ to $V = V_2$ as well for any $V_2 \in (V_1, V_3)$.

A very similar (although simpler) calculus of variations can be used to find a criterion at each velocity for the dynamic pressure.

$$\frac{\partial \dot{m}_f}{\partial q} = 0 \tag{D.6}$$

Therefore, given two velocities V_1 and V_2, we can find the optimum trajectory, which consists of two functions $q(V)$ and $a(V)$, by solving two equations

$$\frac{\partial \dot{m}_f}{\partial a}(V, a^*, q^*) = \frac{\dot{m}_f(V, a^*, q^*)}{a^*} \tag{D.7}$$

$$\frac{\partial \dot{m}_f}{\partial q}(V, a^*, q^*) = 0 \tag{D.8}$$

for a^* and q^* at each velocity.

BIBLIOGRAPHY

[1] Chase, R. L. and Tang, M. H., "A History of the NASP Program from the Formation of the Joint Program Office to the Termination of the HySTP Scramjet Performance Demonstration Program," *AIAA Sixth International Aerospace Planes and Hypersonics Technologies Conference*, 1995, AIAA Paper 1995-6031. 1, 13

[2] Sippel, M. and Klevanski, J., "Preliminary Definition of Supersonic and Hypersonic Airliner Configurations," *14th AIAA/AHI Space Planes and Hypersonic Systems and Technologies Conference*, 2006, AIAA Paper 2006-7984. 1

[3] Steelant, J., "LAPCAT: High-Speed Propulsion Technology," *Advances on Propulsion Technology for High-Speed Aircraft*, Vol. 12, 2008. 1, 6

[4] Kazmar, R. R., "Hypersonic Missile Propulsion System," Tech. rep., DTIC, 1998. 1

[5] Van Driest, E. R., "The Problem of Aerodynamic Heating," *Aeronautical Engineering Review*, Vol. 15, No. 10, 1956, pp. 26–41. 1, 25, 57

[6] Culler, A. J. and McNamara, J. J., "Studies on Fluid-Thermal-Structural Coupling for Aerothermoelasticity in Hypersonic Flow," *AIAA Journal*, Vol. 48, 2010, pp. 1721–1738. 1

[7] Küchemann, D., *The Aerodynamic Design of Aircraft*, Pergamon Press, 1978. 1

[8] Chavez, F. R. and Schmidt, D. K., "Analytical Aeropropulsive/Aeroelastic Hypersonic-Vehicle Model with Dynamic Analysis," *Journal of Guidance, Control, and Dynamics*, Vol. 17, No. 6, 1994, pp. 1308–1319. 1, 10, 19, 56, 80, 109, 123

[9] Bolender, M. A. and Doman, D. B., "Nonlinear Longitudinal Dynamical Model of an Air-Breathing Hypersonic Vehicle," *Journal of Spacecraft and Rockets*, Vol. 44, No. 2, 2007, pp. 374–387. 1, 10, 11, 12, 13, 19, 80, 109, 123

[10] Bowcutt, K. G., "A Perspective on the Future of Aerospace Vehicle Design," *12 AIAA International Space Planes and Hypersonic Systems and Technologies Conference*, 2003, AIAA Paper 2003-6957. 2, 5

[11] Olds, J. R. and Budianto, I. A., "Constant Dynamic Pressure Trajectory Simulation with POST," *36th Aerospace Sciences Meeting & Exhibit*, 1998, AIAA Paper 1998-0302. 2, 3, 11, 15, 68, 128

[12] Hill, P. G. and Peterson, C. R., *Mechanics and Thermodynamics of Propulsion*, Addison Wesley, 2nd ed., 1992. 2

[13] Cox, T. H. and Jackson, D., "Supersonic flying qualities experience using the SR-71," *AIAA Atmospheric Flight Mechanics Conference*, 1997, AIAA Paper 1997-3654. 5

[14] Smart, M. K., "Optimization of Two-Dimensional Scramjet Inlets," *Journal of Aircraft*, Vol. 36, No. 2, 1999, pp. 430–433. 5, 15, 37, 38, 39, 93, 115, 138

[15] Tang, M. and Chase, R., "Hypersonics–A Periodic Quest," *AIAA/CIRA 13th International Space Planes and Hypersonics Systems and Technologies Conference*, 2005, AIAA Paper 2005-3258. 5, 16

[16] Heppenheimer, T. A., *Facing the Heat Barrier*, National Aeronautics and Space Administration, 2007, NASA SP-2007-4232. 5

[17] Dugger, G. L., "Comparison of Hypersonic Ramjet Engines with Subsonic and Supersonic Combustion," *Fourth AGARD Colloquium*, 1961. 5

[18] Van Camp, V. V. and Williams, E. T., "Porpulsion Options for the Hypersonic Research Airplane," *Journal of Aircraft*, Vol. 12, 1975, pp. 611–616. 5

[19] Weidner, J. P., Small, W. J., and Penland, J. A., "Scramjet Integration on Hypersonic Research Airplane Concepts," *Journal of Aircraft*, Vol. 14, No. 5, 19, pp. 460–466. 5

[20] Bowcutt, K. G., "Multidisciplinary Optimization of Airbreathing Hypersonic Vehicles," *Journal of Propulsion and Power*, Vol. 17, 2001, pp. 1184–1190. 5, 9, 14, 50, 55, 56

[21] Anderson, J. D., *Hypersonic and High-Temperature Gas Dynamics Second Edition*, American Institute of Aeronautics and Astronautics, Reston, Virginia, 2006. 5, 82

[22] McClinton, C., "X-43 - Scramjet Power Breaks the Hypersonic Barrier: Dryden Lectureship in Research for 2006," *44th AIAA Aerospace Scieences Meeting and Exhibit*, 2006. 5, 12, 14

[23] Hank, J. M., Murphy, J. S., and Mutzman, R. C., "The X-51A Scramjet Engine Flight Demonstration Program," *15th AIAA International Space Planes and Hypersonic Systems and Technologies Conference*, 2008, AIAA Paper 2008-2540. 5

[24] Stuckey, R. M. and Lewis, M. J., "Hypersonic Missile Requirements and Operational Tradeoff Studies," *Journal of Spacecraft and Rockets*, Vol. 40, No. 2, 2003, pp. 292–293, Technical Note. 6

[25] Hayward, J. T. and Hooks, D. E., "Remarks by Military Research Leaders," *4th AGARD Colloquium*, 1961. 6, 15

[26] Piland, W., "National Aero-Space Plane," *Twenty-fifth Goddard Memorial Symposium*, 1987, pp. 219–222. 6

[27] Bond, A., Varvill, R., Scott-Scott, J., and Martin, T., "SKYLON–a Realistic Single Stage Spaceplane," *Spaceflight*, Vol. 45, 2003, pp. 158–161. 6

[28] Varvill, R. and Bond, A., "The Skylon spaceplane: progress to realisation," *Journal of the British Interplanetary Society*, Vol. 61, 2008, pp. 412–418. 6

[29] Bentley, M. A., *Spaceplanes: From Airport to Spaceport*, chap. Spaceplanes at the Spaceport, Springer, 2009, pp. 183–195. 6

[30] Bowcutt, K., Smith, T., Kothari, A., Raghavan, V., Tarpley, C., and Livingston, J., "The Hypersonic Space and Global Transportation System: A Concept for Routine and Affordable Access to Space," *17th AIAA International Space Planes and Hypersonic Systems and Technologies Conference*, 2011. 6, 68

[31] Ashford, D., "New business opportunities in space," *Space Policy*, Vol. 23, No. 4, 2007, pp. 241–242. 6

[32] Linehan, D., *SpaceShipOne: an Illustrated History*, Zenith Press, 2011. 6

[33] van Foreest, A., Sippel, M., Cremaschi, F., and Bauer, C., "System Investigations of the SpaceLiner Concept in FAST20XX," *17th AIAA International Space Planes and Hypersonic Systems and Technologies Conference*, 2011. 6

[34] Houchin, R., *US Hypersonic Research and Development: The Rise and Fall of Dyna-Soar, 1944-1963*, Routledge, 2006. 6

[35] Mack, A. and Steelant, J., "FAST20XX: First Progress on European Future High-Altitude High-Speed Transport," *17th AIAA International Space Planes and Hypersonic Systems and technologies Conference*, 2011. 6

[36] Doganis, R., *Flying off course: The economics of international airlines*, Routledge, 2002. 6, 15

[37] Lazur, A. J., Sawyer, J. W., Sullivan, B. J., and Hudson, L., "Hypersonic Vehicle Control Surface Development," 1999, AIAA Paper 1999-45426. 7

[38] Oppenheimer, M. W. and Doman, D. B., "A Hypersonic Vehicle Model Developed with Piston Theory," *AIAA Atmospheric Flight Mechanics Conference and Exhibit*, 2006. 7, 10, 56

[39] Skujins, T., Cesnik, C. E. S., Oppenheimer, M. W., and Doman, D. B., "Canard-Elevon Interactions on a Hypersonic Vehicle," *Journal of Spacecraft and Rockets*, Vol. 47, 2010, pp. 90–100. 7

[40] Noll, T. E., "Aeroservoelasticity," 1990, AIAA Paper 1990-1073-CP. 7

[41] Heeg, J., Gilbert, M. G., and Pototzky, A. S., "Active Control of Aerothermoelastic Effects for a Conceptual Hypersonic Aircraft," *Journal of Aircraft*, Vol. 30, 1993, pp. 453–458. 7

[42] Falkiewicz, N. J., Cesnik, C. E. S., Crowell, A. R., and McNamara, J. J., "Reduced-Order Aerothermoelastic Framework for Hypersonic Vehicle Control Simulation," *AIAA Journal*, Vol. 49, 2011, pp. 1625–1646. 7

[43] Chaussee, D. S. and Rizk, Y. M., "Computation of Viscous Hypersonic Flow Over Control Surfaces," *AIAA 20th Aerospace Sciences Meeting*, 1982, AIAA Paper 1982-0291. 7

[44] Lamorte, N. and Friedmann, P., "Hypersonic Aeroelastic Stability Boundary Computations Using Radial Basis Functions for Mesh Deformation," *18th AIAA/3AF International Space Planes and Hypersonic Systems and Technologies Conference*, 2012. 7

[45] Crowell, A. R. and McNamara, J. J., "Hypersonic Aeroelastic Stability Boundary Computations Using Radial Basis Functions for Mesh Deformation," *AIAA Journal*, Vol. 50, 2012, pp. 74–84. 7

[46] Cole, J. D. and Aroesty, J., "Optimum Hypersonic Lifting Surfaces Close to Flat Plates," *AIAA Journal*, Vol. 3, 1965, pp. 1520–1522. 7

[47] Bowcutt, K. G., Anderson, J. D., and Capriotti, D., "Viscous Optimized Hypersonic Waveriders," *AIAA 25th Aerospace Sciences Meeting*, 1987, AIAA Paper 1987-0272. 7

[48] Tarpley, C. and Lewis, M. J., "Stability Derivatives for a Hypersonic Caret-Wing Waverider," *Journal of Aircraft*, Vol. 32, No. 4, 1995, pp. 795–803. 7, 80

[49] Zien, T. F., "Determination of Surface Pressure and temperature Distributions on Hypersonic Waveriders," *26th Applied Aerodynamics Conference*, 2008, AIAA Paper 2008-6574. 7

[50] Gillum, M., Kammeyer, M., and Burnett, D., "Details of a Mach 14 Waverider Wind Tunnel Test," *18th AIAA Aerospace Ground Testing Conference*, 1994, AIAA Paper 1994-2476. 7

[51] Goldman, R. L. and Morkovin, M. V., "Unsteady Control Surface Loads of Lifting Reentry Vehicles at Very High Speeds," *AIAA 5th Aerospace Sciences Meeting*, 1967, AIAA Paper 1967-15. 7

[52] Gong, L., Quinn, R. D., and Ko, W. L., "Reentry heating analysis of space shuttle with comparison of flight data," Tech. rep., NASA, 1982, CP-2216. 7

[53] Schierman, J., Ward, D., Hull, J., Gandhi, N., Oppenheimer, M., and Doman, D., "Integrated adaptive guidance and control for re-entry vehicles with flight-test results," *Journal of Guidance Control and Dynamics*, Vol. 27, 2004, pp. 975–988. 7

[54] Gombosi, T., *Gaskinetic Theory*, Cambridge University Press, 1994. 8

[55] Brown, M., Mudford, N. R., Neely, A. J., and Ray, T., "Robust Optimization of Two-Dimensional Scramjet Inlets," *14th AIAA/AHI Space Planes and Hypersonic Systems and Technologies Conference*, AIAA Paper 2006-8140, 2006. 8, 15, 19, 93

[56] O'Brien, T. F., "Viscous Performance Map of a Blunt Streamline-Traced Busemann Inlet," *17th AIAA International Space Planes and Hypersonic Systems and Technologies Conference*, 2011, AIAA Paper 2011-2255. 8

[57] Sabean, J. W. and Lewis, M. J., "Performance Optimization of a Supersonic Combustion Ram Accelerator Profile," *Journal of Propulsion and Power*, Vol. 13, No. 5, 1997, pp. 592–600. 8

[58] Billig, F. and Kothari, A. P., "Streamline Tracing: Technique for Designing Hypersonic Vehicles," *Journal of Propulsion and Power*, Vol. 16, 2000, pp. 465–471. 8

[59] Taylor, T. M. and VanWie, D., "Performance Analysis of Hypersonic Shape-Changing Inlets Derived from Morphing Streamline Traced Flowpaths," *15th AIAA International Space Planes and Hypersonic Systems and Technologies Conference*, 2008, AIAA Paper 2008-2635. 8

[60] Bussey, G. H. and Lewis, M. J., "Application of Compound Compressible Flow to Hypersonic Three-Dimensional Inlets," *16th AIAA/DLR/DGLR International Space Planes and Hypersonic Systems and Technologies Conference*, 2009, AIAA Paper 2009-7403. 8, 143

[61] Dalle, D. J., Fotia, M. L., and Driscoll, J. F., "Reduced-Order Modeling of Two-Dimensional Supersonic Flows with Applications to Scramjet Inlets," *Journal of Propulsion and Power*, Vol. 26, No. 3, 2010, pp. 545–555. 8, 15, 19, 22, 33, 34, 37, 80, 93, 115

[62] Pandolfini, P. P., Billig, F. S., Corpening, Griffin, P., Corda, S., and Friedman, M. A., "Analyzing Hypersonic Engines Using the Ramjet Performance Analysis Code," *APL Technical Review*, Vol. 2, 1990, pp. 34–45. 8, 89, 145

[63] Pinckney, S. Z. and Walton, J. T., "Program SRGULL: An Advanced Engineering Model for the Prediction of Airframe-Integrated Subsonic/Supersonic Hydrogen Combustion Ramjet Cycle Performance," Tech. rep., NASA, 1991, TM-1120. 8

[64] Pinckney, S. Z., Ferlemann, S. M., Mills, G., and Takashima, N., "Program Manual for SRGULL, Version 1.0: Secon Generation Engineering Model for the Prediction of Airfram-Integrated Subsonic/Supersonic Combustion Ramjet Cycle Performance," Tech. rep., NASA, 2000, Langley Research Center Report HX-829. 8

[65] Ferlemann, S. M., McClinton, C. R., Rock, K. E., and Voland, R. T., "Hyper-X Mach 7 scramjet design, ground test and flight results," *AIAA/CIRA 13th International Space Planes and Hypersonics Systems and Technologies*, 2005, AIAA Paper 2005-3322. 8, 12

[66] O'Brien, T. F., Starkey, R. P., and Lewis, M. J., "Quasi-One-Dimensional High-Speed Engine Model with Finite-Rate Chemistry," *Journal of Propulsion and Power*, Vol. 17, No. 6, 2001, pp. 1366–1374. 9, 80

[67] Olds, J. R. and Bradford, J. E., "SCCREAM (Simulated Combined-Cycle Rocket Engine Analysis Module): A Conceptual RBCC Engine Design Tool," *33rd AIAA/ASME/SAE/ASEE Joint Propulsion Conference and Exhibit*, 1997, AIAA Paper No. 1997-2760. 9

[68] Torrez, S. M., Driscoll, J. F., Ihme, M., and Fotia, M. L., "Reduced Order Modeling of Turbulent Reacting Flows With Application to Scramjets," *Journal of Propulsion and Power*, Vol. 27, No. 2, March-April 2011, pp. 371–382. 9, 16, 17, 18, 42, 43, 80, 83

[69] Torrez, S. M., Dalle, D. J., and Driscoll, J. F., "New Method for Computing Performance of Choked Reacting Flows and Ram-to-Scram Transition," *Journal of Propulsion and Power*, Vol. 29, No. 2, 2013, pp. 433–445. 9, 16, 17, 18, 42, 80, 82, 83, 86

[70] Peterson, D. M. and Candler, G. V., "Hybrid Reynolds-Averaged and Large-Eddy Simulation of Normal Injection into a Supersonic Crossflow," *Journal of Propulsion and Power*, Vol. 26, No. 3, 2010, pp. 533–544. 9

[71] Peterson, D. M., Candler, G. V., and Drayna, T. W., "Detached Eddy Simulation of a Generic Scramjet Inlet and Combustor," *47th AIAA Aerospace Sciences Meeting Including The New Horizons Forum and Aerospace Exposition*, 2009, AIAA Paper 2009-130. 9

[72] Baurle, R. A. and Eklund, D. R., "Analysis of Dual-Mode Hydrocarbon Scramjet Operation at Mach 4-6.5," *Journal of Propulsion and Power*, Vol. 18, No. 5, 2002, pp. 990–1002. 9

[73] Nickerson, G. R. and Dunn, S. S., "Optimized Supersonic Exhaust Nozzles for Hypersonic Propulsion," *AIAA/ASME/SAE/ASEE 24th Joint Propulsion Conference*, AIAA Paper 1988-3161. 9, 15

[74] Sangiovanni, J. J., Barber, T. J., and Syed, S. A., "Role of Hydrogen/Air Chemistry in Nozzle Performance for a Hypersonic Propulsion System," *Journal of Propulsion and Power*, Vol. 9, No. 1, 1993, pp. 134–138. 9, 46

[75] Dalle, D. J., Torrez, S. M., and Driscoll, J. F., "Reduced-Order Modeling of Reacting Supersonic Flows in Scramjet Nozzles," *46th AIAA/ASME/SAE/ASEE Joint Propulsion Conference & Exhibit*, 2010, AIAA Paper 2010-6958. 9

[76] Dalle, D. J., Torrez, S. M., and Driscoll, J. F., "Rapid Analysis of Scramjet and Linear Plug Nozzles," *Journal of Propulsion and Power*, Vol. 28, No. 3, 2012, pp. 545–555. 9, 45, 80

181

[77] Angelino, G., "Approximate Method for Plug Nozzle Design," *AIAA Journal*, Vol. 2, No. 10, 1964, pp. 1834–1835. 9

[78] Giel, Jr, T. V. and Mueller, T. J., "Mach Disk in Truncated Plug Nozzle Flows," *Journal of Spacecraft and Rockets*, Vol. 13, No. 4, 1976, pp. 203–207. 9

[79] Chutkey, K., Balakrishnan, N., and Vasudevan, B., "Experimental analysis of linear plug nozzle," *15th AIAA International Space Planes and Hypersonic Systems and Technologies Conference*, 2008, AIAA Paper 2008-2628. 9, 12, 46

[80] Rommel, T., Hagemann, G., Schley, C.-A., Krülle, G., and Manski, D., "Plug Nozzle Flowfield Analysis," *Journal of Propulsion and Power*, Vol. 13, No. 5, 1997, pp. 629–634. 9

[81] Nasuti, F. and Onofri, M., "Analysis of In-Flight Behavior of Truncated Plug Nozzles," *Journal of Propulsion and Power*, Vol. 17, No. 4, 2001, pp. 809–817. 9

[82] Bolender, M. A. and Doman, D. B., "A Non-Linear Model for the Longitudinal Dynamics of a Hypersonic Air-breathing Vehicle," *AIAA Guidance, Navigation and Control Conference*, AIAA Paper No. 2005-6255, August 2005. 10

[83] Bolender, M. A., Oppenheimer, M. W., and Doman, D. B., "Effects of Unsteady and Viscous Aerodynamics on the Dynamics of a Flexible Air-breathing Hypersonic Vehicle," *AIAA Atmospheric Flight Mechanics Conference and Exhibit*, 2007, AIAA Paper 2007-6397. 10

[84] Frendreis, S. G. V., Skujins, T., and Cesnik, C. E. S., "Six-Degree-of-Freedom Simulation of Hypersonic Vehicles," *AIAA Atmospheric Flight Mechanics Conference*, 2009, AIAA Paper 2009-5601. 10, 109

[85] Frendreis, S. G. V. and Cesnik, C. E. S., "3D Simulation of a Flexible Hypersonic Vehicle," *Atmospheric Flight Mechanics Conference & Exhibit*, 2010, AIAA Paper 2010-8229. 10

[86] Dalle, D. J. and Driscoll, J. F., "Continuous Differentiation of Complex Systems Applied to a Hypersonic Vehicle," *AIAA Atmospheric Flight Mechanics Conference*, 2012, AIAA Paper 2012-4958. 10

[87] Ardema, M. D., "Singular Perturbations in Flight Mechanics," Tech. rep., NASA, July 1977, TM-X-62-380. 10

[88] Mehra, R. K., Washburn, R. B., Sajan, S., and Carroll, J. V., "A Study of the Application of Singular Perturbation Theory," Tech. rep., NASA, 1979, Contractor Report 3167. 10

[89] Halter, M. C. and Cliff, E. M., "Optimal Energy-Heading Transients for an Air-breathing Hypersonic Vehicle," 1991. 10, 15, 70

[90] Chichka, D. F., Shankar, U. J., Cliff, E. M., and Kelley, H. J., "Cruise-Dash-Climb Analysis of an Airbreathing Missle," *Journal of Guidance*, Vol. 11, No. 4, 1988, pp. 293–299. 10, 15, 80

[91] Calise, A. J., Corban, J. E., and Flandro, G. A., "Trajectory optimization and guidance law development for national aerospace plane applications," *American Control Conference*, 1988, pp. 1406–1411. 10, 12, 15, 129

[92] Corban, J. E., Calise, A. J., and Flandro, G. A., "Rapid Near-Optimal Aerospace Plane Trajectory Generation and Guidance," *Journal of Guidance*, Vol. 14, 1991, pp. 1181–1190. 11, 15, 129

[93] Keshmiri, S., Colgren, R., and Mirmirani, M., "Trajectory Optimization for a Generic Hypersonic Vehicle," *14th AIAA/AHI Space Planes and Hypersonic Systems and Technologies Conference*, 2006, AIAA Paper 2006-8157. 11, 15

[94] Gilbert, E. G., Howe, R. M., Lu, P., and Vinh, N. X., "Optimal aeroassisted intercept trajectories at hyperbolic speeds," *Journal of Guidance, Control, and Dynamics*, Vol. 14, 1991, pp. 123–131. 11, 15

[95] Lu, P., "Inverse Dynamics Approach to Trajectory Optimization for an Aerospace Plane," *Journal of Guidance, Control, and Dynamics*, Vol. 16, 1993, pp. 726–732. 11, 15

[96] Lu, P., "Analytical Solutions to Constrained Hypersonic Flight Trajectories," *Journal of Guidance, Control, and Dynamics*, Vol. 16, 1993, pp. 956–960. 11, 15

[97] Brauer, G. L., Cornick, D. E., and Stevenson, R., "Capabilities and applications of the Program to Optimize Simulated Trajectories (POST). Program summary document," 1977. 11

[98] Grant, M. J., Clark, I. G., and Braun, R. D., "Rapid Design Space Exploration for Conceptual Design of Hypersonic Missions," *AIAA Atmospheric Flight Mechanics Conference*, 2011, AIAA Paper 2011-6576. 11, 15

[99] Torrez, S. M., *Design Refinement and Modeling Methods for Highly-Integrated Hypersonic Vehicles*, Ph.D. thesis, University of Michigan, 2012. 11, 16, 17, 18, 42

[100] Hargraves, C. R. and Paris, S. W., "Direct Trajectory Optimization Using Nonlinear Programming and Collocation," *Journal of Guidance*, Vol. 10, No. 31, 1987, pp. 338–342. 11

[101] Spangelo, S. C. and Gilbert, E. G., "Power Optimization of Solar-Powered Aircraft with Specified Closed Ground Tracks," *Journal of Aircraft*, Vol. 50, No. 1, 2013, pp. 232–238. 11

[102] Schmidt, D., "Integrated Control of Hypersonic Vehicles," *AIAA/DGLR Fifth International Aerospace Planes and Hypersonics Technologies Conference*, 1993, AIAA Paper 1993-5091. 11

[103] Raney, D. and Lallman, F., "Control Integration Concept for Hypersonic Cruise-Turn Maneuvers," Tech. Rep. TP 3136, NASA, 1992. 11, 70

[104] Parker, J. T., Serrani, A., Yurkovich, S., Bolender, M. A., and Doman, D. B., "Control-Oriented Modeling of an Air-Breathing Hypersonic Vehicle," *Journal of Guidance, Control, and Dynamics*, Vol. 30, No. 3bow, 2007, pp. 856–869. 11, 12, 75

[105] Fidan, B., Mirmirani, M., and Ioannou, P. A., "Flight Dynamics and Control of Air-Breathing Hypersonic Vehicles: Review and New Directions," *12th AIAA International Space Planes and Hypersonic Systems and Technologies*, 2003. 11

[106] Torrez, S. M., Driscoll, J. F., Bolender, M. A., Oppenheimer, M. W., and Doman, D. B., "Effects of Improved Propulsion Modelling on the Flight Dynamics of Hypersonic Vehicles," *AIAA Atmospheric Flight Mechanics Conference and Exhibit*, 2008, AIAA Paper 2008-6386. 11

[107] Lewis, M. J., "Significance of Fuel Selection for Hypersonic Vehicle Range," *Journal of Propulsion and Power*, Vol. 17, No. 6, 2001, pp. 1214–1221. 11, 13, 14

[108] Robinson, M. J., Mee, D. J., and Paull, A., "Scramjet Lift, Thrust and Pitching-Moment Characteristics Measured in a Shock Tunnel," *Journal of Propulsion and Power*, Vol. 22, No. 1, 2006, pp. 85–95. 12

[109] Emami, S., Trexler, C. A., Auslender, A. H., and Weidner, J. P., "Experimental Investigation of Inlet-Combustor Isolators for a Dual-Mode Scramjet at a Mach Number of 4," Tech. rep., NASA, May 1995, Technical Paper 3502. 12, 35

[110] Fernandez, R., Trefny, C. J., Thomas, S. R., and Bulman, M. J., "Parametric Data From a Wind Tunnel Test on a Rocket-Based Combined-Cycle Engine Inlet," Tech. rep., NASA, 2001, TM–2001-107181. 12

[111] Micka, D. J. and Driscoll, J. F., "Combustion characteristics of a dual-mode scramjet combustor with cavity flameholder," *Proceedings of the Combustion Institute*, Vol. 32, 2009, pp. 2397–2404. 12

[112] Micka, D. J., Torrez, S. M., and Driscoll, J. F., "Measurements and Modeling of the Heat Release Distribution in a Dual-mode Scramjet Combustor with Wall Fuel Injection," *Proceedings of the 6th U.S. National Combustion Meeting*, 2009. 12

[113] Fotia, M. L. and Driscoll, J. F., "Isolator-Combustor Interactions in a Direct-Connect Ramjet-Scramjet Experiment," *Journal of Propulsion and Power*, Vol. 28, No. 1, 2012, pp. 83–85. 12, 42, 80, 83, 86, 87, 88, 89, 98

[114] Fotia, M. L. and Driscoll, J. F., "Ram-Scram Transition and Flame/Shock-Train Interactions in a Model Scramjet Experiment," *Journal of Propulsion and Power*, 2012. 12, 42, 80, 83, 86, 87, 88, 98

[115] Rausch, V. L., Nygen, L. T., and Sitz, J. R., "Flight Test Results from Hyper-X," *55th International Astronautical Congress*, 2004, IAC-04-V.6.01. 12

[116] Sampson, C. and VanNierop, D., "X-51A WaveRider," Tech. rep., Boeing, 2012. 13

[117] Froning, D., Gaubatz, W., and Mathews, G., "NASP: Enabling New Space Launch Options," *AIAA Second International Aerospace Planes Conference*, 1990, AIAA Paper 1990-5263. 13

[118] Chudoba, B., "Aircraft Volume and Mass Guidelines," Tech. rep., National Institute of Aerospace, June 2008, Hypersonic Educational Initiative Hypersonic Vehicle System Integration Short Course. 13, 50, 53, 54

[119] Raymer, D. P., *Aircraft Design: A Conceptual Approach*, AIAA Education Series, Reston, VA, 4th ed., 2006. 13

[120] Ardema, M. D., Chambers, M. C., Terjesen, E. J., and Roberts, C. D., "Body Weight of Advanced Concept Hypersonic Airfcraft," *AIAA Aircraft Design Systems and Operations Meeting*, 1991, AIAA Paper 1991-3180. 13, 55

[121] Ardema, M. D., "Body Weight of Hypersonic Aircraft: Part 1," Tech. rep., NASA TM-101028, 1988. 13

[122] Ardema, M. D. and Chambers, M. C., "Body Weight of Hypersonic Aircraft: Part 2," Tech. rep., NASA TM-102797, 1990. 13

[123] Lewis, M. J. and Takashima, N., "Optimization of Waverider-Based Hypersonic Cruise Vehicles with Off-Design Considerations," *Journal of Aircraft*, Vol. 36, No. 1, 1999, pp. 235–245. 13

[124] Hall, K. R., Brown, S. W., Bennett, A. G., and Rais-Rohani, M., "Construction of a One-Third Scale Model of the NASP," *31st Aerospace Sciences Meeting & Exhibit*, 1993, AIAA Paper 1993-0427. 13

[125] Taube, L. J., "B-70 Aircraft Study Final Report, Volume 1," Tech. rep., North American Rockwell, 1972, SD 72-SH-0003. 14

[126] Schmit, Jr., L. A., "Structural synthesis–precursor and catalyst. Recent experiences in multidisciplinary analysis and optimization," Tech. Rep. CP-2337, NASA, 1984. 14

[127] Martins, J. R. R. A. and Lambe, A. B., "Multidiciplinary Design Optimization: Survey of Architectures," *AIAA Journal*, *To appear*. 14

[128] Bing, C., Xu, X., and Guobiao, C., "Single- and Multi-objective Optimization of Scramjet Components Using Genetic Algorithms Based on a Parabolized Navier-Stokes Solver," *42nd AIAA/ASME/SAE/ASEE Joint Propulsion Conference & Exhibit*, 2006, AIAA Paper 2006-4686. 14

[129] Theisinger, J. E. and Braun, R. D., "Multiobjective Hypersonic Entry Aeroshell Shape Optimization," *12th AIAA/ISSMO Multidisciplinary Analysis and Optimizaition Conference*, 2008, AIAA Paper 2008-5873. 14

[130] Grant, M. J., Clark, I. G., and Braun, R. D., "Rapid Simultaneous Hypersonic Aerodynamic and Trajectory Optimization Using Variational Methods," *AIAA Atmospheric Flight Mechanics Conference*, 2011, AIAA Paper 2011-6640. 14, 15

[131] Torrez, S. M., Driscoll, J. F., Dalle, D. J., and Fotia, M. L., "Preliminary Design Methodology for Hypersonic Engine Flowpaths," *16th AIAA/DLR/DGLR International Space Planes and Hypersonic Systems and Technologies Conference*, 2009, AIAA Paper 2009-7289. 15, 33, 37, 93, 115, 117, 125, 139

[132] Payne, M. D., Chrissis, J. W., Phl, E. A., Bowersox, R. D. W., Gruber, M. R., and Fuller, R. P., "Optimizing Scramjet Fuel Injection Array Design," *35th AIAA/ASME/SAE/ASEE Joint Propulsion Conference*, 1999, AIAA Paper 1999-2251. 15

[133] Loftin Jr., L. K., "Aeronautical vehicles—1970 and Beyond," *Journal of Aircraft*, Vol. 8, 1971, pp. 939–951. 15

[134] Petersen, R. H. and Waters, M. H., "Hypersonic Transports—Economics and Environmental Effects," *Journal of Aircraft*, Vol. 10, 1973, pp. 334–341. 15

[135] Sastre, P., "Supersonic air transport—True Problems and Misconceptions," *Journal of Aircraft*, Vol. 7, 1970, pp. 3–12. 15

[136] Woolley, P. K., "A Cost-Benefit Analysis of the Concorde Project," *Journal of Transport Economics and Policy*, Vol. 6, No. 3, 1972, pp. 225–239. 15

[137] Seebass, R. and Woodhull, J. R., "History and economics of, and prospect for, commercial supersonic transport," *RTO AVT course on Fluid dynamics research on supersonic aircraft*, 1998. 15

[138] Arkes, H. R. and Ayton, P., "The sunk cost and Concorde effects: Are humans less rational than lower animals?" *Psychological Bulletin*, Vol. 125, 1999, pp. 591–600. 15

[139] Cole, J. M., "Russia, China, and Amarica's Hypersonic Missile Race," *The Diplomat*, 2012. 15

[140] Bentley, M. A., *Spaceplanes: From Airport to Spaceport*, chap. Crawling into Suborbit: The Baby Spaceplane, Springer, 2009, pp. 69–81. 15

[141] Argodale, J., Bird, K., Breen, T., Christensen, D., and Dellinger, N., "2001 Industry Studies: Space," Tech. rep., DTIC Document, 2001. 16

[142] Span, Y. S. and Sotomayer, W. A., "Sonic Boom of Hypersonic Vehicles," *AIAA Journal*, Vol. 10, 1972, pp. 550–551. 16

[143] Harris Jr., R. V., "On the Threshold–The Outlook for Supersonic and Hypersonic Aircraft," *Journal of Aircraft*, Vol. 29, No. 1, 1992, pp. 10–19. 16

[144] Bakker, P. and van Leer, B., "Lecture Notes for AERO 520: Compressible Flow," Tech. rep., University of Michigan, 2008, pp. 159-171. 20

[145] Anderson, J. D., *Modern Compressible Flow with Historical Perspective*, McGraw-Hill, 2002. 20

[146] Briggs, J. L., "Comment on Calculation of Oblique Shock Waves," *AIAA Journal*, Vol. 2, No. 5, 1964, pp. 974. 21

[147] Anderson, J. D., *Fundamentals of Aerodynamics*, McGraw-Hill, 2nd ed., 1991. 21, 68

[148] White, F. M., *Viscous Fluid Flow*, McGraww-Hill, third edition, international edition ed., 2006, p. 549, 554, 555. 26

[149] Anon., "CFD++ User Manual," Tech. rep., Metacomp Technologies, Inc., Agoura Hills, California, 2006, Version 8.1. 34

[150] Dalle, D. J., Torrez, S. M., and Driscoll, J. F., "Performance Analysis of Variable-Geometry Scramjet Inlets Using a Fundamental Model," *47th AIAA/ASME/SAE/ASEE Joint Propulsion Conference and Exhibit*, 2011. 37, 39, 77, 93, 115, 125

[151] Heiser, W. H. and Pratt, D. T., *Hypersonic Airbreathing Propulsion*, AIAA Education Series, Washington, DC, 1994. 41, 82, 86, 89

[152] Ikui, T., Matsuo, K., and Nagai, M., "The Mechanism of Pseudo-Shock Waves," *Bulletin of the JSME*, Vol. 17, No. 108, June 1974, pp. 731–739. 42, 83

[153] Smith, S. H. and Mungal, M. G., "Mixing, structure and scaling of the jet in crossflow," *Journal of Fluid Mechanics*, Vol. 357, 1998, pp. 83–122. 43, 44

[154] Hasselbrink, Jr., E. F. and Mungal, M. G., "Transverse jets and jet flames. Part 1. Scaling laws for strong transverse jets," *Journal of Fluid Mechanics*, Vol. 443, 2001, pp. 1–25. 43, 44

[155] Fluent, "FLUENT 6.3 User's Guide," Tech. rep., Ansys, Inc., 09 2006. 44

[156] Dalle, D. J. and Torrez, S. M., "User Manual for the Michigan/AFRL Scramjet in Vehicle Code," Tech. rep., University of Michigan, Ann Arbor, MI, 2013, Version 2.4. 50

[157] Dalle, D. J., Frendreis, S. G. V., Driscoll, J. F., and Cesnik, C. E. S., "Hypersonic Vehicle Flight Dynamics with Coupled Aerodynamics and Reduced-order Propulsive Models," *AIAA Atmospheric Flight Mechanics Conference & Exhibit*, 2010, AIAA Paper 2010-7930. 52

[158] Vick, T. J., Muse, J. A., and Bolender, M. A., "A Hypersonic Vehicle Model Generator for MASIV," *AIAA Modeling and Simulation Technologies Conference*, 2012. 52, 56, 145

[159] Anon., "Department of Defense World Geodetic System 1984," Tech. Rep. TR8350.2, 3rd ed., National Imagery and Mapping Agency (now NGA), 1997. 61, 159

[160] Groves, P. D., *Principles of GNSS, Inertial, and Multisensor Integrated Navigations Systems*, Artec House, 2008. 61, 159, 162

[161] Dalle, D. J., Torrez, S. M., Driscoll, J. F., and Bolender, M. A., "Flight Envelope Calculation of a Hypersonic Vehicle Usinga First Principles-Derived Model," *17th AIAA International Space Planes and Hypersonic Systems and Technologies Conference*, 2011. 64, 80, 117

[162] Tausche, M., Janovsky, R., Scheper, M., Apeldoorn, J., Monti, R., Savina, R., Fumo, M. D. S., Paterna, D., Sotto, E. D., ao Branco, J., and Molina, R., "PHOEBUS: A High Lift-over-Drag Vehicle for Earth Reentry," *16th AIAA/DLR/DGLR International Space Planes and Hypersonic Systems and Technologies Conference*, 2009, AIAA Paper 2009-7411. 69

[163] Eisler, G. R. and Hull, D. G., "Optimal Descending, Hypersonic Turn to Heading," *Journal of Guidance*, Vol. 10, No. 3, 1987, pp. 255–261. 69

[164] Roenneke, A. J. and Cornwell, P. J., "Trajectory Control for a Low-Lift Re-Entry Vehicle," *Journal of Guidance, Control, and Dynamics*, Vol. 16, No. 5, 1993, pp. 927–933. 69

[165] Mooij, E., "Numerical Investigation of Model Reference Adaptive Control for Hypersonic Aircraft," *Journal of Guidance, Control, and Dynamics*, Vol. 24, No. 2, 2001, pp. 315–323. 69

[166] Schöttle, U. M. and Hillesheimer, M., "Performance Optimization of an Airbreathing Launch Vehicle by a Sequential Trajectory Optimization and Vehicle Design Scheme," *AIAA Guidance, Navigation and Control Conference*, 1991, AIAA Paper 91-2655. 70

[167] Dalle, D. J., Torrez, S. M., and Driscoll, J. F., "Sensitivity of Flight Dynamics of Hypersonic Vehicles to Design Parameters," *18th AIAA International Space Planes and Hypersonic Systems and Technologies Conference*, 2012, AIAA Paper 2012-5909. 77, 80, 95, 109

[168] Billig, F. S., "Combustion processes in supersonic flow," *Journal of Propulsion and Power*, Vol. 4, 1988, pp. 209–216. 80, 89

[169] Rodriguez, A. A., Dickeson, J. J., Cifdaloz, O., McCullen, R., Benavides, J., Sridharan, S., Kelkar, A., Vogel, J. M., and Soloway, D., "Modeling and Control of

Scramjet-Powered Hypersonic Vehicles: Challenges, Trends, & Tradeoffs," *AIAA Guidance, Navigation and Control Conference and Exhibit*, 2008, AIAA 2008-6793. 80

[170] Starkey, R. P. and Lewis, M. J., "Critical Design Issues for Airbreathing Hypersonic Waverider Missiles," *Journal of Spacecraft and Rockets*, Vol. 38, No. 4, 2001, pp. 510–519. 80

[171] Starkey, R. P., "Off-Design Performance Characterization of a Variable Geometry Scramjet," *41st AIAA/ASME/SAE/ASEE Joint Propulsion Conference & Exhibit*, 2005, AIAA Paper 2005-3711. 80

[172] Tetlow, M. R. and Doolan, C., "Comparison of Hydrogen and Hydrocarbon-Fueled Scramjet Engines for Orbital Insertion," *Journal of Spacecraft and Rockets*, Vol. 44, No. 2, 2007, pp. 365–372. 80

[173] Rodriguez, A. A., Dickeson, J. J., Sridharan, S., Korad, A., Khatri, J., Benavides, J., Soloway, D., Kelkar, A., and Vogel, J., "Control-Relevant Modeling, Analysis, and Design for Scramjet-Powered Hypersonic Vehicles," *16th AIAA/DLR/DGLR International Space Planes and Hypersonic Systems and Technologies Conference*, 2009, AIAA Paper 2009-7287. 80

[174] Shapiro, A. H., *Dynamics and Thermodynamics of Compressible Fluid Flow*, Ronald Press, NY, 1953. 82

[175] Dalle, D. J., Torrez, S. M., and Driscoll, J. F., "Unstart Margin and Ram-Scram Transition Boundaries Computed for Hypersonic Vehicles," *Journal of Propulsion and Power*, 2013, *Submitted*. 82

[176] Sullins, G. A., "Demonstration of Mode Transition in a Scramjet Combustor," *Journal of Propulsion and Power*, Vol. 9, 1993, pp. 515–520. 86

[177] Cui, T., Tang, S., Zhang, C., and Yu, D., "Hysteresis Phenomenon of Mode Transition in Ramjet Engines and Its Topological Rule," *Journal of Propulsion and Power*, Vol. 28, No. 6, 2012, pp. 1277–1284. 100

[178] "U.S. Standard Atmosphere," U.S. Government Printing Office, 1976, Washington, D.C. 104

[179] Kosmodemyansky, A. and Danko, X., *Konstantin Tsiokovsky His Life and Work*, The Minerva Group, Inc., 2000. 105

[180] Moore, W., *A Treatise on the Motion of Rockets*, Royol Military Academy, 1813, p. 645. 105

[181] Strauss, W. A., *Partial Differential Equations, An Introduction*, John Wiley & Sons, 1992. 106, 174

[182] Dalle, D. J., Torrez, S. M., and Driscoll, J. F., "Turn Performance of an Air-Breathing Hypersonic Vehicle," *AIAA Atmospheric Flight Mechanics Conference*, 2011. 109

[183] Bernstein, A., Heiser, W. H., and Hevenor, C., "Compound-Compressible Nozzle Flow," *Journal of Applied Mechanics*, Vol. 34, No. 3, 1967, pp. 548–554. 143

[184] Ihme, M., Marsden, A. L., and Pitsch, H., "Generation of optimal artificial neural networks using a pattern search algorithm: Application to approximation of chemical systems," *Neural Computation*, Vol. 20, No. 2, 2008, pp. 573–601. 145

[185] Yechout, T. R., Morris, S. L., Bossert, D. E., and Hallgren, W. F., *Introduction to Aircraft Flight Mechanics*, AIAA Education Series, Reston, VA, 2003. 158

[186] Durham, W., "Aircraft Dynamics & Control," http://www.aoe.vt.edu/~durham/AOE5214, accessed March 26, 2012. 165, 169

[187] Durham, W., *Personal communication*. 165

[188] Murthy, D. V. and Haftka, R. T., "Derivatives of eigenvalues and eigenvectors of a general complex matrix," *International Journal for Numerical Methods in Engineering*, Vol. 26, 1988, pp. 293–311. 169

[189] Bellman, R. E., *Dynamic Programming*, Princeton University Press, 1957. 175